



University
of Glasgow

Mari, Nicola (2020) *The formation and evolution of the Martian mantle: a Martian meteorite perspective*. PhD thesis.

<https://theses.gla.ac.uk/81314/>

Copyright and moral rights for this work are retained by the author

A copy can be downloaded for personal non-commercial research or study, without prior permission or charge

This work cannot be reproduced or quoted extensively from without first obtaining permission in writing from the author

The content must not be changed in any way or sold commercially in any format or medium without the formal permission of the author

When referring to this work, full bibliographic details including the author, title, awarding institution and date of the thesis must be given

Enlighten: Theses

<https://theses.gla.ac.uk/>
research-enlighten@glasgow.ac.uk

THE FORMATION AND EVOLUTION OF THE MARTIAN MANTLE: A MARTIAN METEORITE PERSPECTIVE

By

Nicola Mari



Submitted in fulfilment of the requirements for the degree of

Doctor of Philosophy

at the

School of Geographical and Earth Sciences

College of Science and Engineering

University of Glasgow

2020

© Nicola Mari All rights reserved.

The author hereby grants to the University of Glasgow permission to reproduce and redistribute publicly paper and electronic copies of this thesis document in whole or in any part in any medium now known or hereafter created.

Signature of Author:

20th March 2020

Abstract

Revealing the internal composition and evolution of the terrestrial planets is crucial to understanding planetary evolution in the Solar System and beyond. Mars is a perfect source of this information, since its mantle was not homogenized after the earliest phases of planetary differentiation. However, the interior evolution and composition of Mars is still unknown. Martian meteorites are the only rock samples from Mars that are available on Earth. The aim of this research is to obtain new insights about Martian mantle formation and its evolution from the perspective of the Martian meteorites. In particular, this work is divided into three interdisciplinary investigations in order to obtain new constraints on our knowledge about the Martian mantle. Firstly, the Tissint Martian meteorite was investigated since it is the meteorite that is most representative of the Martian mantle. This meteorite was analysed with the objective of obtaining information about the thermal state and convective activity in the Mars' mantle. Major- and trace-element data for Tissint olivine and pyroxene were reported, and these data were used to provide new insights into the dynamics of the Tissint magma chamber, as well as the dynamics and temperature of Martian mantle at the time of Tissint crystallisation. Secondly, the potential for chemical tracing of the different Martian mantle sources was investigated by analysing rhenium-osmium and sulphur isotope compositions in five of the ten known nakhlite lava flows (Nakhla, Lafayette, MIL 090032, Yamato 000593, and Yamato 000749). In addition, these findings were used to suggest a plausible scenario to account for nakhlite magma origins. These findings were also utilised to discuss the implications of this work for fingerprinting the processes responsible for setting Martian mantle compositions during late-stage crystallization of a Martian magma ocean. Thirdly, the abundance of the volatile element chlorine in the Martian mantle was calculated by analysing amphibole and apatite phases in the two shergottites Tissint and Zagami. After finding that these phases record magmatic conditions of the Martian interior, the partition coefficients between chlorine and the parent melt were used to estimate the chlorine abundance of the shergottite magma source. In sum, the importance of the combined new findings are presented to explore their implications for

our understanding of Mars' formation and evolution and, more generally, the evolution of terrestrial planets.

Acknowledgement

I would to express my gratitude to my advisors at the University of Glasgow. First of all, my main supervisor Dr. Lydia Hallis, for her immense help and suggestions about conducting research as a scientist. I would also to thank my co-supervisors: Dr. Martin Lee, for his help and for permitting me to do this PhD, and Dr. Amy Riches, for her useful suggestions and help with extremely challenging laboratory analyses.

I am grateful to NASA Antarctic Search for Meteorites, JAXA, Dr. Caroline Smith of the Natural History Museum of London, University of Alberta Museum, and the Scottish Universities Environmental Research Centre for provision and loan of the Martian meteorite samples, and to P. Chung, H. Jackson, and S. Mcfadzean for their help during SEM-EDS, LA-ICP-MS, and TEM-EDS analyses, respectively. A special thanks to: Robert MacDonald, for its help with sample preparation; John Faithful, for providing unusual geological samples; and Nikki Potts, for her help with tricky experiments.

Funding bodies were involved in funding this research. Thanks to the Australian Research Council, for funding of the microprobe work, and to the Centre for Microscopy, Characterisation and Analysis of University of Western Australia, particularly the assistance and expertise provided by Dr. Malcolm Roberts. Thanks also to Dr. Yves Marrocchi for funding of the SIMS work at the Centre de Recherches Pétrographiques et Géochimiques in France.

I would to thanks all the amazing Planetary Science and Astrobiology Research Group of the University of Glasgow, along with all people of Room 414A. I also thanks all my friends in Glasgow, especially the grotesque Italian group (Giuseppe, Erik, Eugenio, Manuel, etc...) and Mike, David, and Manel. Thanks also to all my hometown friends (really, everyone!). Special gratitude is reserved to my family, Mamma, Papà, and my two sisters. Without their support I would never have done any PhD.

And, I also want to thanks myself for making the dreams of my childhood a reality.

Author's Declaration

The Chapter 3, 4, and 5 of the present thesis are presented in a 'paper format', accordingly to the PGR Code of Practice of the University of Glasgow.

I confirm that this thesis is my own original work. A Declaration of Originality form is attached to this thesis.

Table of contents

Abstract.....	2
Acknowledgement.....	4
Author’s declaration.....	5
Table of contents.....	6
1 - Introduction.....	11
1.1- Formation and evolution of Mars.....	11
1.1.1 - <i>Planetary accretion and early differentiation</i>	11
1.1.2 - <i>Mars formation</i>	13
1.1.3 - <i>Evolution of the Martian mantle</i>	14
1.2- Martian geology.....	16
1.2.1 - <i>Mars geologic history</i>	16
1.2.1.1 - <i>The Pre-Noachian</i>	17
1.2.1.2 - <i>The Noachian</i>	17
1.2.1.3 - <i>The Hesperian</i>	19
1.2.1.4 - <i>The Amazonian</i>	20
1.2.1.5 - <i>Present-day Mars</i>	21
1.2.2 - <i>Mars petrology and crustal processes</i>	22
1.2.2.1 - <i>Magmatic rocks</i>	22
1.2.2.2 - <i>Sedimentary rocks</i>	23
1.2.2.3 - <i>Metamorphic rocks</i>	24
1.2.2.4 - <i>Remote sensing-based characterization of the Martian surface</i>	24
1.2.2.5 - <i>Rover-based characterization of the Martian surface</i>	25
1.3- Martian meteorites.....	26
1.3.1 - <i>Shergottites</i>	26
1.3.2 - <i>Nakhlites</i>	28
1.3.3 - <i>Chassignites</i>	31
1.3.4 - <i>Exceptions</i>	32

1.4 - Samples selected.....	33
1.4.1 - <i>Tissint</i>	33
1.4.2 - <i>Zagami</i>	34
1.4.3 - <i>Nakhla</i>	35
1.4.4 - <i>Lafayette</i>	36
1.4.5 - <i>Miller Range 090032</i>	37
1.4.6 - <i>Yamato 000593 and Yamato 00749</i>	38
1.5 - Purpose of this research.....	40
2 - Methods.....	43
2.1 - Scanning Electron Microscopy/Energy Dispersive Spectroscopy.....	43
2.2 - Laser Ablation Inductively Coupled Plasma Mass Spectrometry.....	44
2.3 - Electron Probe Micro-Analyzer.....	45
2.4 - Highly siderophile elements laboratory method.....	46
2.5 - Thermal Ionization Mass Spectrometer.....	49
2.6 - Secondary Ion Mass Spectrometer.....	52
2.7 - Focused Ion Beam section preparation.....	53
2.8 - Transmission Electron Microscopy.....	54
3 - Temperature and convective activity of the Martian mantle.....	56
3.1 - Introduction.....	56
3.1.1 - <i>The Tissint Martian meteorite</i>	56
3.1.2 - <i>Mineral chemistry as a probe for Martian magma dynamics</i>	57
3.2 - Analytical methods.....	58
3.3 - Results.....	60
3.3.1 - <i>Petrography</i>	60
3.3.2 - <i>Mineral chemistry</i>	63
3.3.2.1 - <i>Olivine major and minor elements</i>	63
3.3.2.2 - <i>Olivine trace elements</i>	67
3.3.2.3 - <i>Chromite inclusions in olivine</i>	69
3.3.2.4 - <i>Pyroxene major and minor elements</i>	69

3.4 - Discussion.....	70
3.4.1 - <i>Origin of P-zoning in olivine.....</i>	70
3.4.2 - <i>Evidence of equilibrium crystallization in a closed-system.....</i>	72
3.5 - Constraint on Martian mantle convection and temperature.....	73
3.5.1 - <i>Equilibration temperatures.....</i>	73
3.5.2 - <i>Vigorous convection in the Tissint magma chamber.....</i>	76
3.5.3 - <i>Implications for the thermal state of the Martian mantle.....</i>	78
3.6 - Conclusion.....	79
4 - Nakhlite mantle source and early Mars differentiation.....	81
4.1 - Introduction.....	81
4.2 - Methodology.....	84
4.2.1 - <i>Sample preparation and chemical mapping.....</i>	84
4.2.2 - <i>Sulphur isotope systematic.....</i>	85
4.2.3 - <i>Analytical procedure for Os-isotope systematics and HSE.....</i>	86
4.3 - Results.....	89
4.3.1 - <i>Textural characterization of the chips.....</i>	89
4.3.2 - <i>Sulphur isotopes.....</i>	91
4.3.3 - <i>Rhenium-Os isotope systematics and HSE.....</i>	94
4.4 - Discussion.....	97
4.4.1 - <i>Potential for terrestrial alteration and weathering.....</i>	97
4.4.2 - <i>Origin of sulphur isotopic anomalies in sulphides of nakhrites.....</i>	98
4.4.2.1 - <i>Isotopic fractionation of $\Delta^{33}\text{S}$ in sulphides of nakhrites.....</i>	98
4.4.2.2 - <i>Isotopic fractionation of $\delta^{34}\text{S}$ in sulphides of nakhrites.....</i>	101
4.4.2.3 - <i>Assimilation versus acquisition of Martian regolith during lava emplacement.....</i>	103
4.4.2.4 - <i>$\Delta^{33}\text{S}$ of the nakhlite mantle source.....</i>	105
4.4.3 - <i>Constraining the magmatic and chemical-physical processes in controlling Re-Os isotope systematics and HSE.....</i>	105
4.4.3.1 - <i>Low-temperature and post-crystallization impact disturbance.....</i>	106
4.4.3.2 - <i>Magmatic processes.....</i>	106

4.4.3.2.1 - Magmatic fractionation of HSE from the nakhlite and shergottite mantle source.....	107
4.4.3.2.2 - HSE fractionation due to late-stage sulphide saturation and residual alloys formation.....	109
4.4.4 - Implications for nakhlite mantle source and early Mars differentiation.....	111
4.5 - Conclusions.....	115
5 - Shergottite mantle source and volatile abundance.....	117
5.1 - Introduction.....	117
5.2 - Materials and Methods.....	119
5.2.1 - Tissint.....	119
5.2.2 - Zagami.....	120
5.2.3 - SEM imaging and X-ray microanalysis.....	120
5.2.4 - FIB-section preparation and TEM analysis.....	121
5.3 - Results.....	122
5.4 - Discussion.....	127
5.4.1 - Amphibole and apatite occurrence in Martian meteorites.....	127
5.4.2 - Enriched versus depleted shergottites.....	128
5.4.3 - Cl content of the Tissint and Zagami parental melts.....	128
5.5 - Conclusion.....	130
6 - Conclusions: implications for Mars evolution and terrestrial planets....	131
6.1 - New insights on Mars formation.....	132
6.2 - Geochemical constraints on Martian mantle sources.....	134
6.2.1 - New evidences of heterogeneity in the Martian mantle.....	134
6.2.2 - HSE abundances of the Martian mantle.....	136
6.3 - Considerations on viscosity and energetics of the Martian mantle.....	139
6.3.1 - Viscosity of the Martian mantle.....	139
6.3.2 - Energy of the Martian mantle.....	140
6.4 - Implications for thermal evolution of terrestrial planets.....	140

6.4.1 - <i>Thermal evolution of terrestrial planets interior</i>	141
6.4.2 - <i>Comparison with terrestrial exoplanets</i>	143
6.5 - <i>Conclusion</i>	144
Bibliography	147
Appendices	179
Appendix A - <i>Experimental petrology data</i>	179
A.1 - <i>Attempts for studying Martian mantle oxidation state</i>	179
A.1.1 - <i>Using oxygen fugacity to interpret the oxidation state of magmatic systems</i>	179
A.1.2 - <i>Sample selected: NWA 8159</i>	181
A.1.3 - <i>Description of the experimental work planned and preliminary SEM-EDS data</i>	184
A.1.4 - <i>Acquisition of the experimental material</i>	187
A.1.5 - <i>Withdrawal of the experimental phase</i>	189
Appendix B - <i>Supplementary information on chapters</i>	191
B.1 - <i>Supplementary information on Chapter 3</i>	191
B.2 - <i>Supplementary information on Chapter 4</i>	205
B.3 - <i>Supplementary information on Chapter 5</i>	216
Appendix C - <i>Sample information and logistics</i>	220
Appendix D - <i>Supplementary references</i>	221

Chapter 1 Introduction

1.1 – Formation and evolution of Mars

1.1.1 – Planetary accretion and early differentiation

According to the most recent literature (Pfalzner et al., 2015, and references therein), the Solar System's formation was triggered by a perturbation that occurred in a star cluster, likely catalysed by the explosion of a nearby supernova. This event resulted in the creation of a protoplanetary disk with a central protostar at 4.56 Gyr ago, as constrained by the Pb-Pb age of the first solids in the Solar System (e.g., Amelin et al., 2002; Bouvier and Wadhwa, 2010; Connelly et al., 2012). Subsequently, planetesimals were formed from dust and ice aggregations. Gravity enabled the accretion of planetesimals of ~1 km in diameter in order to form planetary embryos and, subsequently, planets (Fig. 1.1) (McSween and Huss, 2010).

Planetary embryos were affected by a significant melting period due to radiogenic heating coming from short-lived radiogenic isotopes, in particular ^{26}Al , which became extinct 3 Ma after the formation of the first solids in the Solar System (Lee et al., 1976). The ^{26}Al is the best candidate source for heating in planetesimals during the early stage (~2 Ma) of Solar System formation, this is evidenced by the actual existence of ^{26}Mg , its isotopic daughter (Gray and Compston, 1974; Lee et al., 1976).

Successively, terrestrial planets also experienced a further melting phase due to conversion of kinetic energy into heat during accretion and several impacts with planetesimals. During accretionary impacts a transformation from kinetic energy to heat occurs. If we take into account the metal-silicate differentiation (core formation) that occurs at the same time, we have a lot of generated "heat" during these events, inducing melting (Chambers, 2004; Hustoft and Kohlstedt, 2006). Energy released during impact processes defined a phase termed "magma ocean" on the surface of the terrestrial planetary bodies (Wetherill, 1980; Tonks and Melosh, 1993; Halliday, 2001). There are two factors that define a magma ocean (Taylor and Norman, 1992): (1) the rheology of the magma is liquid, with

crystals suspended into the liquid without forming complex crystalline networks; (2) 10% of the planetary body is magma. Melting in magma oceans is due to heating that can reach the surface by conduction following a black-body law, but in many cases also convection could be possible (Warren, 1985; Morbidelli et al., 2012; Elkins-Tanton, 2012). The pressure range of a planet likely determine the crystallinity and viscosity of its magma ocean (Elkins-Tanton, 2012, see especially Figure 2). Magma ocean crystallization determines the final chemical-physical composition of a terrestrial planet or other minor bodies (Warren, 1985; Morbidelli et al., 2012; Elkins-Tanton, 2012).

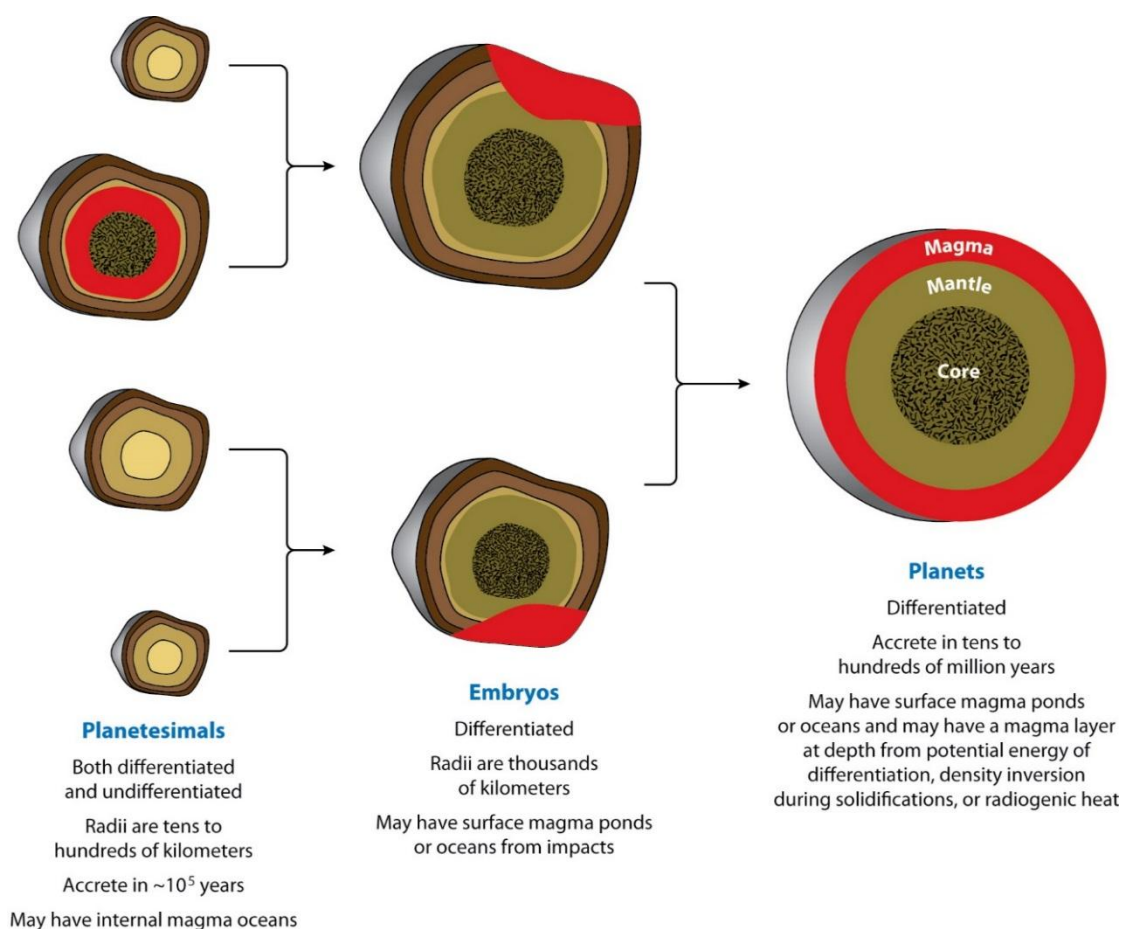


Fig. 1.1- Sketch for accretion and differentiation of planetary bodies, starting from planetesimals to embryos to planets (Elkins-Tanton, 2012). Magma oceans (in red) can occur several times during these processes.

1.1.2 – Mars formation

Mars formed before the Earth and Moon (e.g., Klein et al., 2004). A Martian magma ocean is very likely to have developed because of its early and fast accretion as a planet, measured by a core-mantle fractionation of 13 ± 2 Myr after the origin of the Solar System in ^{182}W and ^{142}Nd studies, due to their siderophile and lithophile geochemical behaviour, respectively (Blichert-Toft et al., 1999; Klein et al., 2002; Foley et al., 2005). The accretion and differentiation of Mars was very quick, just tens of Myr after Solar System formation, and within ~ 1.8 Myr by planetary embryos accumulation (Lee and Halliday, 1997; Brandon et al., 2000; Nyquist et al., 2001; Borg et al., 2003; Dauphas and Pourmand, 2011). In effect, Mars seems to be an extremely early-formed planet or a surviving planetary embryo ('oligarch'). The preservation of ^{182}W and ^{142}Nd anomalies suggest that no crustal recycling occurred since the formation of the primordial magma ocean (Elkins-Tanton, 2012). After accretion, Mars subsequently differentiated in roughly 10 Myr (Shih et al., 1999). However, several authors proposed different periods for the duration of magma ocean crystallization on Mars. Foley et al. (2005) suggested a differentiation of around 60 Myr for the shergottite and nakhlite source reservoirs; Marty & Marti (2002) found an age of 30 Myr by using noble gas isotopes; on the other hand, both Blichert-Toft et al. (1999) and Debaille et al. (2007) leveraged ^{142}Nd isotope data to argue for silicate differentiation over a 100 Myr period. Also, highly siderophile element (HSE) abundance and silicate partitioning data suggest that the actual depths of the Martian magma ocean ranged from ~ 400 km (Righter et al., 1998) to ~ 1100 km (Righter and Chabot, 2011). Yet multiple magma oceans have probably occurred, so mantle abundances are the cumulative results of all of these early differentiation events (Rubie et al., 2011).

The degassing of volatile element inventories are produced during solidification of the magma ocean (Elkins-Tanton, 2012). The abundance and distribution of hydroxyl and carbon influence the viscosity/temperature of the mantle and thus the nature of convection, volcanism, planetary atmosphere compositions, and surface conditions that can constrain the timing of habitability (Elkins-Tanton, 2012). In order for a magma ocean to form an atmosphere, the magma needs to be supersaturated in water or hydroxyl phases and able to generate opportune bubble nucleation processes that reach the

surface layer (Abe and Matsui, 1985; Zahnle et al., 1988; Elkins-Tanton, 2008; Elkins-Tanton, 2012). The duration of crystallization of the initial Martian magma ocean was interpreted from Sm-Nd isotope ratio to be ~100 Myr after core formation, i.e. 7-15 Myr after solar nebula condensation (Debaille et al., 2007), implying a thick early Martian atmosphere in order to reduce the cooling rate (Abe, 1997).

1.1.3 – Evolution of the Martian mantle

The thermal evolution of the Mars' interior is not yet fully constrained. On Mars, the model of mantle convection is a stagnant-lid, because it is a one-plate planet (Fraeman and Korenaga, 2010). In this sense, some authors reported that the Martian mantle could have retained heat for the majority of the history of the planet, by modelling paleo-heat flows deduced from lithospheric strength (Hauck and Phillips, 2002; Grott and Breuer, 2010; Fraeman and Korenaga, 2010; Ruiz et al., 2011).

Thermal evolution of a terrestrial planet is likely controlled by cooling induced by mantle convection and partial melting (Stevenson et al., 1983; Spohn, 1991; Hauck and Phillips, 2002; Fraeman and Korenaga, 2010). Partial melting sequesters incompatible heat-inducing elements (e.g., Th and U) into the planetary crust - that became hot enough to obstruct surface cooling of the mantle (Phillips and Malin, 1983). Besides, the residual mantle (post-partial melting) would be less dense and much more buoyant, influencing the geometry and evolution of the thermal boundary layer (Parmentier and Hess, 1992; Fraeman and Korenaga, 2010). The residual mantle would also be more viscous because of dehydration, i.e. H is partitioned into the liquid phase (Karato et al., 1986; Hirth and Kohlstedt, 1996). Hauck and Phillips (2002) found a degree of dehydration of the Martian mantle of 5-10% while other models calculated dehydration at more than 80% (Fraeman and Korenaga, 2010).

As for every planetary mantle, the Martian mantle experienced natural cooling, even if in a stagnant-lid regime. This can be probed via the evolution of global Martian volcanism from olivine-rich assemblages to olivine and pyroxene assemblages that suggests cooling of the Martian mantle over time (Baratoux et al., 2013; Wilson and Mustard, 2013). This switching in cooling mode happens at

the boundary between the Noachian and Hesperian eras on Mars (3.7 Ga), when other significant changes occurred. These changes include a decrease in the amount of water at Mars' surface. This is evidenced by a decrease in hydroalteration and erosion as testified to be lesser proportions of phyllosilicates. This observation has been linked to switching the mineralogy from phyllosilicate-based to more acidic and evaporitic (Bibring et al., 2006; Carr and Head, 2010; Ehlmann et al., 2011; Fassett and Head, 2011; Mangold et al., 2012).

The evolving lithospheric thickness on Mars likely contributed to the formation of deeper magma chambers and, consequently, in the inferred shift toward a more energetic volcanic style (Ruiz et al., 2011). The subsequent halt of the planetary geodynamo would have led to the cessation of Mars' magnetic field (Nimmo and Stevenson, 2000; Breuer and Spohn, 2003). This change is a critical in Mars' history in that it permitted a rapid increase in the loss of the atmosphere to space, while also modifying the Martian surface environment (water state, climate, erosion style). In general, conditions in the environment shifted from wetter to dryer over Mars' history (Bibring et al., 2006; Ehlmann et al., 2011; Ruiz, 2014).

The estimated water inventory of the Martian mantle during accretion could have been up to 0.4 wt.% based on modelling that assumed OH^- was dominantly accommodated by nominally anhydrous minerals (Medard and Grove, 2006). Hydrogen-deuterium isotope ratios constrain the origin of Martian water from asteroids or comets beyond 2.5 AU (Lunine et al., 2004). Only 5-10% of the mantle water would have been degassed by global Martian volcanism after planetary accretion (Hauck and Phillips, 2002). The presence of this quantity of water would substantially change the rheology/viscosity of the mantle (Karato et al., 1986), resulting in vigorous convection that during 4 Gyr of time could change the style, according to analogues of convection processes in the terrestrial mantle system (Ito et al., 1999; Ruedas, 2006). The present water content of the Martian mantle can instead be inferred from the water content of both hydrous and nominally anhydrous minerals (e.g., amphibole or apatite) within Martian meteorites. There is no consensus about the precise abundance of water on Mars, but several authors defined a range from 36 ppm (Wanke and Dreibus, 1994) to 100-200 ppm (Ruedas et al., 2013; Filiberto and Treiman, 2009) to 18,000 ppm H_2O (McSween et al., 2001). The amount of water extracted

from the mantle would have been very low (only 5%) so that the 90-95% of the water could still be retained in the Martian mantle (Hauck and Phillips, 2002). Ringwoodite and wadsleyite, high-pressure forms of olivine, can take up much more water than olivine. Considering that the lower part of the Martian mantle is likely dominated by ringwoodite and wadsleyite, half of the Martian mantle could be, or could have been, a significant planetary water reservoir (Kubo et al., 1998; Chen et al., 1998; Karato, 2008; Ruedas et al., 2013).

1.2 – Martian geology

1.2.1 – Mars geologic history

The geological eras of Mars can be divided into: (1) Pre-Noachian, from the accretion of the planet at 4.5 Ga to 4.1 Ga; (2) Noachian, from the formation of the Hellas Basin at ~4.1-3.8 to 3.7 Ga; (3) Hesperian, from 3.7 to 3.1 Ga; and (4) Amazonian, from 3.1 Ga to present. Dates are based on relationships between superimposed impact craters and their number (Scott and Carr, 1978; Tanaka, 1986; Hartmann and Neukum, 2001; Ivanov, 2001; Carr and Head, 2010). Bibring et al. (2006) proposed a naming of the Martian eras based on the mineralogical characteristics of each period, from older to younger: phyllosian (dominated by clays), theiikian (dominated by sulphates), and siderikian (dominated by anhydrous ferric oxides) (Fig. 1.2). All facts reported in the next sub-paragraphs below result from space mission data (orbiter, lander, rovers), meteorite chemical analysis, and modelling.

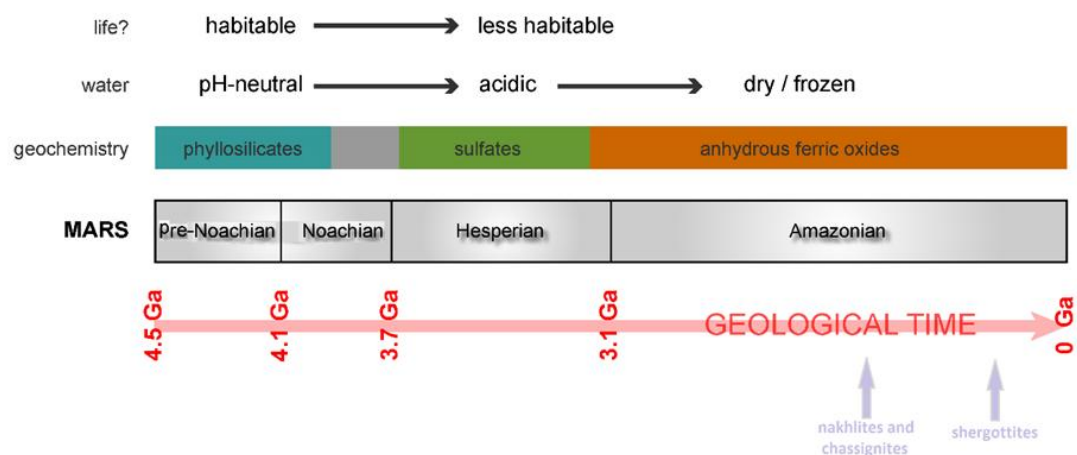


Fig. 1.2 - Geological timescale of Mars, based on Bibring et al. (2006). Arrows indicate the time of genesis of the main groups of Martian meteorites.

1.2.1.1 – The Pre-Noachian

In the early phase of its geological history, Mars was a wet and warm world. This environment was possible due to a large amount of volcanic outgassing that generated an early atmosphere, that largely contributed to the retention of a high amount of liquid water on early Mars (Dreibus and Wanke, 1987; Matsui and Abe, 1987; Melosh and Vickery, 1989; Lunine et al., 2004). Then, late veneer processes, i.e. addition of chondritic material by impacts, also served to increase the amount of water available on Mars (Jakosky and Jones, 1997; Greeley and Schneid, 1991; Phillips et al., 2001).

A large number of impacts characterized the pre-Noachian epoch (from 4.5 Ga to 4.1 Ga). These impacts made the crust inefficient for keeping water on the surface and increased the surface temperature by hundreds of degrees (Sleep and Zanhle, 1998; Segura et al., 2002). The global Martian dichotomy in crustal thickness likely formed during this period (Nimmo and Tanaka, 2005; Carr, 2006). There are controversies about the formation of this dichotomy, where contrasting hypothesis suggest that the cause could be a giant impact or, alternatively, could reflect the presence of an early and extensive ocean (e.g., Clifford and Parker, 2001; Marinova et al., 2008; Canup and Salmon, 2018). In addition, the notable Tharsis volcanic region likely formed during this era (Nimmo and Tanaka, 2005).

1.2.1.2 – The Noachian

During the Noachian era (from 4.1 Ga to 3.7 Ga) there was probably a temporary Martian geomagnetic field, as evidenced by the Mars Global Surveyor mission that localized magnetic anomalies in the southern highlands of Mars (Acuna et al., 1999; Connerney et al., 1999). These magnetic anomalies suggested the presence of a Noachian magnetic field would have been subsequently disrupted by a giant impact, disabling sustained conditions in the planetary core. Such an impact could have been the one that formed the Hellas, Utopia or Argyre basins (Solomon et al., 2005).

The Noachian era was characterized by intense crater formation, development of valleys, canyons, and erosional processes; all of these geomorphological features were due to the presence of water (Strom et al., 1992; Carr and Head, 2010) that was physically stable in the liquid state due to the presence of an atmosphere. The presence of water/erosion during this period was necessary to the production of phyllosilicates by weathering (Carr and Head, 2010). The majority of large impacts during the Noachian would have deposited ~300 m of ejecta at the global scale (Strom et al., 1992; Segura et al., 2002), with the Hellas-generating impact depositing 0.5 km of ejecta material (Ivanov, 2001). The majority of ejecta were fine-grained. Material that filled the craters was primarily volcanic (mostly basalts rich in pigeonite) or volcanic rocks reworked by impacts (Bandfield et al., 2000; Mustard et al., 2005; Poulet et al., 2005; Bibring et al., 2006). Many Noachian volcanic rocks retain evidence of alteration from water and hydrothermal fluids (Carr and Head, 2010).

The Noachian was the period characterized by the highest erosion rate (2-5 orders of magnitude higher than the subsequent periods), and at the start of the Hesperian the erosion rate dropped dramatically (Craddock and Howard, 2002; Carr and Head, 2010). During the Noachian the presence of valleys generated by rivers and lakes, that filled impact basins, would imply that the climate was warm and that precipitation followed by surface runoff must have occurred, even if episodically (Craddock and Howard, 2002; Irwin and Howard, 2002; Hynek and Phillips, 2003; Stepinski and O'Hara, 2003; Howard et al., 2005; Carr, 2006). Some geomorphic features could have been formed only by the presence of large outflow channels, as for example Mawrth Vallis (Carr and Head, 2010). All these erosional processes produced a large amount of erosional material. Weathering during the Noachian generated a specific mineralogy that derives from the alteration of basalts (Murchie et al., 2008; Zolotov and Mironenko, 2007): overall phyllosilicates (nontronite, Fe-rich chlorites, saponite, montmorillonite).

The Tharsis volcanic bulge, around 5,000 km across and 9 km high, was generated during the Noachian (Phillips et al., 2001). The formation of Tharsis deformed the Martian lithosphere globally creating a trough and gravitational anomalies (Squyres et al., 2007). Volcanism was likely accompanied by outgassing of volatiles, mostly water and sulphur that were added to the atmosphere (Carr and Head, 2010).

An interesting but controversial hypothesis suggest that Mars had an ocean of liquid water during the Noachian and post-Noachian periods (Carr and Head, 2010). There are several important lines of evidence in support of this theory: the presence of Noachian shorelines within the Hellas Basin (Moore & Wilhelms, 2001); the absence of valleys at North-West of Arabia Terra that could be due to oceanic sediment filling (Howard et al., 2005); evidence of a possible mega-tsunami event, in the northern hemisphere, due to an impact on this early Mars ocean (Costard et al., 2017).

1.2.1.3 – The Hesperian

The Hesperian era began at the end of the Late Heavy Bombardment at about 3.7 Gyr ago to 3 Gyr ago, close to the early Archean on Earth (Hartmann and Neukum, 2001; Carr and Head, 2010). The Hesperian was characterized by an increase in volcanism, canyon formation, accumulation of sulphate-rich deposits, and a significant decrease in erosion rate, weathering, and valley formation. Evidence suggests that the Noachian "hydrosphere" was only episodically present during the Hesperian (Carr and Head, 2010).

Hesperian volcanism was widespread and resurfaced around the 30% of the planet (Carr and Head, 2010). During this period the paterae (low shield-like volcanoes) formed, as for example Apollonaris, Alba, and Hadriaca (Greeley and Spudis, 1981). Both the eastern and the western hemisphere were characterized by large lava plains (as Hesperia Planum and Syrtis Major Planum). Some shield volcanoes in Tharsis probably formed during the Hesperian, including Olympus Mons (Watters & Maxwell, 1986; Scott and Tanaka, 1986; Greeley and Guest, 1987; Head et al., 2002). The transition Noachian-Hesperian shifted the nature of volcanism from low-Ca pyroxene-dominated to high-Ca pyroxene-dominated, continuing during the Amazonian period (Baratoux et al., 2013). This transition could have been caused by the thermal evolution of the mantle, characterized by a decrease in heat flow (Baratoux et al., 2013).

Episodic valley network formation during the Hesperian could have been caused by local snow/ice melting on the summit of volcano edifices or local impact events inducing melting of the ice (Fassett and Head, 2008). Outflow channels may have formed though a rapid release of great quantity of liquid

water during the Hesperian (Carr and Head, 2010). The storage of this water could have been a groundwater aquifer, a lake, or ice. The rate of groundwater eruptions during the Hesperian contributed in generating a thick cryosphere (Carr and Head, 2010). The fact that the outflow channels were formed by floods necessarily implies that at the end of these channels a sort of "sea" or "ocean" was still present (Carr and Head, 2010). However, there remains dispute concerning this hypothesis, even though potential shorelines and burial ridges/craters have been detected (Parker et al., 1993; Clifford and Parker, 2001; Moore and Wilhelms, 2001; Kreslavsky and Head, 2002).

The Valles Marineris, which formed in this period, is recognized as a series of parallel normal faults that may extend into the lithosphere, thereby creating a graben (Sharp, 1973; Blasius et al., 1977). The system of canyons in the Valles Marineris was probably generated due to lithospheric stress by the Tharsis load (Anderson et al., 2001). The canyon system started at the end of the Noachian, but faulting, subsidence, and wall erosion occurred during and until the late Hesperian (Carr and Head, 2010).

The Hesperian was also characterized by many sulphate-rich deposits, overall detected in the Columbia Hills, at Meridiani Planum and in the western hemisphere in general (Milliken et al., 2009; Carr and Head, 2010). There are controversies regarding the origin of sulphates during the Hesperian: if they derive from evaporation or if they are the product of weathering (Madden et al., 2004; Tosca et al., 2005; Tosca and McLennan, 2006). Sulphates in Meridiani Planum and Gale Crater appear to have been transported by wind (Andrews-Hanna et al., 2007). The transition from phyllosilicate geochemistry in the Noachian to sulphates in the Hesperian is primarily due to loss of the atmosphere to space and dehydration at the surface (Bibring et al., 2006; Carr and Head, 2010).

1.2.1.4 – The Amazonian

The Amazonian era began 3 Ga (broadly coincident with the middle of Archean on Earth) and continues to the present day (Carr and Head, 2010). The geomorphological modifications and erosion rates were much less than in the past Martian geological periods (Golombek et al., 2006). The most important

processes during the Amazonian period were impacts and the actions of the glaciers: ice was the main erosional agent during the Amazonian (Lucchitta, 1981; Kargel and Strom, 1992). These glaciological processes are due to variation in the planet's obliquity over time (Laskar et al., 2004). Latitudes of 30-55° were covered by a thin veneer of ice-rich material (Mustard et al., 2001), while thicker deposits occurred at middle latitudes (Carr, 2001) and on the flanks of some of the Tharsis volcanoes (Lucchitta, 1981).

Volcanic activity during the Amazonian was located preferentially at the Tharsis and Elysium volcanic regions (Greeley and Schneid, 1991; Carr and Head, 2010), even if episodically, in respect to the previous eras (Neukum et al., 2007; Werner, 2009). The eruption rate dropped from 1 km³ yr⁻¹ to 0.1 km³ yr⁻¹ on average (Greeley and Schneid, 1991). The style of volcanic structures and plains changed from high to a few wrinkle ridges and toward numerous flow fronts and lava tubes with skylight features (Wilson et al., 2001; Werner 2009).

Fluvial activity during the Amazonian is much less evident than in the Hesperian, with only a few outflow channels (Carr and Head, 2010). The youngest outflow channels are Athabasca, Rahway, and Marte Valles in southern Elysium. These outflow channels are principally generated by faulting and the presence of liquid water that can persist during present day conditions on the subsurface of Mars (e.g., Head et al., 2003; Ojha et al., 2015). Recurrent slope lineae are one of the major geomorphic features during the Amazonian (Carr & Head, 2010). They seem to be formed due to episodic events of ice melting at mid-latitudes, during high-obliquity periods (Head et al., 2003).

1.2.1.5 – Present-day Mars

Today it is still unknown whether Mars has volcanic activity or, in general, if the Martian interior is geologically active. Also, at present it is still unknown whether the Martian core is in a solid or liquid state. Based on crater counting using Mars Express orbiter data, some authors argue for geologically recent (< 40 Ma) volcanic activity at Olympus Mons (Basilevsky et al., 2006).

Recurrent slope lineae are episodically present on the surface of Mars, and a recent theory argue that they are formed by brine flows due to detected salt (Ojha et al., 2015). Wind is a strong erosional process during the present

Amazonian. Dust is composed mainly of basaltic sands and sulfate particles (Carr and Head, 2010).

Both the present North and South Poles on Mars are thin-layered and with a thickness of about 3-4 km (Carr and Head, 2010). The North Pole deposit is divided in two units: a basal unit up to 1 km and an overlying finely layered deposit of 3 km (Byrne and Murray, 2002; Tanaka et al., 2005), surrounded by an immense dune field rich in gypsum (Langevin et al., 2005). The South Pole deposit is a mound of 3 km high, surrounded by older ice deposits such as the Dorsa Argentea Formation (Byrne, 2009). The layering is probably due to accumulation of dust and ice during orbital motions of the planet. The first evidence of subglacial liquid water on Mars has been found below the South Pole deposit by investigating orbiter data from the Mars Express mission (Orosei et al., 2018).

1.2.2 – Mars petrology and crustal processes

1.2.2.1 – Magmatic rocks

The Martian crust is mainly composed of tholeiitic basalts, generated by partial melting and without evidence of weathering, while calc-alkaline and siliceous rocks are very rare (McSween et al., 2009). The abundance of tholeiitic basalts on the surface of Mars could be due to the lack of a hydrous mantle or to the product of early melting that dehydrated the mantle, inducing consequent tholeiitic melting (McSween et al., 2009). Other calc-alkaline composition detected among the crust are probably artefacts of alteration (Wyatt and McSween, 2002).

All rover-based chemical analysis on the surface of the planet have revealed a chemical compositional range for basalts that, if plotted on a Total Alkali-Silica (TAS) diagram, show correlations with terrestrial alkali-basalts, thus higher silica content than Martian meteorites, for example on Gusev Crater (Fig. 1.3) (McSween et al., 2009). However, even these rocks sometimes are picobasalts and this could be due to fractional crystallization processes occurred at various depths (McSween et al., 2006).

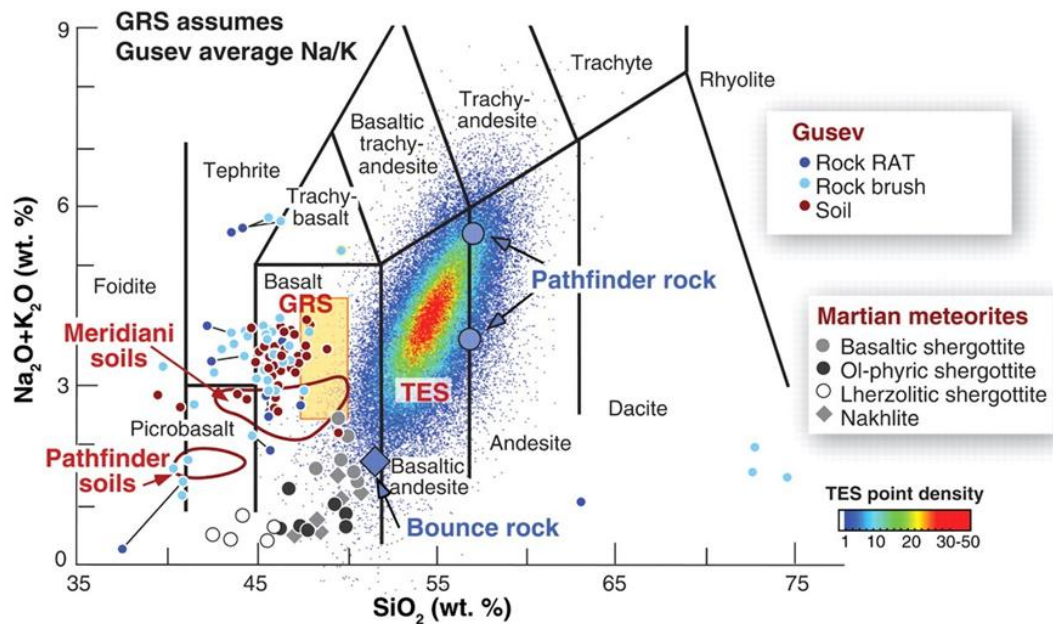


Fig. 1.3 - TAS diagram with plotted Martian meteorites and rover-based analysis from planetary exploration missions on the surface (GRS = Gamma-Ray Spectrometer; TES = Thermal Emission Spectrometer; RAT = Rock Abrasion Tool). Results indicate that the Martian crust is in average basaltic in composition, TES data may reflect alteration. (Modified from McSween et al., 2009).

1.2.2.2 – Sedimentary rocks

Martian sedimentary rocks are divided according to their genesis (McSween et al., 2015) into: clastic rocks (sandstone and siltstone, mudstone, and conglomerate) and chemical deposits (evaporitic sulphate and minor carbonate). The majority of clastic rocks on Mars are derived from basalts. The variability of these sedimentary rocks is linked with different wet or dry periods on Mars, and with varying pH (Hurowitz et al., 2006). The NWA 7034 meteorite is the only "Martian sedimentary rock" sample that we have on Earth. It is a polymict breccia composed of igneous detritus, proto-breccia clasts and impact melt fragments, formed by impact. Its composition matches almost perfectly that of the Martian regolith, as reported from the Spirit rover (McSween, 2015).

A "Martian rock cycle" was defined and divided in two different environments (McSween, 2015): (1) in the Noachian and Hesperian, where water was available, chemical-physical weathering produced sediments which were transported and deposited by water flows; (2) during the Amazonian the rock cycle changed: because of the absence of surface water, sediments were produced only by physical weathering and transported by winds.

1.2.2.3 – Metamorphic rocks

Metamorphic Martian rocks are created by shock metamorphism caused by impacts and by thermal metamorphism (e.g., contact and hydrothermal). Lava flows contact metamorphism was particularly important in the Noachian when the heat production was five times greater (McSween, 2015).

1.2.2.4 – Remote sensing-based characterization of the Martian surface

Two differing volcanic morphologies that characterize the Martian surface have been classified from remote sensing data: a) central volcanoes, that are volcanic landforms generated by continued eruptions from a vent; and b) volcanic plains, recognized by the presence of mare ridges and flow lobes (Greeley and Spudis, 1981). Central volcanoes are divided into: (1) shields: very low-profile volcanic structures, e.g. Olympus Mons; (2) domes: steep-sided constructs that are the result of lower rate of eruption and/or more Si-rich lava, e.g. Tharsis Tholus; (3) highland paterae: low-profile volcanoes interpreted as ash shields that are located in cratered regions; (4) Alba Patera: unique volcanic structure with a volcanic center of 1500 km across with extremely low flank slopes; (5) smaller features, e.g. cinder cones. Volcanic plains are divided into: (1) simple flows - thick single-cooled units of lava flows with different characteristics as mare ridges and lobes; (2) complex flows - multiple-cool units of flow lobes overlapped; (3) undifferentiated flows - atypical flows that are considered as volcanic for their vicinity to volcanic centers.

Global widespread clay minerals have been studied by a number of orbiter missions. For the Noachian terrains of Mars the results suggest a long-term early interaction between liquid water and basalts in the Martian crust (Poulet et al., 2005; Bibring et al., 2006; Mustard et al., 2008; Ehlmann et al., 2011). The

contrast within Noachian altered terrain filled by clay minerals and the younger crystalline terrains is very marked (Rogers et al., 2007). This finding further indicates a transition from an early water-rich era to an arid era with acidic water (Bibring et al., 2006; Chevrier et al., 2007). Also, geomorphic features of Noachian and Hesperian highlight this transition (Tanaka, 1997; Fassett and Head, 2008). Clays on Mars occur in different settings (Murchie et al., 2009; Ehlmann et al., 2011): (1) in crustal settings, mostly ancient terrains generated by magmatic processes and successively degraded by impacts; (2) in sedimentary settings, fan-shaped or layered deposits in basins due to material transportation; (3) in stratigraphies, multiple units with clays and other alteration minerals that are stratigraphically in contact with each other. The majority of the clay minerals in all the geological settings are smectites (Mustard et al., 2008), ranging from nontronite (Fe-rich endmember) to saponite (Mg-rich endmember). Evidence from the mineral assemblages of smectites and chlorites resulting from Martian rock analysis (Harder, 1976), and the significant presence of clay minerals among Mars' deep crustal materials, suggests that most clay minerals formed in subsurface waters at temperatures ranging from ambient temperature to $< 400^{\circ} \text{C}$ (Ehlmann et al., 2011).

1.2.2.5 – Rover-based characterization of the Martian surface

Rover-based analysis carry important constraints on the petrological characterization of the Martian crust. At Gusev and Meridiani sites there are rocks that are mixtures of basaltic minerals plus silica and minor sulphates, Fe-oxides, clay, and chloride (Bish et al., 2013). The Spirit rover discovered sedimentary or volcanoclastic rocks at the Columbia Hills in Gusev Crater (McSween, 2015). Rocks in the Gusev Crater have been identified to be highly oxidized float basalts probably formed by a local magma source close to the crater or beneath the same (Lang et al., 2010). The same float basalts appear in the Gale Crater as seen by Curiosity rover (McSween, 2015) and in the Columbia Hills (Squyres et al., 2006): there are debates about the origin and source of these rocks, whether they are fine-grained volcanic rocks or sedimentary rocks (Schmidt et al., 2014).

The Curiosity's Alpha-Particle X-ray Spectrometers (APXS) evaluation of volcanic rocks in Gale Crater identified the strong alkalinity of these rocks (all

characterized by high contents in K and Fe), with compositions that vary from hawaiite to mugearite (Stolper et al., 2013; Schmidt et al., 2014). ChemCam analyses distinguished two types of rocks (Sautter et al., 2014): fine-grained monzonitic (with feldspar phenocrysts) and coarse-grained dioritic (with augite, Na-rich plagioclase, and orthoclase). Of particular importance, the Yellowknife Bay formation (Hesperian) in the Gale Crater analysed by the Curiosity rover consists of laminated to massive mudstones with Ca-sulphate veins that crosscut the formation (Grotzinger et al., 2014; Siebach et al., 2014).

1.3 – Martian meteorites

The only available rock samples from Mars are the Martian meteorites, and most are divided into shergottites (basalts), nakhlites (clinopyroxenites), and chassignites (olivine cumulates). The most compelling evidence that these meteorites derive from Mars is the abundance and isotopic ratios of Ar-Kr-Xe-N gases trapped within the meteorites, which perfectly matches the composition of the Martian atmosphere, as analyzed by the Viking mission (Pepin, 1985; Becker and Pepin, 1984; Wiens et al., 1986; McSween, 1984).

1.3.1 – Shergottites

Shergottites (170-475 Ma; Early to Late Amazonian) are mostly basalts crystallized from a sub-alkaline magma (Fig. 1.4) (McSween, 2015). There is only one exception: a shergottite (NWA 7635) with a crystallization age of 2.4 Ga (Lapen et al., 2017). The main difference between shergottites and Earth's basaltic chemistry is their higher Fe/(Fe+Mg) ratio and lower Al₂O₃ content (Nyquist et al., 2001). Shergottites depleted in incompatible trace elements are thought to come directly from their mantle source (Symes et al., 2008; Herd et al., 2002), while enriched shergottites could either be the product of metasomatized mantle or crustal assimilation (McSween, 2015; Day et al., 2018). The parent magmas of shergottites could have been moderately hydrous before their ascent/eruption where volatiles may have subsequently been lost via degassing (McSween et al., 2001; McCubbin et al., 2012).

Depleted shergottites are divided into two main groups (Nyquist et al., 2001): basaltic shergottites and ultramafic shergottites.

Basaltic shergottites consist primarily of augitic and pigeonitic pyroxenes, with a sort of non-regular chemical zoning, and of diaplectic plagioclase (maskelynite). Secondary mineral assemblages comprise pyrrhotite, ilmenite and Ti-rich magnetite (McSween, 1994). Sometime amphibole (mostly kaersutitic), as well as spinel and sulphides, can be found in melt inclusions in pyroxene, suggesting that it formed in the primary melt (Treiman, 1985). Almost all the basaltic shergottites contain evidence of very similar pyroxene alignments suggesting crystallization in a lava flow on Mars rather than in a shallow magma chamber (McCoy et al., 1992; McSween, 1994). Textural characteristics of the basaltic shergottites resemble that of terrestrial basaltic lava flows. A possible petrogenesis of the basaltic shergottites requires a first stage involving a slowly cooling magma chamber at depths > 7.5 km on Mars, as inferred from amphibole crystallization. Subsequently, a second stage is required in which the pyroxene was incorporated into a magma that erupted on the Martian surface as a lava flow or cooled in a shallow dike/sill (Nyquist et al., 2001).

Ultramafic shergottites contain less than 10 vol. % of plagioclase, being composed mainly of coarse-grained olivine and chromite enclosed by large crystals of orthopyroxenes (Harvey et al., 1993; McSween, 1994; Mikouchi and Miyamoto, 1997). Accessory minerals in the interstices are maskelynite, pyroxenes, and whitlockite. These shergottites contain more Mg than the basaltic shergottites and disequilibrium has been demonstrated for coexisting olivines and pyroxenes (Harvey et al., 1993). Further, the ultramafic shergottites are LREE-depleted (Dreibus et al., 1982). Models of ultramafic shergottites petrogenesis suggest that they are cumulates formed in plutons in sub-surface environments on Mars (Berkley and Keil, 1981; Harvey et al., 1993; McSween, 1994).

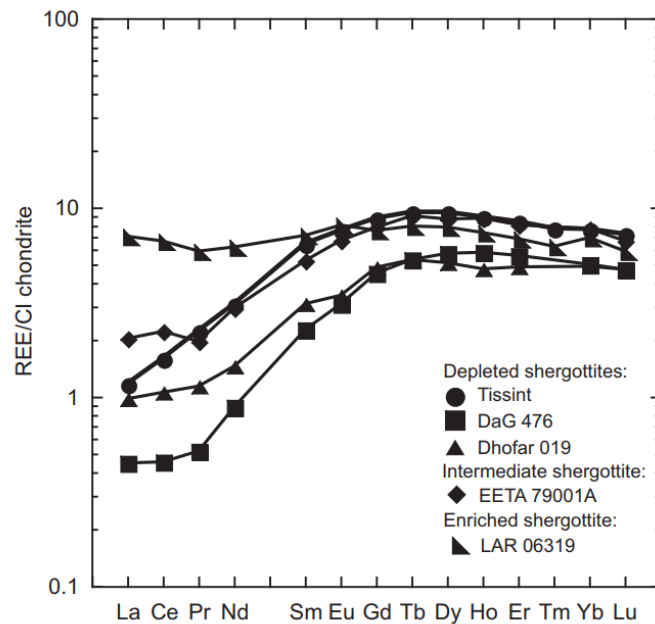


Fig. 1.4 - Rare Earth Elements (normalized to CI-chondrite) abundances and comparison between depleted, intermediate, and enriched shergottites. Figure modified from Balta et al. (2015).

1.3.2 – Nakhlites

The nakhlites (1.3 Ga; Middle Amazonian) sample a series of lava flows erupted on Mars between 1416 ± 7 and 1322 ± 10 Ma, probably by a single volcano, as suggested by ^{40}Ar - ^{39}Ar dating (Fig. 1.5) (Cohen et al., 2017). Ten separate nakhlites have been found: Nakhla, Lafayette, Governador Valadares, the Antarctic Miller Range (MIL) and Yamato (Y) nakhlite pairs, North West Africa (NWA) 817, NWA 6148, NWA 998, and Caleta el Cobre 022. Of these only Nakhla was seen to fall.

The nakhlites are clinopyroxenites composed primarily of augite and less abundant olivine, plagioclase, K-feldspar in the mesostasis, Fe-Ti oxides, FeS in form of pyrrhotite, pyrite, and iddingsite (Bunch and Reid, 1975). Their modal mineralogy consists mostly of augite (~80%), olivine (~15%) and the remnant are mesostasis of oxides, sulphides, Na-rich plagioclase, and K-feldspar (Treiman, 2005; Day et al., 2006). They are characterized by minor aqueous alteration (Hallis and Taylor, 2011). The texture is dominated by elongated prisms of clinopyroxene with a preferred alignment. Olivine grains are larger than the

augite grains. Between olivine and augite grains there is mesostasis composed of titanomagnetite, plagioclase, K-feldspar, and FeS (Treiman, 2005). Phenocrysts are interpreted as cumulus grains, also characterized by post-cumulus overgrowth (Treiman, 2005). Nakhrites show evidence of minor shock (below 45 GPa; Stoffler, 2000), in fact plagioclase is always fully crystalline (Greshake et al., 2004).

The texture of the nakhrites resembles those of terrestrial basaltic cumulates, especially those rapidly cooled in lava lakes or thick flows (Arndt, 1977; Wright and Peck, 1978); in particular, the nakhrites are very similar to the Theo's Flow complex on Earth (Arndt, 1977; Friedman-Lentz et al., 1999). Crystals show a preferred orientation (Berkley et al., 1980), it is possible to see elongate and aligned augite crystals typical of lava flows (Mikouchi et al., 2003). Augite and olivine crystals can contain inclusions (Treiman, 2005). Inclusions of magnetite are present in augite phenocrysts, while olivine contains sparse grains of augite (Harvey and McSween, 1992). Both minerals can also contain multiphase and glassy inclusions, remnant of magma, and symplectite lamellae (Treiman, 1990; Harvey and McSween, 1992; Mikouchi et al., 2000).

The major element chemical composition is very similar among all the nakhrites, they are rich in CaO and poor in Al₂O₃ and alkalis compared to terrestrial basalts (Treiman, 2005). The only difference among samples is the content of Al₂O₃ and alkalis. All nakhrites are strongly enriched in REE (mostly La with an average of ~ 10 x CI chondritic) and enriched in LREE (Treiman, 2005), and have slight negative Eu anomalies and no Ce anomalies, probably resulted from terrestrial weathering or loss of magmatic volatiles (Fig. 1.6) (Lentz et al., 2001; Crozaz et al., 2003). Inorganic carbon in nakhrites is due to the presence of carbonate minerals (Treiman, 2005), but the majority of carbon is organic (90-800 ppm abundance) (Wright et al., 1989; Jull et al., 2000).

Paradoxically, the nakhrites are enriched in highly incompatible elements (in relation to moderately incompatible elements) but their mantle source should have been highly depleted in these elements (Treiman, 2005). The source mantle must, therefore, have been augite and olivine rich with a low abundance of pigeonite or Al-rich phases (Treiman, 2005). The volatile content of the Al-poor Ca-rich parent magma of nakhrites is unknown, even if a high abundance of volatiles and presence of magmatic water in Nakhla have been proposed

(Treiman, 2003; Hallis et al., 2012). Mechanism of enrichment in LREE and other highly incompatible elements in nakhlites (with respect to their presumably long-lived magma source) may have been due to mantle metasomatism (Treiman, 2003; Day et al., 2018) or periodic recharge of fractionating magma chambers (Bohrson and Spera, 2003).

Nakhlites present alteration features attributed to infiltration by Martian liquid water (Bridges et al., 2001; Lee et al., 2015). In particular veinlets and patches of iddingsite, that is a sub-micrometer mixture of smectite, Fe-oxi-hydroxides, and other salts (Reid and Butch, 1975). This suggests low-temperature aqueous alteration on Mars (Smith et al., 1979; Delvigne, 1998; Lee et al., 2015).

Nakhlite petrogenesis is summarized by Treiman (2005). The source magma for nakhlites was depleted in Al_2O_3 and enriched in incompatible elements. The rocks formed as cumulates (accumulation of olivine and pyroxene in excess of the parent magma), thus the bulk composition is not direct reflection of the parent magma from which these crystallized. After accumulation, nakhlites experienced igneous crystallization and post-igneous alteration processes to varying degrees. During these events, later-stage magmas may have percolated. After solidification, other chemical reactions that affected iron and sulphide minerals continued, and nakhlites were modified by liquid water that formed the alteration mineral assemblages. Ultimately, these rocks were impacted and ejected from Mars, transited through space and subsequently fell on Earth, where they were affected by terrestrial alteration. The Tharsis or Elysium volcanic province could have been the source location for the ejection of this volcanic rocks (Scott et al., 1986; Hartmann and Berman, 2000).

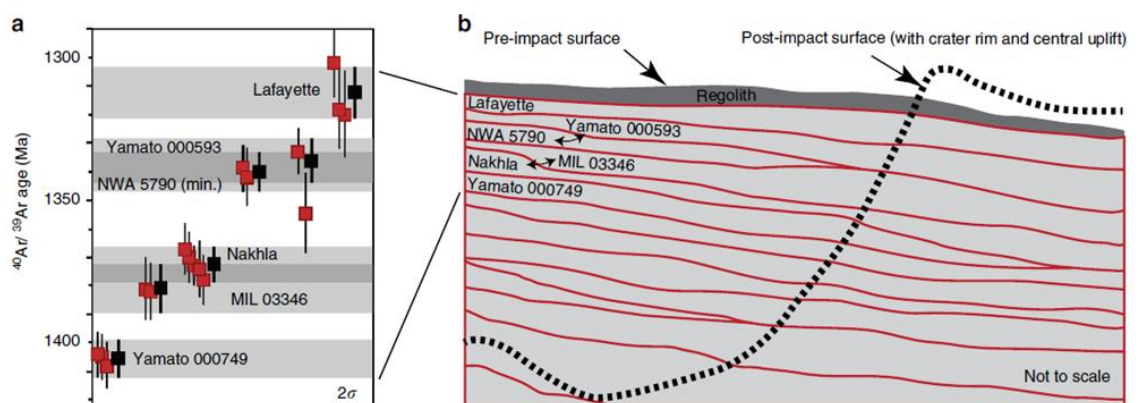


Fig. 1.5 - Schematics of the nakhlite lava flows. a) Ar-ages for six nakhlites; b) nakhlite lava flow stratigraphy on Mars as inferred from the Ar-ages. Figure taken from Cohen et al. (2017).

1.3.3 – Chassignites

Chassignites (1.3 Ga; Middle Amazonian) are olivine cumulates with a mineralogy that consists primarily of olivine (~90%) and the remaining ~10% of more or equal proportions of augite, chromite, feldspar, and minor accessory minerals (Johnson et al., 1991; Beck et al., 2006). These rocks are more depleted in REE than the nakhlites (Fig. 1.6).

Chassignite petrogenesis has been interpreted by Winter (2010). Initially a local area of the Martian mantle underwent partial melting, at this point the parental melt of chassignites stagnated at some distance and started the cooling process. Then, at the liquidus of this melt olivines began to crystallize for the time necessary to form a Martian dunite (Floran et al., 1978; Beck et al., 2006; Treiman et al., 2007), this stage of cumulus crystallization probably occurred at temperatures between 1230° C and 900° C (Johnson et al., 1991; Treiman et al., 2007). The chassignite magma cooled very rapidly and this resulted in finely exolved pyroxene and marked Ca zoning in olivine (Monkawa et al., 2004; Mikouchi et al., 2005). After the magmatic emplacement on the Martian surface, the chassignites experienced two shock phases, one strong event followed by a weaker event (Treiman et al., 2007), before the impact that ejected them from Mars.

Both Chassignites and Nakhlites were ejected from Mars at the same time and they have the same crystallization age (McSween, 2015); a possible comagmatic origin has been proposed (McCubbin et al., 2013).

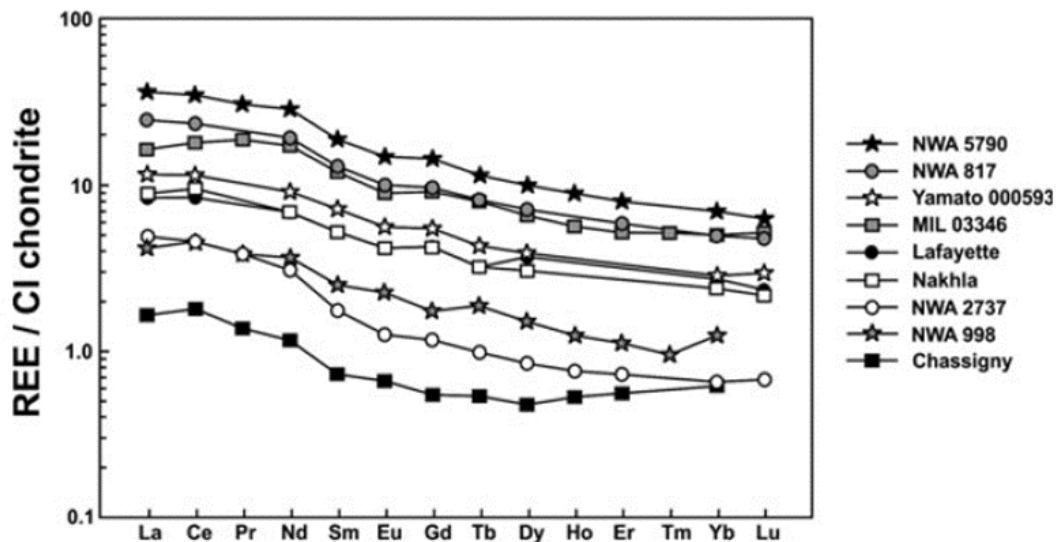


Fig. 1.6 - Rare Earth Elements (normalized to CI-chondrite) comparison between nakhlites and chassignites. Image taken from McCubbin et al. (2013).

1.3.4 – Exceptions

Allan Hills (ALH) 84001 (4.1 Ga; Noachian) is an ungrouped orthopyroxene cumulate (Mittlefehldt, 1994), which has experienced numerous shock events and for this reason is highly fractured. It is the oldest known Martian meteorite. It was the subject of media attention in 1996 when traces of ancient Martian bacteria were mistakenly identified within it (McKay et al., 1996; McKay et al., 2004).

Recently, other ungrouped Martian meteorites have been found and investigated. NWA 8159 is an augite-rich basalt (2.4 Ga; Early Amazonian) containing plagioclase with minor olivine and oxides (Agee et al., 2014). NWA 7034 and its other paired meteorites are sedimentary volcanic breccias (Agee et al., 2013), in part composed of basalt, mugearite and trachyandesite grains (Santos et al., 2013) and with very different crystallization ages. These rocks resemble the Martian regolith as analyzed from the rovers in Gusev and Gale craters (McSween et al., 2015).

1.4 - Samples selected

For this study, two shergottites (Tissint and Zagami) were selected along with five nakhlites (Nakhla, Lafayette, Miller Range 090136, Yamato 000749, and Yamato 000593) and the unique Martian augite basalt (NWA 8159).

1.4.1 – Tissint

Tissint is an exceptional Martian sample, both for its mineralogy, which is the most representative of a primary Martian mantle melt, and for the unweathered condition in which it was found, permitting confidence in a range of studies concerning Mars' planetary surface and internal processes (Balta et al., 2015).

Petrographic characteristics show that Tissint is a depleted olivine-phyric shergottite (Balta et al., 2015) with very large olivine crystals (>2 mm), which can contain small melt pockets and melt inclusions. Olivine show the greatest range in Fe-Mg composition ever found in a Martian meteorite, from Mg# 81.2 in the olivine megacryst cores to Mg# 27.6 in the olivine phenocryst rims. The olivine crystal size distribution (CSD) is in accordance with a steady-state crystallization system that was characterized by continuous growth/nucleation (Balta et al., 2015). A lot of veins and pockets filled by glass are also present (Chennaoui Aoudjehane et al., 2012).

The olivine-pyroxene-chromite assemblage for Tissint (Peslier et al., 2010) was used to calculate a subliquidus temperature close to 1200° C and a fO_2 close to Quartz-Fayalite-Magnetite buffer (QFM) -4 (Balta et al., 2015). The crystallization sequence shows how, in contrast to other olivine-phyric shergottites, chromite crystallized before olivine (Balta et al., 2015) while the olivine megacrysts could be due to pre-crystallization in a previous melt of the active magmatic system and then accumulation, as glomerocrysts, and entrainment in the final host magma (Balta et al., 2013). The presence of these olivine glomerocrysts combined with the relatively young age of Tissint could be an important constraint for a long-term active magmatic system on Mars during the last few hundred million years (Balta et al., 2015).

The shock experienced by Tissint reached pressures of 25 GPa (Ioannis et al., 2013), with a shock duration of 10-20 ms that support the idea of the generation from a small young crater on the Martian surface (Walton et al., 2014).

1.4.2 – Zagami

The Zagami meteorite is a shergottite that fell on the 3rd October 1962 near Zagami Rock in Nigeria (Graham et al., 1985). Zagami is an unusual shergottite because it seems to be the product of multiple incorporation or assimilation of irradiated old Martian soil (Hidaka et al., 2009), in fact it also display variations in age and initial isotopic composition in its different lithologies (Nyquist et al., 2010). The age of Zagami from Rb-Sr and Sm-Nd isotope systematics is ~170 Ma (Nyquist, 1995).

Zagami is a heterogeneous sample, characterized by different lithologies. The "normal" lithology is called Normal Zagami (NZ) and is a basaltic shergottite similar to the Shergotty meteorite (Stolper and McSween, 1979; McCoy and Lofgren, 1999). A Dark-Mottten Lithology is also present (DML; McCoy et al., 1995) and a Fe-rich lithology, obtained from David New, called (DN) (Agerkvist and Vistisen, 1993).

Different lithologies in Zagami, with complex pyroxene grains zoning (sometime normal zoning and sometime reverse zoning), would evidence a complex magmatic history after the initial differentiation of the Zagami parent melt (Niihara et al., 2015). In particular, Rb-Sr isotope systematics of NZ and DML lithologies suggest as Zagami may have experienced magma mixing and/or wallrock assimilation (Nyquist et al., 2006). Experimental data suggest that the texture matching that of the NZ lithology is consistent with a low nucleation density and a relatively slow cooling rate (i.e., $< 1^{\circ} \text{C/h}$) during its emplacement on the Martian surface (McCoy and Lofgren, 1999).

Two different crystallization theories exists for Zagami: (1) a two-stage magmatic history with crystallization of Mg-rich pyroxene in a deep magma chamber (1-2 kbar) and subsequent eruption of a thick lava flow with phenocrysts. This theory implies a cooling rate of $\sim 0.1\text{-}0.02^{\circ} \text{C/h}$ along with the possibility of a thick lava flow emplacement (McCoy et al., 1992); (2) a single-

stage magmatic history with cooling rates of 5-20° C/h with thinner lava flows (Treiman and Sutton, 1992). According to the former theory (McCoy et al., 1992), during the first stage Zagami experienced slow cooling crystallization in a deep magma chamber, at depth > 7.5 km evidenced by the pressure of crystallization of the amphibole. Successively, the evolution of the augite rims into pigeonite is explained as an interruption in pyroxene crystallization; during the subsequent stage, the pigeonites were incorporated into a magma that intruded in the near-surface as a dike or erupted to the surface as a >10 m thick lava flow. By estimating the depth of the magma chamber and the thickness of the lava flow, the Tharsis volcanic region on Mars seems a likely candidate for the source of Zagami, and likely for all the shergottites (McCoy et al., 1992).

Shock effects in Zagami comprise thin veins and pockets of black glass (Langenhorst and Poirier, 2000). The presence of melt pockets that contain Martian atmospheric gases into Zagami also suggest a near-surface environment for its origin along with local impact pressure of 80 GPa (Marti et al., 1995). Isotopic and elemental ratio of N, Ar, and Xe in melt pockets of Zagami strongly matches that of the Martian atmosphere as analysed by the Viking mission (Marti et al., 1995).

1.4.3 – Nakhla

Nakhla is a nakhlite that fell in Egypt on the 28th June 1911. The ^{40}Ar - ^{39}Ar dating, by Cohen et al. (2017), suggests a crystallization age of 1383 ± 7 Ma, while previous measurements suggested less defined values of ^{40}Ar - ^{39}Ar and Rb-Sr calculated crystallization age of 1.3 Ga (Bogard and Husain, 1977; Gale et al., 1975) and a Sm-Nd age of 1.26 Ga (Nakamura et al., 1982), with a CRE age of 12.30 Ma (Korochantseva et al., 2011). Nakhla is a medium-grained augite-olivine cumulate with a groundmass composed of Na-rich plagioclase, alkali feldspar, pyroxene and olivine, both Fe-rich (McKay et al., 1993). Nakhla has some terrestrial affinity for its petrology (Berkley et al., 1980), REE abundances (Schmitt and Smith, 1963), Rb/Sr linked with oxygen isotopic ratio, and oxygen fugacity (Gale et al., 1975). It has highly fractionated whole rock REE patterns (Nakamura and Masuda, 1973). Nakhla is a cumulate rock (Gale et al., 1975), in fact it formed by crystallization of pyroxene and olivine in a slowly cooling melt environment (Wager et al., 1960). Precipitation of other mineral phases

occurred as overgrowths to the pre-existing cumulus crystals. The intercumulus material is composed by 0.1 mm long plagioclase and clinopyroxene crystals with some grains of magnetite and sulphide (Gale et al., 1975).

Secondary alteration minerals are abundant in Nakhla. Glass in melt inclusions were sometime altered by water to generate berthierine, an Al-Fe-serpentine mineral (Lee and Chatzitheodoridis, 2016). The Nakhla hydrous silicate minerals saponite, opal-A, and berthierine were formed by interaction of water derived from the atmosphere and crust on Mars (Lee and Chatzitheodoridis, 2016). The ingredients for the formation of opal-A (and ferrihydrite minerals) derived by olivine dissolution by oxidizing and acidic aqueous fluids on Mars (Lee et al., 2015). Nakhla present clay and gypsum veins in olivine crystals with siderite, anhydrite and halite in interstitial sites, rich in Mg and Mn, and minor phases of goethite, and this would constrain a parent fluid derived by dissolution of LREE-enriched feldspathic mesostasis (Bridges and Grady, 2000). Iddingsite veins in Nakhla are composed by Fe-Mg silicate, siderite, and ferric (oxy)hydroxide. Secondary minerals in Nakhla (siderite, smectite, phyllosilicate, gypsum) formed by cementation of intragranular pores. Aqueous solutions could access the interior of the grains through fractures produced by shock (Tomkinson et al., 2012). Also, etching of olivine crystals augmented the porosity and permeability of the parent rock where dissolution and mineralization took place (Lee et al., 2013).

A possible petrogenetic scenario for Nakhla was first outlined by Nakamura et al. (1982) and would start with the partial melting of the Nakhla source followed by fractional crystallization (that removed clinopyroxene and olivine) and then a phase of accumulation and successive crystallization of clinopyroxene with minor olivine and intercumulus liquid, prior to quench crystallization of plagioclase, glass, and other minerals (Berkley et al., 1980).

1.4.4 - Lafayette

The Lafayette meteorite fell prior to 1931 near Lafayette (Indiana, USA) and it was then found in a museum draw (Niniger, 1935). Lafayette is a Ca-rich nakhlite composed of abundant cumulus clinopyroxene and minor Fe-rich olivine, with rare feldspar. The overall texture of the rock resembles that of a cumulate

volcanic rock (Boctor et al., 1976). Its opaque mineralogy comprises magnetite-ilmenite intergrowths, a Ca-Ti-rich magnetite, and some ilmenite (with some troilite inclusions). Pyrite is also present and displays lamellar intergrowths of marcasite. The mesostasis are rich in magnetite crystals with skeletal textures (Boctor et al., 1976). The composition of carbonate is siderite (Vincenzi et al., 1997). ^{39}Ar - ^{40}Ar suggests 1330 ± 15 Ma for the crystallization age of Lafayette (Cohen et al., 2017). It has a CRE age of 12.36 Ma (Korochantseva et al., 2011).

Sm-Nd systematics on Lafayette indicate a crystallization age of 1.32 ± 0.05 Ga, concordant with all the nakhlites, while the Rb-Sr isochron age define a younger age of 1.26 ± 0.07 Ga (Shih et al., 1998) and ^{39}Ar - ^{40}Ar estimate an age of 1.33 ± 0.03 Ga (Posodek, 1973). Additionally, the Rb-Sr data of iddingsite-rich samples and K-bearing phyllosilicates yield an age of 679 ± 66 Ma or 633 ± 23 Ma, this age could reflect the aqueous alteration events that formed the iddingsite veins (Shih et al., 1998; Borg & Drake, 2005). A secondary low-grade thermal event may have affected Lafayette, as suggested by other measurements of Ar-Ar systematics with an age of 1.09 Ga (Korochantseva et al., 2010).

Lafayette displays evidence of mineral carbonation in olivine and a plagioclase feldspar-rich mesostasis: olivine was particularly susceptible to this carbonation process because of the presence of smectite veins that made possible for CO_2 -rich fluids to reach the grain interiors (Tomkinson et al., 2013). This would imply atmospheric CO_2 sequestration and storage on Mars during the Noachian (Tomkinson et al., 2013).

1.4.5 – Miller Range 090032

The MIL 090032 meteorite is a nakhlite that was recovered in Antarctica, in the Miller Range area during the 2003-2004 Antarctic Search for Meteorites (ANSMET) field season (Dyar et al., 2005). It contains ~ 70% of augite, 3% of olivine, and a fine-grained mesostasis with basaltic glass, olivine, Ti-rich magnetite, and pyrrhotite. The FeO/MnO and Fe/Mg ratio of augite and olivine crystals is almost identical to the other nakhlites. Petrological, mineralogical and textural analysis suggests that MIL 03346 is paired with MIL 090030, MIL 090032, and MIL 090136 (Hallis and Taylor, 2011; Udry et al., 2012). Also, these meteorites were altered on Mars by weakly HCO_3^- -depleted acidic brine, as

observed by olivine-bound alteration assemblages (Hallis and Taylor, 2011). The obtained ^{39}Ar - ^{40}Ar crystallization age is 1392 ± 10 Ma (Cohen et al., 2017).

The paired MIL 03346 meteorite is the Martian meteorite with the highest Fe^{3+} abundance in augite suggesting high-T of equilibration near the QFM oxygen buffer. Thus, this meteorite has come from a large oxidizing magmatic environment on Mars (Dyar et al., 2005). Experimental petrology studies on MIL 03346 reveals that the cooling rate would have been around 20°C per hour and occurred in a solidifying lava at a depth of around 0.4 m on Mars (Hammer, 2009). In particular, its magmatic emplacement results in an inflated pahoehoe sheet, by basing on textural observations, and features indicating fast cooling rates, up to 6°C per hour, have been argued (Day et al., 2006; Hammer & Rutherford, 2005).

The MIL 03346 meteorite is characterized by many secondary alteration phases by aqueous processes: iddingsite-veins in olivine, precipitation of Ca-sulphates and Fe,K-sulphates, oxidized titanomagnetite, and dissolution of primary Ca-phosphates. In particular, Si-rich alteration veins in olivine may have been formed on Mars suggesting multiple episodes of alteration of this meteorite. In general, each nakhlite seems to have its own alteration history (Stopar et al., 2013). Also, when magmatic-hydrothermal fluids are in contact with sulphide grains in MIL 03346 a reaction of sulphide oxidation occur and form jarosite, this continue to cool and then precipitate forming hematite (McCubbin et al., 2009).

1.4.6 – Yamato 000593 and Yamato 000749

The Yamato meteorites (Y-000593, Y-000749, and Y-000802) are nakhlites found by the 41st Japanese Antarctic Research Expedition in the same ice field in Antarctica, and very close to each other (Imae et al., 2002). As they were all found spatially very close, with very similar weathering degrees (Misawa et al., 2003a), and the same chemical composition and rare gas abundances (Okazaki et al., 2003), it was generally accepted that they are paired meteorites. However, this may be not true, because their $^{40}\text{Ar}/^{39}\text{Ar}$ ages differ by 70 ± 10 Ma (Cohen et al., 2017) and the modal abundance of olivine is slightly different between Y-000749 and Y-000593 (Imae et al., 2003). Sm-Nd and Rb-Sr isotope systematics

are also in agreement with the nakhlite crystallization age of 1.3 Ga for Y-000593 (Misawa et al., 2003b). They derive from a LREE-depleted magmatic source (Misawa et al., 2005). Initial isotopic abundances of Sm and Nd suggest that Y-000593 is comagmatic with Lafayette and may derive from chemically very similar magmas (Misawa et al., 2005).

The modal mineralogy of the Yamato nakhlites is: euhedral augitic pyroxenes as the major mineralogical phase (75-80 vol. %) with very thin Fe-rich rims, anhedral Fe-rich olivine (8-18 vol. %) and subhedral titanomagnetites (< 1 vol. %). The rest is mesostasis of plagioclase, pyrrhotite, apatite, pigeonite, tridymite, and iddingsite (Imae et al., 2003). In particular, the modal mineralogy of Y-000539 is: ~80 vol. % of augite, 10 vol. % of olivine and 10 vol. % of mesostasis. Augite present Fe-rich thin rims (normal zoning) that were likely crystallized by interaction with the mesostasis (Mikouchi et al., 2003).

Several authors support the idea of pairing of the Yamato nakhlites (Imae et al., 2003; Misawa et al., 2003b; Okazaki et al., 2003) by arguing for: (1) similarity in chemistry (major elements and REE distributions) also in respect to the other nakhlites; (2) very similar weathering degrees; (3) very similar cosmic ray exposure; (4) their finding location that is spatially very close in the same ice field in Antarctica. There are, however, other possible explanation for these 4 points: (1) Similarity in chemistry could also means that the volcanic source of nakhlites had a long period characterized by a certain chemistry of magmatism (prior to a shift in chemistry) but the two lava flows (Y-000593 and Y-000749) were erupted in different Myr apart from each other in this period. Also, the Ar-Ar dating is incompatible with their formation at the same time (Cohen et al., 2017) and the range of trace element concentrations in the augites of these Yamato nakhlites is slightly different (Wadhwa et al., 2004) and the mineralogy is not totally the same because the modal abundance of olivine is different between Y-000749 and Y-000593 (Imae et al., 2003); (2) (3) (4) same weathering degree, CRE and finding location could simply be explained as a natural consequence of ejection from Mars at the same time.

Secondary Martian alteration minerals in Y-000593 are laihunite and iddingsite (overall within olivine phenocrysts), while terrestrial alteration appear to be characterized mainly by phyllosilicates (Breton et al., 2015). Laihunite in Y-000539 and Y-000749 is extraterrestrial in origin because it show evidence of

thermal modification during atmospheric entry and it appear to have been formed before the fusion crust (Noguchi et al., 2009). Noble gases analyzed with laser ablation in the Y-000593 shows a high concentration of ^4He and ^{40}Ar in the mesostasis and relatively lower in olivine and pyroxene. This implies that the mesostasis are the likely trapping sites of Martian atmosphere (Nagao et al., 2009).

Yamato nakhlites petrogenesis was interpreted as follows (Imae et al., 2005): (1) Initially phenocrysts of augite cores, olivine cores, and titanomagnetite accumulated on the floor of a magma chamber, and olivine trapped some melt inclusion; (2) after the eruption and magmatic emplacement on the surface of Mars as a lava flow, the crystals of augite and magnetite started to aggregate and olivine cores develop lamellae and symplectites; (3) overgrowth of olivine and augite rims with normal zoning; (4) crystallization of the mesostasis with plagioclastic composition. Mantle source conditions and magmatic emplacement have also been studied in the Yamato nakhlites. The partitioning behaviour of Eu in the augite of the Yamato nakhlites was used to infer that they derive from an oxidized mantle source (Wadhwa et al., 2004). From geothermobarometric calculations on mineralogical phases of Y-000593 it is possible to notice how after clinopyroxene crystallization at 1150 °C the magma was quickly emplaced near the Martian surface as a lava flow, with a cooling rate of 0.002 °C/hr (Szymanski et al., 2003).

1.5 – Purpose of this research

Martian meteorites are the only rock samples from Mars that are available on Earth. **The aim of this research is to obtain new insights about Martian mantle formation and evolution from the perspective of the Martian meteorites.** Mars is characterised by a stagnant-lid geodynamic regime, without evidence of homogenization of the mantle after the end of the last magma ocean phase (~4.5 billion years ago). Thus, Mars' magmatic rocks are extremely important in understanding how the Martian interior formed and evolved, and this is the specific motivation for the work that has been done in this thesis.

This work was divided into 3 different parts:

(1) *Temperature and convective activity of the Martian mantle.* The Tissint Martian meteorite was investigated since it is the meteorite that is most representative of the Martian mantle, as it has a depleted composition and is thought to derive from a deep magma chamber on Mars. Major- and trace-element data for Tissint olivine and pyroxene were reported, and these data were used to provide new insights into the dynamics of the Tissint magma chamber, as well as the dynamics and temperature of the Martian mantle at the time of Tissint crystallisation. For the first time, the temperature of the Martian mantle was obtained from the chemistry of olivine megacrysts formed in depth in a magmatic system on Mars, and evidences of convection were detected.

(2) *Nakhlite mantle source and early Mars differentiation.* Five of the ten known nakhlite lava flows (Nakhla, Lafayette, MIL 090032, Yamato 000593, and Yamato 000749) were studied. These nakhlites likely acquired S-rich particles from the regolith during their emplacement on the planet's surface and here has been investigated the potential implications that this process has on chemical tracing of nakhlite Martian mantle source(s). In addition, these findings were used to suggest a plausible scenario to account for nakhlite magma origin and implication for late-stage crystallization of a Martian magma ocean. For the first time, multiple nakhlite samples were analysed using Re/Os isotope systematics to understand how many mantle reservoirs generated the nakhlites, the sulphur isotopic composition of the nakhlite source was characterized, HSE were used to constrain a sulphide melt for the nakhlite magma, and an enriched component derived from the crystallization of the Martian magma ocean was suggested as a contaminant of the nakhlite source.

(3) *Shergottite mantle source and volatile abundance.* Amphibole and apatite phases were analysed in the two shergottites Tissint and Zagami, in order to retrieve chemical abundance of the volatile element chlorine in the shergottite magma source and to compare this with the nakhlite/chassignite magma source(s). After finding that these amphiboles/apatites record magmatic conditions of the Martian interior, the partition coefficients between chlorine and the parent melt were used to estimate the Cl abundance of the shergottite mantle source. For the first time, a Cl-poor mantle source for the shergottites was inferred and compared with the volatile composition of the nakhlite and chassignite mantle source.

To conclude, all these parts are discussed in terms of new implications in the context of Mars formation and evolution and, more generally, evolution of terrestrial planets. In particular, it is discussed how the assimilation of an enriched component during the early differentiation of Mars may contribute to the generation of different mantle reservoirs on Mars. In addition, new evidences of heterogeneity in the Martian mantle are discussed based on the outcomes of this work, better constrained by the presence of different mantle sources on Mars, for the different group of Martian meteorites, based on geochemistry of the highly siderophile elements, sulphur isotopes, and volatile content. Further, new thermodynamical constraints about the presence of convective activity in the Martian mantle until the most recent period (at around 500 Ma) are discussed also in terms of mantle viscosity and energetics, implying an active Martian mantle was in place in relatively recent geological period. Consequently, I used all this original results to better constrain a model of terrestrial planets evolution.

Chapter 2 Methods

2.1 – Scanning Electron Microscopy/Energy Dispersive Spectroscopy

In the Scanning Electron Microscope (SEM) a very narrow beam of electrons, with energy up to 30 KeV, is focused on the surface of the sample inside a chamber under vacuum (Fig. 2.1). This electron beam scans in form of a succession of parallel lines. Once the electrons impacts on the sample surface, they generate the emission of secondary electrons and the re-emission or reflection of high-energy electrons, or electrons that belong to the primary beam. The secondary electrons are used to obtain images of the sample (back-scattered electron images), while the chemical microanalysis is accomplished by measuring the energy and the distribution of the intensities of the X-rays generated by the electron beam in the sample by using energy dispersive spectrometry (EDS). These analyses can be both of a selected area or a point of interest on the surface of the sample (microanalysis). In essence, the generation of X-rays is due to collisions of the electrons of the beam with the electrons located in the inner shells of the atom in the sample. When the electrons are ejected they leave a vacancy in the orbit, so that subsequently a higher-shell electron falls into the vacancy releasing a sort of energy (that is the X-ray, and they are unique for each element).



Fig. 2.1 - Photo of the Scanning Electron Microscope (SEM) used at the University of Glasgow.

A Zeiss-Sigma variable pressure field emission gun scanning electron microscope (VP-FEG-SEM), at the Imaging Spectroscopy and Analysis Centre of the University of Glasgow, was used in this work. Specific conditions for each sample analysis, standards, results and discussion of the SEM-EDS data are reported in [Chapter 3](#), [Chapter 4](#), and [Chapter 5](#).

2.2 – Laser Ablation Inductively Coupled Plasma Mass Spectrometry

Laser Ablation Inductively Coupled Plasma Mass Spectrometry (LA-ICP-MS) is an analytical technique that permit highly sensitive chemical analysis of geological samples ([Fig. 2.2](#)). A laser beam is focused on the sample surface and this results in the phenomenon of ablation - inducing fine particles blusted from the sample. These particles subsequently reach the ICP-MS excitation source, where they are ionized. This source is a plasma that is ionized due to gas heated by an electromagnetic coil - in this sense, the gas itself is conductive. A flow of argon or helium is normally used as the gas carrier. These ions are then acquired by a mass spectrometer for detecting chemical abundances or isotopic ratios. National Institute of Standards and Technology (NIST) glasses are in general used as standards for trace element analysis of geological samples at LA-ICP-MS, the three most common glasses used are NIST 612, NIST 614, and NIST 616.



Fig. 2.2 - Laser Ablation Inductively Coupled Plasma Mass Spectrometry (LA-ICP-MS) system used at the University of Glasgow.

Table 2.1 - Measurement parameters at the LA-ICP-MS system.

Parameter	Value
Gas carrier	Argon
Laser energy	3.60 mJ
Repetition rate	10 Hz
Plasma power	1350 Watt
Auxiliary gas flow	0.8 l/m
Focus potentials	-162.8 V
CCT focus lens	-1.59 V
Collision gas	CP grade helium
Cones	Nickel

In this work an iCAP-RQ ICP-MS, equipped with a RESOLution 193 nm Excimer laser, at the University of Glasgow, was used to analyse trace elements of mineral phases. A NIST 612 glass standard was analysed throughout each analytical session, and an Ar gas carrier was utilised. Measurement parameters are tabulated in [Table 2.1](#). Specific conditions, results, and discussion of the data obtained with LA-ICP-MS are reported in [Chapter 3](#).

2.3 – Electron Probe Micro-Analyzer

The electron probe micro-analyzer (EMPA) use a microbeam for *in situ* chemical analyses that can be considered non-destructive ([Fig. 2.3](#)). It can be used to analyse very small samples and with lower detection limits in respect to the SEM - for the rest it works essentially like a SEM (see [Paragraph 2.1](#)). The main difference in respect to the SEM is the possibility to conduct chemical microanalyses at spot sizes reaching 1-2 μm with wavelength-dispersive spectroscopy (WDS). It can also be used to acquire analyses of specified transects in a mineral or an area of the sample: for example, it is able to obtain a chemical profile from core to rim of a mineral to see how the major and trace elements abundances changes. In particular, different types of detectors can be used for imaging, like BSE and cathodoluminescence imaging (CL), and for chemical analyses, like EDS and WDS, or even analyses of crystal-lattice preferred orientations (EBSD).



Fig. 2.3 - Electron Probe Micro-Analyzer (EMPA) used at the University of Western Australia.

In this work, a JEOL 8530F Field Emission Gun Electron Microprobe equipped with 5 tuneable wavelength dispersive spectrometers at the Centre for Microscopy, Characterisation and Analysis at the University of Western Australia, was used for analysis of major and minor elements. Specific conditions, results, and discussion of the data obtained with EMPA are reported in [Chapter 3](#).

2.4 – Highly siderophile elements laboratory method

Highly siderophile elements (HSE; Re, Os, Ir, Ru, Pt, Rh, Pd, and Au) separation, digestion, and extraction is a destructive technique that consist in chemically extracting these elements from a given geological sample ([Fig. 2.4](#)). This method is commonly applied in an ultra-clean laboratory under controlled conditions, in order to avoid any sort of contamination due to the anticipated low HSE abundances, as can be expected especially in small quantities of precious Martian samples. This methodology was used for the separation of HSE to then determine their abundances and corresponding Re-Os isotope systematics in four Martian meteorite chips (Nakhla, Lafayette, MIL 090032, four Tissint fragments). All the Re-Os and part of the HSE chemical separation was conducted in the ultra-clean laboratory at the Durham Geochemistry Centre of the Durham University. The sample MIL 090032 was analysed in the laboratories at the Freie Universität Berlin. Results and discussion of the data obtained are reported in [Chapter 4](#).

Below the details of the methodology used for HSE separation at the Durham laboratory is divided into 4 different parts:

(1) *Sample powdering and weighting of chemistry fraction.* Textural characterization of the samples and the fragments was retained prior of destruction of the same. All samples were weighted before and after crushing and a sample ID for each sample and sub-sample was chosen. A virgin pestle and mortar of alumina was used for sample crushing and it was cleaned with Milli-Q H₂O and quartz after crushing of each sample. After crushing, > 0.4 gr of sample for the nakhlites were obtained. We chose a basalt spike for Nakhla, Lafayette and the TPB, and a picrite spike for the Tissint fragments (Tissint-A, B, C, D): all the spikes used were weighed in dedicated Teflon wares prior to addition to the sample powder in a high purity quartz asher vessels. For digestion, 0.40 gr for Nakhla, 0.41 gr for Lafayette, 0.03 gr for Tissint-A, 0.04 gr for Tissint-B, 0.03 gr for Tissint-C, and 0.01 gr for Tissint-D were used. A mixed ¹⁹⁰Os-¹⁹¹Ir-⁹⁹Ru-¹⁹⁴Pt-¹⁰⁶Pd-¹⁸⁵Re basalt spike was used. Four blanks were determined. Blank contributions are: 8.4 % Re; 24 % Ir; 3.8 % Ru; 1.1 % Pt; 2.9 % Rh; 17.5 % Pd; 24 % Au at Berlin; while blank contributions at Durham are Re, 0.42-0.49 %; Os, 0.70-4.20 %, ¹⁸⁷Os/¹⁸⁸Os = 0.132; Ir, 0.10-0.26 %; Ru, 0.04 %; Pt, 0.25-0.4 %; Pd, 0.87-1.0 %.

(2) *Asher digestion.* At this point, complete dissolution and spike equilibration is obtained. The vials with the spikes for each sample were first diluted with ~2 mL of chilled 12N HCl and then poured into vessels that has been previously cleaned in the asher. The vessels were agitated at the base to make sure that all powder was wetted. Successively, 5 mL of chilled 16N HNO₃ was added to each vessel, these were sealed with Teflon tape for overnight digestion.

(3) *HSE separation.* Vessels from the asher were opened and diluted with 4mL of MilliQ-H₂O into the inverse aqua regia. With different pipettes for each sample, the aqua regia + MilliQ-H₂O mixture was isolated in a pre-cleaned 50 ml centrifuge vessel. Then, 3 mL chloroform was added to the sample remaining in the asher vessel and then transferred to the vessel containing inverse aqua regia. The aqua regia + chloroform vessel was then vigorously agitated prior to being placed on a rocker for ~30 minutes.

(4) *Os fraction through HBr back-extraction.* During the next step, pipette was used to extract chloroform + Os from the solution comprising aqua regia + H₂O. The extracted liquid (chloroform + Os) was added to 4 mls of HBr in Teflon wares. Then 2 mL of chloroform was added to the centrifuge vessel and this was

again agitated prior for a further ~30 minutes on the rocker; repetition of these procedures meant that the chloroform extraction was performed in triplicate to ensure efficient isolation of Os in the HBr fraction. Successively, the aqua regia + H₂O mixture remaining in the centrifuge vessels (and containing Ir, Pt, Pd, Ru, Re) was then taken up by pipette and added to separate Teflon wares so as to dry down on a hot plate overnight at 90° C. Following several hours on the rocker, Teflon wares were opened and the chloroform was extracted using a fine-tipped pipette and poured in the waste, leaving only the HBr containing Os for processing. The HBr + Os solution was then placed on a hot plate overnight at 80° C.

(5) *Os microdistillation.* For the purification of osmium we used a microdistillation technique. 30µl 12N H₂SO₄ was added to the apex of the sample vials from HBr dry-down, and 10 µl of HBr was added to the tip of a separate 'rocket-vial'. Then, ≥15µl of H₂SO₄ + Os were taken from the sample vials and installed as a single droplet at the centre of the lid to each rock vial. At the exact centre of this droplet 15µl of CrO₃ were added. Successively, the rocket body with the HBr droplet was used to gently close the vial in an inverted position. Then, the rocket vial was held level and foil was folded to its top making sure to leave the HBr droplet exposed before carefully placing the inverted rocket vial on to a hot plate for ~2 hours at 90° C. After this time, the rocket vial was opened and visually checked prior to returning the right-way-up and open body of the rocket vial to the hot plate at 85° C for ~40 minutes to reduce the size of the HBr bead at its apex.

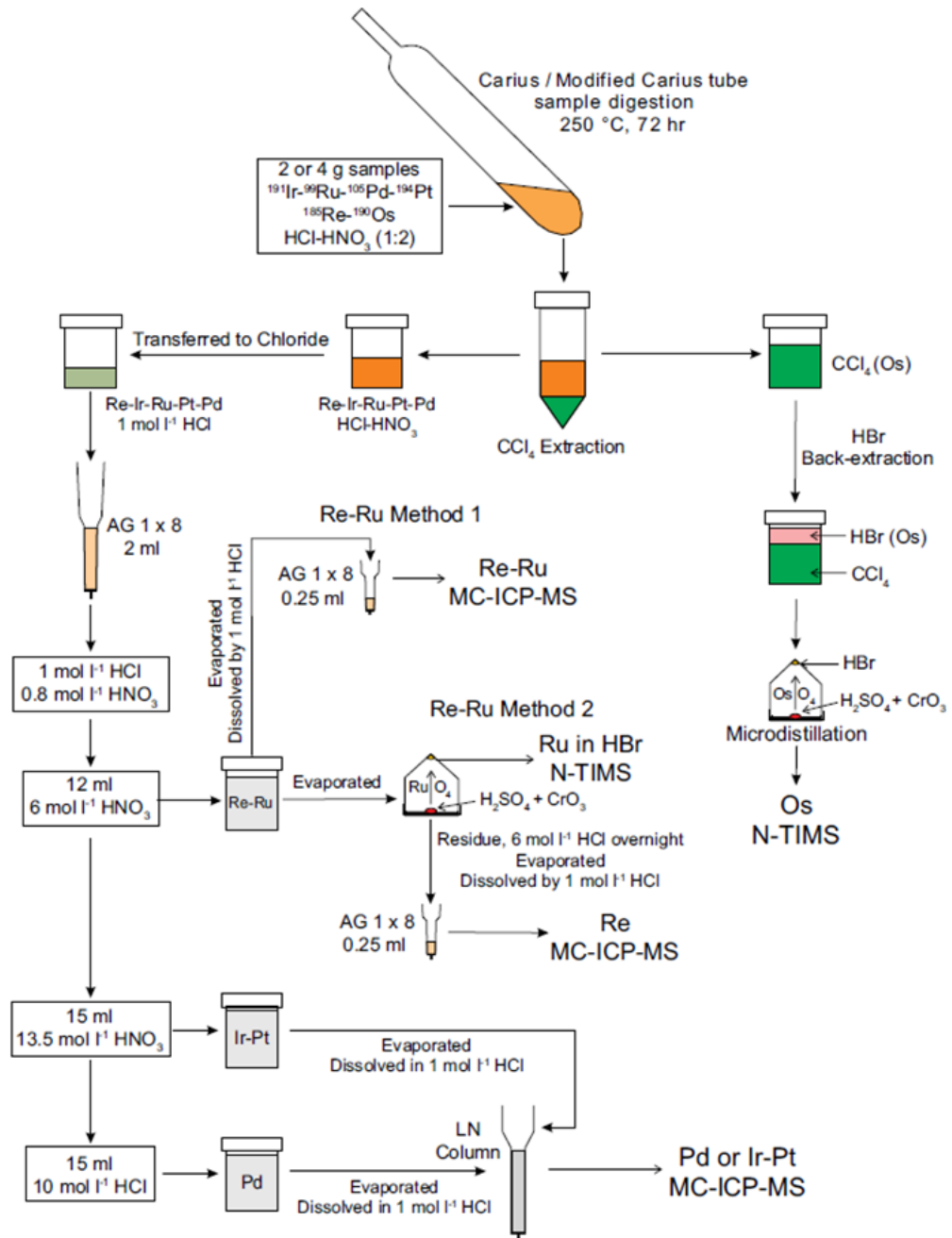


Fig. 2.4 - Highly siderophile elements (HSE) laboratory technique schematics. Note: chloroform was used instead of carbon tetrachloride.

2.5 – Thermal Ionization Mass Spectrometer

A Thermal Ionization Mass Spectrometer (TIMS) is used to obtain extremely precise (0.01-0.001%) measurements of isotope ratios through a magnetic sector mass spectrometer (Fig. 2.5). The elements chosen for isotopic analysis need to be ionized thermally: this is achieved by a current that passes through a very

thin metal ribbon (sometimes involving more than one ribbon) under high vacuum. Ions are generated on the ribbon (in the case of osmium, a pre-cleaned Pt-ribbon), then accelerated up to 10 KV and, subsequently, focused into a beam with the help of slits and plates. When the ion beam passes through the magnetic sector the beam separates accordingly to the differences in mass to charge ratio of the element(s). The beams produced terminate at the collectors, with conversion of the ion beam into voltage: from the voltage value it is possible to infer the isotope ratios of the elements. For isotopic tracer studies, the sample needs an artificial spike isotopically enriched to better determine isotopic concentrations and ratios. Loading of the elements for analysis is accomplished by inserting acid solutions on metal ribbons.



Fig. 2.5 - Thermal Ionization Mass Spectrometer (TIMS) used at the Durham University.

A Thermo Fisher Triton TIMS at the Durham University was used on the same samples used for HSE separation, in order to acquire their Re-Os isotope systematics. Data were processed using the Tune-Triton software, measuring Re-Os from the filaments. Below the details of the method used are described, while results and discussion derived from these data are reported in [Chapter 4](#). MIL 090032 was analysed at the Berlin laboratories, but owing to a problem in processing this sample osmium failed to run for MIL 090136.

After making filaments with platinum ribbon, each filament was outgassed for 10-15 minutes at 2A until they glowed orange in colour. Then, the filaments were mounted and heated with 0.5A of current and the sample (droplet from the rocket after microdistillation - see [Paragraph 2.4](#)) was applied using a catheter and dried on the filament. After this, $\text{Ba}(\text{OH})_4$ was applied as an Os activator ensuring that the sample was covered. We access two dilutions of the DROsS

standard solution for loading onto the filaments (4b and 5b); where 50 pg and 10 pg loads were applied. The filaments were loaded onto a magazine and into the source chamber of the TIMS.

Initial conditions for analysis of the four Tissint fragments were: HV source pressure of 2.92×10^{-7} mbar; FV pressure of 3.06×10^{-2} mbar; Ion getter pressure of 2.67×10^{-9} mbar; filament temperature of 700° C; filament current of 700 mA; setting of 20 minutes for each analysis. Initial conditions for analysis of Nakhla and Lafayette were: HV source pressure of 2.95×10^{-7} mbar; FV pressure of 3.14×10^{-2} mbar; Ion getter pressure of 3.46×10^{-9} mbar; filament temperature, current and timing for analysis were the same of Tissint. The osmium isotope ratios were measured as OsO_3^- by TIMS operating in negative mode (Creaser et al., 1991, Völkening et al., 1991) and masses were measured via peak hopping protocols on an axial secondary electron multiplier. Mass 233 ($^{185}\text{ReO}_3$) was monitored throughout the run to assure that potential isobaric interferences from $^{187}\text{ReO}_3$ were insignificant. Data were processed offline to correct for spike contributions, ^{17}O and ^{18}O oxide interferences and mass fractionation assuming a $^{192}\text{Os}/^{188}\text{Os}$ normalising ratio of 3.08271 and an exponential law. The electrical noise in the instrument (darknoise) was of 0.000047 $\mu\text{V}/0.0029$ cps/0.176 cpm for all the analyses.

For the Os1 method on the N-TIMS that collected via the secondary electron multiplier (static), the integration times were as follows: 192Os16O3 = 2.097 seconds; 190Os16O3 = 2.097 seconds; 189Os16O3 = 1.049 seconds; 188OsO3 = 4.194 seconds; 187Os16O3 = 8.389 seconds; 186Os16O3 = 1.049 seconds; 185Re16O3 = 4.194 seconds. This method applied an internal standard normalization for $192/188 = 3.08271$ using an exponential law. Typical intensities (in counts per second) specific to each measurement were: 3,41E+04 for mass of 240; 2,42E+04 for mass of 238; 1,35E+04 for mass of 237; 1,10E+04 for mass of 236; 2,04E+03 for mass of 235; 1,39E+03 for mass of 234; 1,64E+01 for mass of 233. A sort of oxygen bleed was used to ensure that Osmium-oxide species form as the osmium is ionized from the filament. Then, the masses of osmium oxides are measured on the detector and corrected for "known" oxygen proportions (i.e., oxygen masses of 16-17-18) to determine the osmium mass versus osmium ratio values. For reasons of extreme caution with the understood limited osmium load, each analysis by N-TIMS was run twice. The first measurement at a lower filament temperature and current and the second at a

very slightly higher temperature and current. The values measured from the second filament run were taken (slightly higher temperature) in preference as these were slightly more precise. In following this protocol, generally the osmium load of the filament for the nakhlite specimens was exhausted.

2.6 – Secondary Ion Mass Spectrometer

The Secondary Ion Mass Spectrometer (SIMS), also called “ion microprobe”, focus a primary beam of positive or negative ions on the surface of a specimen in order to generate secondary ions (Fig. 2.6). These secondary ions then enter a mass spectrometer where they pass through a high electrostatic potential. Some of the atoms sputtered out of the sample became then ionized and enter the mass spectrometer. All this is done under vacuum. What happens in the instrument depend on the primary beam, if it is composed of ions that are positively charged then negative ions will be produced due to ionization, and *vice versa*.

Two main SIMS modes are possible: dynamic and static. The dynamic mode is primarily used for analysis of isotopes and elements; in this mode the primary beam ion fluency exceeds the limit of $\sim 1E12$ ions/cm² (called “static limit”) generating a high yield of secondary ions. The static mode is instead used to acquire information on molecular species in the surface of several materials (even biological); this mode use a primary beam with much lower energy. A special multicollection mode is sometime also available in a SIMS: this mode permit highly precise acquisition of the sample chemistry and isotopes because each ion image is detected from the same exact volume of the sample.



Fig. 2.6 - Secondary Ion Mass Spectrometer (SIMS) used at the Centre de Recherches Pétrographiques et Géochimiques (CRPG) in Nancy (France).

In this work, a CAMECA IMS 1280 ion microprobe was used in multicollection mode at the Centre de Recherches Pétrographiques et Géochimiques (CRPG) in Nancy (France) to collect sulphur isotope data ($\delta^{34}\text{S}$, $\delta^{33}\text{S}$, and $\Delta^{33}\text{S}$). Sample preparation, specific conditions, results, and discussion of the data obtained with SIMS are reported in [Chapter 4](#).

2.7 – Focused Ion Beam section preparation

The Focused ion beam (FIB) is a technique for thin section preparation ([Fig. 2.7](#)). The way in which FIB systems works resemble the SEM, but the major difference is that a FIB use a highly focused beam of ions rather than electrons like in a SEM. The ion used in the primary beam is generally the gallium (Ga^+), and this can also operate at low beam currents for the purpose of imaging or at high current for milling of the sample.

Initially, the hit of the Ga^+ primary beam sputters out a little quantity of sample material from the surface. Secondary ions or even neutral atoms are then ejected from the surface, in the meantime also the primary beam generate electrons: signals deriving from secondary ions is collected in order to create an image. The higher is the current of the primary beam and the higher precision can be achieved. Samples can be loaded even if they are not conductive (and so without coating), in this case a low energy electron flood gun is used to charge the sample.

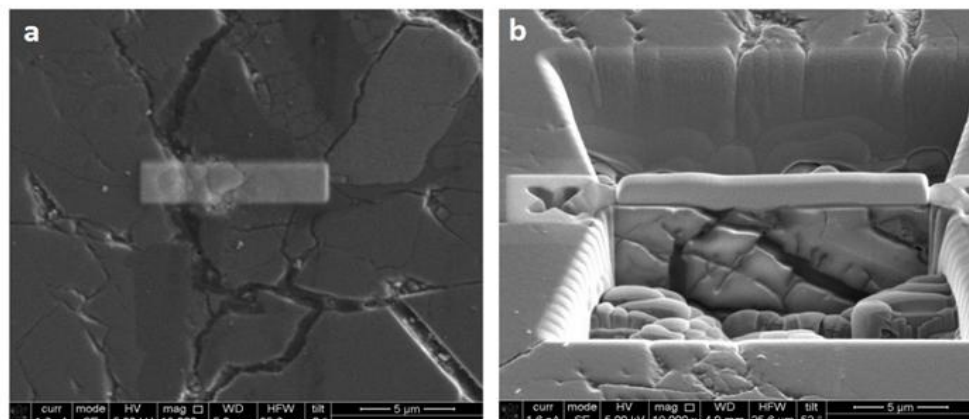


Fig. 2.7 - Focused Ion Beam (FIB) section preparation. a) Example of a FIB-section preparation in a particular area (brighter area) in Tissint; b) trench area excavated in the bright area in (a).

In this work, a FEI Nanolab dual beam focused ion beam (FIB) was used to extract two amphiboles for Tissint and two for Zagami, at the University of Glasgow. All the 4 foils extracted were 11 x 5 x 0.1 μm in size. Results and discussions of the data obtained by analysing these foils are reported in [Chapter 5](#).

2.8 – Transmission Electron Microscopy

A Transmission Electron Microscope (TEM) transmits a beam of electrons through a sample in order to form an image ([Fig. 2.8](#)). Usually, the “sample” is a less than 100 nm thin section and this extremely thin thickness is useful for the beam to be transmitted through the sample and can be also suspended on a grid. The electrons coming from the beam interact with the sample while passing through it and, in the end, an image is formed - that is then magnified and focused in an imaging layer. Imaging at TEM is several times better and detailed than a normal light microscope.

The magnetic lenses of a TEM instrument can be arranged in order to place the back focal plane of the lens on the imaging apparatus - in this way, a diffraction pattern can be created. A diffraction pattern product is an image consisting of a pattern of bright ordered dots when a crystal is analysed, but it can be seen as a circle when a glass or amorphous material is analysed. In this sense, with the diffraction pattern of a crystal, information like the space group symmetry can be inferred. Particular types of TEM instruments allow for chemical analyses of the sample in EDS, by following the same methodology described in [Paragraph 2.1](#).



Fig. 2.8 - Transmission Electron Microscope (TEM) used at the University of Glasgow.

In this work, a FEI T20 TEM at 200kV was used to acquire high-resolution images along with selected area electron diffraction (SAED) patterns and a JEOL Atomic Resolution Microscope 200cF at 200 keV/~180 pA was used in STEM mode and using a Bruker 60 mm² SDD/EDX spectrometer for quantitative chemical analysis. These analysis have been conducted on the FIB-sections prepared as described in [Paragraph 2.7](#). Diffraction patterns have also been acquired. Results and discussion of the data obtained by using TEM are reported in [Chapter 5](#).

Chapter 3 Temperature and convective activity of the Martian mantle

The following chapter is taken from the paper titled “Convective activity in the Martian upper mantle recorded by P-zoning in Tissint olivine”. This paper has been accepted with revisions in the peer-review journal *Meteoritics & Planetary Science*.

This paper has been used as [Chapter 3](#) of the present thesis because it is about determining the temperature of the Martian mantle, which is useful to define viscosity and actual thermal state of the Mars’ interior, and is one of the goal of this research.

The Author of the thesis is the First Author of the paper, having conducted the vast majority of the work, data acquisition, data processing, data interpretation, and writing. Other co-authors of the paper include: Lydia J. Hallis, who helped during sample preparation, SEM analysis, and manuscript revision; Luke Daly, who helped in acquiring the ion microprobe data and in revising the manuscript; and Martin R. Lee, who helped during SEM analysis and in revising the manuscript.

3.1 – Introduction

3.1.1 – The Tissint Martian meteorite

Tissint is one of the least terrestrially weathered Martian meteorites, having been seen to fall in Morocco in 2011 (Irving et al., 2012), and collected shortly after (~4 months) (Chennaoui Aoudjehane et al., 2012). Tissint’s crystallization age is 574 ± 20 Ma, based on Rb-Sr and Sm-Nd isotopic systematics (Brennecka et al., 2014), making it one of the oldest known shergottites. However, its cosmic ray exposure (CRE) is in line with some other shergottite meteorites, at 1.05 Ma (Brennecka et al., 2014).

Tissint is an olivine-phyric shergottite, which exhibits large olivine crystals (up to 2 mm diameter), commonly containing melt inclusions (Balta et al., 2015).

Plagioclase is completely converted to maskelynite, and shock produced melt glass is observed within Tissint, consistent with shock metamorphism up to pressures of 25 GPa (Baziotis et al., 2013), suggesting post-shock temperatures of $\sim 200^\circ$ C for the whole rock (Stöffler et al., 1991). Low-Ca clinopyroxene (pigeonite) phenocrysts evolve to augite toward the rims, and subsequently to a high-Fe composition at the very end of crystallization (Balta et al., 2015). Oxides include ilmenite, ulvospinel, magnetite and chromite, and rare pyrrhotite is also present. Phosphate is present in the form of merrillite only - no apatite has been reported (Balta et al., 2015). A fine-grained (<0.25 mm size) olivine- and clinopyroxene-rich mesostasis is observed (Balta et al., 2015; Liu et al., 2016).

Tissint is an unusual depleted olivine-phyric shergottite, characterised by a whole-rock that is depleted in LREE and has a flat HREE pattern indicative of a mantle derived melt (Balta et al., 2015). Petrogenetic calculations have located the depth of the Tissint magma chamber at ~ 40 -80 km, corresponding to a pressure of ~ 4 Kbar within the Martian upper mantle (Basu Sarbadhikari et al., 2016).

3.1.2 – Mineral chemistry as a probe for Martian magma dynamics

Paleo-heat flows deduced from lithospheric strength suggest that the ‘stagnant-lid’ tectonic regime of Mars has enabled mantle heat retention for the majority of the planet history (Hauck & Phillips, 2002; Breuer & Spohn, 2006; Grott & Breuer, 2010; Fraeman & Korenaga, 2010; Ruiz et al., 2011). Mars’ present-day partially fluid core (e.g., Yoder et al., 2003) is further evidence for inefficient cooling of the Martian interior. Ages for the Martian surface derived from crater counting (Berman & Hartmann, 2002), as well as the crystallization ages of shergottites as young as 175 Ma (McSween, 2002; Nyquist et al., 2001), suggest that Mars could still be an episodically volcanically active planet (Carr & Head, 2010).

Observations of chemical-physical variations in minerals within the shergottite group of Martian meteorites can be used to reveal the temperature and, by inference, the degree of convective activity of their respective magma chambers. Mg-Fe zoning of pyroxene has also been widely used to infer evolution of magmas after partial melting or metamorphism on asteroids (e.g., Hollister &

Hargraves, 1970; Scott, 1980; Duncan & Preston, 1980; Barton et al., 1982; Miyamoto et al., 1985; Spear & Markussen, 1997; Mikouchi et al., 1999; Meado et al., 2017).

In addition, zoning of phosphorus in olivine is an effective tool to explore variations in crystal growth rate in magmatic systems (e.g., Milman-Barris et al., 2008; Shearer et al., 2013). Phosphorus behaves as an incompatible element (Toplis et al., 1994). However, during rapid growth, olivine can incorporate high concentrations of phosphorus (up to 0.48 wt. % P_2O_5 in experimental products (Milman-Barris et al., 2008)) in its crystal structure via solute trapping (Aziz, 1982; Reitano et al., 1994; Milman-Barris et al., 2008; Shearer et al., 2013; McCanta et al., 2016; Bouvet de Maisonneuve et al., 2016). The maximum P_2O_5 content recorded for terrestrial olivine is 0.2 wt. %, whereas the maximum P_2O_5 content observed in Martian meteorite olivine is 0.4 wt. % (Milman-Barris et al., 2008).

Here we report major- and trace-element data for Tissint olivine and pyroxene. We focus on the core-to-rim compositional evolution of pyroxene and olivine in order to provide new insights into the dynamics of Tissint's parental magma chamber. Based on these results, equilibration temperature calculations in olivine are used to estimate the thermal state of the Martian mantle at the time of Tissint's formation.

3.2 – Analytical methods

A total of four Tissint epoxy-mounted polished thick slices were investigated during this study (P18492, P18494, P18495, and P18497), on loan from the Natural History Museum of London, and cut from Tissint sample BM2012,M3.

Modal mineralogy was calculated by using the Aztec software on backscattered electron images. Major-element mineral chemical data and X-ray elemental images were collected at the Imaging Spectroscopy and Analysis Centre of the University of Glasgow, using a Zeiss-Sigma variable pressure field emission gun scanning electron microscope (VP-FEG-SEM). Energy dispersive X-ray spectroscopy (EDS) data were collected using Oxford Instruments X-Max 80 mm² Silicon Drift Detector. These data were processed using Oxford Instruments

Aztec 3.3 and INCA software. EDS and SEM data were acquired using a working distance of 8.5 mm, a beam current of 2.15 nA, and an accelerating voltage of 20 kV. EDS X-ray spectra were calibrated using reference materials of wollastonite (Si, Ca), jadeite (Na, Al), periclase (Mg), orthoclase (K), rutile (Ti), chromite (Cr), rhodonite (Mn), hematite (Fe), apatite (P), tugtupite (Cl), and pyrite (S), following the procedures outlined in Hallis et al. (2017). Major elements for olivine and pyroxene, collected via SEM-EDS, were used as input for equilibration temperature calculations following the method described in Putirka (2008).

Electron microprobe (EMPA) analyses of olivine were conducted on the JEOL 8530F Field Emission Gun Electron Microprobe equipped with 5 tuneable wavelength dispersive spectrometers at the Centre for Microscopy, Characterisation and Analysis at the University of Western Australia. P-chemical profiles (elemental P) were collected across two olivine megacrysts (~2-2.5 mm) and two other, much smaller, olivine phenocrysts (~300 μm) in Tissint. Wavelength dispersive (WD) data were collected using a fully focussed beam with a takeoff angle of 40° , 15 keV accelerating voltage and a 50 nA beam current. The $K\alpha$ peaks for elements Na, Si, Al, Mg, Cr, Mn, Fe, K, Ca, Ti, Ni and P were measured using analysing crystals LiF (Cr, Ti) PETJ (K, Ca, P) and TAP (Na, Si, Al, Mg) and quantified using reference materials of Durango apatite (P and Ca), Ni-olivine (Ni), rutile (Ti), orthoclase (Si and K), magnetite (Fe), Cr_2O_3 (Cr), periclase (Mg), spessartine (Mn), corundum (Al), and jadeite (Na). For all elements, peaks were counted for 20s. The intensity data was corrected for Time Dependent Intensity (TDI) loss (or gain) using a self-calibrated correction for Na, Si, Cr, Mn, and K. The mean atomic number background correction was used throughout (Donovan and Tingle, 1996; Donovan et al., 2016). Unknown and standard intensities were corrected for deadtime. Interference corrections were applied to Mg for interference by Ca, and to Mn for interference by Cr, and to Fe for interference by Mn (Donovan et al., 1993). Detection limits, based on 1σ , were: 0.004 wt. % for Al, 0.005 wt. % for Mg, 0.008 wt. % for Na, 0.010 wt. % for Fe, 0.028 wt. % for Ti, and 0.009 wt. % for P. Oxygen was calculated by cation stoichiometry and included in the matrix correction. Analytical uncertainties for each measurement were variable but are generally better than 0.3% for major elements (>1 wt. %) and better than 20% for trace elements (<0.1 wt. %).

Uncertainties for each measurement are listed in the **Appendix**. The matrix correction method was Phi-Rho-Z (Armstrong, 1988).

Ni and Co were measured using an iCAP-RQ inductively coupled plasma-mass spectrometer (ICP-MS), equipped with a RESOLUTION 193 nm Excimer laser, at the University of Glasgow. Data were collected from two olivine megacrysts and several phenocrysts of olivine (divided into Mg-rich, Mg-poor, and intermediate), pyroxene (both pigeonite and augite), and low-Ti chromite. We analysed a NIST 612 glass standard throughout each analytical session (at the session beginning, end, and after every 3rd analysis). An Ar gas carrier was utilised, and the dwell time for each laser analysis was 0.35 s. In order to avoid low signal we chose a different laser spot size for the different minerals analysed: 10µm for Ni and Co in olivine, with 20 µm for pyroxene and chromite. NIST standards were always analysed with the same laser spot size as the analyses. Uncertainties are calculated based on the standard deviation of NIST analyses, and are reported in the Supplementary Material. Elemental abundances were calculated using the GeoStar software, while data processing was performed using lolite data reduction analytical software, by quantifying the trace element abundances in the flat regions of the time-lapse plots. The detection limits for Ni are 0.025 ppm, while for Co are 0.037 ppm.

3.3 – Results

3.3.1 – Petrography

Tissint has a porphyritic texture (Fig. 3.1), inclusive of olivine megacrysts (up to 2.5 mm) and smaller phenocrysts (up to 0.8 mm) (Fig. 3.2). The average modal mineralogy from all four samples is: 55 vol. % pyroxene, 25 vol. % olivine, and 15 vol. % maskelynite. The remaining 5 vol. % is composed of minor amounts of chromite, merrillite, ilmenite, pyrrhotite, and mesostasis. These observations are in agreement with previously published data (Balta et al., 2015; Liu et al., 2016).

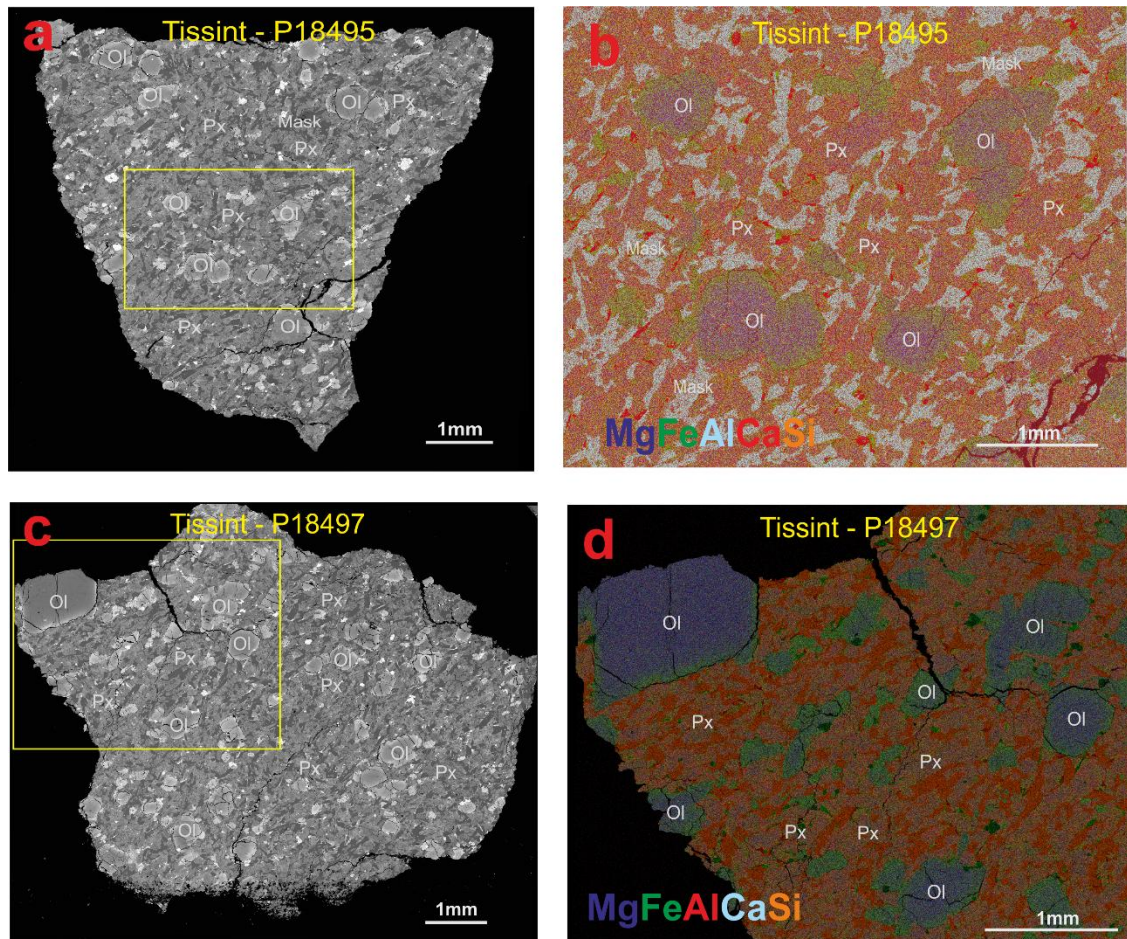


Fig. 3.1 - BSE images (a,c) and false-coloured X-ray images (b,d) of two Tissint thin-sections (P18495 and P18497) analysed during this study. (a) BSE image of Tissint (P18495). The yellow box corresponds to the area shown in (b). (b) False coloured EDS map of Tissint, Mg (blue), Fe (green), Al (aqua), Ca (red), and Si (orange), highlighting olivine (Ol) phenocrysts within intergrown pyroxene (Px) and maskelynite (Mask). (c) BSE image of Tissint (P18497) with fusion crust visible at the bottom of the section. The yellow box corresponds to the area shown in (d). (d) False coloured EDS map of Tissint, Mg (blue), Fe (green), Al (red), Ca (aqua), and Si (orange), highlighting a large olivine megacryst at the top left corner of the sample.

Olivine in Tissint includes megacrysts (~2 mm diameter) and phenocrysts (~200 μm diameter) (Fig. 3.1 and 3.2). The textures of olivine phenocrysts are variable: many are fractured, and contain a high abundance of melt inclusions and oxides (mostly spinel). The olivine grains are often observed in clusters of two or three (Fig. 3.2a). Conversely, olivine megacrysts, the largest of which is >2.5 mm diameter (cut off at the sample edge), are not observed to be

clustered, although this may be due to sampling bias as only two megacrysts are present within the four samples studied.

The earliest crystallising pyroxene (cores of the largest grains) is pigeonite, evolving to augite towards the rims. Smaller phenocrysts are entirely made up of augite ([Fig. 3.6](#)). Fe-rich pyroxene rims surround each pyroxene phenocryst. Plagioclase is converted to maskelynite, which is intergrown with pyroxene. Olivine and pyroxene are heavily shock fractured, and shock melting is evident in some regions ([Fig. 3.2c](#)).

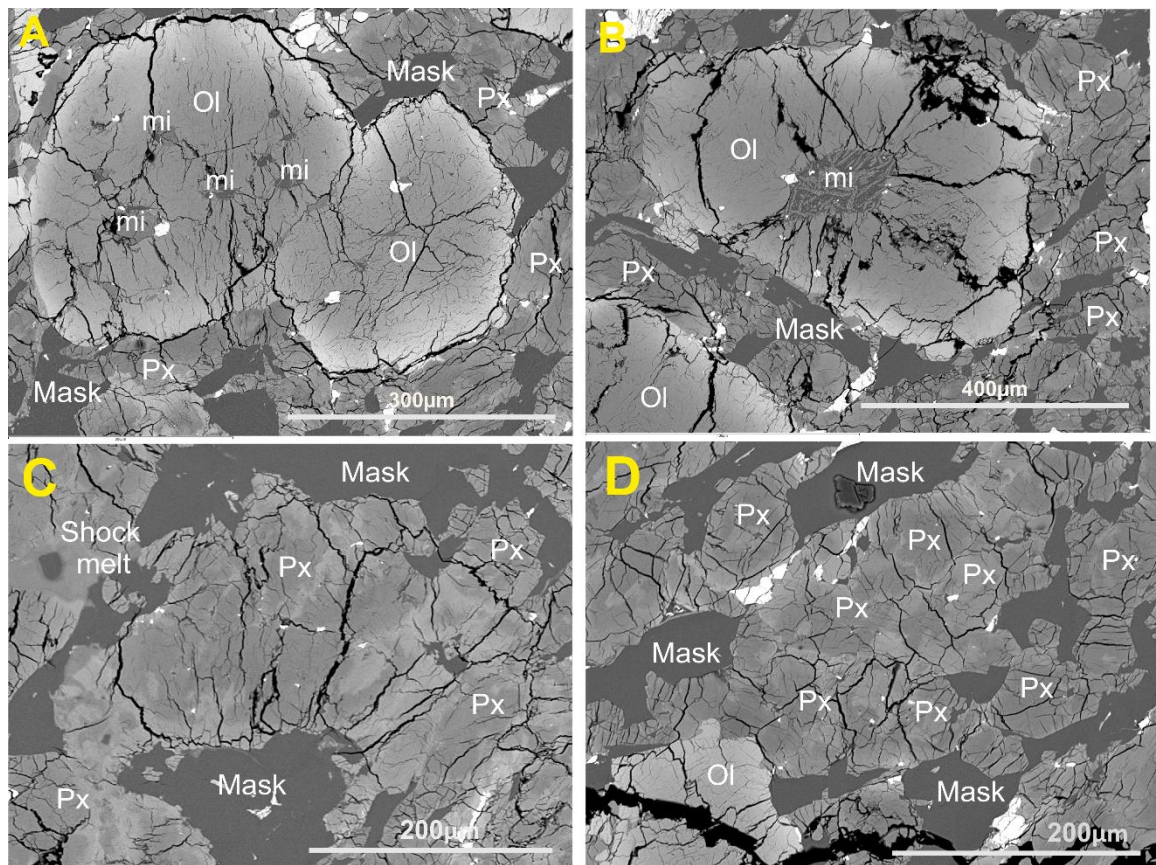


Fig. 3.2 - BSE images of olivine (Ol), and pyroxene (Px) phenocrysts in Tissint. All grains are heavily fractured. A) A cluster of two euhedral olivine phenocrysts, the upper left of which contains numerous melt inclusions (mi). B) A euhedral olivine phenocryst with large melt inclusion. C) A large area of pyroxene, where Fe-rich pyroxene appears to penetrate through areas of augitic composition. An area of shock-melted pyroxene is highlighted in the top left of the image. D) Clusters of augite grains surrounded by Fe-rich pyroxene, and penetrated by a high density of fractures. Maskelynite (Mask) is present within the gaps between pyroxene clusters. White grains are oxides.

3.3.2 – Mineral chemistry

3.3.2.1 – Olivine major and minor elements

Both megacrysts ($n = 2$) and phenocrysts ($n = 26$) of olivine exhibit exclusively normal zoning, from Mg-rich cores to Fe-rich rims. The abundance of MgO in olivine is variable (37-29 wt. %) and correlates with the crystal size - the cores of the larger olivine megacrysts are more Mg-rich than the olivine phenocrysts. Olivine megacrysts composition ranges from Fo₇₃ in the cores to Fo₄₀ in the rims, while the olivine phenocrysts range from Fo₆₆ in the cores to Fo₂₂ in the rims (Fig. 3.2, 3.6).

Olivine megacrysts have absent or low P₂O₅ abundances (~0.02-0.03 wt. %, EMPA detection limits) in their cores and rims, with P₂O₅ concentration increasing towards the very outer rims (~0.5 wt. %). The phenocryst P₂O₅ contents are higher and lower than megacryst cores (ranging from ~0.02 to 0.23 wt. %; Table 3.1, Fig. 3.3).

Table 3.1 - SEM-EDS major elements and LA-ICP-MS trace elements composition of representative Tissint minerals and phases.

	Olivine megacryst		Olivine phenocryst		Pigeonite		Maskelynite	Chromite
wt. %	core	rim	core	rim	core	rim		
SiO ₂	39,34	36,37	35,82	34,27	53,37	50,49	51,82	0,35
TiO ₂	–	–	0,05	–	0,16	0,71	0,11	0,72
Al ₂ O ₃	0,21	0,23	0,26	0,16	0,90	1,06	29,37	7,65
Cr ₂ O ₃	0,24	0,52	0,16	0,04	0,51	0,34	0,04	58,35
MgO	42,62	33,44	32,71	24,00	22,57	14,51	0,17	7,29
CaO	0,22	0,24	0,25	0,37	4,34	8,79	12,98	0,04
MnO	0,34	0,53	0,53	0,74	0,56	0,74	0,03	0,67
FeO	17,84	26,99	28,09	39,64	15,78	23,28	0,78	24,88
NiO	–	–	–	–	0,03	–	0,12	–
Na ₂ O	0,13	0,10	0,16	0,07	0,17	0,11	3,54	0,10
K ₂ O	–	–	–	–	0,05	0,00	0,00	0,01
P ₂ O ₅	0,01	0,07	0,08	0,03	0,04	0,05	–	0,04
S ₂	–	–	0,13	–	0,03	0,10	–	–
Total	100,95	98,5	98,25	99,32	98,52	100,18	98,96	100,08
Mg#	70,49	55,33	53,79	37,71	58,85	38,39	–	–
En	–	–	–	–	52,86	31,15	–	–
Wo	–	–	–	–	10,16	18,87	–	–
ppm	core	rim	Mg-rich	Fe-rich	Mg-rich	Ca-rich		
Ni	13,7	13,2	9,9	1,78	1,94	1,63	–	1,81
Co	1,51	1,47	1,27	0,73	0,62	0,52	–	1,42

Wo = $100 \times \text{Ca}/(\text{Ca}+\text{Mg}+\text{Fe}^{2+})$; En = $100 \times \text{Mg}/(\text{Ca}+\text{Mg}+\text{Fe}^{2+})$; Mg# = $100 \times \text{Mg}/(\text{Fe}+\text{Mg})$

Olivine - Phosphorus variations due to crystal size and location

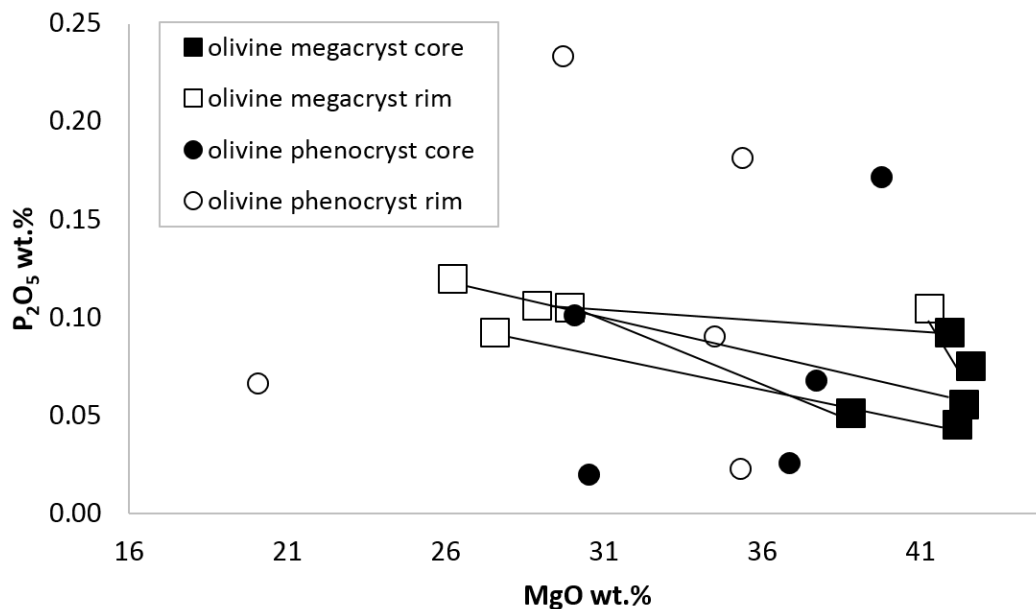


Fig. 3.3 - A plot showing P₂O₅ vs. MgO (both in wt. %) collected via SEM-EDS, depicting the chemical variations between the rim and core of both olivine phenocrysts (n = 5) and megacrysts (n = 5) in Tissint. The olivine megacrysts have a slight rimwards enrichment in P₂O₅ and depletion in MgO. Conversely, the olivine phenocrysts exhibit no trend in the concentration of P₂O₅ with proximity

to the core or rim, and exhibit a larger variability in P_2O_5 . Lines link cores and rims of individual olivine megacrysts.

EMPA data were collected from a transect through one olivine megacryst and one phenocryst. Within both the megacryst and the phenocryst P is distributed in oscillatory bands - as also observed by Balta et al. (2015) and Liu et al. (2016). The olivine megacryst has P-rich bands 40-50 μm wide and ~ 200 μm apart, with increasing P enrichment at the very rim of the grain (Fig. 3.4c). The olivine phenocryst has P-rich bands of a similar width (20-50 μm wide), but much closer together at ~ 25 μm apart - it, also has a P enrichment at the very rim of the grain (Fig. 3.4d).

In addition to P, chemical profiles were collected for Al and Cr (Fig. 3.4), because all three elements have similar diffusion coefficients (e.g., Watson et al., 2015). Within terrestrial olivine Cr and Al oscillatory zoning is generally weak or absent, but previous publications observed a positive correlation between Al-, Cr-, and P-rich bands within synthetic and extraterrestrial olivine (Milman-Barris et al., 2008), although these oscillations are noted to never correlate to Fe-Mg major element zoning. Tissint olivine shows a slight correlation of P-rich bands with Al-rich bands, but little correlation with Cr-rich bands, although the olivine megacryst does show definite oscillations in Cr content (Fig. 3.4g).

The complete dataset of the EMPA transects is reported in the **Appendix** (where the crystals reported in this Chapter in Fig. 3.4 refer to 'Olivine megacryst 2' and 'Olivine phenocryst 1').

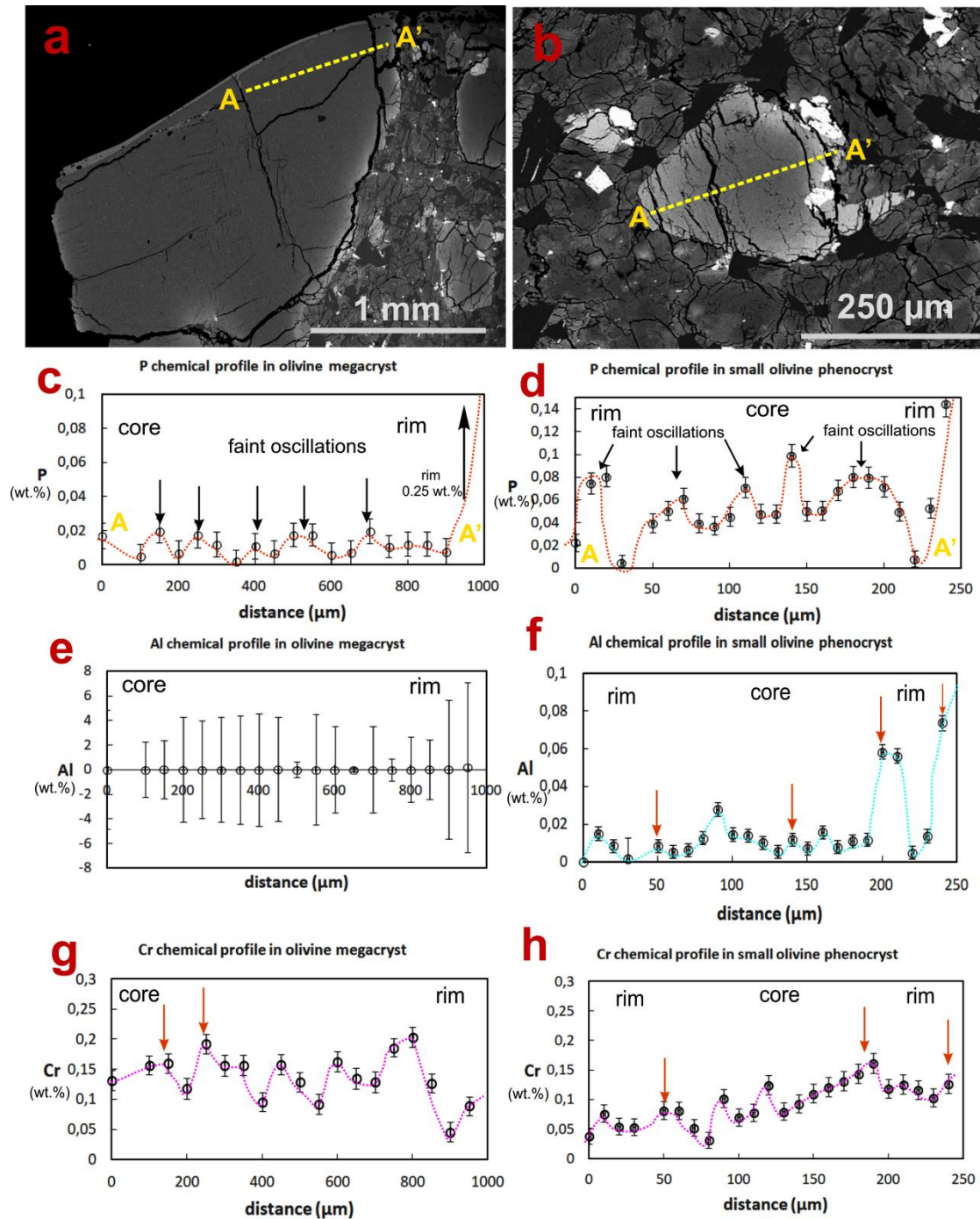


Fig. 3.4 - BSE images (a, b), along with P (c, d), Al (e, f), and Cr (g, h) chemical profiles for an olivine megacryst and a small olivine phenocryst in Tissint. The yellow dashed lines between A and A' represent the analytical transects. Axis value is different for some figures in order to enhance oscillations visualization. The megacryst transect (a) shows oscillations in P content (black arrows), with spacings of ~200 μm and band widths of ~40-50 μm (c). A great increase in P up to 0.25 wt. % is detected at the rim (not shown here). The olivine phenocryst (b) shows stronger P oscillations (d), with a generally higher P content. Oscillations are not assured for Al in the olivine megacryst due to the large uncertainties (e)

but they are visible in Al in the olivine phenocryst (f); Cr oscillations are visible in both olivine types (g,h), and direct correlation of Al and Cr with P are shown (orange arrows). Data obtained using EMPA.

The olivine megacryst profile runs from core to rim, a distance of 1000 μm . Unfortunately, a direct correlation between P and Al cannot be assured from the EMPA data due to the large uncertainties for the olivine megacrysts. A direct correlation between P and Cr is only located at 180 and 250 μm , with no large enrichment in Cr at the rim. The same degree of correlation within P- and Al-rich bands can be found for the chemical profile of the olivine phenocryst. Here the profile goes from rim to rim, with a total distance of 250 μm . Al-rich bands are directly correlated with P-rich bands at 50, 140, 200, and 240 μm distance, with an enrichment on both rims (up to 0.14 wt. % P and 0.08 wt. % Al). Correlations between Cr-rich bands and P-rich bands are only shown at 60, 180 and 240 μm in the phenocryst. However, anti-correlations are also present: a decrease in P is associated with increasing in Al and Cr at 90, 160 μm within the phenocryst.

3.3.2.2 – Olivine trace elements

Ni and Co are more abundant in olivine megacrysts than olivine phenocrysts (Fig. 3.5). Only the most Mg-rich phenocrysts approach the Ni and Co abundances of the megacrysts. Ni and Co contents within olivine megacrysts do not vary between cores and rims (Ni 14.4-12.5 ppm and Co 1.6-1.4 ppm for both). In contrast, Ni is more abundant in Mg-rich phenocrysts (13.1-8.52 ppm) vs. Fe-rich phenocrysts (2.74-0.52 ppm), as is Co (1.45-1.23 ppm in Mg-rich vs. 0.9-0.4 ppm in Fe-rich olivine) (Table 3.1, Fig. 3.5).

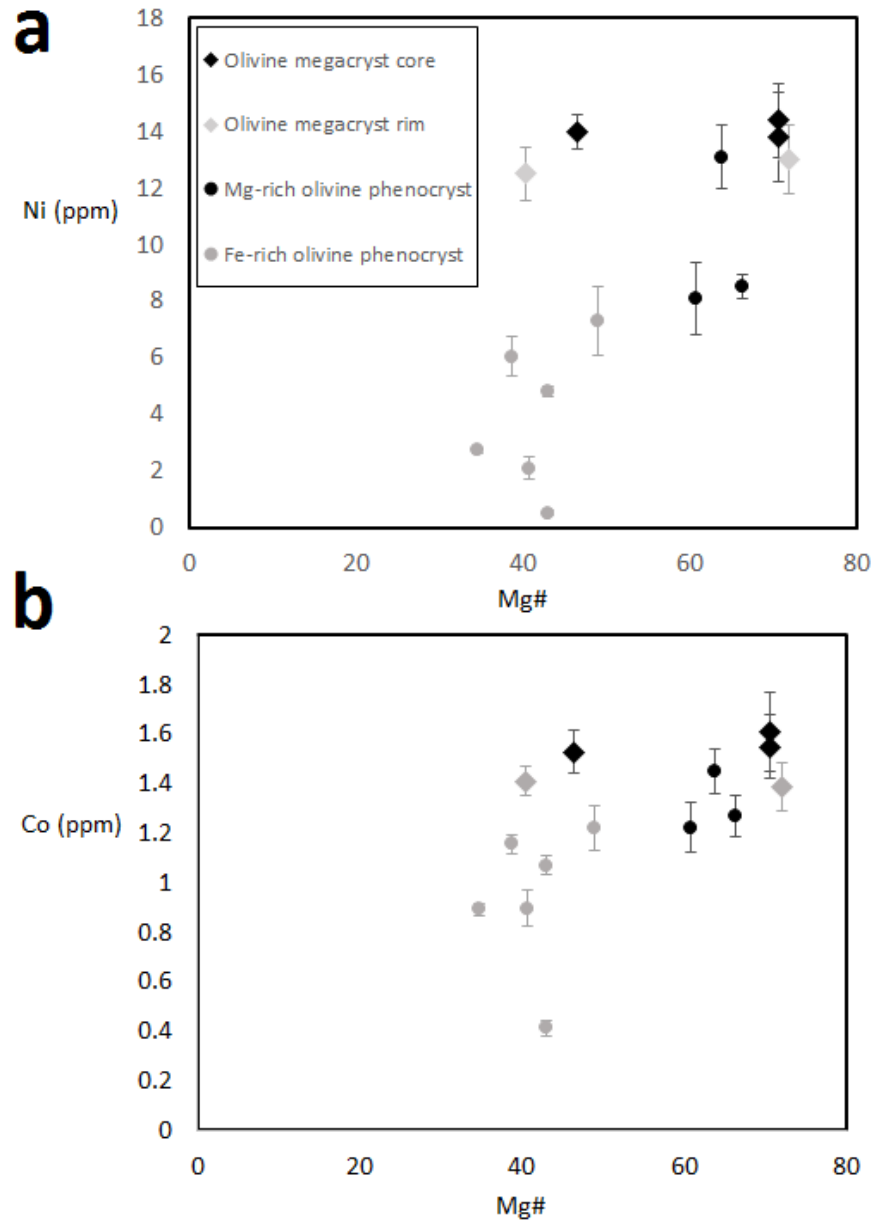


Fig. 3.5 - Mg# vs. Ni (a) and Co (b) ppm of olivine megacrysts (cores and rims), alongside Mg-rich and Fe-rich olivine phenocrysts. Elevated Ni and Co abundances within the megacryst cores in particular indicate they represent an earlier crystallising population to the olivine phenocrysts, as both Ni and Co are compatible in olivine. Error bars represent the 2σ errors of LA-ICP-MS analyses for Ni and Co.

3.3.2.3 – Chromite inclusions in olivine

Chromite can be found as inclusions only in the olivine phenocrysts (both in cores and rims) and not in the olivine megacrysts. Chromite major element analyses show an increase in TiO_2 (~1.16 wt %) and a decrease in Cr_2O_3 (~55 wt %) towards the rim of each grain. Na and Fe also increase towards the grain rims, to a maximum of ~0.23 wt % Na_2O and ~30.8 wt % FeO. Trace element data indicate that Ni is slightly more abundant than Co (1.81 and 1.42 ppm, respectively).

3.3.2.4 – Pyroxene major and minor elements

The morphology of the majority of Tissint pyroxene phenocrysts is subhedral, with rare euhedral exceptions (Fig. 3.2). Pyroxene phenocryst grain size varies from 80 to 200 μm across the short axis and from 0.1 to 0.8 mm across the long axis ($n = 20$). Compositional variation from Mg-rich to Fe-rich pyroxene exists in both pigeonite ($\text{En}_{51}\text{Wo}_{10}$) and augite ($\text{En}_{44}\text{Wo}_{16}$) grains (Table 3.1, Fig. 3.6). Mg-rich pigeonite has slightly elevated Co and Ni (0.43-0.82 ppm and 0.98-2.9 ppm, respectively) compared to Ca-rich pigeonite (0.49-0.56 ppm, and 0.95-2.32 ppm, respectively) (Table 3.1).

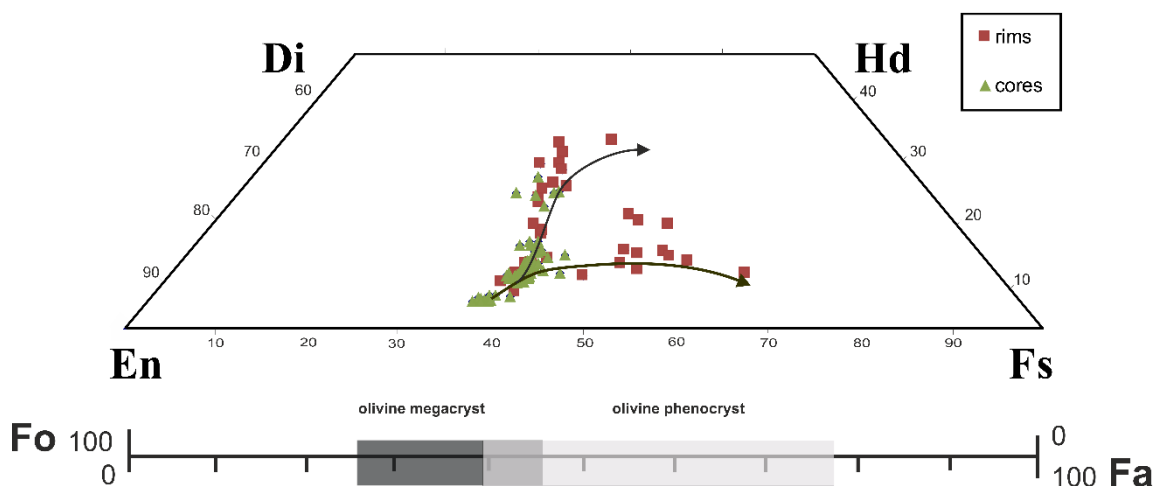


Fig. 3.6 - Core-to-rim compositional variation for pyroxene and olivine composition in Tissint. Chemical data were collected via SEM-EDS. Two zoning patterns are present in pyroxene: from Mg-rich cores to Fe-rich rims, and from Mg-rich cores toward Fe-Ca-rich rims. Olivine megacrysts (black box) and phenocrysts (grey box) are displayed in terms of percentage of Fo vs. Fa.

Abbreviations: Di, diopside; Hd, hedenbergite; En, enstatite; Fs, ferrosilite; Fo, forsterite; Fa, fayalite.

3.4 - Discussion

3.4.1 – Origin of P-zoning in olivine

P-zoning in Tissint olivine is comparable to previously reported P oscillatory zoning in olivine grains within other olivine-phyric shergottites (Shearer et al., 2013; Ennis and McSween, 2014; Jean et al., 2017). Previously reported P_2O_5 abundances for Tissint olivine phenocrysts range from below EMPA detection limits in the cores (<0.02 wt. %) to 0.2 wt. % in the rims (Balta et al., 2015; Liu et al., 2016).

The occurrence of oscillatory zoning in olivine and pyroxene is rare on Earth (Thompson, 1972; Downes, 1974; McBirney and Noyes, 1979; Eriksson, 1985; Clark et al., 1986; Pearce & Kolisnik, 1990; Simonetti et al., 1996; Cioni et al., 1998; Milman-Barris et al., 2008; Shearer et al., 2013) and is thought to be inconsistent with compositional changes due to open-system processes in magma chambers (Clark et al., 1986). In addition to Tissint, phosphorus-zoning in Martian olivine was previously observed in Yamato 980459, Northwest Africa (NWA) 1183, Allan Hills (ALHA) 77005, Elephant Moraine (EETA) 79001, Dar al Gani (DaG) 476, and Dhofar 019 (Milman-Barris et al., 2008; Shearer et al., 2013; Ennis & McSween, 2014). All these Martian meteorites are variously depleted shergottites, suggesting that P oscillatory zoning is not linked to the degree of melt depletion. Milman-Barris et al. (2008) reproduced olivine P-oscillatory zoning within experimental products, but the experimental olivine contained regularly spaced and fine bands, unlike the irregularly spaced bands in Tissint and other natural samples (e.g., Balta et al., 2015; Elardo et al., 2014). Here a possible scenario for the occurrence of irregular oscillatory P-rich bands in Tissint is presented.

Phosphorus oscillatory zoning can be interpreted as the product of intrinsic or extrinsic phenomena in the magmatic system (Pearce, 1994; Shore and Fowler, 1996; Schleicher et al., 2016). Intrinsic processes are due to crystallization

kinetics and can occur without change in the P content of the magma. For example, if the crystal growth rate exceeds the diffusion of P in the melt (a chemical process known as solute trapping; Aziz, 1982)), oscillatory zoning would form due to incorporation of P in the crystals, probably in relation to undercooling in the magma chamber (Aziz, 1982; Pearce, 1994; Reitano et al., 1994; Lofgren et al., 2006; Milman-Barris et al., 2008). On the other hand, extrinsic phenomena generate oscillatory zoning due to changes in melt chemical composition induced by external processes, such as magma mixing and magmatic replenishment events (Pearce, 1994; Shore and Fowler, 1996; Cioni et al., 1998; Reubi et al., 2003; Milman-Barris et al., 2008). These extrinsic phenomena would also typically generate characteristic resorption bands, reflecting the injection of more primitive magma into the magma chamber (Pierce, 1994; Ginibre et al., 2002). Intrinsic solute trapping commonly produces finely banded (~10-20 μm) regular or irregular P oscillatory zoning (Milman-Barris et al., 2008), while extrinsic magma mixing or replenishment produces coarse and mostly irregular banding (Pierce, 1994). P oscillations are visible throughout the Tissint megacryst and phenocryst olivine grains, from core to rim. In contrast, P-zoning of terrestrial olivine normally shows a P-rich core surrounded by a P-poor area (Milman-Barris, 2008). Olivine megacryst cores analysed in Y-980459 are P-rich but with higher Mg#, V, and Ti relative to the Y-980459 olivine phenocrysts, implying a xenocrystic origin for the megacrysts, thus P-oscillatory zoning was caused by magma mixing (Shearer et al., 2013). P-poor cores were reported in the enriched shergottite NWA 1183 olivine megacrysts, surrounded by phosphorus oscillatory bands in which P is correlated with Al (Shearer et al., 2013). NWA 1183 is reported to have crystallized in a closed system from a single melt.

Milman-Barris et al. (2008) produced regularly spaced P-zoning in olivine during constant cooling rate experiments. However, these authors also report that in natural samples oscillatory P-zoning is irregularly spaced, as a consequence of irregular variations in temperature and cooling rates. Milman-Barris et al. (2008) thus argued that irregularly spaced P zoning in natural olivine may be related to solute trapping during cooling events, probably due to convection in a magmatic system.

3.4.2 – Evidence of equilibrium crystallization in a closed-system

Olivine and pyroxene zoning patterns, both in terms of major and trace element abundances, could record 1) the evolution of a single magma composition within Tissint, or 2) two different magmas in the Tissint magmatic system (Table 3.1, Fig. 3.2, 3.5, 3.6).

As well as the size disparity between the megacrysts and phenocrysts, differences in Mg, Ni, and Co abundances indicate the presence of two distinct olivine populations and/or multiple liquid lines of descent (Fig. 3.5; Table 3.1). The cores of the megacrysts are richer in Mg, Ni, and Co, indicating early crystallisation or crystallization in a different magma. The total separation of core vs. rim in terms of megacryst MgO content, in contrast to the gradual evolution shown by the phenocrysts, suggests a gap in crystallisation between the core and rim development. In addition, the presence of thin P-rich rims on the olivine megacryst studied via EMPA (Fig. 3.3, 3.4) suggests a second, short, growth stage at the end of crystallisation. Therefore, the olivine megacrysts appear to have evolved as antecrysts - defined as phenocrysts that crystallize from a magma chemically similar to the sample groundmass, which subsequently spends time in a cumulate pile environment prior to entering the magma chamber system (Davidson et al., 2007; Jerram & Martin, 2008). This conclusion is in agreement with Balta et al. (2015) and Liu et al. (2016). As suggested by Balta et al. (2015), the presence of olivine antecrysts, combined with the relatively young age of Tissint, could be an important constraint for a long-term active magmatic system on Mars during the last few hundred Ma.

There is, however, a second possibility in which the olivine megacrysts could actually be xenocrysts, crystallized from a different magma that was rich in Ni and Co - this could explain the enrichment in Ni and Co in both core and rims of the megacrysts and the fact that the Mg# vs. Ni and Co in Fig. 3.5 could represent two different magmas and not only two different olivine populations.

The presence of chromite only in the olivine phenocrysts and not in the antecrysts supports the presence of two separate olivine populations. Previous authors used the olivine-pyroxene-chromite assemblage to calculate a subliquidus temperature close to 1200° C and a fO_2 close to QFM-4 for Tissint (Balta et al., 2015). These data were used to determine a crystallization sequence that included chromite crystallisation prior to olivine, in contrast to

other olivine-phyric shergottites (Balta et al., 2015). The absence of chromite in Tissint olivine antecrysts/xenocrysts can thus only be explained by a deeper and earlier origin in the magmatic system, in respect to the olivine phenocrysts.

The two trends of pyroxene crystallization as represented in Fig. 3.6 reflect a normal condition of magmatic evolution in a magma chamber, with high-Ca augites as the product of later crystallization in the same magma (e.g., Poldervaart and Hess, 1951). The elevated Co and Ni in Mg-rich pyroxene in respect to Ca-rich pyroxene (Table 3.1) reflects the onset of pigeonite crystallisation prior to that of augite, as both Co and Ni are compatible in pyroxene. These observations indicate the absence of open-system processes that would influence pyroxene chemistry from core to rim.

3.5 – Constraint on Martian mantle convection and temperature

3.5.1 – Equilibration temperatures

To test for mineral equilibrium and to see whether magma mixing processes may have affected the magmatic system of Tissint, olivine-melt equilibration temperature (T_{eq}) calculations were performed. Equilibration temperature calculations were also performed for the Tissint Ca-rich and Mg-rich pyroxene compositions.

The test described by Roeder and Emslie (1970) was used for this purpose. An Fe-Mg exchange coefficient (K_D) of 0.37 ± 0.04 for Martian olivine and pyroxene was calculated by Putirka (2016) after >100 experiments using Martian melt compositions. This exchange coefficient is independent of fO_2 and other compositional parameters. This value was used as the exchange coefficient for both olivine ($K_D(Fe-Mg)^{ol-liq}$) and pyroxene ($K_D(Fe-Mg)^{cpx-liq}$). A Rhodes Diagram was used (Fig. 3.7) to determine whether each mineral was in equilibrium, based on displacement from the experimentally determined Martian Fe-Mg exchange coefficient curves (Rhodes et al., 1979). The Tissint black glass data and groundmass data of Chennaoui Aoudjehane et al. (2012) were taken to represent the parental melt, while the cores of olivine and clinopyroxene were used as input for the mineral compositions. Using the black glass composition, calculated

temperatures show an olivine T_{eq} range of 1641-1541° C with a $K_D(\text{Fe-Mg})^{\text{ol-liq}}$ of ~0.58, and a clinopyroxene T_{eq} range of 1562-1125° C and a $K_D(\text{Fe-Mg})^{\text{cpx-liq}}$ of ~0.32; using the groundmass composition, calculated temperatures show an olivine T_{eq} range of 1566-1475° C with a $K_D(\text{Fe-Mg})^{\text{ol-liq}}$ of ~0.53, and a clinopyroxene T_{eq} range of 1418-1200° C and a $K_D(\text{Fe-Mg})^{\text{cpx-liq}}$ of ~0.31 (Table 3.2). Olivine megacryst cores were found to be in equilibrium based on these calculations with both chosen liquids (Fig. 3.7), while cores of olivine phenocrysts and pyroxene show slight disequilibrium conditions (see Supplementary Material), indicating that initial crystallization occurred in different chemical conditions than the Tissint whole rock composition. This is commonly found also for clinopyroxene in terrestrial volcanic systems, where slight displacements from the experimentally derived curve are present without large disequilibrium between minerals and liquid (Putirka et al., 2007; Sheehan & Barclay, 2016). Thus, here we use the core of the olivine megacrysts for mantle thermometrical calculations.

Table 3.2 - Equilibration temperatures (T_{eq}) and Fe-Mg distribution coefficients (KD) for selected Tissint olivine megacryst cores, olivine phenocryst cores, and Ca-rich and Mg-rich clinopyroxene. Elemental compositions of olivine and clinopyroxene were determined via SEM-EDS (expressed in wt. %).

Phase	SiO ₂	TiO ₂	Al ₂ O ₃	FeO	MnO	MgO	CaO	Na ₂ O	K ₂ O	Cr ₂ O ₃	P ₂ O ₅	T _{eq} (°C)**	K ₀ (Fe-Mg) ^{min-liq}
liquid 1*	44,86	0,56	4,09	21,84	0,51	19,99	6,03	0,63	0,04	0,81	0,46	—	—
olivine megacryst	39,26	0,02	0,22	17,95	0,34	42,39	0,25	0,11	0,00	0,30	0,06	1541	0,388
olivine megacryst	39,07	0,00	0,25	17,57	0,35	41,93	0,18	0,07	0,00	0,77	0,09	1541	0,384
olivine megacryst	39,09	0,00	0,21	17,85	0,36	42,20	0,19	0,16	0,01	0,22	0,05	1541	0,387
olivine megacryst	40,61	0,00	0,31	17,07	0,35	42,70	0,20	0,14	0,00	0,00	0,07	1542	0,366
olivine megacryst	39,94	0,00	0,23	17,57	0,39	41,77	0,24	0,19	0,00	0,00	0,09	1545	0,385
olivine phenocryst	35,82	0,05	0,26	28,09	0,53	32,71	0,25	0,16	0,00	0,16	0,08	1618	0,786
olivine phenocryst	35,83	0,01	0,16	29,11	0,63	31,94	0,22	0,14	0,00	0,15	0,26	1628	0,834
olivine phenocryst	35,81	0,00	0,29	26,33	0,45	33,90	0,28	0,15	0,00	0,21	0,23	1603	0,711
olivine phenocryst	36,19	0,00	0,27	25,94	0,55	34,48	0,25	0,14	0,00	0,19	0,19	1600	0,689
olivine phenocryst	35,19	0,01	0,20	30,48	0,61	30,64	0,31	0,14	0,00	0,08	0,01	1641	0,910
Ca-pyroxene	49,90	0,35	0,78	14,04	0,68	14,89	5,75	0,16	0,00	0,22	—	1125	0,272
Ca-pyroxene	52,94	0,20	1,39	14,16	0,53	18,46	12,36	0,15	0,00	0,84	—	1528	0,343
Ca-pyroxene	49,58	0,32	1,82	14,09	0,51	16,13	12,96	0,21	0,00	0,81	—	1551	0,346
Mg-pyroxene	52,54	0,12	0,87	17,08	0,53	22,58	3,72	0,14	0,00	0,50	—	1562	0,358
Mg-pyroxene	53,74	0,12	0,89	16,99	0,59	22,63	5,30	0,13	0,00	0,56	—	1382	0,322
Mg-pyroxene	51,64	0,22	1,00	16,66	0,62	20,85	6,05	0,11	0,00	0,69	—	1325	0,311

Phase	SiO ₂	TiO ₂	Al ₂ O ₃	FeO	MnO	MgO	CaO	Na ₂ O	K ₂ O	Cr ₂ O ₃	P ₂ O ₅	T _{eq} (°C)**	K ₀ (Fe-Mg) ^{min-liq}
liquid 2*	45	0,67	6,37	18	0,49	15,09	7,16	1,13	0,09	0,7	0,44	—	—
olivine megacryst	39,26	0,02	0,22	17,95	0,34	42,39	0,25	0,11	0,00	0,30	0,06	1475	0,355
olivine megacryst	39,07	0,00	0,25	17,57	0,35	41,93	0,18	0,07	0,00	0,77	0,09	1490	0,351
olivine megacryst	39,09	0,00	0,21	17,85	0,36	42,20	0,19	0,16	0,01	0,22	0,05	1490	0,355
olivine megacryst	40,61	0,00	0,31	17,07	0,35	42,70	0,20	0,14	0,00	0,00	0,07	1491	0,335
olivine megacryst	39,94	0,00	0,23	17,57	0,39	41,77	0,24	0,19	0,00	0,00	0,09	1494	0,353
olivine phenocryst	35,82	0,05	0,26	28,09	0,53	32,71	0,25	0,16	0,00	0,16	0,08	1558	0,720
olivine phenocryst	35,83	0,01	0,16	29,11	0,63	31,94	0,22	0,14	0,00	0,15	0,26	1566	0,764
olivine phenocryst	35,81	0,00	0,29	26,33	0,45	33,90	0,28	0,15	0,00	0,21	0,23	1530	0,651
olivine phenocryst	36,19	0,00	0,27	25,94	0,55	34,48	0,25	0,14	0,00	0,19	0,19	1526	0,631
olivine phenocryst	35,19	0,01	0,20	30,48	0,61	30,64	0,31	0,14	0,00	0,08	0,01	1563	0,834
Ca-pyroxene	49,90	0,35	0,78	14,04	0,68	14,89	5,75	0,16	0,00	0,22	—	1418	0,331
Ca-pyroxene	52,94	0,20	1,39	14,16	0,53	18,46	12,36	0,15	0,00	0,84	—	1364	0,312
Ca-pyroxene	49,58	0,32	1,82	14,09	0,51	16,13	12,96	0,21	0,00	0,81	—	1382	0,315
Mg-pyroxene	52,54	0,12	0,87	17,08	0,53	22,58	3,72	0,14	0,00	0,50	—	1385	0,325
Mg-pyroxene	53,74	0,12	0,89	16,99	0,59	22,63	5,30	0,13	0,00	0,56	—	1247	0,296
Mg-pyroxene	51,64	0,22	1,00	16,66	0,62	20,85	6,05	0,11	0,00	0,69	—	1200	0,316

*Tissint melt composition 1 is estimated based on the Tissint glass data of Chennaoui Aoudjehane et al. (2012), representing Tissint black glass composition, while melt composition 2 represent the groundmass data. T_{eq} and K₀(Fe-Mg) for olivine and pyroxene are calculated using the methods of Putirka et al. (2007) and Putirka (2008).

**The T_{eq} (°C) were calculated from Putirka (2007; Equation (4)). This equation included element partition coefficients, pressure, water content, and other coefficients that were derived by non-linear regression of experimental data (Putirka et al., 2007; Putirka, 2008; Beattie, 1993). For olivine T_{eq}, we used values of P(GPa) = 0.8 (Basu Sarbadhikari et al., 2016). For pyroxene T_{eq}, we used P(GPa) = 0.5 (Kinzler & Grove, 1992 a,b).

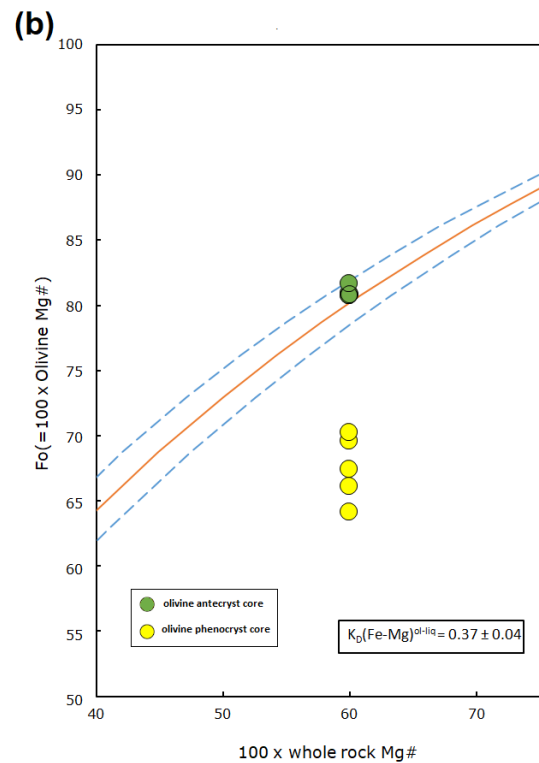
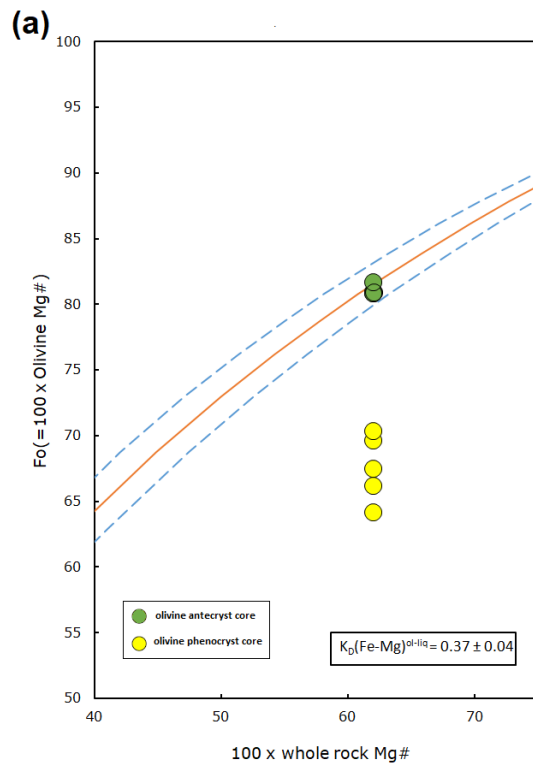


Fig. 3.7 - Rhodes diagrams used to test for equilibrium for Tissint olivine megacryst cores (green dots) and olivine phenocryst cores (yellow dots) (Rhodes et al., 1979). Values in the continuous curves represent the experimentally deduced $K_D(\text{Fe-Mg})$ for olivine-liquid for Mars (Putirka, 2016; Equation 10a) while the dashed curves represent the error intervals of these values, as reported in captions for each diagram. Data are plotted from values reported in [Table 3.2](#). Olivine megacryst cores are inside the equilibrium range both using the black glass Tissint composition (a) and the groundmass (b) from Channaoui Aoudjehane et al. (2012); olivine phenocryst cores are displaced from this range.

3.5.2 – Vigorous convection in the Tissint magma chamber

In the absence of open-system behaviour for the Tissint magmatic system, an intrinsic process for the generation of olivine P-zoning in the Tissint magma chamber is required. The zoning of P in the smallest olivine and toward the rim of the largest grains is likely a result of solute trapping, enhanced by the slow diffusion of P in the melt in combination with a fast magma cooling rate. Solute trapping of P within the crystal structure occurs when the crystal growth rate exceeds the diffusion of P in the melt (Aziz, 1982). The occurrence of this phenomenon in olivine was previously described for experimental samples by Milman-Barris et al. (2008) and Toplis et al. (1994). This process could be related to convection-induced differential cooling in the magma chamber (Martin et al., 1987). In order for oscillatory P-zoning to form in terrestrial basalts transient fast cooling rates of $15\text{-}30^\circ\text{C h}^{-1}$ are required in the magma chamber, as deduced from crystallization experiments (Milman-Barris et al., 2008). Magma chamber convection and changes in melt composition could have also contributed to oscillatory P-zoning in olivine, as these processes commonly result in oscillatory zoning in pyroxene (Elardo et al., 2014).

The process of solute trapping is evidenced also from the olivine chemical profiles. According to Grant and Kohn (2013), during normal elemental partitioning accompanying melt fractionation in olivine, P shows absent or weak correlation between Al and Cr. Solute trapping is instead clearly evidenced when the P-rich bands are correlated to Al- and Cr- rich bands; we notice these

correlations for part of the P-rich bands in the olivine megacryst and phenocryst in Fig. 3.4.

Considering all the above evidence, oscillatory P-zoning could have occurred due to transient fast cooling rates during vigorous convection. By following this logic, when olivine grains were in the cooler parts of the magma chamber (exterior walls and possibly upper region), they were likely affected by solute trapping, forming P-rich bands within the grains. When the same grains were removed via convection to hotter regions of the magma chamber (central or lower regions) solute trapping would cease and P-poor olivine bands would be produced (Fig. 3.8). In addition, Fe-rich pyroxene rims, even at boundaries with other pyroxene or olivine grains (Fig. 3.2d; Fig. 3.3), implies the pyroxene grains did not settle or cluster until the very late stages of crystallisation (e.g., Day et al., 2006).

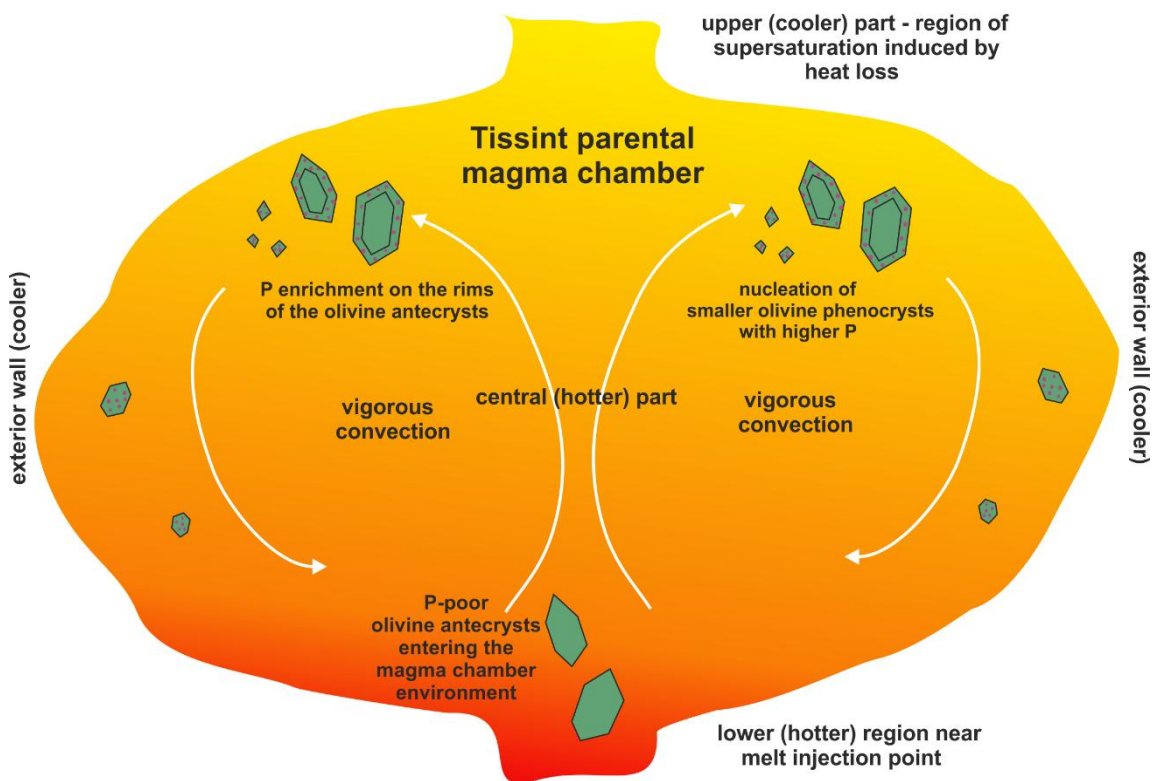


Fig. 3.8 - Schematic representation of the convective activity present in the plume-fed Tissint parental magma chamber on Mars. Different thermal regions are defined: the lower region and central regions (hotter), the upper region (cooler, closer to the Martian crust) and the exterior walls (cooler). Cycling due to vigorous convection (here represented by the arrows) would bring olivine crystals (green) from hotter to cooler regions, and vice versa, causing P solute trapping (purple dots) whilst the olivine grains are cool, producing P-rich bands,

which ceases when the olivine grains are in hotter regions of the magma chamber, producing P-poor bands.

3.5.3 – Implications for the thermal state of the Martian mantle

Thermal evolution in a planetary body is likely controlled by, among other mechanisms, cooling induced by mantle convection and partial melting (Stevenson et al., 1983; Spohn, 1991; Hauck & Phillips, 2002; Fraeman & Korenaga, 2010). Convection speeds in magma chambers of terrestrial volcanic systems have been estimated to vary from $\sim 0.5 \text{ mm s}^{-1}$ for normal degrees of convection to $\sim 0.3 \text{ m s}^{-1}$ for vigorous convection (Moussallam et al., 2015; Carey et al., 2013). For comparison, the convection speed for the Earth's upper mantle is typically $\sim 20 \text{ mm yr}^{-1}$ (Liu et al., 2007; Takeuchi & Sugi, 1971) with a complete convective cycle once every 50 Myr.

Below, we calculate the Tissint magma source temperature (T_p) using EDS chemical data from Tissint olivine megacryst cores in equilibrium with the parental melt. The average equilibration temperature for olivine-melt (Table 3.2), and an equilibration pressure of 8 Kbar, were consistent with the most accurate estimates of the depth of the Tissint magma chamber ($\sim 40\text{-}80 \text{ km}$; Basu Sarbadhikari et al., 2016). The following equation from Putirka (2008) was used for this purpose:

$$T_{\text{Tissint magma } T_p} = T^{\text{ol-liq}}(^{\circ}\text{C}) + \left(\text{melt fraction} \cdot \frac{\text{Heat of fusion } \left(\frac{\text{KJ}}{\text{mol}} \right)}{\text{Heat capacity } \left(\frac{\text{J}}{\text{mol} \cdot \text{K}} \right)} \right) - P^{\text{ol-liq}}(\text{Kbar}) \cdot \frac{dT}{dP} \left(\frac{\text{K}}{\text{Kbar}} \right)$$

(Equation 3.1)

where $T^{\text{ol-liq}} = 1542^{\circ} \text{ C}$ (taken from the average of T_{eq} from the olivine megacrysts) when is calculated using the black glass composition of Tissint and $T^{\text{ol-liq}} = 1488^{\circ} \text{ C}$ when is calculated using the groundmass composition of Tissint; melt fraction = 0.22; heat of fusion = 130,000 kJ/mole; heat capacity = 192.4 (J/mole*K); $P^{\text{ol-liq}} = 8 \text{ Kbar}$; and $dT/dP = 0.001331471 \text{ (K/bar)}$. See Putirka (2008) for details of these experimentally determined parameters.

These calculations produced a Tissint magma source temperature of $\sim 1680 \pm 55^\circ \text{C}$, using black glass Tissint composition for calculations, and $\sim 1631 \pm 55^\circ \text{C}$, using groundmass composition, during late Amazonian ($\sim 574 \pm 20 \text{ Ma}$, Brennecka et al., 2014). Taking the average between the two results ($1655 \pm 55^\circ \text{C}$), this value is in line with the previously calculated source temperature of $\sim 1700^\circ \text{C}$ (Putirka, 2016) and $1540 \pm 10^\circ \text{C}$ (Musselwhite et al., 2006) for Y-980459, and $\sim 1745^\circ \text{C}$ for olivine-phyric shergottites in general (Filiberto, 2017). This temperature is also comparable to Phanerozoic terrestrial mantle plume heads with a calculated temperature of $\sim 1700^\circ \text{C}$ (Thompson & Gibson, 2000), which matches estimates of the temperature of some modern terrestrial plumes (Putirka, 2016). Martian mantle plume temperatures are calculated to be 120°C hotter than their surrounding ambient mantle, using numerical simulations with temperature-dependent Arrhenius viscosity (Li & Kiefer, 2007). Thus, a Tissint magma source temperature of $\sim 1655^\circ \text{C}$ reflects a Martian mantle temperature of $\sim 1535^\circ \text{C}$, this value matches precisely the values predicted from stagnant-lid evolution of the Martian mantle (e.g., Spohn, 1991; Breuer & Spohn, 2006; Parmentier & Zuber, 2007; Kiefer, 2003; Nimmo & Stevenson, 2000). This is also a reasonable value when compared with the average ambient mantle temperature of $\sim 1650^\circ \text{C}$ for Archean Earth (Green et al., 2001), implying that Mars was able to retain more heat in its interior due to its stagnant-lid regime (in contrast to Earth's plate tectonics) and inefficient cooling of the Martian interior (Hauck & Phillips, 2002; Grott & Breuer, 2010; Fraeman & Korenaga, 2010; Breuer & Spohn, 2006; Ruiz et al., 2011; Kiefer, 2003).

3.6 – Conclusion

The Tissint depleted shergottite contains two populations of olivine - large early-crystallising antecrysts/xenocrysts, and smaller later crystallising phenocrysts. Irregular oscillatory zoning of phosphorus is present within both antecrysts/xenocrysts and phenocrysts, with P-enriched bands containing up to 0.25 wt. % P_2O_5 . Mineral chemistry shows no evidence of melt mixing within the magma chamber, thus solute trapping caused by convective crystal movement from hotter to cooler regions of the magma chamber may explain oscillatory zone formation within Tissint olivine.

Olivine equilibration temperatures for the megacryst cores are used to infer the potential temperature of the Tissint source region during the late Amazonian. These calculations suggest a temperature of 1655° C for the Tissint magma source, and a Martian mantle temperature of 1535° C - the latter being consistent with the ambient mantle temperature of Archean Earth (~1650° C, Green et al., 2001). Ultimately, these calculations suggest the Martian mantle was hot enough to possibly permit a state of activity during the late Amazonian, a conclusion that may be confirmed in the future via the ongoing NASA InSight (Interior Exploration using Seismic Investigations, Geodesy and Heat Transport) mission.

Chapter 4 – Nakhlite mantle source and early Mars differentiation

The following chapter is taken from the paper titled “Syneruptive incorporation of Martian crustal sulphur in the nakhlite lava flows revealed by S and Os isotope and highly siderophile elements: implication for mantle sources in Mars”. This paper has been published in the Special Issue in honor of Lawrence A. Taylor under the section ‘Origin and Evolution of Mars’ in the peer-review journal *Geochimica & Cosmochimica Acta*.

This paper has been used as [Chapter 4](#) of the present thesis because it is about determining how many mantle reservoirs are present on Mars and if mixing between them occurred, which is useful in revealing Martian magmatic processes and parental melt compositions with implications for Mars’ early formation processes. These are also main objectives of this research.

The Author of the thesis is the First Author of the paper, having conducted the vast majority of the work, data acquisition, data processing, data interpretation, and writing. Other co-authors of the paper include: Amy J. V. Riches, who supervised the main author with the Re-Os isotope and HSE extraction method in the laboratory and helped in revising the manuscript; Lydia J. Hallis, who helped during sample preparation, SEM analysis, and in revising the manuscript; Yves Marrocchi and John Villeneuve, who helped during NanoSIMS measurements of S-isotopes and in revising the manuscript; Harry Becker and Philip Gleissner, who helped with the Re-Os isotope and HSE measurements of the MIL 090136 sample and in revising the manuscript; and Martin R. Lee, who helped during SEM analysis and in revising the manuscript.

4.1 – Introduction

Magmas represent windows to comprehend the interior evolution and geochemical diversity of terrestrial planets. Magmatic activity and degassing are key processes for transferring sulphur, along with other elements, from the interior to the surface during the evolution of a planetary body. In the case of

Mars, low water activity, low temperatures, and the lack of plate tectonics has favoured the preservation of a sulphur-rich regolith during the last ~2 billion years (King and McLennan, 2010). In fact, the Martian regolith contains concentrations of SO₂ up to 8 wt.% (Clark et al., 1976; Foley et al., 2003).

The terrestrial and Martian mantles have been reported to contain similar and chondrite-relative highly siderophile elements (HSE; Os, Ir, Ru, Rh, Pt, Pd, Au, and Re) abundances (Birck & Allegre, 1994; Warren & Kallemeyn, 1996; Brandon et al., 2000, 2012; Dale et al., 2012; Tait and Day, 2018), which has important implications for accretion theory and astrophysical modelling of Solar System evolution (e.g., Bottke et al., 2010). However, sulphur abundance estimates for the Martian mantle range between 400 and 2200 ppm (Wang and Becker, 2017 and references therein) - much higher than the Earth's mantle (around 250 ppm; McDonough and Sun, 1995). The aim of this study was to use rhenium-osmium (Re-Os) isotope systematics and HSE abundances, alongside S-isotope systematics, to test whether the nakhlite group of Martian meteorites preserve robust isotopic information from the Martian interior (Morgan, 1986; Shirey & Walker, 1998; Righter et al., 2000; McSween & Huss, 2010; Walker, 2016).

Martian meteorites are the only available rocks from the surface of Mars. These meteorites can be divided into shergottites (basalts), nakhlites (clinopyroxene-rich rocks), and chassignites (olivine cumulates), with a few other exceptional meteorites. Berkley et al. (1980), Treiman (1986, 2005), and Bridges & Grady (2000) argued that nakhlite petrographic features are consistent with this suite of meteorites sampling a single cumulate pile. However, recent ⁴⁰Ar-³⁹Ar geochronology suggests that their crystallization ages differ by ~93 Ma, consistent with the nakhlites being derived from a series of lava flows or sills that were emplaced between ~1416 and 1322 Ma, probably from the same source (Cohen et al., 2017; Udry and Day, 2018). In this work, we refer to the nakhlites as a series of lava flows.

Franz et al. (2014) used a combination of bulk rock sulphur analyses ($\delta^{34}\text{S}$, $\Delta^{33}\text{S}$, $\Delta^{36}\text{S}$) and *in situ* pyrrhotite mineral analyses ($\delta^{34}\text{S}$, $\Delta^{33}\text{S}$) to determine sulphur isotope anomalies in Martian meteorites. These authors determined the $\Delta^{33}\text{S}$ of the shergottite mantle source to be 0.009 ‰, based on the mean value of 28 meteorites. This value closely corresponds to the value measured for the shergottite Yamato (Y)-980459, which reportedly retains the most reliable

signatures of the Martian mantle (e.g., Usui et al., 2012). However, Franz et al. (2014) were unable to calculate a robust value for the nakhlite mantle source region, as *in situ* secondary ion mass spectrometry (SIMS) analyses of sulphide grains were acquired from only two of the nakhlites (Nakhla and Miller Range (MIL) 03346) and their $\Delta^{33}\text{S}$ values varied widely ($0.06 \pm 0.21 \text{ ‰}$ and $-0.72 \pm 0.13 \text{ ‰}$, respectively). This variation was reported to have been caused by sulphate assimilation during melt eruption, affecting subsequent pyrrhotite crystallization. Franz et al. (2014) argued that sulphides and sulphates in the Martian meteorites can thus be affected by assimilation of sulphur derived from atmospheric UV photochemical reactions, which was deposited at the surface as oxidized sulphur and incorporated in the Martian regolith. This data is in agreement with other previously published sulphur isotope data for the nakhlites, including evidence for mass independent fractionation (MIF), which suggests assimilation of sulphur occurred at some point during nakhlite formation (e.g., Farquhar et al., 2000, 2007; Greenwood et al., 2000a,b; Dottin III et al., 2018).

These sulphur isotope systematics can be used to discern if the HSE abundances in nakhlite magmas are affected by crustal assimilation, or if they represent Mars mantle reservoirs. The HSE systematics of Martian meteorites have been used to infer chondritic relative abundances of these elements in the Martian mantle, and to thereby trace late-accretion of broadly chondritic materials to Mars after the last major magma ocean phase at ~ 4.5 Ga (e.g., Brandon et al., 2000, 2012; Riches et al., 2011; Tait and Day, 2018). Crucially, the HSEs exhibit chalcophile element behaviour when metal is absent from the mineralogical assemblage, preferring to partition into sulphides (Day et al., 2016, and references therein), which is important in terms of HSE partitioning.

Rhenium-Os isotope data are available for many shergottites and one chassignite, but with respect to the nakhlite meteorites there are only two analyses of Nakhla (Brandon et al., 2000; Dale et al., 2012). This lack of published data is, in part, due to the low abundance of HSE (0.1-2 ppb or less) in the nakhlites (Treiman et al., 1986; Jones et al., 2003). In addition, a large age correction needs to be applied (1.3 Ga since nakhlite crystallization), and the effects of crustal assimilation within Nakhla are not clear (McCubbin et al., 2003; Franz et al., 2014; Udry and Day, 2018). Therefore, Nakhla may not be a reliable indicator of the nakhlite's true Os-isotopic mantle source composition.

To address these challenges, we have expanded the nakhlite Re-Os isotope and HSE dataset to include Lafayette and one of the paired Miller Range nakhlites (MIL 090032). These two meteorites are potentially highly informative as they plot at the two extremes of S-isotope composition for the nakhlites (Farquhar et al., 2000; Greenwood et al., 2000; Franz et al., 2014). We also analysed a fraction of Nakhla. This nakhlite is known to have S-isotope composition of aggregated sulphides intermediate to the Miller Range and Lafayette meteorites. Sulphur isotope ($\Delta^{33}\text{S}$ and $\delta^{34}\text{S}$) data were acquired from sulphide grains in Nakhla, Lafayette, MIL 090032, Y-000749, and Y-000593 to determine the amount of crustal assimilation that has occurred in each meteorite during eruption, and to define the possible $\Delta^{33}\text{S}$ range for the nakhlite mantle source.

4.2 – Methodology

4.2.1 – Sample preparation and chemical mapping

Chips were used for Re-Os isotope and HSE analysis, while thin sections were used for S-isotope analyses. The chips (~0.5 g) were from Nakhla (BM.1913,25), Lafayette (BM.1979,755), and MIL 090032 (100); thin sections were from Nakhla (BM.1913,26#2), Lafayette (BM.1979,755), MIL 090032 (28), Y-000593 (37), and Y-000749 (59). Samples were obtained from the Natural History Museum of London (Nakhla, Lafayette), NASA Johnson Space Center (MIL 090032), and JAXA (Y-000593, Y-000749). All samples were from the interior portions of the meteorite, lacking any fusion crust.

We used a novel methodology in which petrographic information was constrained, for the first time, prior to destruction of that same sample volume via acid digestion. This approach provides mineralogical context to inform our interpretations of HSE-abundance and Re-Os isotopic data. To achieve this, we polished the sample chips of Nakhla (0.4 g) and Lafayette (0.6 g) using disks of SiC and 0.3 μm of Al_2O_3 , then rinsed with MQ H_2O . The procedure was undertaken to remove any potential contamination to the chips' surface from earlier cutting and processing by the meteorite curators. As the final step of this treatment involved repeated rinsing in MQ H_2O and visual inspection, we believe that any potential contamination of the sample by Al_2O_3 residue was removed.

However, it remains possible that microscopic traces of Al₂O₃ could introduce Re, very small amounts of radiogenic Os, and potentially perturb the HSE and Os-isotopic systematics, in which case we would anticipate variable chondrite-relative HSE patterns for the analysed nakhlites. The MIL 090032 chip (0.5 g) had a flat surface and did not require polishing. These chips were not subject to carbon coating during the acquisition of high spatial resolution images and compositional mapping. Corresponding thin sections for each of the nakhlites used in this work were carbon coated to a thickness of 20-25 nm for compositional mapping by secondary electron microscopy prior to ion microprobe work.

A Zeiss field-emission Scanning Electron Microscope (SEM), housed in the Imaging Spectroscopy and Analysis Centre of the University of Glasgow, was used to characterise thin-sections and the flat side of the prepared chips. Operating conditions were: 8.5 mm working distance, 2.15 nA beam current, and 20 kV accelerating voltage. Acquired X-ray spectra were calibrated using mineral standards. Backscattered electron (BSE) images and energy dispersive spectroscopy (EDS) X-ray element maps (for Si, Mg, Fe, Ca) were obtained for the chips lacking carbon coating with the SEM operated in low vacuum. Backscattered electron images and EDS X-ray spectra were generated for carbon coated thin sections of Nakhla, Lafayette, MIL 090032, Y-000749, and Y-000593 with the SEM operated at high vacuum. Of particular interest were the sulphides (pyrrhotite/pyrite). Every recognized sulphide on the exposed surface was imaged and quantitatively chemically analysed to determine its mineralogy (see the thesis **Appendix** for further details).

4.2.2 – Sulphur isotope systematics

To obtain the desired spatial resolution during *in situ* analysis of pyrrhotite and pyrite for $\delta^{34}\text{S}$, $\delta^{33}\text{S}$, and $\Delta^{33}\text{S}$, five polished thin-sections (one each of Nakhla, Lafayette, MIL 090032, Y-000749, and Y-000593) were analysed via SIMS. Samples were cleaned with ethanol and coated with gold to a thickness of ~20 μm , to permit conductivity, before loading into the sample chamber of the ion probe.

Sulphur isotope compositions were measured on the CAMECA IMS 1280 ion microprobe (SIMS) at the Centre de Recherches Pétrographiques et Géochimiques (CRPG) in Nancy (France) by simultaneous measurements of ^{32}S -, ^{33}S -, and ^{34}S - in multicollection mode with three off-axis Faraday cups (FCs) in slit 2 mode that allows for a mass resolution $M/\Delta M = 5000$. The FCs were intercalibrated before the analytical session to determine their relative yields. Samples were sputtered with a Cs^+ primary beam of 3-nA intensity, accelerated at 13 kV and focused on a spot of $\sim 15 \mu\text{m}$ diameter. Pyrite, pyrrhotite and galena standards were used to determine the instrumental mass fractionation (IMF) and the reference mass instrumental law (allowing $\Delta^{33}\text{S}$ to be calculated). Standards were run to check that the SIMS was well tuned and stable. The accuracy and reproducibility of the S-isotope data was calculated using these standards (average and standard deviation) and the internal errors on the measurements of the samples. The IMF of the pyrite sample was corrected with the pyrite standard and the IMF of the pyrrhotite sample with the pyrrhotite standard. Typical ^{32}S count rates were between $\sim 1.2 \times 10^9$ and 1.5×10^9 cps, depending on the sulphide standard analysed. A typical analysis consisted of 2 min of pre-sputtering with a $20 \mu\text{m}$ raster, followed by data acquisition for 40 cycles of 5 s each. Faraday cup backgrounds were measured during the pre-sputtering before each analysis and then used for correcting the data. Automatic mass and transfer deflector centerings were implemented in the analysis routine to ensure reproducible analytical conditions during the session. Each measurement takes around 7 minutes per spot. Typical $\pm 2\sigma$ standard errors achieved under these conditions were $\sim 0.1\text{-}0.3 \text{‰}$ for $\delta^{34}\text{S}$, $\sim 0.1\text{-}0.2 \text{‰}$ for $\delta^{33}\text{S}$, and $\sim 0.1\text{-}0.25 \text{‰}$ for $\Delta^{33}\text{S}$.

4.2.3 – Analytical procedure for Os-isotope systematics and HSE

Nakhla, Lafayette, and MIL 090032 were analysed for HSE abundances and Re-Os isotope compositions. Textural characterisation of each sample fragment was obtained prior to destruction of the same material fraction. All samples were weighed before and after crushing so that any loss of sample during this process could be quantified. The HSE chemical separation for Nakhla and Lafayette was conducted in ultra-clean laboratories at the Durham Geochemistry Centre (class

100), Durham University. We used a mixed ^{190}Os - ^{191}Ir - ^{99}Ru - ^{194}Pt - ^{106}Pd - ^{185}Re basalt spike for Nakhla and Lafayette. This spike was selected because we anticipated fractionated HSE in the nakhlites relative to chondrite or peridotite-like HSE abundances; the basalt spike has high Re/Os thereby ensuring accurate spiking. The Total Procedural Blank (TPB) and sample digestions were processed in a high pressure asher and run at 270° C for 18 hours to liberate the HSE from sample powders and to achieve sample-spike equilibration. Following this digestion step, extraction of Os from the solution was performed using a chloroform solvent extraction approach (after Cohen and Waters, 1996). Osmium was then back-extracted into HBr, and was purified via microdistillation (Birck et al., 1997) prior to filament loading. All the other analysed HSE were separated and purified using anion exchange and LN-spec chromatography (cf., Pearson and Woodland, 2000; Puchtel et al., 2008; Chu et al., 2015).

MIL 090032 was analysed in the laboratories at the Freie Universität Berlin following similar laboratory processing protocols to those of Durham University. The polished surface of the sample chip was cleaned with some ethanol but not further abraded because the surface appeared porous and the chip fragile. Afterwards the chip was powdered in an agate mill. Sample digestion and chemical separation was conducted following the protocol of Fischer-Gödde et al. (2010, 2011). To remove Zr an additional clean-up step was applied for Pd following the protocol of Chu et al. (2015). Acquisition of $^{187}\text{Os}/^{188}\text{Os}$ for this one sample fragment was unsuccessful.

The HSE were measured using an Element XR instrument (Berlin) and Element 2 (Durham). The sample was introduced via a conventional Scott-type glass spray chamber. An Aridus I membrane desolvation system was used for HSE at Berlin. Highly siderophile element signals were detected in low resolution mode with a secondary electron multiplier. To determine HSE abundances the samples were run as a series in which solutions were measured separately for Re-Ir-Pt, Ru, and Pd. Each of these measurement routines had a typical collection time of 60 to 120 seconds per sample. During these analyses the sample introduction system was cleaned via MQ H₂O and a 0.5% TD HNO₃ solution. In addition, two ~0.5 % HCl instrument wash solutions were interspersed with samples and measured as unknowns to ensure that no memory effects were observed during each of the data collection runs. Rubidium, Sr, Y, Zr, Mo, Cd, Tm, Yb, Lu, Hf, Ta, Os, and Hg were analyzed as 1 ppb solutions as part of the three data collection sets so as

to monitor isobaric interferences and potentially interfering oxide species. Oxide formation rates (quantified via Ce:CeO values of the multi-element instrument tuning solution) were <4.5 % and <0.8 % for the Scott-type spray chamber at Berlin and Durham, respectively, and <0.15 % using the Aridus at Berlin. The internal precision of measured isotope ratios ranges from 0.2 to 0.8 % (2σ). Background-corrected element ratios were corrected for mass discrimination and used IUPAC values by comparison with ratios in a 1 ppb HSE standard solution measured in the same sequence and as a tracer of instrumental accuracy. Isotopic ratios of $^{99}\text{Ru}/^{101}\text{Ru}$, $^{105}\text{Pd}/^{108}\text{Pd}$, $^{185}\text{Re}/^{187}\text{Re}$, $^{191}\text{Ir}/^{193}\text{Ir}$ and $^{194}\text{Pt}/^{195}\text{Pt}$ were used for isotope dilution calculations. Isotope ratios $^{105}\text{Pd}/^{106}\text{Pd}$ and $^{194}\text{Pt}/^{196}\text{Pt}$ were used to monitor possible interferences. Concentrations of monoisotopic Rh and Au were determined via a combined internal/external standardization technique for the $^{197}\text{Au}/^{191}\text{Ir}$ and $^{103}\text{Rh}/^{101}\text{Ru}$ ratios (Fischer-Gödde et al., 2010). Consistency and possible interferences were checked by comparison to results from $^{197}\text{Au}/^{195}\text{Pt}$ and $^{103}\text{Rh}/^{191}\text{Ir}$ ratios. In practical terms, all offline processing utilized a two stage spreadsheet treatment for each element of each sample. Due to limitations to the number of samples to be processed for this project, and in a restricted time-frame in this case, powdered and broadly basaltic HSE reference materials were not digested separately as a means of determining the accuracy/reproducibility specific to the laboratory processing. However, it is well understood that though a few community-based ‘reference materials’ are available for HSE studies, these are subject to their own limitations (cf., Meisel and Moser 2004; Meisel et al., 2004; Ishikiawa et al., 2014). These additional digestions would have required a doubling in the duration of the analytical visit and the fully-dedicated supervisory time associated with that. However, the high-pressure asher digestion method is the ideal approach to ensure all potential HSE host-phases are accessed and that full sample-spike equilibration is thereby achieved (not necessarily so for NiS-fire assay routines couple with Te-coprecipitation, for example, which are known not to fully access Os, Ir, and Pt when occurring as refractory alloys; cf., Harvey et al., 2006; Lorand et al., 2008). As discussed in the text comparison of Nakhla and Lafayette HSE systematics with those published elsewhere provided for a means of monitoring accuracy. Four blanks were determined. Blank contributions are: 8.4 % Re; 24 % Ir; 3.8 % Ru; 1.1 % Pt; 2.9 % Rh; 17.5 % Pd; 24 % Au at Berlin; while blank contributions at Durham are Re, 0.42-0.49 %; Os, 0.70-

4.20 %, $^{187}\text{Os}/^{188}\text{Os} = 0.132$; Ir, 0.10-0.26 %; Ru, 0.04 %; Pt, 0.25-0.4 %; Pd, 0.87-1.0 %.

4.3 – Results

4.3.1 – Textural characterization of the chips

The Nakhla chip (Fig. 4.1a) was characterized by a high proportion of mostly euhedral augite (~80%; 1-1.5 mm), and a lesser volume of euhedral to subhedral olivine (~8%; 0.3-1 mm in maximum dimension) - extensive areas of the chip had no olivine crystals. Plagioclase made up ~5 vol.% of the sample, while mesostasis represented ~7 vol.%. Texturally, a low degree (< 10%) of fracturing was observed among the minerals. A single 0.3 mm long sulphate grain was present in a Si-rich area of the chip (Fig. 4.1a). Other smaller (< 0.1 mm) sulphates and sulphides were present throughout the chip.

The Lafayette chip (Fig. 4.1b) was characterized by a higher proportion of euhedral to subhedral olivine (~15%; 200-800 μm crystal size) and a lower volumetric percentage of pyroxene (~75%; 500-1800 μm in maximum dimension) relative to the Nakhla chip; mesostasis was ~10 vol.%. Pyroxene was mostly subhedral and in some cases contained olivine inclusions of <50 μm . The chip was characterized by a low degree (< 10%) of mineral fracturing and several small (< 0.1 mm) sulphates and sulphides.

The MIL 090032 chip (Fig. 4.1c) was characterized by a high proportion of mostly euhedral pyroxene (~80%; 1000-1300 μm crystal sizes), with a minor amount of olivine (~10%; generally 500-700 μm in maximum dimension) and a magnetite/olivine-rich mesostasis (~10%) that contains numerous microcrystals (<5 μm) of olivine. The chip shows a low degree (< 15%) of fracturing. In some areas, both olivine and pyroxene contained glassy inclusions of 30 μm in maximum dimension. Olivine was distributed heterogeneously and it occurred only in one area.

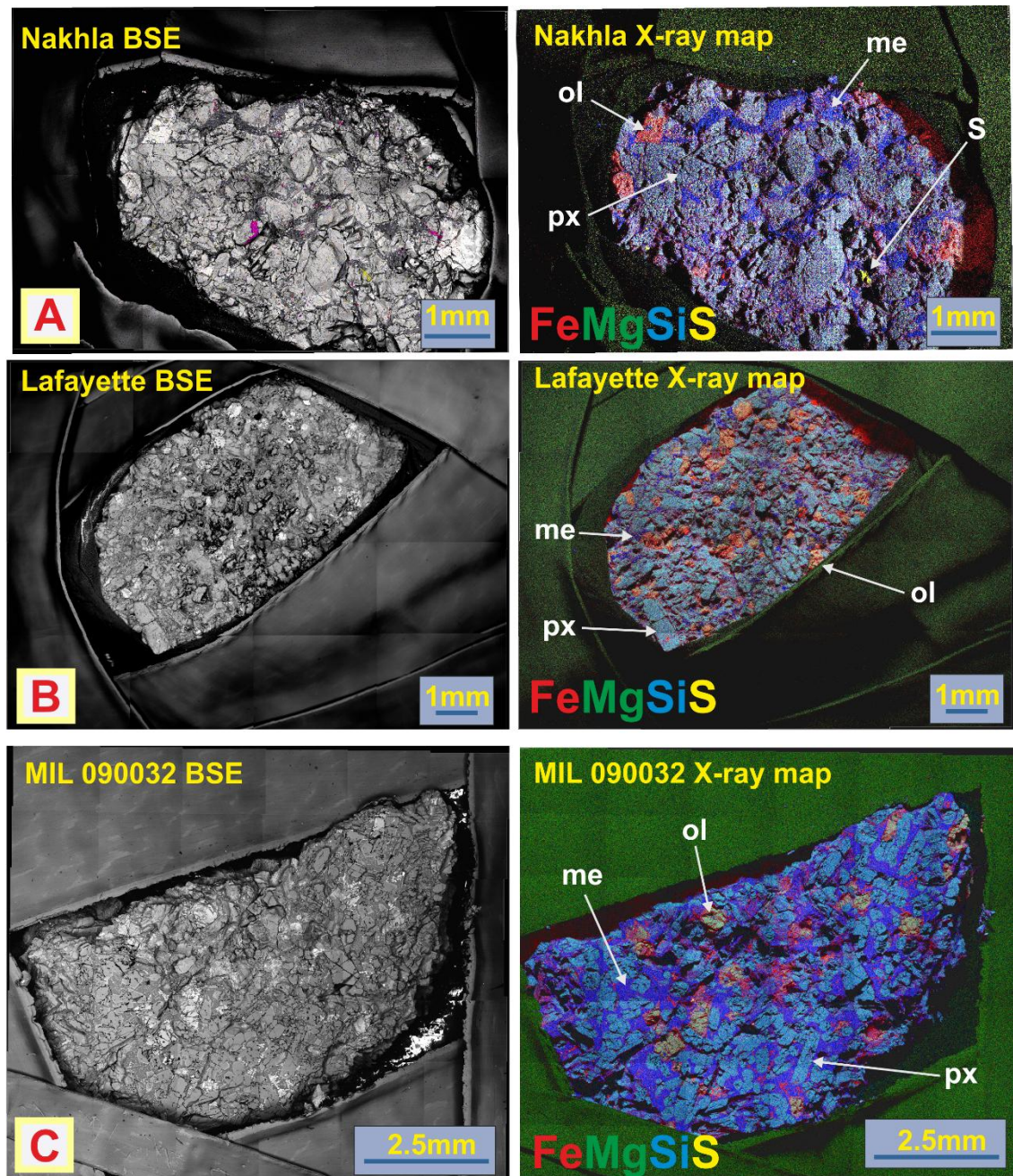


Fig. 4.1 - Backscatter electron (BSE) images, along with false-colour Fe-Mg-Si-S X-ray elemental maps of the nakhlite chips used to retain information on the crystallographic features of our samples prior to destructive analyses for HSE abundances and Os isotopic compositions. The colour-coded elemental key is given at the bottom left of each X-ray image - olivine appears green to red, sulphide/sulphate appears yellow, clinopyroxene appears cyan, and mesostasis appears dark blue. (a) BSE image and X-ray map of Nakhla. In both images a 0.3 mm long sulphate is evident at the bottom right corner, and salt is highlighted in purple in the BSE image; (b) BSE image and X-ray map of Lafayette; (c) BSE

image and X-ray map of MIL 090032. Ol, olivine; px, pyroxene; s, sulphate; me, mesostasis.

Our observations of these nakhlite chips are in agreement with previous petrographic observations of thin sections and chips of Nakhla (Treiman, 1990; Lentz et al., 1999; Corrigan et al., 2015; Udry and Day, 2018), Lafayette (Bunch and Reid, 1975; Boctor et al., 1976; Treiman et al., 1993; Corrigan et al., 2015; Udry and Day, 2018), and MIL 090032 (Day et al., 2005, 2006; Stopar et al., 2005; Udry et al., 2012; Corrigan et al., 2015; Udry and Day, 2018). The modal abundance of sulphides/sulphates is very low (< 0.1 vol. %) in respect to other phases, in all chips studied. However, the Nakhla chip studied here differs from previous observations in hosting a large sulphate grain, supporting heterogeneously distributed HSE-carrying trace phases in nakhlites.

4.3.2 – Sulphur isotopes

Pyrrhotite and pyrite grains were identified adjacent to mesostasis (glass) in each thin section, and also occur as inclusions within augite (Fig. 4.2). These sulphides differ in size between meteorites: Nakhla 20-40 μm ; Lafayette 20-60 μm ; MIL 090032 10-60 μm ; Y-000593 50-250 μm ; and Y-000749 15-40 μm . The sulphide grains are relatively pure, containing few inclusions, or exsolved blebs/lamellae, of other phases. Sulphide chemistry is not significantly variable among the grains, with CaO, 0.06-0.22 wt.%; TiO₂, 0.08-0.45 wt.%; MnO, 0.00-0.05 wt.%; Ni, 0.04-1.71 wt.%; Co, 0.25-0.60 wt.%; but with FeO abundance that differs for Lafayette sulphides (44.4-47.4 wt.%) in respect to the other samples (57.2-61.3 wt.%).

Sulphides in the five nakhlites analysed here show significant variation in sulphur isotopic composition, with $\Delta^{33}\text{S}$ from -0.76 to 0.04 ‰ and $\delta^{34}\text{S}$ from -13.2 to 15.1 ‰ (Table 4.1; Fig. 4.4). Sulphur isotopes analysed from five pyrrhotite grains in Nakhla give a range of $\Delta^{33}\text{S}$ from -0.12 to 0.02 ‰, with an average of -0.05 ± 0.08 ‰ and an average $\delta^{34}\text{S}$ of -1.59 ± 0.10 ‰. These values are in agreement with $\Delta^{33}\text{S} = -0.09$ ‰ analysed via acid extraction and with $\delta^{34}\text{S}$ of -1.6 ‰ analysed via chrome reducible sulphur extraction in sulphides from Nakhla by Farquhar et al. (2007). However, our data show a slightly more negative result

relative to the data of Franz et al. (2014) (mean $\Delta^{33}\text{S} = 0.08 \text{ ‰}$ with some grains as low as -0.33 ‰ , and mean $\delta^{34}\text{S} = -0.51 \text{ ‰}$. The SIMS measurements of Greenwood et al. (2000b) for pyrrhotite grains in Nakhla agree well with our values, having a range in $\Delta^{33}\text{S} = -0.4 \pm 0.5$ to $-0.07 \pm 0.5 \text{ ‰}$ and a $\delta^{34}\text{S} = -4.5 \pm 0.4$ to $1.4 \pm 0.4 \text{ ‰}$.

Table 4.1 - S-isotopic compositions for pyrrhotite and pyrite in Nakhla, Lafayette, MIL 090032, Y-000749, and Y-000593. Data on $\delta^{34}\text{S}$, $\delta^{33}\text{S}$, and $\Delta^{33}\text{S}$ values are expressed in permil (‰) and associated 2σ standard errors are reported. Uncertainties count statistics. The mean in sulphur isotope abundance for each meteorite is also shown. Sulphur isotope ratios are reported in standard δ notation with respect to Canyon Diablo Troilite (CDT), where $\delta^{34}\text{S} = [({}^{34}\text{S}/{}^{32}\text{S})_{\text{sample}}/({}^{34}\text{S}/{}^{32}\text{S})_{\text{CDT}} - 1] \times 1,000$, $\delta^{33}\text{S} = [({}^{33}\text{S}/{}^{32}\text{S})_{\text{sample}}/({}^{33}\text{S}/{}^{32}\text{S})_{\text{CDT}} - 1] \times 1,000$, and $\Delta^{33}\text{S} = [({}^{33}\text{S}/{}^{32}\text{S})_{\text{sample}}/({}^{33}\text{S}/{}^{32}\text{S})_{\text{CDT}} - [({}^{34}\text{S}/{}^{32}\text{S})_{\text{sample}}/({}^{34}\text{S}/{}^{32}\text{S})_{\text{CDT}}]^{0.515}] \times 1,000$.

Sample	Phase	$\delta^{34}\text{S}$ (‰)	$\pm 2\sigma$	$\delta^{33}\text{S}$ (‰)	$\pm 2\sigma$	$\Delta^{33}\text{S}$ (‰)	$\pm 2\sigma$
Nakhla	pyrrhotite	-0.4	0.11	-0.33	0.08	-0.12	0.08
Nakhla	pyrrhotite	-2.2	0.10	-1.15	0.08	0.02	0.07
Nakhla	pyrrhotite	-1.0	0.09	-0.55	0.09	-0.03	0.09
Nakhla	pyrrhotite	-2.5	0.11	-1.36	0.08	-0.06	0.08
Nakhla	pyrrhotite	-1.7	0.08	-0.97	0.08	-0.08	0.07
	mean	-1.5		-0.87		-0.05	
	variance	0.62		0.14		0.00	
Lafayette	pyrite	-13.2	0.10	-6.78	0.09	0.03	0.08
Lafayette	pyrite	-10.1	0.11	-5.51	0.08	-0.26	0.08
Lafayette	pyrite	-10.7	0.30	-5.65	0.19	-0.12	0.24
Lafayette	pyrite	-8.5	0.11	-4.56	0.09	-0.16	0.09
Lafayette	pyrite	-11.1	0.10	-5.72	0.12	0.04	0.11
	mean	-10.7		-5.64		-0.09	
	variance	2.28		0.49		0.01	
MIL090032	pyrrhotite	7.6	0.08	3.25	0.08	-0.65	0.07
MIL090032	pyrrhotite	9.7	0.08	4.34	0.08	-0.65	0.06
MIL090032	pyrrhotite	9.9	0.10	4.33	0.09	-0.76	0.08
MIL090032	pyrrhotite	15.2	0.11	7.14	0.18	-0.62	0.18
MIL090032	pyrrhotite	10.2	0.08	4.58	0.08	-0.69	0.07
	mean	10.5		4.73		-0.67	
	variance	6.22		1.66		0.00	
Yamato000749	pyrrhotite	-1.6	0.08	-0.83	0.13	0.00	0.13
Yamato000749	pyrrhotite	-0.9	0.11	-0.59	0.13	-0.08	0.13
Yamato000749	pyrrhotite	-0.9	0.14	-0.71	0.20	-0.23	0.20
	mean	-1.1		-0.71		-0.10	
	variance	0.09		0.00		0.00	
Yamato000593	pyrrhotite	-0.7	0.07	-0.57	0.07	-0.21	0.05
Yamato000593	pyrrhotite	-2.0	0.08	-1.19	0.10	-0.16	0.09
	mean	-1.3		-0.88		-0.18	
	variance	0.42		0.09		0.00	

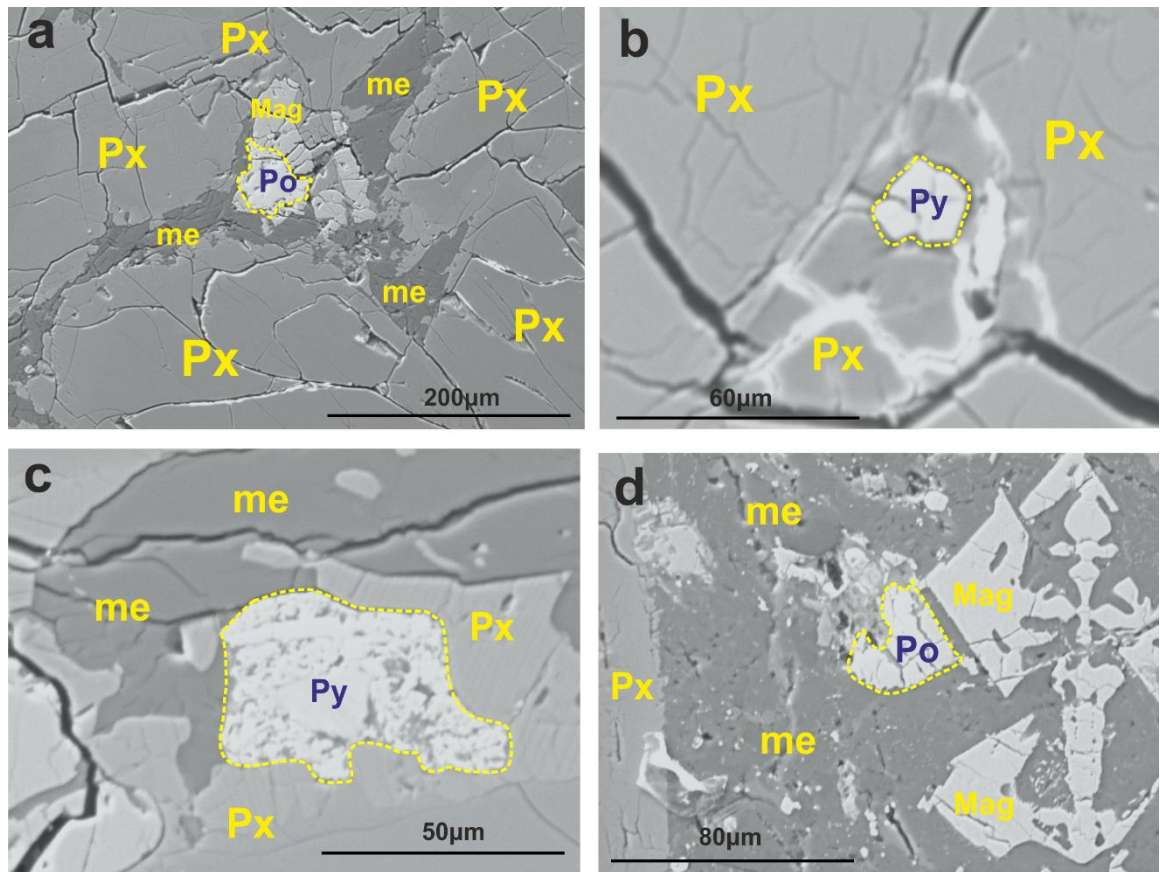


Fig. 4.2 - Backscatter electron (BSE) images of sulphides in Nakhla, Lafayette, and MIL 090032 showing their petrographic relationships with the other minerals. Sulphides that have been selected for sulphur isotopic analysis are rimmed in yellow. A) pyrrhotite (Po) grain in Nakhla; B, C) Pyrite (Py) grains in Lafayette; D) pyrrhotite grain in MIL 090032. Po, pyrrhotite; Py, pyrite; Px, pyroxene (augite); Mag, magnetite; me, mesostasis.

Similar to Nakhla, two pyrrhotite grains in Y-000749 gave an average $\Delta^{33}\text{S} = -0.10 \pm 0.15 \text{ ‰}$ and $\delta^{34}\text{S} = -1.1 \pm 0.11$, while only one pyrrhotite was analysed for Y-000593 ($\Delta^{33}\text{S} = -0.18 \pm 0.07 \text{ ‰}$; $\delta^{34}\text{S} = -1.3 \pm 0.08$). Lafayette pyrite analysis (five grains) yielded a range of values in $\Delta^{33}\text{S} = -0.26$ to 0.04 ‰ and a $\delta^{34}\text{S} = -13.2$ to -8.53 ‰ , with an average $\Delta^{33}\text{S} = -0.09 \pm 0.12 \text{ ‰}$, which approaches the $\Delta^{33}\text{S} = 0.07 \text{ ‰}$ in Lafayette pyrite analysed by Farquhar et al. (2000). Sulphur isotope

data obtained for five grains of MIL 090032 show a $\Delta^{33}\text{S} = -0.76$ to -0.62 ‰ and a $\delta^{34}\text{S} = 7.60$ to 15.1 ‰, with an average $\Delta^{33}\text{S} = -0.67 \pm 0.10$ ‰ and $\delta^{34}\text{S} = 10.5$ ‰. Previous measurements via chemical extractions from the four paired Miller Range nakhlites gave a range of $\Delta^{33}\text{S}$ from -0.43 to -0.53 ‰, in particular an earlier study of the MIL 090136 material gave values that are in the range of our own analysis, with an average $\Delta^{33}\text{S} = -0.4$ ‰ and $\delta^{34}\text{S} = 7.66$ ‰ (Franz et al., 2014; Dottin III et al., 2018).

4.3.3 – Rhenium-Os isotope systematics and HSE

Lafayette and Nakhla have broadly similar CI-normalized HSE patterns (Fig. 4.3a), with a general depletion of Os, Ir, and Ru relative to Pd and Re (Table 4.2). However, osmium normalised to CI-chondrite/10,000 (Os_N) is slightly more abundant (1.69) in Lafayette than in Nakhla (0.25). Osmium, Ir, Ru, and Pt are in agreement with earlier HSE-abundance studies of Nakhla (as reviewed by Jones et al., 2003), with the exception of Pd and Re that show higher abundances in our new data (2.24 and 0.117 ppb, respectively). In general, Os, Ir, Ru, and Pt in Nakhla fall in the range between previous HSE analyses of Nakhla by Dale et al. (2012) and Jones et al. (2003). Platinum, Pd, and Re of Nakhla and Lafayette show similarities with measured Pt and Pd in Chassigny (Jones et al., 2003). Nakhla has the highest $(\text{Re}/\text{Ir})_N = 148$ and $(\text{Pt}/\text{Ir})_N = 96$ among the studied set of samples, while Lafayette has the highest value in $(\text{Os}/\text{Ir})_N = 3.44$ for these nakhlites (Fig. 4.5). The MIL 090032 CI-normalised HSE pattern is slightly different from the patterns of Nakhla and Lafayette, with higher absolute Os, Ir, and Ru, and Pt (4.54 ppb) having the highest CI-chondrite normalised value.

Nakhla and Lafayette display different Re and Os abundances and Re-Os isotope systematics (Table 4.2; Fig. 4.3b). Lafayette has a $^{187}\text{Re}/^{188}\text{Os}$ and $^{187}\text{Os}/^{188}\text{Os}$ of 6 ± 6 and 0.1849 ± 0.0003 (uncertainties are expressed as 2σ internal precision), respectively. Nakhla is characterized by the highest $^{187}\text{Re}/^{188}\text{Os}$ value of 49 ± 49 and an $^{187}\text{Os}/^{188}\text{Os}$ of 0.4542 ± 0.0018 . Despite large uncertainties on $^{187}\text{Re}/^{188}\text{Os}$ and crystallisation ages >1 Gyr (likely due to underspiking), we tried to calculate the initial $^{187}\text{Os}/^{188}\text{Os}$ composition of the sample with its percent deviation from the chondritic reference (Shirey & Walker, 1998) using the γOs_i notation. The assumed crystallization ages of the

most recent ^{39}Ar - ^{40}Ar dating (Cohen et al., 2017) were used for our calculations. The calculated γOs_i is strongly negative. Data on initial $^{187}\text{Os}/^{188}\text{Os}$ and γOs_i are reported in Table 4.2.

Table 4.2 - Re-Os isotope systematics and HSE abundances (in ppb) for all samples. The γOs_i notation is given by $\gamma\text{Os}_i = 100 \times [({}^{187}\text{Os}/{}^{188}\text{Os}_{\text{sample}(t)})/({}^{187}\text{Os}/{}^{188}\text{Os}_{\text{chondrite}(t)}) - 1]$. HSE ratios normalized to Orgueil chondrite are denoted by (N). Uncertainty = 2σ , for HSE refers to the CI-normalized values. Initial ^{143}Nd are from Nakamura et al. (1982) and Shih et al. (1998). Ages are from Cohen et al. (2017).

	Sample		
	Lafayette	Nakhla	MIL 090032
Mass (g)	0.417	0.405	0.5
Os ($\pm 2\sigma$)	0.078 (0.01)	0.012 (0.01)	0.036 (0.01)
Ir ($\pm 2\sigma$)	0.022 (0.00)	0.009 (0.00)	0.025 (0.14)
Ru ($\pm 2\sigma$)	–	0.04 (0.06)	0.27 (0.15)
Pt ($\pm 2\sigma$)	1.01 (0.05)	1.66 (0.05)	4.54 (0.58)
Pd ($\pm 2\sigma$)	1.89 (0.35)	2.24 (0.35)	1.18 (3.52)
Re ($\pm 2\sigma$)	0.098 (0.13)	0.117 (0.13)	0.065 (1.26)
Rh ($\pm 2\sigma$)	–	–	0.21 (0.45)
Au ($\pm 2\sigma$)	–	–	0.081 (1.34)
$^{187}\text{Re}/^{188}\text{Os}$ ($\pm 2\sigma$)	6 (6)	49 (49)	–
$^{187}\text{Os}/^{188}\text{Os}$ ($\pm 2\sigma$)	0.1849 (0.0003)	0.4542 (0.0018)	–
γOs_i ($\pm 2\sigma$)	-64 (34.3)	-636 (5)	–
Re/Os	1	10	2
Pt/Os	12.9	138.3	126.1
Os/Ir	3.54	1.33	1.44
(Pt/Pd)N	0.35	0.48	2.51
(Pd/Os)N	19.6	131.3	26
$\epsilon^{143}\text{Nd}$ ($\pm 2\sigma$)	16.3 (0.4)	16	–
Age (Ma) ($\pm 2\sigma$)	1383 (7)	1330 (15)	1392 (10)
Lab	Durham	Durham	Berlin

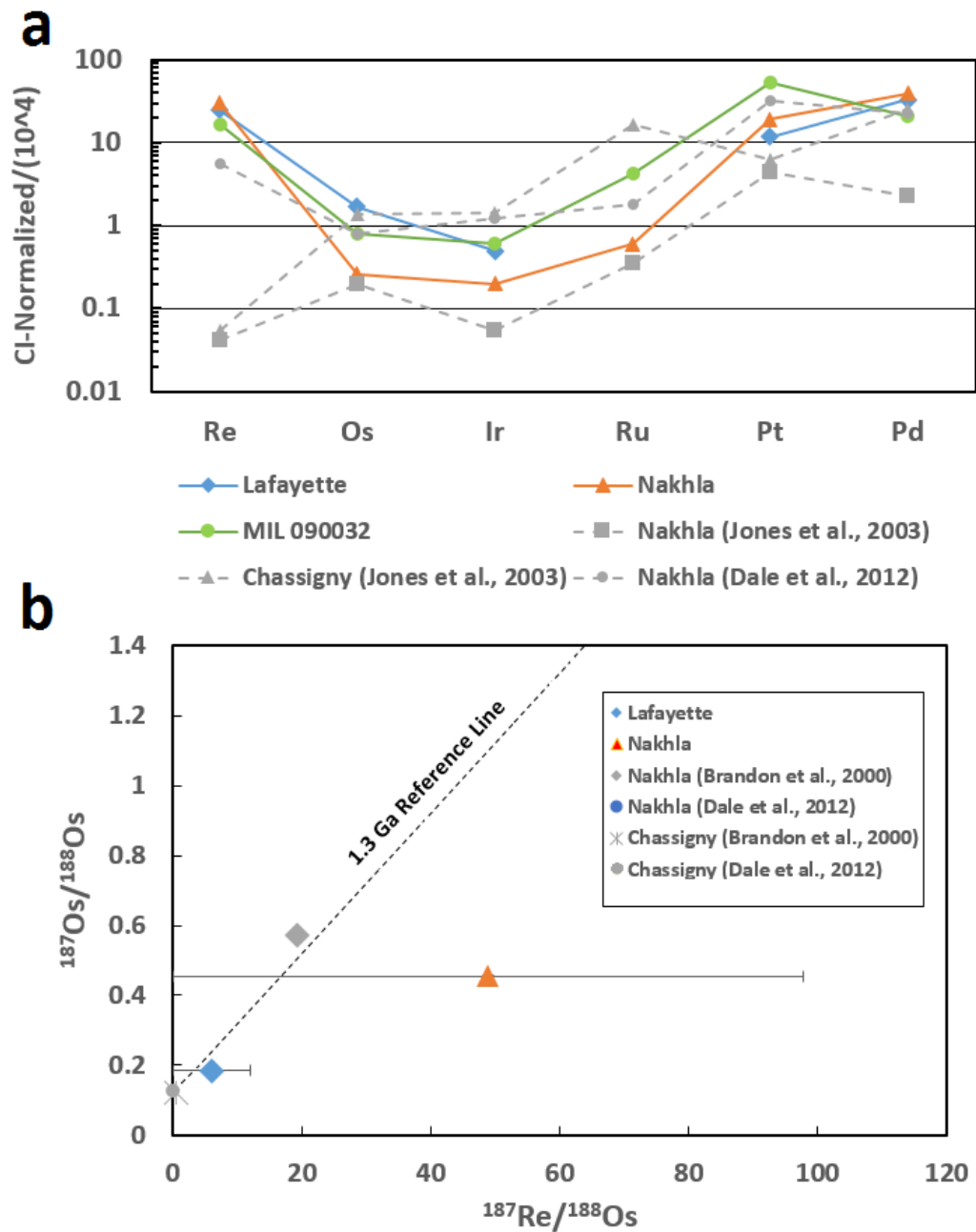


Fig. 4.3 - Highly siderophile element (HSE) abundances and Re-Os isotope systematics in nakhlites. (a) CI chondrite normalized HSE data for Nakhla, Lafayette, and MIL 090032 are shown, along with previously published data in grey (from Jones et al., 2003; Dale et al., 2012). Uncertainty = 2σ , error bars are less than symbol size; (b) $^{187}\text{Re}/^{188}\text{Os}$ vs. $^{187}\text{Os}/^{188}\text{Os}$ data for Nakhla and Lafayette are shown, along with previous literature data (from Brandon et al., 2000; Dale et al., 2012). The 1.3 Ga reference line is shown for comparison and

represents single-stage Re-Os isotope evolution from a chondritic $^{187}\text{Os}/^{188}\text{Os}$ reservoir, assuming a Solar System initial $^{187}\text{Os}/^{188}\text{Os} = 0.9524$ (Smoliar et al., 1996). Uncertainty = 2σ , vertical error bars are less than symbol size.

4.4 – Discussion

4.4.1 – Potential for terrestrial alteration and weathering

Some of the nakhlites analysed here could have been affected by alteration during their residence on Earth. In samples recovered from hot deserts the formation of terrestrial clay and carbonate (e.g., Crozaz et al., 2003) can modify lithophile isotope systematics (e.g., Symes et al., 2008) and potentially perturb the Re-Os isotope system. Nakhla was seen to fall, and was recovered shortly thereafter. The provenance of Lafayette is less clear, but its fresh fusion crust suggests it was collected soon after it fell (e.g., Graham et al., 1985). However, even weathering events lasting a few hours have been shown to cause Re and minor Os redistribution in chondrites from fresh falls (Walker et al., 2018). Terrestrial clays or carbonates are not found within either of these nakhlites, hence the Re-Os isotope system and their sulphides (as supported by our petrographic observations) should not be significantly affected by terrestrial alteration. In addition, initial $^{87}\text{Sr}/^{86}\text{Sr}$ ratios of Nakhla and Lafayette (0.70254 and 0.70260, respectively) also show little variation (Gale et al., 1975; Shih et al., 1998), suggesting minor or no modification of Sr isotope due to clay and carbonate mineralization.

In contrast, the Miller Range and Yamato nakhlites are Antarctic finds, hence have had greater exposure to the terrestrial environment. The light rare earth element, cerium (Ce) can act as an alteration tracer via the conversion of Ce^{3+} to Ce^{4+} due to oxidation, with pigeonite being the most susceptible mineral (Crozaz et al., 2003). Cerium anomalies can be found in silicates of the Antarctic Yamato nakhlites (Crozaz et al., 2003), and terrestrially derived jarosite sulphate has been reported towards the exterior of Yamato 000749 (Changela and Bridges, 2011). However, Pb isotope systematics within these nakhlites reflect minimal terrestrial contamination (Yamashita et al., 2002), and the Rb-Sr and Sm-Nd isotope systematics provide little evidence for terrestrial weathering.

Olivine and sulphide within the Miller Range nakhlites has suffered aqueous corrosion during residence in Antarctica (Dyar et al., 2005; Hallis and Taylor, 2011; Hallis, 2013; Velbel, 2016). Long exposure to water/snow may have resulted in an addition of anthropogenic radiogenic osmium (Chen et al., 2009). However, terrestrial alteration in the Miller Range nakhlites was considered in previous studies to have no significant impact on the $\Delta^{33}\text{S}$ and $\delta^{34}\text{S}$ of its unweathered sulphides, which thereby robustly trace processes on Mars (Dottin III et al., 2018).

The potential effects of terrestrial alteration on HSE abundances and Re-Os isotopic compositions are addressed in [Paragraph 4.3.1](#).

4.4.2 – Origin of sulphur isotopic anomalies in sulphides of nakhlites

The variation of $\Delta^{33}\text{S}$ and $\delta^{34}\text{S}$ in the nakhlites, in reference to our dataset, could be due to differences in the chemistry of the atmosphere and surface or alteration by subsurface Martian fluids (Farquhar et al., 2000; Franz et al., 2014). To have confidence in which of our nakhlite HSE and Re-Os isotope data are the most representative of the Martian magma source(s) for nakhlite meteorites, it is useful to know the extent to which each nakhlite might have been affected by regolith assimilation; where with ‘regolith’ we refer to heterogeneous, unconsolidated, and relatively superficial Martian surface deposits.

4.4.2.1 - Isotopic fractionation of $\Delta^{33}\text{S}$ in sulphides of nakhlites

Our analyses of Nakhla, Lafayette, MIL 090032, Y-000749, and Y-000593 sulphide grains gave mean $\Delta^{33}\text{S}$ values of $-0.05 \pm 0.08 \text{ ‰}$, $-0.09 \pm 0.12 \text{ ‰}$, $-0.67 \pm 0.10 \text{ ‰}$, $-0.10 \pm 0.15 \text{ ‰}$, and $-0.18 \pm 0.07 \text{ ‰}$, respectively ([Fig. 4.4a](#)). Assuming that some of these sulphide grains may be more isotopically fractionated than others, it is important to determine whether the sulphur isotopic signatures are representative of the sample as a whole, and if they are magmatic or non-magmatic in origin.

Appraisal of the petrographic characteristics of our studied samples prior to SIMS analyses showed that we sampled a representative set of pyrite and pyrrhotite grains in terms of textural associations, but that we observed a bias toward grains $> 10 \mu\text{m}$ in size. Virtually, the magma involved in the generation of the nakhlites can be considered as affected by a degree of crustal assimilation coincident with eruption onto the Martian surface (e.g., Franz et al., 2014). The challenge is to disentangle the degree to which the chemistries of the analysed nakhlites were affected by assimilation during the transit of magmas through Mars' crust and during eruptive processes.

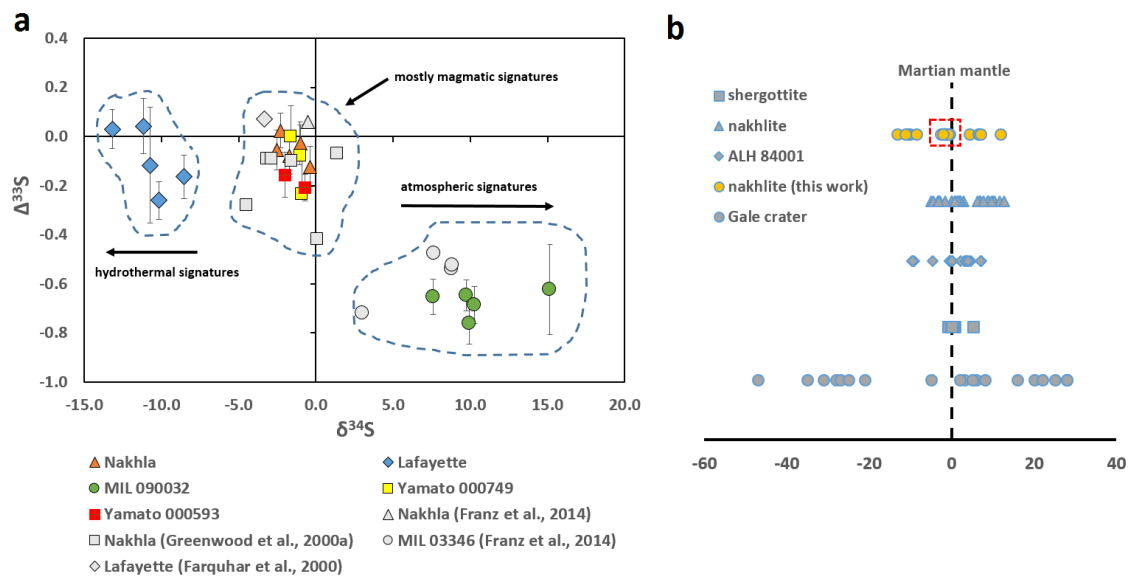


Fig. 4.4 - Sulphur isotope ratios for the nakhlites, compared with previous data from Martian meteorites and Mars rover missions data. (a) $\delta^{34}\text{S}$ vs. $\Delta^{33}\text{S}$ isotope ratios for the nakhlites analysed in this work, compared with the same nakhlites analysed by previous authors. Labels serve to emphasise which processes are inferred to have affected the sulphur isotopic composition of each data cluster. 2σ uncertainties are shown, with X-axis uncertainties smaller than the symbols; (b) Comparison of $\delta^{34}\text{S}$ value between the present study (yellow symbols) and literature data from Martian meteorites (Farquhar et al., 2000; Greenwood et al., 2000a; Franz et al., 2014; Franz et al., 2017) and the Curiosity rover (Franz et al., 2017). The $\delta^{34}\text{S}$ value of the Martian mantle (from Franz et al., 2014) is shown by the dashed line. The red box identifies the nakhlites that have a $\delta^{34}\text{S}$ very close to the Martian mantle $\delta^{34}\text{S}$ value and so have been least affected by regolith assimilation (Nakhla, Y-000749, and Y-000593). Some of the data used in

the graphs are from previous studies (Farquhar et al., 2000; Greenwood et al., 2000a; Franz et al., 2014; Franz et al., 2017).

Anomalous sulphur is constrained by its mass-independent fractionation (MIF) signature. Large variations in $\delta^{34}\text{S}$ can modify the $\Delta^{33}\text{S}$ of a sulphide by chemical mixing. However, it has been demonstrated that the values of $\delta^{34}\text{S}$ in Martian meteorites do not vary enough to be able to explain the observed variation in $\Delta^{33}\text{S}$ (Farquhar et al., 2000; Farquhar et al., 2007; Franz et al., 2014). Detection of MIF or non-MIF signatures for sulphur could be constrained by the displacement of non-zero values of $\Delta^{33}\text{S}$ for each meteorite analysed here, where a magmatic only $\Delta^{33}\text{S}$ is characterized by near zero values (i.e., $\Delta^{33}\text{S} = 0$). Lafayette has zero ($0.03 \pm 0.08\text{‰}$) to slightly negative ($-0.26 \pm 0.08\text{‰}$) $\Delta^{33}\text{S}$ in its sulphide grains. This inter-grain variation in Lafayette is the largest heterogeneity in $\Delta^{33}\text{S}$ of the meteorite dataset that we analysed, implying the presence of both non-MIF (i.e., magmatic) and MIF signatures (assimilation) in Lafayette sulphur. In the case of MIF signatures, these were likely induced by assimilation of regolith-derived sulphur (including regolith affected by brines) during emplacement of Lafayette lava flow on the Martian surface. Though relevant for the present-day Mars, data from NASA's Curiosity rover shows a $\delta^{34}\text{S}$ with a range far in excess of that observed among nakhlites (-47 to 28‰ ; Franz et al., 2017), it is reasonable to conclude that these observations imply that the assimilation of even a small percentage of Mars' regolith at the time of nakhlite formation could significantly shift the sulphur isotopic composition of these nakhlites (by several ‰).

For Nakhla we obtained a $\Delta^{33}\text{S}$ equal to zero ($-0.05 \pm 0.08\text{‰}$, $n = 5$), suggesting a magmatic origin (non-MIF signature) for all sulphur in Nakhla. This value is in accordance with a previously reported mean $\Delta^{33}\text{S}$ of 0.06‰ for Nakhla sulphides (Franz et al., 2014). However, Nakhla is internally variable and some of the studied sulphides show more negative $\Delta^{33}\text{S}$, with $\Delta^{33}\text{S}$ as low as -0.33‰ and -0.4‰ (Greenwood et al., 2000a,b; Franz et al., 2014). We report similar near zero values of $\Delta^{33}\text{S}$ from the three sulphide grains in Y-000749 (average $\Delta^{33}\text{S} = -0.10 \pm 0.15\text{‰}$; with one sulphide having a magmatic $\Delta^{33}\text{S} = 0.00 \pm 0.13\text{‰}$) and from the sulphide grain in Y-000593 ($\Delta^{33}\text{S} = -0.18 \pm 0.07\text{‰}$). However, we were not able to analyse sulphide grains smaller than $10\text{ }\mu\text{m}$ in these nakhlites and $\Delta^{33}\text{S}$ values may be somewhat internally variable. Based on the analysed sulphide grains, we

suggest a non-primordial mantle sulphur signal but still a dominantly magmatic origin for the sulphur isotopic systematics of Nakhla, Y-000749, and Y-000593, without large extents of regolith assimilation during their magmatic emplacement. Miller Range 090032 represents the meteorite with the most marked MIF signatures in sulphide grains, with a negative mean $\Delta^{33}\text{S}$ of $-0.67 \pm 0.10\%$, with wide variability between grains (Fig. 4.4). Large variability in $\Delta^{33}\text{S}$ in sulphides of the Miller Range paired nakhlites is also in agreement with Franz et al. (2014) and Dottin III et al. (2018). These values suggest that sulphides in MIL 090032 are affected by MIF signatures, probably caused by secondary processes that occurred on Mars (Mikouchi et al., 2003), as suggested by Franz et al. (2014) for the paired stone MIL 03346. Secondary processing possibilities are explored below.

4.4.2.2 - Isotopic fractionation of $\delta^{34}\text{S}$ in sulphides of nakhlites

The absence of crustal recycling on Mars may have been effective in leaving heterogeneous sulphur signatures on the surface. Sulphur isotope ratios can be fractionated by three main processes: hydrothermal (e.g., Ohmoto & Goldhaber, 1997), photochemical (e.g., Zmolek et al., 1999; Farquhar et al., 2001), and biological (e.g., Parnell et al., 2010). In addition to these processes, we discuss also possible magmatic processes that can fractionate $\delta^{34}\text{S}$. Large isotopic fractionations of $\delta^{34}\text{S}$ have been investigated recently by the NASA's Curiosity rover from a 13 km long transect in Gale Crater (Franz et al., 2017). The measured $\delta^{34}\text{S}$ ranged from $-47 \pm 14 \%$ to $28 \pm 7 \%$ (Fig. 4.4b); whether the negative values occurred in sulphides and the positive values occurred in sulphates or sulphites (mudstone and sandstone) is yet to be resolved. The reason Curiosity reported a greater range in $\delta^{34}\text{S}$ than that observed in Martian meteorites is probably due to the accumulation of fine crustal materials in Gale crater following long periods of fluvial and/or aeolian transport.

Nakhlite sulphur isotopic signatures have been interpreted as reflecting both equilibrium fractionation in a warmed Martian groundwater environment (low $\delta^{34}\text{S}$) or atmospheric photochemical processes (high $\delta^{34}\text{S}$) (Franz et al., 2017). In particular, the $\delta^{34}\text{S}$ enrichment is reported to derive from atmospheric processing of SO_2 and H_2S via Martian volcanic activity (processes capable of

producing positive $\delta^{34}\text{S}$ signatures) with subsequent incorporation of these products into the Martian surface/subsurface (Franz et al., 2017, see Fig. 2). This was also deduced experimentally (Franz et al., 2013) and from oxidation of SO_2 in volcanic ashes (Savarino, 2003).

Fractionation of $\delta^{34}\text{S}$ differs for all the five nakhlites analysed here (Fig. 4.4b). However, it is important to notice that the $\delta^{34}\text{S}$ variation could not be a full signature of the contaminant. It is possible that S loss processes can fractionate $\delta^{34}\text{S}$, and such processes would not be expected to significantly shift the $\Delta^{33}\text{S}$. Thus, the $\delta^{34}\text{S}$ of the samples with the most anomalous $\Delta^{33}\text{S}$ might reflect a different combination of processes, related to addition of sulphur, that would exert the first order control on $\Delta^{33}\text{S}$, and then loss of sulphur that would exert a first order control on $\delta^{34}\text{S}$ due to kinetic stable isotopic fractionation. Sulphides in Nakhla, Y-000749, and Y-000593 have the most convincing magmatic signatures, being characterized by a near zero mean $\delta^{34}\text{S}$ (mean $-1.59 \pm 0.10\%$, $-1.18 \pm 0.11\%$, and $-1.36 \pm 0.08\%$, respectively), supported also from their magmatic $\Delta^{33}\text{S}$ values described above. Conversely, MIL 090032 has an enriched $\delta^{34}\text{S}$ (mean $+10.54 \pm 0.09\%$), that is the largest intra-meteorite variation in sulphur isotopic fractionation and the largest positive $\delta^{34}\text{S}$ value obtained in a Martian material ($+15.2 \pm 0.1\%$). These values suggest enrichment of $\delta^{34}\text{S}$ due to Martian atmospheric processes characterised by oxidation of H_2SO_4 or photolysis of sulphur compounds (gases) introduced by volcanic eruptions and outgassing (Savarino, 2003; Franz et al., 2017). This finding is similar to reported measurements of $\delta^{34}\text{S}$ fractionation close to the vents of terrestrial volcanoes ($+7.7 \pm 0.8\%$; Mather et al., 2006).

Lafayette has the greatest $\delta^{34}\text{S}$ depletion yet described for a Martian meteorite (average of $-10.7 \pm 0.2\%$), with values of $\delta^{34}\text{S}$ reaching $-13.2 \pm 0.1\%$ - and lower than the Allan Hills (ALH) 84001, $\delta^{34}\text{S}$ values ($\sim -9\%$) previously reported for pyrite grains (Greenwood et al., 2000a). These values are suggestive of late-stage equilibrium fractionation with Martian groundwater, consistent with the Lafayette $\Delta^{33}\text{S}$ results. Previous analysis of Lafayette reported values of $\delta^{34}\text{S}$ of $-3.2 \pm 2.1\%$ (Greenwood et al., 2000b; Farquhar et al., 2000). The greater depletion in our $\delta^{34}\text{S}$ values may reflect heterogeneous assimilation of sulphur from the Martian regolith. Alternatively (or in addition), Lafayette sulphides have 'spongy' textures (Fig. 4.2c), which could be the product of alteration by shock melting with subsequent volatilisation effects

(e.g., Gattacceca et al., 2013). Both Greenwood et al. (2000b) and Farquhar et al. (2000) proposed mixing of fluids with heavy ($\delta^{34}\text{S} > 0$) and light sulphur ($\delta^{34}\text{S} < 0$) as a hydrothermal process that can produce negative $\delta^{34}\text{S}$. Some of the nakhlite lava flows may have been in contact with, or in close proximity, to a heavy sulphur source, while, in general, all may have been affected by mixing with fluids characterized by contrasting $\delta^{34}\text{S}$ values.

At temperatures $< 1200^\circ\text{C}$ the magmatic degassing of SO_2 can modify the sulphur isotope ratios of magmas (Sakai et al., 1982), depending on the $f\text{O}_2$ (Carroll and Webster, 1994). Two cases are possible: 1) if $f\text{O}_2 \gg$ quartz-fayalite-magnetite (QFM) buffer, sulphate is the dominant sulphur phase in the magma. The consequent equilibrium isotopic fractionation factor will be positive ($\Delta\text{SO}_4 - \text{SO}_2 > 0$; Sakai et al., 1982), hence the residual melt is enriched in $\delta^{34}\text{S}$ due to SO_2 degassing, producing sulphides enriched in $\delta^{34}\text{S}$. 2) If $f\text{O}_2 = \text{QFM}$ or $f\text{O}_2 < \text{QFM}$ sulphide is the dominant sulphur phase in the magma, with consequent negative equilibrium isotopic fractionation factor ($\Delta\text{S}_2 - \text{SO}_2 < 0$; Sakai et al., 1982). In this way, the melt may become depleted in $\delta^{34}\text{S}$. This mechanism leads to crystallization of sulphides that are depleted in $\delta^{34}\text{S}$.

Magmatic degassing could have been the cause of the positive $\delta^{34}\text{S}$ signature in MIL 090032, by shifting the SO_4 in the silicate melt structure sulphates can be reduced to yield more positive $\delta^{34}\text{S}$ values (see Labidi et al., 2015; Mandeville et al., 2009; Dottin III et al., 2018), that was subsequently reduced to form the sulphides. In the same way, even the Lafayette sulphides may be indicative of degassing (especially due to the detected spongy textures in the sulphides). In addition, given the HSE patterns reported in Fig. 4.3, it is possible that degassing played a role in the abundance of Re. In fact, magmatic degassing induce loss of Re and thus can be highlighted by Re depletion or low Re/Os (Sun et al., 2003); in this sense, low Re and low Re/Os in Lafayette could have been the product of magmatic degassing.

4.4.2.3 – Assimilation versus acquisition of Martian regolith during lava emplacement

The $\Delta^{33}\text{S}$ and $\delta^{34}\text{S}$ values presented here (Fig. 4.4), along with the fact that nakhlite sulphides are associated with the mesostasis (hence are some of the last

phases to crystallise) (Chevrier et al., 2011; Fig. 4.2), indicate assimilation of an S-rich Martian regolith occurred within at least some of the nakhlite lava flows (Lafayette and MIL 090032). The range in $\Delta^{33}\text{S}$ among the nakhlites may be broadly related to the total sulphur content of each lava flow, where nakhlites with larger $\Delta^{33}\text{S}$ anomalies were in proximity of a "sulphur source", contrary to nakhlites with smaller $\Delta^{33}\text{S}$ anomalies (Dottin III et al., 2018). This sulphur source could be represented by the S-rich Martian regolith (Foley et al., 2003). Sulphides also occur in several different sizes and modal abundances in all nakhlite meteorites. In the meteorite samples studied sulphide grain sizes range from 10 μm to 250 μm (Fig. 4.2). The recently recovered nakhlite Caleta el Cobre 022 has unusually abundant and coarse grained pyrrhotite (up to 200 μm) (Gattacceca et al., 2018). These inter-meteorite differences in sulphide grain sizes are therefore further evidence to support the suggestion that sulphur-rich material was acquired at different points of lava extrusion on the Martian surface.

Nakhla and the two Yamato nakhlites contain dominantly magmatic sulphur isotope signatures (near zero $\Delta^{33}\text{S}$ and $\delta^{34}\text{S}$), indicating a lack of regolith incorporation. A ^{17}O excess of sulphate in Nakhla reportedly suggests it spent a significant period of time in contact with the Martian atmosphere (Farquhar et al., 2000). The simplest way of reconciling this atmospheric exposure with minimal regolith uptake is to place Nakhla at the top of a lava flow. Alternatively, it could have been present inside the carapace of a lava tube, where the main flow is in contact with the surface and easily acquires sulphide/sulphate material from the Martian regolith while the carapace of the lava tube is never in contact with the regolith but can be in contact with the atmosphere. This hypothesis could also explain the regolith uptake of MIL 090032, if it was part of the main lava tube. These two nakhlites have the same age (within uncertainty; Cohen et al., 2017), but they have different $\delta^{34}\text{S}$ (Nakhla = $-1.59 \pm 0.10 \%$, MIL 090032 = $+10.54 \pm 0.09 \%$). This lava emplacement scenario is supported by the quench-textured mesostasis of MIL 090032 and the other paired MIL nakhlites, indicating surface exposure (Hallis and Taylor, 2011), possibly as a break-out event at the front or side of the lava flow (Hammer, 2009). Further, skeletal mineral phases, glass, and thin hedenbergite pyroxene rims in the MIL nakhlites has been taken as evidence of the fastest cooling rate among all the nakhlites (6 $^{\circ}\text{C}/\text{h}$) (Hammer and Rutherford, 2005; Day et al.,

2006). Alternatively, if the MIL nakhlites and Nakhla are not from the same lava flow, mineralogical evidence suggests that after quenching the MIL nakhlite lava flow may have been blanketed with another flow that slowed down the cooling rate (Domeneghetti et al., 2013) - this flow may have been that containing Nakhla.

4.4.2.4 - $\Delta^{33}\text{S}$ of the nakhlite mantle source

Nakhla and the two Yamato meteorites have $\delta^{34}\text{S}$ close to zero, and the smallest fractionation of $\Delta^{33}\text{S}$. This signature is interpreted to have a magmatic origin, hence these meteorites represent the least isotopically disturbed of the nakhlites analysed here (from a sulphur isotope perspective), and by inference the most appropriate to constrain a possible $\Delta^{33}\text{S}$ for the nakhlite mantle source region. The average $\Delta^{33}\text{S}$ value obtained for Nakhla, Yamato 000749, and Yamato 000593 sulphide grains is $-0.1 \pm 0.09\text{‰}$. This is slightly more negative than the shergottite mantle source value ($\Delta^{33}\text{S}$ of 0.009‰) calculated by Franz et al. (2014), possibly due to the fact that different mantle reservoirs were involved in the genesis of the shergottites and the nakhlites (e.g., Harper et al., 1995; Lee and Halliday, 1997; Wadhwa, 2001; Jones et al., 2003; Foley et al., 2005).

It is unlikely that a $\Delta^{33}\text{S}$ of a mantle reservoir shifted by 0.1‰ from an initial value of zero. Instead, we attribute this $\Delta^{33}\text{S}$ value to contamination by mass-independent sulphur that would have originated in the Martian atmosphere (Farquhar et al., 2000). It is conceivable that such atmospheric sulphur (SO_2 , H_2S), after its deposition as oxidized sulphur on the Martian surface, could have affected the source of the nakhlite magmas by mobilization beneath the Martian crust due to geochemical cycling, therefore suggesting the presence of a shallow magma chamber for the generation of the nakhlites.

4.4.3 - Constraining the magmatic and chemical-physical processes in controlling Re-Os isotope systematics and HSE

Several different chemical-physical processes may have influenced the HSE-abundance Re-Os isotope systematics of the nakhlites. These processes can be distinguished essentially as: low-temperature disturbance(s), post-crystallization impact disturbance, and HSE partitioning under magmatic conditions. To

discriminate which of these processes may have affected each of our samples, and to what degree, we discuss each sequentially and begin by appraising those processes that could modify the HSE and Re-Os isotope chemistry of a magmatic sample after its crystallisation.

4.4.3.1 - Low-temperature and post-crystallization impact disturbance

Late-stage open-system effects on nakhlite HSE due to alteration on Mars' or Earth's surface have the potential to disturb nakhlite Re-Os isotope systematics and to mobilise and/or add HSE present in potentially susceptible phases. For example, the possibility of low-temperature alteration in deserts could result in the addition of Re (Peucker-Ehrenbrink and Jahn, 2001) (Fig. 4.3). However, there is limited variation of inter-element HSE ratios and we conclude that nakhlite HSE-abundance has not been significantly affected by low-temperature alteration on Earth or Mars after their magmatic crystallisation.

Impact disturbance as considered here refers to the process(es) through which materials of chondritic composition are transferred to Martian magmatic materials due to impacts/shock events after their crystallisation. Such processes are capable of enriching the sample toward chondrite-relative HSE abundances following magmatic crystallisation (e.g. as was observed by Riches et al. 2012). All studied nakhlites are characterised by highly fractionated HSE patterns relative to CI-chondrite (e.g., Pd/Os = 19.6 to 131.3), have relatively low total osmium abundances (< 0.08 ppb), and suprachondritic $^{187}\text{Os}/^{188}\text{Os}$ (0.18 to 0.45 ± 0.0010). These nakhlite HSE characteristics do not tend toward a potential chondritic contaminant and thereby preclude significant late-stage modification of the studied samples by chondritic materials on the Martian surface or during their impact liberation.

4.4.3.2 – Magmatic processes

All three nakhlites analysed in this work display similar HSE patterns. It is unlikely that these similarities in HSE patterns are the product of alteration on Earth or Mars, instead these primarily reflect magmatic fractionation during formation of the nakhlite parent magma(s) and lava crystallisation. These

nakhlite HSE characteristics indicate that the incorporation of small amounts of Martian regolith (as testified by S-isotope systematics) resulted in a generally negligible modification to the nakhlite HSE inventory, suggesting a low HSE abundance of the Martian regolith. Had significant contributions of regolith modified the overall HSE abundances of the studied nakhrites, we would anticipate variable HSE systematics among the nakhrites and a degree of correlation with sulphide S-isotope compositions. Such nakhrite HSE variability and a clear relationship to corresponding sulphide S-isotope systematics is lacking. However, Os-isotope compositions of nakhrites are variable and are decoupled from the overall nakhrite HSE-abundance systematics. The intra-sample variability in Re concentration and Os-isotopic composition testified by two Nakhla fractions (0.117 ppb, this work; 0.052, Brandon et al., 2000) supports perturbation of the Re-Os isotope systematics in these Martian magmas, but with little consequent effect to the abundances of Os, Ru, Ir, Pt, Pd, ± Au. Such a process requires interaction with a Martian regolith of variable Re content and low Os abundance, but with highly radiogenic $^{187}\text{Os}/^{188}\text{Os}$ (> 0.7 at total HSE abundances much less than 2 ppb and with 0.005 ppb Os in the ancient Martian regolith) such that a small proportion of assimilated material has perturbed the Os-isotopic signature of the nakhrite lava flows. Fractionation of HSE during partial melting of the mantle and during possible late-sulphide saturation in evolved magmas will change HSE inventories in different ways (Jones et al., 2003; Sun et al., 2003; Fonseca et al., 2007; Mallmann & O'Neill, 2007). In the following sub-paragraphs we explore these possible processes.

4.4.3.2.1 - Magmatic fractionation of HSE from the nakhrite and shergottite mantle source

Regression approaches using MgO content have been used to infer Mars mantle composition and give similar abundances of Re, Os, Ir, and Ru for the mantle of Earth and Mars (e.g., Warren et al., 1999; Tait and Day, 2018). In addition, Martian meteorites are characterised by Re abundances that are high, somewhat close to the terrestrial basalts, and define a broad anti-correlation of HSE abundances with the degree of magmatic evolution (e.g., Jones et al., 2003). Several prior studies have appraised Martian magmatic process through the HSE

abundances of Martian meteorites (e.g. Warren et al., 1999; Jones et al., 2003; Riches et al., 2011; Brandon et al., 2012; Dale et al., 2012; Filiberto et al., 2012; Tait et al., 2015; Tait and Day, 2018). In general, what the HSE datasets of these previous studies show are CI-normalised HSE patterns that vary from absolutely flat to increasingly fractionated (elevated Pd/Os) with decreasing total HSE abundance.

Nakhla, Lafayette, and MIL 090032 all show broadly similar HSE patterns (Fig. 4.3a). Though previous data showed that Nakhla and Chassigny are similar in their HSE patterns (Jones et al., 2003), here isotope dilution approaches show that Nakhla has more Pd and Re relative to Chassigny and that Lafayette and MIL 090032 are very similar to this pattern, rather than the HSE pattern of Chassigny. These substantial differences in the HSE fractionation evident among different classes of Martian meteorite and thus their magmas, extended also to shergottite groups. Primitive shergottites ($Mg/Mg+Fe > 0.7$) have high Os/Pt, Ir/Pd and Ru/Pt (Brandon et al., 2012; Tait and Day, 2018). A broadly similar pattern was observed for the high MgO shergottites ($Mg/Mg+Fe = 0.5-0.7$), but with higher Re/Pt and Re/Pd than the primitive shergottites. Nakhrites analysed here diverge from the patterns of the primitive and high MgO shergottites in terms of relative abundances, but they approach the HSE patterns of the intermediate/low MgO shergottites having high Re/Ir, Pt/Ir, and Pd/Ru (Fig. 4.5). These differences could reflect different initial magmatic conditions between the nakhlite and shergottite parental melt(s), as for example, melting temperature, fO_2 , and parental melt composition (including sulphur concentration and its relation to the point of sulphide saturation).

Magmatic depletion events would be evidenced by low Re/Os and selective HSE depletion of incompatible (Re, Pt, Pd) versus compatible (Os, Ir, Ru) elements (Barnes et al., 1985). The HSE patterns of the nakhlite samples show depletion of Re, Pt, and Pd in relation to the other HSE and do not conform with magma depletion hypothesis. MIL 090032 is definitely not affected by magmatic depletion events due to the depletion of compatible (Os, Ir, Ru) versus incompatible elements (Re, Pt, Pd), linked with a Re/Os of 1.8.

We address the possible late-stage sulphide saturation as well as potential involvement of residual alloys during the production of magmas parental to nakhlite lavas below.

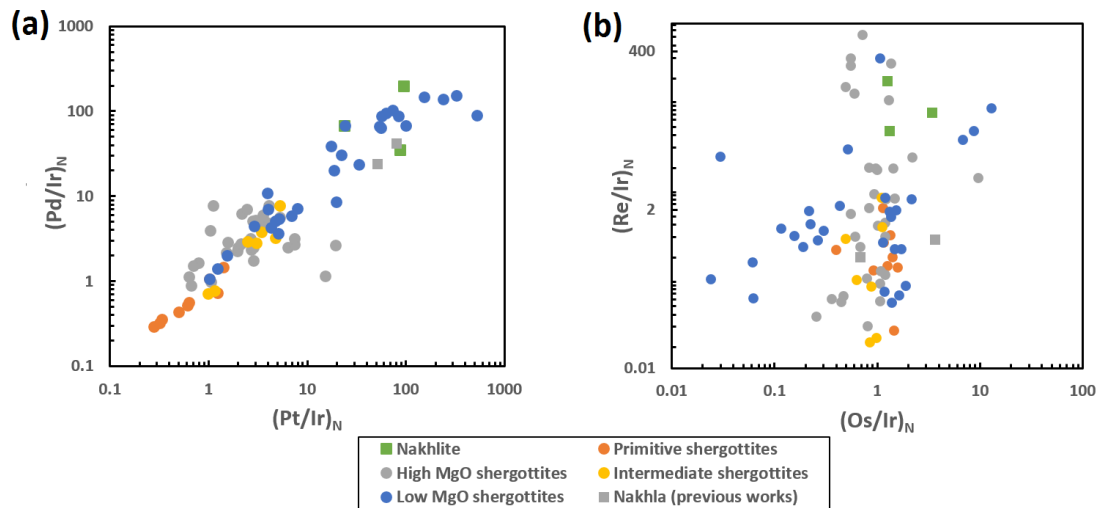


Fig. 4.5 - CI chondrite normalized HSE abundance comparison between nakhlites, primitive shergottites ($Mg/Mg+Fe = > 0.7$), high MgO shergottites ($Mg/Mg+Fe = 0.5-0.7$), shergottites with intermediate MgO ($Mg/Mg+Fe = 0.4-0.5$), and low MgO shergottites ($Mg/Mg+Fe < 0.4$). (a) $(Pt/Ir)_N$ vs. $(Pd/Ir)_N$; (b) $(Os/Ir)_N$ vs. $(Re/Ir)_N$. The nakhlites plot closest to the low MgO shergottites in (a), and within the scatter of these shergottites in (b). Highly siderophile element data for shergottites are from Jones et al. (2003), Riches et al. (2011), Brandon et al. (2012), Dale et al. (2012), and Tait and Day (2018).

4.4.3.2.2 - HSE fractionation due to late-stage sulphide saturation and residual alloys formation

Sulphides, silicate phases, and spinel can control the geochemical behaviour of the HSE during partial melting (Fonseca et al., 2007; Mallmann & O'Neill, 2007), with Os inclined to be partitioned into sulphide melts (Brenan, 2008). The solubility of Os and Ir has been constrained experimentally in sulphide melts, over a range of fO_2 ($-1.5 < QFM < +1.5$) and fS_2 (Iron-Wüstite (IW) ~ -1) at $T = 1300^\circ C$ (Fonseca et al., 2011). It is important to take into account that these experimental approaches can generally only replicate batch melting, and that a fractional melting scenario (\pm aggregation of those fractional melts) may be applicable to both ancient and recent Martian magmatic systems. Nevertheless, experimental approaches provide a useful framework through which we can infer key aspects of nakhlite petrogenesis. The outcome of these experiments has

shown that Os and Ir have low solubilities in silicate melts and that high fO_2 conditions can inhibit the solubility of Os and Ir in sulphide melts (Fonseca et al., 2011). Oxygen fugacity for nakhlites is higher than shergottites. For Nakhla, fO_2 is equal to the quartz-fayalite-magnetite (QFM) oxygen buffer (at an equilibration temperature of 810° C) while for Lafayette the fO_2 is equal to QFM +0.1 (at an equilibration temperature of 780° C; Szymanski et al., 2010). For MIL 03346 (paired with MIL 090032) the proportion of Fe^{3+} in augite was found to be in agreement with high-temperature equilibration near the QFM buffer (Dyar et al., 2005). Conversely, estimated fO_2 for the shergottites are low and varies from -1 to -4 QFM (e.g., Herd, 2003). These differences in fO_2 would limit the solubility of Os and Ir in nakhlite sulphide melts, due to their higher fO_2 than shergottites.

Residual alloys crystallised from parental melts and the formation of platinum group minerals throughout a magmatic column are able to control fractionation of Os, Ir, Ru, Rh, Pt, and Pd during magma genesis (Mungall and Brenan, 2014). In particular, Mungall and Brenan (2014) reported how, at low pressure, partial melting of Earth's mantle retains HSE in chondritic relative abundances (if correct as the starting proportions of these elements) until complete sulphide saturation, then evolving to very high Pt/Pd and low Pd/Ir - due to Pt and Ir alloy formation in the restite phase. Ruthenium, Os, and Ir are thought to be initially present in parts per million abundances in mantle sulphide melts, then, a decrease in fS_2 during partial melting leads to the exolution of Ru-Os-Ir alloys from a refractory residue in the mantle (Fonseca et al., 2012). In particular, a sulphide melt appears to be required for Os-rich alloy formation since Os is likely the element that triggers the exolution of the Ru-Os-Ir alloys (Fonseca et al., 2012).

As described above, the higher fO_2 in Nakhla, Lafayette, and MIL 090032 likely prevented the solubility of Os and Ir in possible late-stage sulphide melts, inducing formation of Pt- and Ir-alloys in the restite phase. Accordingly to Fonseca et al. (2011), the lower solubility of Os and Ir at high fO_2 would imply the existence of a melt saturated in sulphides (sulphide melt) for the generation of the nakhlite parent magmas. This process has been shown also in other works, as Amossé et al. (1990), Bezmen et al. (1994), and Fleet et al. (1996).

In contrast to nakhlite magmas, for which present data sets and constraints are relatively limited, it is well established that the parent magmas of the relatively well-studied shergottites were sulphide-undersaturated in their mantle sources (Wang and Becker, 2017). In particular, Pd/Pt in shergottites tend to reflect chondritic abundances, but this is not the case for Os-Ir-Ru, as indicated by suprachondritic Pd/Ir or Pt/Ir (Wang and Becker, 2017). The reason of this difference could be attributed to the formation of residual alloys of Os-Ir-Ru in the Martian mantle (similar to the Earth's mantle; e.g., Fonseca et al., 2012 and references therein).

4.4.4 - Implications for nakhlite mantle source and early Mars differentiation

Mantle heterogeneities have been proposed for Mars based on the trace element and ^{182}Hf - ^{182}W , ^{146}Sm - ^{142}Nd , ^{87}Rb - ^{87}Sr , and ^{187}Re - ^{187}Os isotope systematics of magmatic products represented by Martian meteorites (e.g., Harper et al., 1995; Lee and Halliday, 1997, 1995; Brandon et al., 2000, 2012; Wadhwa, 2001; Herd, 2003; Jones et al., 2003; Foley et al., 2005; Debaille et al., 2008, 2009; Herd et al., 2017; Lapen et al., 2017; Tait and Day, 2018; Day et al., 2018). In general, at least four mantle reservoirs have been previously argued to exist on Mars: two for the shergottites, one for the nakhlites/chassignites, and one for NWA 8159. These different mantle domains can be tapped by magmas and these magmas can mix producing different compositions as noticeable from the different groups of Martian meteorites.

Magma mixing phenomena have been argued to be responsible of the generation of the depleted and enriched shergottites (Borg et al., 1997; Wadhwa, 2001; Herd, 2003; Borg and Draper, 2003; Shearer et al., 2008). However, the clear isotopic gaps that are present for their lithophile elements (Ferdous et al., 2017) are difficult to reconcile with magma mixing, since this process would not result in large isotopic gaps. This is especially noticeable for the nakhlites since they do not present clear signs of disequilibrium textures in their mineral assemblages. Instead, we propose a single magma composition for the generation of the nakhlites (as also suggested by their trace element compositions; Udry and Day, 2018), whether after the Nakhla eruption

assimilation with an unknown enriched component affected the nakhlite source during 61 Myr, producing subsequently the Lafayette parent melt at 1321 ± 9 Ma (ages accordingly to Cohen et al., 2017).

To better investigate a crustal contamination possibility it was tested which type of end-member has been involved during mixing with the nakhlite source - crust or mantle derived. It were checked situations of mixing relationships via radiogenic isotope compositions versus the abundance or the reciprocal of osmium concentration as a first test of this hypothesis. To assess the level of crustal contamination, the correlation of Os with ^{143}Nd composition was then used, since that Nd is considered a robust marker, independent of terrestrial alteration (Brandon et al., 2012). It was first checked that these criteria are indicative of mixing relations, since that apparent mixing in isotope-isotope space can sometimes appear in datasets. It was then investigated possible mixing with respect to other major chemical elements and isotope systems. The reason for this was to establish whether or not mixing of a mantle source within the Martian crust or another mantle source occurred, and if this is the case which is the mixing end-member (i.e., the Martian crust or a mantle component). The $^{187}\text{Os}/^{188}\text{Os}$ versus $1/\text{Os}$ for Lafayette and Nakhla are reported in the **Appendix**, and suggests that some sort of mixing within two different isotopic end-members is a possibility.

Assimilation of crustal materials with markedly elevated $^{187}\text{Re}/^{188}\text{Os}$ could be a cause of the higher $^{187}\text{Re}/^{188}\text{Os}$ of Nakhla in respect to Lafayette. This enriched component possibly included ancient (primordial?) crustal materials, with consequent highly radiogenic Os isotopic compositions for which a very small fraction would significantly shift a magmatic Os isotopic signature but with potentially negligible effects on HSE abundances. On the other hand, this characteristic could also reflect phenomena of mantle metasomatism as recently argued for Mars magmatism (Day et al., 2018), or even inheritance from an interior reservoir that experienced variable earlier magmatic fractionation resulting in reservoirs with long-term high $^{187}\text{Re}/^{188}\text{Os}$ and/or complementary low $^{187}\text{Re}/^{188}\text{Os}$.

Mixing within mantle sources or enriched cumulates may have happened during early differentiation of Mars. By following this logic, the enriched crustal component of our hypothesis likely can be represented by a component

generated during the last stages of a Martian magma ocean (MMO). This possibility has been investigated for Nakhla and Lafayette by looking at their $^{187}\text{Os}/^{188}\text{Os}$ versus Nd and Sr isotope distributions. The γOs versus $\epsilon^{143}\text{Nd}$ constrain a possible end-member for the nakhlite source mixing. The calculated γOs and $\epsilon^{143}\text{Nd}$ values of the primitive Martian crust and the evolved Martian crust at 180 Ma from Brandon et al. (2000) and Norman (1999) were used (Fig. 4.6). The distribution of the nakhlites in respect to the primitive and evolved Martian crust is inconsistent with their magma sources being affected by assimilation of modern Martian crust. The γOs vs. $\epsilon^{143}\text{Nd}$ appear instead decoupled suggesting preferential/selective mixing of the nakhlite reservoir with an unknown enriched component that must have occurred early during Mars differentiation, possibly represented by assimilated ancient MMO cumulates. However, drawing conclusions from the initial γOs for Nakhla and Lafayette are currently thwarted by large uncertainties for these relatively ancient magmas with low Os abundances. Similarly, the correlation between $\epsilon^{143}\text{Nd}$ and γOs in shergottites suggested that the endmember sources were generated by mixing between residual melts and cumulates during the crystallization stages of a MMO (Debaille et al., 2008; Brandon et al., 2012).

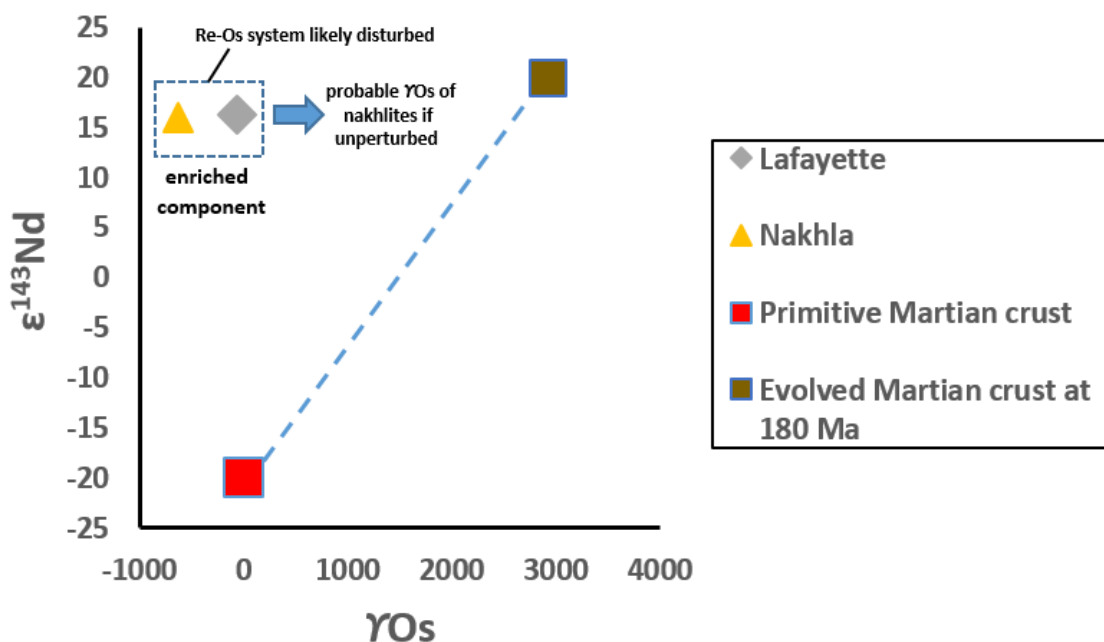


Fig. 4.6 - Initial γOs vs. $\epsilon^{143}\text{Nd}$ for nakhlites used to identify a possible end-member for the nakhlite source mixing. The primitive Martian crust and the evolved Martian crust at 180 Ma are plotted with values taken from Brandon et

al. (2000) and Norman (1999). The plotted samples follow a direction that diverge from the Martian crust evolution (here represented by the dashed line), thus implying that the mixing end-member is likely represented by a different enriched component (dashed box) rather than the evolved Martian crust. Alternatively, decoupling of the data could suggest that the γ Os is a sensitive tracer of strictly different process to that which $\epsilon^{143}\text{Nd}$ provides evidence - potentially recording involvement of early Martian crust whereas $\epsilon^{143}\text{Nd}$ may be more effective in probing the nature of nakhlite mantle reservoirs. Error bars are less than symbol size. As the calculated γ Os in Lafayette and Nakhla is negative and below the Solar System initial of Smoliar et al. (1996) disturbance of the Re-Os isotope system in these samples has taken place (linked to crustal contamination). For these reasons, the strongly negative calculated γ Os should be considered as an extreme minimum at ~1.4 Ga. Unperturbed samples, not impacted by crustal assimilation, would likely have been derived from internal reservoirs characterized by higher γ Os at that time (blue arrow).

Mixing within MMO cumulates and evolved liquids may explain our observed Re-Os isotope systematics as seen in Nakhla and Lafayette, as well as previously reported Rb and Sr isotope systematics. In fact, sulphides crystallisation from the last stage of MMO's melts could result in locally fractionated $^{187}\text{Re}/^{188}\text{Os}$ within the Martian mantle thereby presenting the possibility to trace different mantle reservoirs and to discern this from assimilation of primordial crust characterized by long-term elevated $^{187}\text{Re}/^{188}\text{Os}$. In addition, the first MMO cumulates that crystallize would be extremely depleted in REE, Rb and Sr, with the last more evolved liquids characterised by a $\epsilon^{142}\text{Nd}$ of +0.64 (Debaille et al., 2009).

Magma ocean overturn could explain the early formation and isolation of these different local heterogeneities in the Martian mantle (Debaille et al., 2009; Bouvier et al., 2018). This process likely happens as a result of instabilities due to the density stratification that occurs during the crystallisation of magma oceans on terrestrial planets (Elkins-Tanton et al., 2003).

4.5 – Conclusions

Sulphur isotopic compositions were determined for sulphides in five nakhlites to ascertain the degree to which they have been affected by assimilation of the Martian regolith. Nakhla, Yamato 000749, and Yamato 000593 are the meteorites that have most faithfully retained a magmatic signature, and which are therefore the most reliable for using osmium isotopes and HSEs to reveal the nature of nakhlite petrogenesis. For the first time, Re-Os isotope systematics and HSE abundances have been investigated for two different nakhlites, to constrain the degree to which they have been affected by crustal assimilation and the ability of Martian meteorite HSE to testify to Mars' interior composition. The following results have been obtained:

(1) The Lafayette and MIL 090032 lava flows acquired S-rich Martian regolith material that carry information about Martian atmospheric and hydrological processes. Results show that UV-photochemistry and hydrothermal processes are the main cause of $\Delta^{33}\text{S}$ and $\delta^{34}\text{S}$ fractionation. This result may have implications for the nature of the Martian atmosphere and hydrothermal activity prior to nakhlite eruption.

(2) Nakhla, Yamato 000593, and Yamato 000749 retained a magmatic signature in their sulphides, and were unaffected by assimilation of Martian regolith. Using these meteorites we estimate the $\Delta^{33}\text{S}$ of the nakhlite source to be -0.1‰ .

(3) Nakhlite HSE patterns are in agreement with the presence of a sulphide melt involved in nakhlite petrogenesis. Ruthenium-Os-Ir alloys likely formed in this sulphide-saturated melt and controlled the abundances of Ru, Os, Ir in the final lava products.

(4) Our Re-Os isotope data for nakhlites hint at perturbation and potential decoupling of nakhlite $^{187}\text{Os}/^{188}\text{Os}$ isotope systematics from other isotopic systems as a result of small degrees of assimilation of an S-rich regolith with low total HSE contents but highly radiogenic $^{187}\text{Os}/^{188}\text{Os}$ (> 0.7 at total HSE abundances much less than 2 ppb and with 0.005 ppb Os in the ancient Martian regolith).

(5) Nakhlites formed from a primary magma that we consider to have been generated from a well-mixed Martian mantle that subsequently (at some point

after the Nakhla emplacement) assimilated an enriched component during ascent toward the surface, and where this enriched mantle material was potentially represented by a late-stage crystallization cumulate from a Martian magma ocean.

Chapter 5 – Shergottite mantle source and volatile abundance

The following chapter is taken from the paper titled “Amphibole and apatite composition in the Tissint and Zagami shergottites: constraints on chlorine abundance in the Martian interior”. This paper has been submitted in the peer-review journal *Meteoritics & Planetary Science*.

This paper has been used as [Chapter 5](#) of the present thesis because it is about determining the chlorine abundance of the Martian mantle, which is useful for revealing possible heterogeneity of volatile elements in the Martian mantle, that is one of the goal of this research.

The Author of the thesis is the First Author of the paper, having conducted the vast majority of the work, data acquisition, data processing, data interpretation, and writing. Other co-authors of the paper include: Lydia J. Hallis, who helped during sample preparation, SEM analysis, and in revising the manuscript, and Martin R. Lee, who helped during TEM analysis and in revising the manuscript.

5.1 – Introduction

Martian volatiles have been carried from the interior to the surface of Mars through outgassing of erupted magmas (Greenwood and Blake, 2006; Treguier et al., 2008). The abundance of volatiles (including H₂O, Cl, F) in these volcanic products may be used to determine their abundance in the mantle source regions (Eichelberger, 1995), especially if early crystallized volatile-rich phases are analysed.

Amphibole and apatite are the major volatile-bearing magmatic minerals in Martian meteorites, and as such can be used to calculate the volatile content of the parental melt of these igneous rocks. These values can subsequently be used to calculate the volatile content of the meteorite source region, assuming no assimilation occurred after partial melting. For example, the chemical composition of amphibole in the Shergotty, Governador Valadares, Chassigny,

and Lewis Cliff 88516 meteorites was used to calculate H₂O content of 1.4 wt. % for the Martian interior (McSween and Harvey, 1993). Conversely, calculations based on apatite chemistry indicate a much lower value of ~100 ppm H₂O for the Martian mantle (McCubbin et al., 2012; Gross et al., 2013). Furthermore, recently obtained H₂O, Cl, and F ratios of amphibole and apatite suggest a Martian interior volatile content similar to terrestrial mid oceanic ridge basalts (MORB), with H₂O/Cl and H₂O/F ratios of 0.4-18, and a H₂O content of 56 ± 71 ppm (Filiberto et al., 2016).

Amphibole in Martian meteorites occurs within olivine and pyroxene-hosted melt inclusions, and is one of the first minerals to form during the sequence of crystallization (e.g., Williams et al., 2013). Amphibole differs in composition between different groups of Martian meteorites. In the nakhlites it is Cl-rich and interpreted to be a product of interaction between the nakhlite parental melt(s) and a Cl-rich exogenous fluid within the planet's sub-surface (McCubbin et al., 2013). The comparatively high H₂O and low Cl contents of amphibole within the chassignites (a group of meteorites interpreted to be from the same site on Mars as the nakhlites, but lower in the stratigraphic sequence; McSween, 2015) is interpreted to be due to the timing of infiltration of Cl-rich fluids. Specifically, the fluids entered after the crystallisation of olivine, which is host to the amphibole-bearing melt inclusions, but before the crystallisation of chassignite mesostasis and the nakhlite parental melts (McCubbin et al., 2013).

In contrast to amphibole, apatite in Martian meteorites is commonly a later crystallising phase and occurs within the mesostasis. However, it has been reported from within melt inclusions in the nakhlites (Hallis, 2013). The chemical composition of Martian meteorite apatite is variable, although often Cl-rich, thus suggesting that the parental melts were enriched in Cl compared to F and H₂O (McCubbin et al., 2013; Howard et al., 2015).

In an effort to better understand the volatile content of the interior of Mars, we determined the chemical compositions of amphibole and apatite in the depleted shergottite Tissint, and amphibole in the enriched shergottite Zagami. We used previously published Cl partition coefficients (Filiberto and Treiman, 2009) to determine the Cl abundance of parental melts for both shergottites, and compared our results with the proposed Cl abundance for the nakhlite and chassignite parental melts (Filiberto and Treiman, 2009; Filiberto et al., 2016).

5.2 – Materials and methods

5.2.1 – Tissint

Tissint is an observed fall (July 18th 2011, Morocco; Irving et al., 2012) and, consequently, was recovered with minimal terrestrial weathering (Chennaoui Aoudjehane et al., 2012). Tissint is one of the oldest known shergottites with a crystallization age of 574 ± 20 Ma, based on Rb-Sr and Sm-Nd isotopic systematics (Brennecka et al., 2014), and has a cosmic ray exposure (CRE) of 1.05 Ma (Brennecka et al., 2014). Tissint is a depleted olivine-phyric shergottite with large olivine crystals (up to 2.5 mm), commonly containing melt inclusions (Balta et al., 2015). Low-Ca pyroxene phenocrysts are also present, evolving from pigeonite to augite, with some low-Ca, high-Fe grain rims. Tissint is highly shocked, and former plagioclase phenocrysts have been completely converted to maskelynite (Chennaoui Aoudjehane et al., 2012). In addition, Tissint contains pockets of shock melt glass, with evidence of pressures up to 25 GPa (Baziotis et al., 2013). Merrillite phosphate is present within the fine-grained mesostasis (<0.25 mm diameter), which is mostly composed of the same minerals as the phenocrysts (Balta et al., 2015). Accessory minerals include ilmenite, ulvospinel, magnetite, chromite, and pyrrhotite. Its mineralogy is reported to resemble that of the Martian mantle (Balta et al., 2015) and its melt generation depth was calculated to be close to the Martian upper mantle (40-80 km depth; Basu Sarbadhikari et al., 2016).

Four epoxy-mounted polished thick slices of Tissint were investigated (P18492, P18494, P18495, and P18497). These slices were obtained on loan from the Natural History Museum of London, and had been cut from Tissint sample BM2012,M3. All the thick sections have porphyritic textures, with an average modal mineralogy of 55% pyroxene, 25% olivine, 15% maskelynite, and 5% of minor phases (merrillite, chromite, pyrrhotite, oxides, apatite, amphibole) and mesostasis. Both olivine and pyroxene grains contain melt inclusions. The pigeonite cores of pyroxene crystals contain the amphibole and apatite bearing melt inclusions.

5.2.2 – Zagami

The Zagami meteorite is a shergottite that fell on the 3rd October 1962 near Zagami Rock in Nigeria (Graham et al., 1985). It is a heterogeneous sample, characterized by different lithologies. The standard lithology is called Normal Zagami (NZ) and is an enriched basaltic shergottite similar to Shergotty (McCoy and Lofgren, 1999). The modal mineralogy of the NZ lithology includes: 76% pyroxene, 19% maskelynite, 3% oxides, and 2% mesostasis (Stolper and McSween, 1979). A Dark-Mottled Lithology is present (DML; McCoy et al., 1995) and a Fe-rich lithology (DN) (Agerkvist and Vistisen, 1993); they differ from the NZ lithology by the minor amount of pyroxene present and abundant phosphates. These differing lithologies seem to be the product of multiple incorporations or assimilations of irradiated Martian regolith (Hidaka et al., 2009), as suggested by variations in age and initial isotopic composition (Nyquist et al., 2010). The age of Zagami NZ from Rb-Sr and Sm-Nd isotope systematics is on average ~170 Ma (Nyquist, 1995), which is much younger than Tissint. A slightly older age of the NZ lithology from Lu-Hf systematics (~190 Ma) could record a resetting event by acid solution of geochronometers within phosphate phases (Bouvier et al., 2005).

A single indium-mounted polished chip of Zagami was prepared at the University of Glasgow from a small fragment, obtained from the Scottish Universities Environmental Research Centre (SUERC), which itself had been cut from Zagami sample BM.1993,M10 (loaned by the Natural History Museum, London). This Zagami sample is from the NZ lithology and has a porphyritic texture, with an average modal mineralogy of 75% pyroxene, 20% maskelynite, 3% oxides, 1% accessory phases (apatite, amphibole, merrillite, pyrrhotite, oxides), and 1% mesostasis. Amphibole grains are always located in pyroxene-hosted melt inclusions.

5.2.3 – SEM imaging and X-ray microanalysis

Major element chemical data and X-ray elemental maps were collected at the Imaging Spectroscopy and Analysis Centre of the University of Glasgow using a Zeiss-Sigma variable-pressure field emission-gun scanning electron microscope (VP-FEG-SEM), equipped with backscattered electron (BSE) and energy-dispersive X-ray spectroscopy (EDS) detectors. AZTEC and Oxford Instruments INCA

software were used for data processing. Operating conditions (in spot mode) included: a working distance of 8.5 mm, beam current of 2.15 nA, and accelerating voltage of 20 kV. Acquired EDS spectra for amphibole and apatite were calibrated using the following standards: wollastonite (Si, Ca), jadeite (Na, Al), periclase (Mg), orthoclase (K), rutile (Ti), chromite (Cr), rhodonite (Mn), hematite (Fe), apatite (P), tugtupite (Cl), pyrite (P), fluorite (F), and elemental nickel (Ni). EDS detection limits were 0.1 wt.%.

5.2.4 – FIB-section preparation and TEM analysis

Amphibole areas of interest were lifted out using the focused ion beam (FIB) technique for imaging and analysis by Transmission Electron Microscopy (TEM) at the University of Glasgow. These areas were selected based on their size (the largest amphibole grains were selected), the accuracy of EDS stoichiometric data, and comparisons with previously reported amphibole chemistry in Tissint (Williams et al., 2014) and Zagami (Treiman, 1985). One area containing apatite and one amphibole grain were selected from Tissint (Tiss A and Tiss B, respectively), and two amphibole grains were selected from Zagami (Zag A and Zag B). No apatite was observed within our Zagami sample. FIB-sections of these grains and the surrounding melt-inclusion mineralogy were made using the FEI Nanolab dual beam FIB instrument following the procedure of Lee et al. (2003). FIB-sections were thinned to 100 nm thickness. A FEI T20 TEM operated at 200kV was used to acquire high-resolution images along with selected area electron diffraction (SAED) patterns of all phases within each FIB-section. Scanning transmission electron microscope (STEM) images and EDS analyses of these samples were then obtained using a JEOL Atomic Resolution Microscope (ARM) 200cF operated at 200 keV/~180 pA. The ARM is equipped with a Bruker 60 mm² SDD-EDX spectrometer for quantitative EDS, and the spectra were quantified using Bruker software, following the Cliff-Lorimer procedure.

5.3 – Results

In Tissint, amphibole and apatite grains were located within melt inclusions hosted in the cores of pigeonite phenocrysts (Fig. 5.1a,b,c). In Zagami, amphibole grains occur in melt inclusions in the cores of pyroxene phenocrysts (Fig. 5.1b,e,f). Most amphibole and apatite grains are subhedral. Amphibole grains range in size from <2 μm to ~4 μm in Tissint and from <5 μm to ~10 μm in Zagami. Tissint apatite grains are ~2 μm in size (Fig. 5.2). Mineral stoichiometry for amphibole analyses was calculated on the basis of 15 cations (Table 5.1) and following the methodology of McCubbin et al. (2013). Results show that Zagami and Tissint amphibole is kaersutitic, with Zagami amphibole containing more Ti and Na, and less K (Table 5.1). Chlorine content was below detection for the majority of the Zagami amphibole analyses, although Zag B did show a Cl content of 0.23 wt %. Similarly, Cl was only detected in one area of Tissint (Tiss D), showing a slightly higher Cl content of 0.81 wt %.

The negative values calculated for amphibole stoichiometry in Table 5.1 are due to the small size of the amphibole grains, especially in Tissint. As a consequence, material surrounding the amphibole grains was sometimes included in the analyses, resulting in cation/anion ratios that were too high. Only Zag A, which is the largest amphibole grain analysed (~10 μm), has a stoichiometrically accurate amphibole formula. The overlapping phases are not consistent between analyses, with some having high Fe and Mg contents (possibly an amphibole and pyroxene mixture), and others high Al and Si contents (amphibole and glass or maskelynite mixture). Changing the stoichiometric calculations to be based on 13 anions does not resolve the problem and negative cation values are still present for all analyses excepting Zag A. Thus, TEM-EDS analyses were performed to get a better picture of amphibole and apatite chemistry.

TEM-EDS data for amphibole and apatite are reported in Table 5.2. The Zag A amphibole was found in association with pyroxene, spinel, Ti-magnetite, and maskelynite (see Appendix), and has Mg, Al, Si, and Ti proportions similar to kaersutite, magnesiohornblende, and/or ferro-hedenite. The Cl content of Zagami amphibole was below the TEM-EDS detection limits, in agreement with previous reports (Treiman, 1985). Calcium, Ti, and Fe in Tissint amphibole (within both Tiss A and Tiss B) are consistent with a kaersutite-

magnesiohornblende composition, with a Cl content up to 0.4 at. %. Amphibole grains in Tissint are smaller and rarer than in Zagami (Fig. 5.2, 5.3), and they have a Cl content often <0.2 wt.% and in one case of 0.81 wt.%. Tiss A apatite has a Cl content of ~2 at. % (Table 5.2), and was found in the FIB-section in association with high-Al pyroxene and maskelynite (see Appendix).

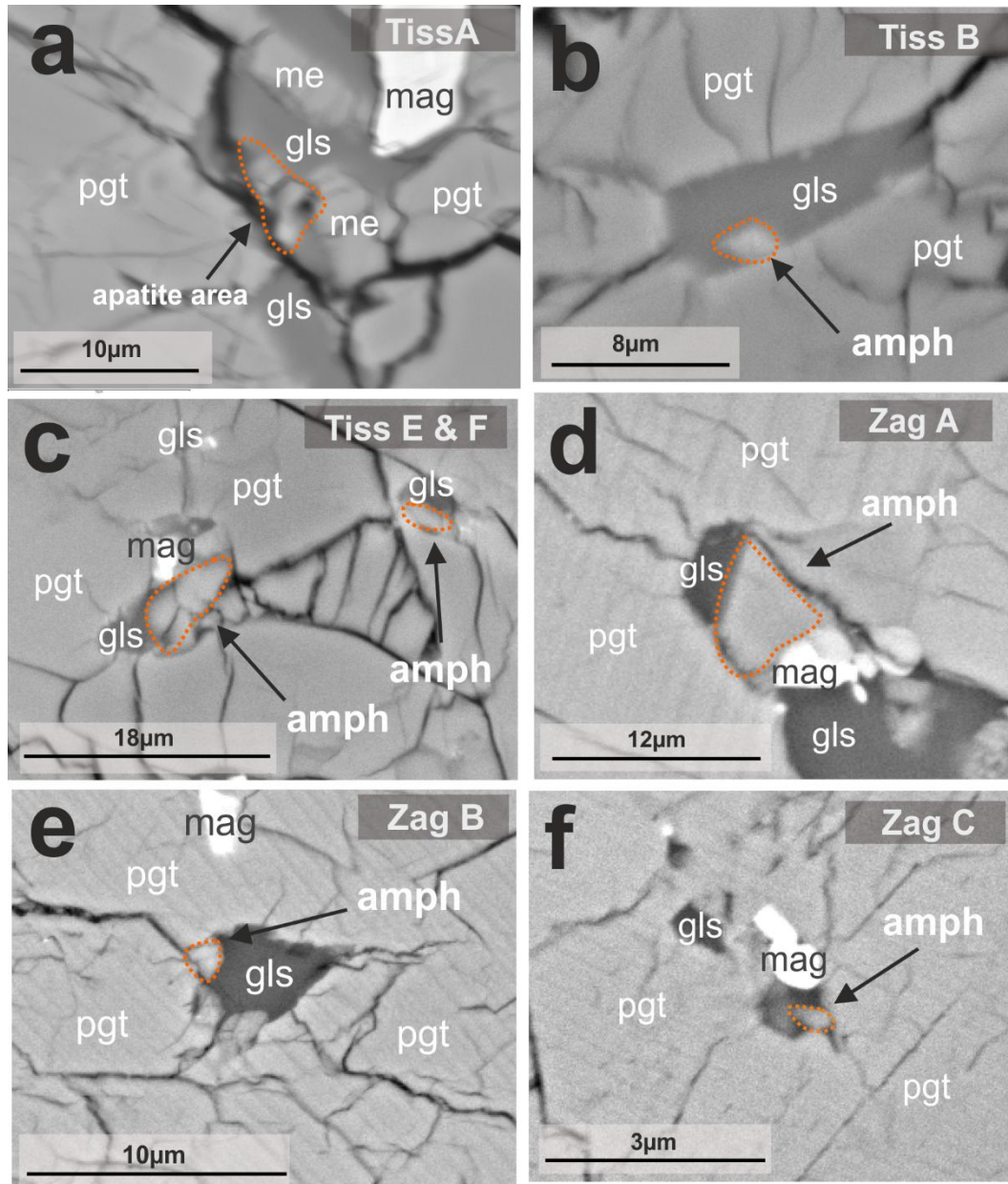


Fig. 5.1 - Backscattered electron images showing the location of amphiboles (located in the direction of the black arrow and highlighted in orange) and apatite analysed in Tissint and Zagami. a) The area in Tissint in which we detected apatite in a pigeonite-hosted melt inclusion, in proximity to a merrillite; b) and c) amphiboles in Tissint in pigeonite-hosted melt inclusions;

d), e), and f) a series of amphiboles in Zagami pyroxene-hosted melt inclusions - note they are larger than the Tissint amphiboles. FIB-sections for TEM analyses were cut from a) and d). Abbreviations: Amph, amphibole; pgt, pigeonite; mag, magnetite; me, merrillite; gls, glass.

Table 5.1 - Chemistry for all the amphiboles analysed in this work in Tissint and Zagami, acquired using SEM-EDS. Structure formula has been calculated according to McCubbin et al. (2013) and is based on 15 cations per formula.

Oxide	Tiss B	Tiss C	Tiss D	Tiss E	Tiss F	Tiss amph ¹	Zag A	Zag B	Zag C	Zag amph ²
SiO ₂	51.05	53.32	52.94	48.84	55.29	38.22	47.96	56.24	49.08	35.15
TiO ₂	d.l.	d.l.	d.l.	d.l.	d.l.	7.64	2.95	0.58	1.55	8.94
Al ₂ O ₃	17.70	4.28	1.58	5.49	10.32	16.07	8.53	9.15	2.36	15.13
FeO	14.20	25.31	16.70	21.83	16.85	14.28	14.60	14.53	24.31	16.18
MnO	d.l.	d.l.	d.l.	d.l.	d.l.	0.24	0.39	0.39	0.71	0.29
MgO	5.98	13.90	16.90	15.35	7.93	5.21	9.95	7.44	11.94	6.40
CaO	6.82	5.01	10.15	4.88	3.61	9.29	19.39	9.45	8.97	11.48
Na ₂ O	3.13	0.69	0.64	0.41	2.08	2.87	0.59	1.86	0.37	2.38
K ₂ O	d.l.	d.l.	d.l.	0.21	1.03	0.79	d.l.	0.82	0.19	0.20
Cr ₂ O ₃	d.l.	d.l.	d.l.	d.l.	d.l.	0.19	0.33	0.10	0.37	0.37
P ₂ O ₅	2.58	d.l.	d.l.	1.43	2.59	0.94	d.l.	2.11	0.18	d.l.
Cl	d.l.	d.l.	0.81	d.l.	d.l.	d.l.	d.l.	0.23	d.l.	d.l.
-O ≡ Cl	0.00	0.01	0.18	0.00	0.00	0.00	0.00	0.05	0.00	0.00
Total	101.54	102.55	99.58	98.45	99.72	95.76	104.79	102.85	100.04	96.52
Element										
Si	7.657	7.572	7.575	7.205	8.529	6.180	6.622	8.333	7.242	5.531
^{IV} Al	0.343	0.428	0.425	0.795	-0.529	1.820	1.378	-0.333	0.758	2.469
∑ T-site	8	8	8	8	8	8	8	8	8	8
^{VI} Al	2.786	0.289	-0.159	0.160	2.406	1.242	0.010	1.931	-0.348	0.337
Ti	0.000	0.000	0.000	0.000	0.000	0.929	0.306	0.065	0.172	1.058
Mg	1.337	2.943	3.605	3.376	1.824	1.256	2.048	1.643	2.626	1.501
Mn	0.000	0.000	0.000	0.000	0.000	0.033	0.046	0.049	0.089	0.039
Fe ²⁺	4.242	1.820	1.597	2.215	4.531	2.954	0.785	4.818	2.207	1.757
Fe ³⁺	-3.364	-0.051	0.401	0.479	-3.760	-1.413	0.901	-3.018	0.793	0.307
Ca	0.000	0.000	-0.444	-1.229	0.000	0	0.868	-0.500	-0.582	0
∑ M1-3 sites	5	5	5	5	5	5	5	5	5	5
Ca	1.096	0.762	2.000	2.000	0.597	1.609	2.000	2.000	2.000	1.936
Fe ²⁺	0.904	1.238	0.000	0.000	1.403	0.391	0.000	0.000	0.000	0.064
∑ M4 site	2	2	2	2	2	2	2	2	2	2
∑ M1-4 sites	7	7	7	7	7	7	7	7	7	7
Na	0.910	0.190	0.178	0.117	0.622	0.900	0.158	0.534	0.106	0.726
K	0.011	0.000	0.005	0.040	0.203	0.163	0.004	0.155	0.036	0.040
∑ A-site	0.922	0.190	0.183	0.157	0.825	1.063	0.161	0.689	0.142	0.766
Cl	0.005	0.007	0.196	0.003	0.005	0.005	0.000	0.058	0.003	0.000
F	0.000	0.000	0.000	0.000	0.000	0.153	0.000	0.000	0.000	0.040
OH	1.995	1.993	1.804	1.997	1.995	1.841	2.000	1.942	1.997	1.960
∑ O(3)-site	2	2	2	2	2	2	2	2	2	2
Fe ³⁺ /∑Fe	-1.889	-0.017	0.201	0.178	-1.730	-0.732	0.534	-1.676	0.264	0.144

¹Williams et al., 2014

²Treiman, 1985

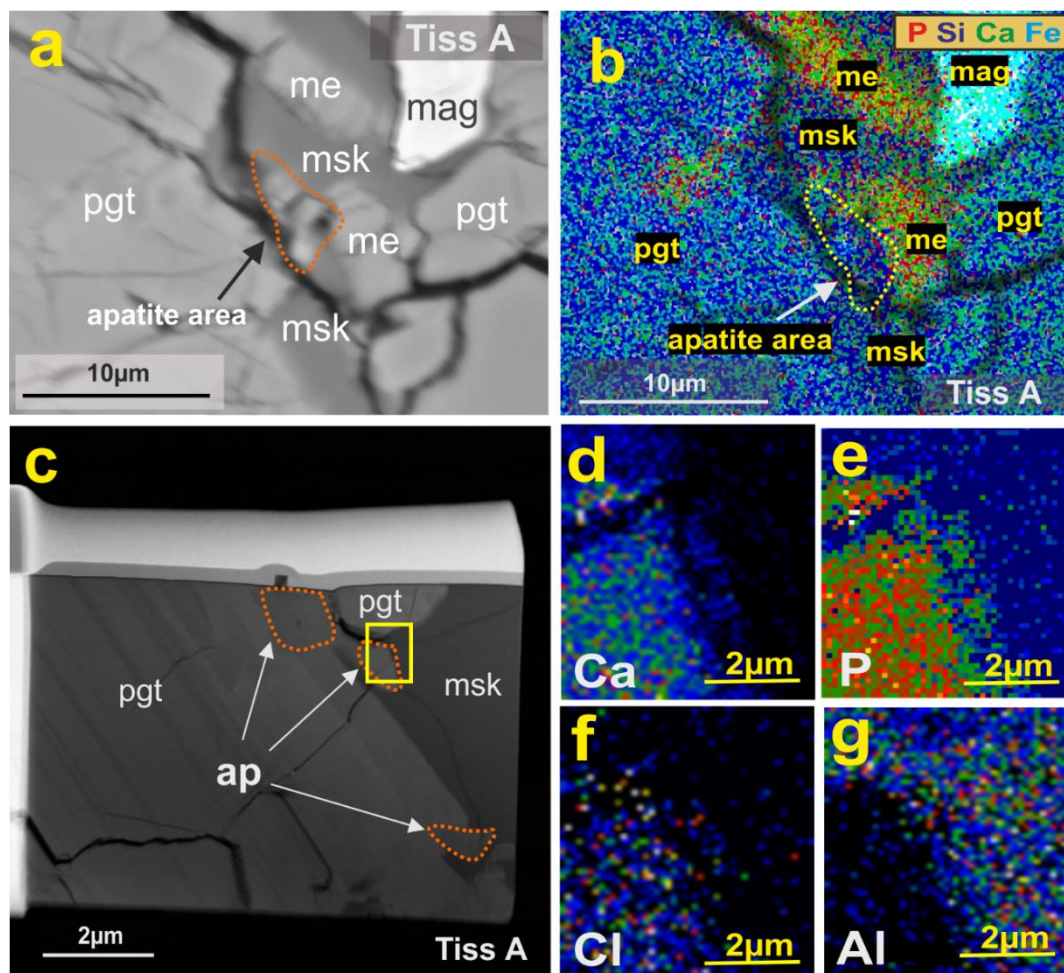


Fig. 5.2 - Tissint apatite in melt inclusion Tiss A. (a) Backscattered electron image of the pigeonite-hosted (pgt) melt inclusion, containing apatite, merrillite (me), maskelynite (msk) and magnetite (mag); (b) P, Si, Ca, and Fe elemental map of the melt inclusion in (a), highlighting merrillite (green areas), magnetite (in cyan), and maskelynite; (c) FIB-section extracted from Tiss A melt inclusion, white arrows indicate the presence of apatite grains; (d, e, f, g) Ca, P, Cl, and Al elemental maps of the area highlighted in yellow in (c). Colours blue to red indicate increasing abundance. Abbreviations: Amph, amphibole; ap, apatite; pgt, pigeonite; mag, magnetite; me, merrillite; msk, maskelynite.

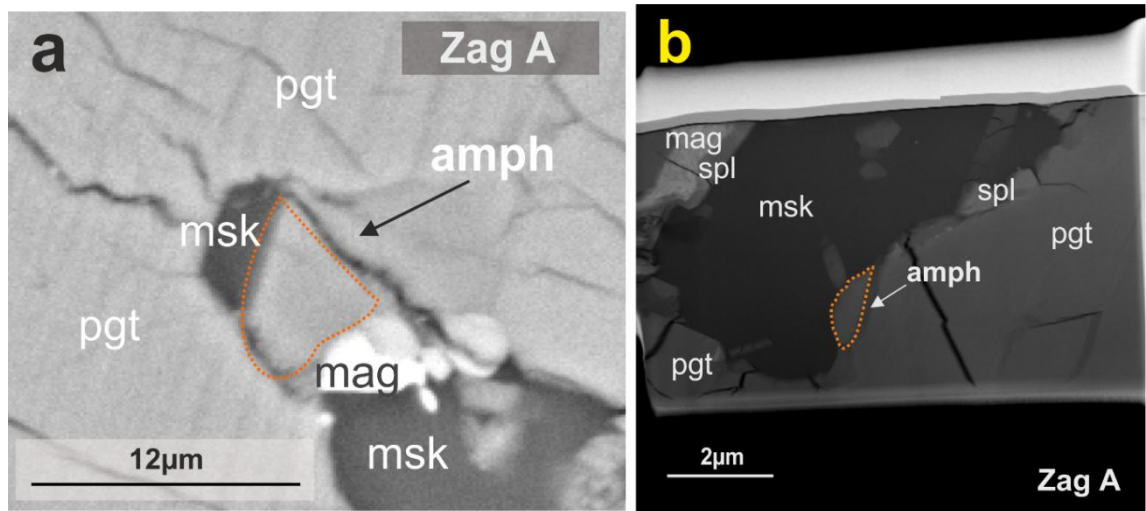


Fig. 5.3 - Distribution of the amphibole phase Zagami melt inclusion Zag A. (a) Backscattered electron image of the amphibole-bearing melt-inclusion; (b) FIB-section area of Zag A. Abbreviations: Amph, amphibole; pgt, pigeonite; mag, magnetite; spl, spinel; msk, maskelynite.

Table 5.2 - Chemical composition (at %) of apatite and amphibole in FIB-sections extracted from Tiss A, Tiss B, and Zag A, acquired via TEM-EDS. All totals are 100%. See **Appendix** for the exact location in the FIB-section of each analysis.

	TissA3	TissA5	TissA6	TissB7	TissB7a	ZagA4
Atomic %	Apatite	Apatite	Apatite	Amph	Amph	Amph
O	50.6	46.2	53.8	56.9	55.5	56.9
Na	—	—	—	—	1.4	0.4
Mg	1.6	—	—	2.3	2.2	5.0
Al	2.1	0.2	—	15.1	14.6	4.6
Si	5.1	0.4	1.1	14.1	14.8	20.7
Cl	1.9	2.6	2.0	—	0.4	—
K	0.2	—	—	1.0	0.7	—
Ca	22.2	31.4	27.5	4.5	4.4	3.5
Ti	—	—	—	0.6	0.7	0.7
Fe	2.1	—	—	5.6	5.6	8.0
P	14.0	19.1	15.7	—	—	—
Mn	—	—	—	—	—	0.4
H	—	—	—	—	—	—

5.4 – Discussion

5.4.1 – Amphibole and apatite occurrence in Martian meteorites

Tissint and Zagami amphiboles occur mainly within early crystallising pyroxene cores, suggesting that their Cl content will be representative of the meteorite parental melt. Kaersutitic amphiboles in Tissint have previously been reported in pigeonite melt inclusions (Williams et al., 2014), but no other depleted shergottite has been reported to contain amphibole. Kaersutitic amphiboles with low halogen contents were previously detected in both Zagami and Shergotty (both enriched shergottites) within pigeonite-hosted melt inclusions (Treiman, 1985). The H₂O-rich compositions of amphibole in these two meteorites (1.88-1.95 wt.% H₂O) indicates that the enriched shergottite parental melt was relatively hydrous (Treiman, 1985).

In addition to the shergottite meteorites, some chassignites and nakhlites contain amphibole. The chassignite Northwest Africa (NWA) 2737 contains kaersutitic amphibole, although this is found within olivine-hosted melt inclusions rather than pyroxene-hosted melt inclusions. NWA 2737 amphibole is H₂O-rich (0.15 wt.%), and is reported to have lost a further ~0.6 wt.% H₂O due to shock (Giesting et al., 2015). Amphibole within the Miller Range (MIL) nakhlites is also olivine-hosted, but more Cl-rich than the chassignite or shergottite amphiboles, with up to ~5 wt.% Cl (McCubbin et al., 2009; Hallis, 2013). The Cl-rich nature of these amphiboles, along with the variation in Cl content within nakhlite apatite grains, indicate the incorporation of a Cl-rich fluid into the nakhlite parental melts (McCubbin et al., 2013).

Apatite composition in Martian meteorites estimated by differences of hydroxyl mole fractions show an enrichment in OH and Cl relative to F in the shergottite apatites, whereas the nakhlite and chassignite apatites are comparatively Cl- and F-rich (Patino Douce and Roden, 2006; McCubbin et al., 2012); these compositions are in agreement with our detection of 1.9-2.6 at. % Cl in Tissint apatite (Table 5.2). The only other depleted shergottite reported to contain apatite is Queen Alexandria Range 94201, which has a similar apatite Cl content of ~2 wt.% (along with ~1.5 wt.% F, McCubbin et al., 2012).

5.4.2 – Enriched versus depleted shergottites

The enriched shergottites are believed to be the result of varying degrees of incorporation of an enriched source into the depleted shergottite source or parental melt. It is unknown whether this enriched source is present within the crust (thus incorporated via assimilation) or the mantle (thus incorporated via mantle source mixing) (i.e., Borg and Draper, 2003; Borg et al., 1997; Herd et al., 2002; Basu Sarbadhikari et al., 2009, 2011; McCubbin et al., 2012). Our analyses provide Cl abundance data for Zagami amphibole, and for Tissint amphibole and apatite. Without knowing the method of enriched source incorporation it is not possible to calculate the source region Cl content from the parental melt contents of the enriched shergottites (e.g., Zagami). However, these calculations can be completed for the depleted shergottites (e.g., Tissint) if it is assumed that no crustal assimilation has occurred.

5.4.3 – Cl content of the Tissint and Zagami parental melts

As an early-forming phase, the Cl content in the amphibole can be used to constrain the Cl content of the Tissint parental melt by using the partition coefficient (D) of Cl between the amphibole and melt. In the absence of an amphibole/melt partition coefficient for the shergottites, the D_{Cl} value of 0.38 that has been calculated for the nakhlites and chassignites was used (Filiberto and Treiman, 2009), as this is the best experimentally constrained value for amphiboles as was determined by Gillis et al. (2003).

Given the EDS detection limits of ~0.1 wt.% for Cl, it can only be taken into account amphiboles with Cl > 0.2 wt.% for calculations of realistic Cl abundances in the parent melt. For this purpose, only Tiss D and Zag B were selected for estimation of Cl abundances, and the data reported in [Table 5.1](#) were used. We assume that surrounding minerals that may have contaminated the EDS data do not influence Cl abundance since no other phases present in the FIB-sections, apart from amphibole and apatite, contain Cl in their stoichiometry (apart one spinel grain in Zag A, see [Appendix](#)).

The Cl concentration of the parental melt (in ppm) was calculated by dividing the Cl abundance measured by its partition coefficient (see [Appendix](#)). These

calculations produced a parental melt Cl content of 21300 for Tissint and 6000 for Zagami.

Firstly, the Cl ppm of the parental melt was calculated by dividing the Cl abundance measured for each amphibole in Tissint and Zagami by its partition coefficient (see **Appendix**). Subsequently, assuming perfect equilibrium during melting, the following equation was used to calculate Cl abundance in the mantle source:

$$\frac{C_l}{C_0} = \frac{1}{F + D(1 - F)}$$

(Equation 5.1)

where C_0 is the abundance of Cl in the magma source, C_l is the Cl abundance in the parental melt, F is the melt fraction assumed as $F = 0.15$ (15% melting, in agreement with McCubbin et al. (2012)), and D is replaced with the partition coefficient for chlorine.

This calculation results in a Cl content of 8094 ppm for the Tissint depleted shergottite mantle source. The same calculation for Zagami amphibole gives a value of 2280 ppm Cl, but, as stated above, due to possible crustal assimilation this value could be imprecise. Both these values are similar to the calculated parental melt Cl abundance of chassignites (0.3 wt.%; Filiberto and Treiman, 2009), but differ substantially to the Cl-rich nakhlite value calculated from MIL 03346 (16 wt.%; Filiberto and Treiman, 2009). Therefore, the relatively low Cl content of the shergottite mantle source reinforces the theory that the nakhlites assimilated a Cl-rich component prior to crystallisation (McCubbin et al., 2013). All these values - the nakhlite, chassignite, and shergottite parental melt Cl contents - are much higher than the estimated value of ~1 ppm Cl within the terrestrial upper mantle, based on MORB melt inclusion compositions (Saal et al., 2002). Thus, either the Martian interior is inherently enriched in Cl compared to the terrestrial upper mantle, or none of the meteorite values measured for Cl are entirely representative of the Martian interior - i.e., some form of Cl assimilation has occurred to varying degrees for all samples measured.

5.5 – Conclusion

The Cl content of amphibole in Tissint and Zagami, and apatite in Tissint, was investigated. Amphibole grains in both meteorites are small in size (up to 10 μm in Zagami and $< 8 \mu\text{m}$ in Tissint), and their presence in the early-crystallised pigeonite-hosted melt inclusions suggests that their Cl content should be consistent with their parental melt prior to any degassing. The amphibole composition within both meteorites is kaersutite-magnesiohornblende, with a Cl content up to 0.81 wt.% in Tissint and 0.23 wt.% in Zagami. The Tissint value was used to calculate a Cl abundance of 8094 ppm within the depleted shergottite magma source. This value is much lower than that calculated for the nakhlite mantle source, supporting the idea that the nakhlites assimilated a Cl-rich exogenous fluid, but much higher than that calculated for the terrestrial upper mantle.

Chapter 6 – Conclusions: implications for Mars evolution and terrestrial planets

The scope of this final chapter is to combine all of the information acquired in the previous chapters. This approach permits me to place new constraints on the formation and evolution of Mars and, more generally, on the interior evolution of terrestrial planets.

In summary, in the previous chapters both shergottites and nakhlites have been studied for the purpose of obtaining information about the nature, composition, heterogeneity, and activity of the Martian mantle. In particular, phenocrystic and megacrysts olivines in the Tissint shergottite, reportedly sourced from a mantle-derived melt within a deep magma chamber, were used to provide new insights into the dynamics of magma chambers on Mars. These findings were utilised to evaluate models of convection in the Martian mantle and to provide a calculated mantle temperature that supports the hypothesis of an active Martian mantle during the late Amazonian. Martian lava flows (five nakhlites) were then analysed to constrain the potential implications that crustal sulphur assimilation during lava emplacement has on chemical tracing of Martian mantle source(s). These sulphur grains assimilated from the Martian regolith were also used to obtain results on the proportionate influence of atmospheric and hydrothermal processes on Mars at the time of nakhlite eruption and to define the sulphur isotope composition of the nakhlite mantle source in respect to the shergottites. Also, substantial differences among highly siderophile elements (HSE) data for the primary melt of the nakhlites in respect to the shergottites were obtained; and HSE data were then used to suggest assimilation of an enriched component to this primary nakhlite melt, potentially a late-stage crystallization cumulate from the Martian magma ocean stage. Finally, amphibole and apatite phases were found and analysed in the shergottites Tissint and Zagami, in order to determine the abundance of Cl in the shergottite magma source, by using previously published Cl partition coefficients for amphibole. This result indicated a Cl-poor magma source for the shergottites in contrast with the Cl-rich reservoirs tapped by the nakhlites.

6.1 – New insights on Mars formation

Several lines of evidence in the Solar System account for the past existence of magma oceans during the first stage of planetary formation and differentiation for the terrestrial planets (Elkins-Tanton, 2012): (1) samples from the Moon, Mars, and Vesta are indicative of a very early differentiation of silicate from fractional crystallization; (2) the crystallization ages of these samples (around 4.4 Ga) suggest an extremely short timescale for accretion, and this would imply a high accretionary and radiogenic energy that produced melting; (3) the ^{182}W and ^{142}Nd isotope systematics in planetary rocks suggest early core formation (as on Mars) and a subsequent short period of accretion that would induce melting. In addition, large and severe impacts on the early crusts of the terrestrial planets would likely generate magma oceans or ponds (Tonks and Melosh, 1993; Gelman et al., 2011).

Differences and instabilities in density stratification during magma ocean crystallization can result in magma ocean overturns that induce the creation of long-living heterogeneities in the mantle of a terrestrial planet (Elkins-Tanton et al., 2003). To better analyse how this may happen, it is useful to know what precise physiochemical conditions and processes operate during solidification of a magma ocean. Planets with free surfaces solidify in 10^5 or 10^6 years (rapid), if there is a solid conductive lid the heat flux is significantly reduced (Elkins-Tanton, 2008). According to Elkins-Tanton (2012), the formation of a conductive lid could be due to: (1) unmelted crust of a planetesimal with an internal magma ocean; (2) buoyant crystalline phases that may form in a magma ocean and float on the surface (e.g., the Moon); (3) the surface portion of a magma ocean could quench in a solid crust due to the cold of space. Methods (1) and (3) are considered unlikely to happen and the only likely method is (2). However, large planets require an atmosphere before this can happen. In the Martian magma ocean, plagioclase can crystallize close to the planetary surface, where there is the highest crystal density and thus a hindrance to flotation (Elkins-Tanton, 2012), this process will start to generate overturn. Such a process will stir an enriched component from an early crust into the deep mantle. In particular, the enriched component(s) in the Martian mantle that were argued in this work ([Chapter 4](#)) could be the product of an early Martian magma ocean overturn that isolated these local heterogeneities in the mantle. These heterogeneities may

survive until present thereby influencing the nature of volcanomagmatic processes over Mars' history. The presence of these enriched components in the Martian mantle have also been proposed in previous studies (e.g., Debaille et al., 2009; Bouvier et al., 2018).

As can be seen from [Chapter 4](#), one of the conclusions of this work suggests that mixing with an enriched cumulate derived from the last stages of a Martian magma ocean (MMO) may have occurred to generate the differences in $^{187}\text{Os}/^{188}\text{Os}$ versus Nd and Sr isotope distributions between Nakhla and Lafayette. In particular, the decoupling of γOs versus $\epsilon^{143}\text{Nd}$ constrained an unknown enriched end-member that may have mixed with the nakhlite source. Due to decoupling of γOs versus $\epsilon^{143}\text{Nd}$, this enriched component must have occurred during early Martian differentiation, likely represented by MMO cumulates. This component would likely be one of the last liquids that crystallized from the MMO, since that the first MMO cumulates are largely depleted in REE (Debaille et al., 2009). Based on their correlation between $\epsilon^{143}\text{Nd}$ and γOs (Debaille et al., 2008; Brandon et al., 2012) earlier studies suggested that a similar petrogenetic model may account for shergottites isotopic systematic.

Enriched components generated during early planetary differentiation could survive in the mantle due to long-term isolation. For example, correlation of O, Hf, and Nd isotope on a series of Earth's komatiites suggested derivation from a terrestrial magma ocean followed by long-term isolation from mantle convection processes, resulting in early mantle heterogeneity on Earth (Byerly et al., 2017; Puchtel et al., 2013). In particular, the extremely light $\delta^{18}\text{O}$ (~3-4‰) implied fractionation from deep magma ocean phases (Byerly et al., 2017). Evidence of this process in these komatiites are inferred from their Re-Os isotope systematics and HSE abundances (Puchtel et al., 2014). This type of isolation and early mantle heterogeneity on Earth could have been protracted for a terrestrial planet characterized by a stagnant-lid regime like Mars. In supporting this statement, whole rock $\delta^{18}\text{O}$ versus Sm-Nd and Hf-W isotope systematics for Nakhla and Lafayette show a broad correlation and the very light $\delta^{18}\text{O}$ (5.2-4.7‰) is in agreement with fractionation from MMO cumulates (Clayton and Mayeda, 1996; Borg et al., 1997; Lodders, 1998; Franchi et al., 1999; Barrat et al., 2006).

6.2 – Geochemical constraints on Martian mantle sources

In this work, two important geochemical constraints concerning the Martian mantle were obtained: 1) new evidence of the heterogeneity of the Martian mantle. This would be in agreement with the lack of large-scale and highly-efficient geodynamics processes during Mars' geological history that were unable to homogenize the different mantle sources - as is also the case for the Earth; 2) new data on the composition of the Martian mantle. These two results are discussed in the sections below.

6.2.1 – New evidences of heterogeneity in the Martian mantle

Several studies of Martian meteorites suggested the presence of a heterogeneous Martian mantle, characterized by chemically different mantle reservoirs. Studies of silicate differentiation, based on Rb-Sr and Lu-Hf isotope systematics (Norman, 1999), evidenced how the nakhlite and shergottite magmas may sample reservoirs that were generated synchronously during the magma ocean crystallization phase of Mars, however no strong petrogenetic relationship between the nakhlites and the shergottites has been shown and interior reservoirs are likely to have been isolated from each other for the entire Martian history, as evidenced by their different values in several radionuclides (Nyquist et al., 2001). This isolation would require an inefficient homogenization of the Martian mantle or the absence of especially large impacts after the mantle source reservoirs were established (Shih et al., 1982; Harper et al., 1995; Borg et al., 1997; Foley et al., 2005). In particular, W-Nd isotope systematics of Martian meteorites indicate the coexistence of three different silicate reservoirs on Mars (Fig. 6.1).

New evidence of the geochemical heterogeneity of the Martian mantle that were obtained in the present work include the following:

(1) The estimations of chlorine abundance that were obtained in [Chapter 5](#) were used to constrain a 0.8 wt.% Cl in the magma source for the depleted shergottites, implying a Cl-poor shergottite source in contrast with the Cl-rich sources for the nakhlites (16 wt.%; Filiberto and Treiman, 2009; Filiberto et al.,

2016). This is a clear evidence of marked differences in the volatile element inventories, particularly halogens, among mantle sources in Mars.

(2) As seen from [Chapter 4](#), Nakhla and the two Yamato meteorites were able to retain pristine magmatic $\delta^{34}\text{S}$ and $\Delta^{33}\text{S}$ signatures, having assimilated negligible or no fractions of Martian regolith. Thus, these samples were chosen as the most appropriate to find the $\Delta^{33}\text{S}$ for the nakhlite mantle source. This resulted in a nakhlite mantle source $\Delta^{33}\text{S}$ of -0.1 ‰, a value that is more negative than the calculated shergottite mantle source ($\Delta^{33}\text{S} = 0.009\text{‰}$; Franz et al., 2014) - this is a further argument that sustain the differences in mantle sources between the shergottites and the nakhlites.

(3) The HSE patterns of the samples analysed in [Chapter 4](#) suggest that the nakhlite magmas result from a sulphide-saturated melt where Ru-Os-Ir alloys were likely crystallised during earlier phases of magmatic processing in Mars leading to the fractionated HSE patterns of the nakhlite lava products. This is in contrast to the shergottite magmas that instead were sulphide-undersaturated (Wang and Becker, 2017), further implying different mantle sources for the generation of the nakhlites and the shergottites.

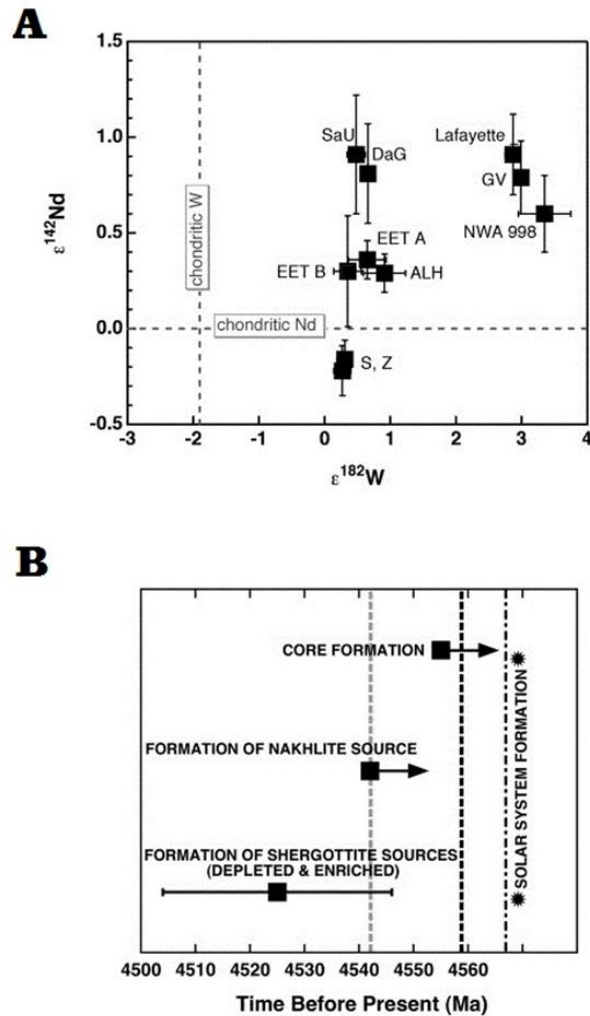


Fig. 6.1 - Constraints on Martian mantle sources and Mars' differentiation events. A) $\epsilon^{182}\text{W}$ vs. $\epsilon^{142}\text{Nd}$ in different types of Martian meteorites: LREE-enriched basaltic shergottites (S = Shergotty; Z = Zagami), LREE-depleted basaltic shergottites (EETA = EETA79001; EETB = EETA79001; DaG 476; SaU 008), a lherzolithic shergottite (ALH = ALHA77005), and nakhlites (GV = Governador Valadares; Lafayette; NWA 998); B) timing of significant differentiation events on Mars inferred by W-Nd isotope systematics. Modified from Foley et al. (2005).

6.2.2 – HSE abundance of the Martian mantle

New data on the composition of the Martian mantle were estimated based on my new HSE abundance data. Assuming no crustal contamination for the nakhlite mantle reservoir, the comparison in the abundances of two HSEs with different

compatibility can be used to estimate the HSE abundances of the Martian mantle. This can be achieved by using [HSEa] vs. HSEb/HSEa plots and generating a linear regression with intersection on the chondritic value. The newly HSE data from Nakhla, Lafayette, and MIL 090032 from [Chapter 4](#) have been used in addition to the data on four Martian meteorites used by Dale et al. (2012), Jones et al. (2003), Treiman (1986), and the high MgO shergottites from Brandon et al. (2012). In taking this approach, different regression lines have been obtained depending on whether all the HSE data or only HSE data that do not present signs of regolith assimilation (as attested to sulphur isotope compositions) have been chosen.

Previous studies (e.g., Dale et al. 2012) used a similar methodology for obtaining Martian mantle HSE abundances (in ppb: Os, 2.4; Ir, 2.4; Ru, 3; Pt, 4; Pd, 3; Re, 0.1; Dale et al., 2012). However, this previous work only filtered meteorite HSE data for impact contributions, and omitted to apply a crustal contamination filter based on sulphur isotope compositions as added here. As described in [Chapter 4](#), Lafayette and MIL 090032 may be affected by regolith assimilation - thus, several approaches to better constrain HSE abundances of the Martian mantle have been tested. Firstly, HSE values available for Martian meteorites (Jones et al., 2003; Dale et al., 2012; Brandon et al., 2012; Tait and Day, 2018) including the new data obtained in this work for Nakhla, Lafayette, and MIL 090032, have been used obtaining the following HSE abundances for Mars' mantle (in ppb): Os, 3.5; Ir, 2.02; Ru, 4.49; Pt, 5.52; Pd, 6.37; Re, 0.7 ([Fig. 6.2](#)). In respect to Dale et al. (2012) estimation, here an increase in Os, Ru, Pt, Pd, and Re is clearly noticeable. Subsequently, only the value for Nakhla was used, interpreted here as the nakhlite with the most convincing magmatic signatures in its S-isotope systematics (meaning minor or absent regolith assimilation), and only the shergottites without an anomalous $\delta^{34}\text{S}$ in its sulphates were chosen (Franz et al., 2014). Applying this second filter, somewhat higher ppb abundances of Os, Ir, Ru, and Re were obtained, with a less ppb abundance of Pd; Pt do not define a reliable abundance when this filter is applied, thus the previous value was kept (5.52 ppb). Precise HSE abundances when this second method is used are as follows (in ppb): Os, 4.02; Ir, 2.21; Ru, 4.7; Pd, 5.74; Re, 0.8 ([Fig. 6.3](#)).

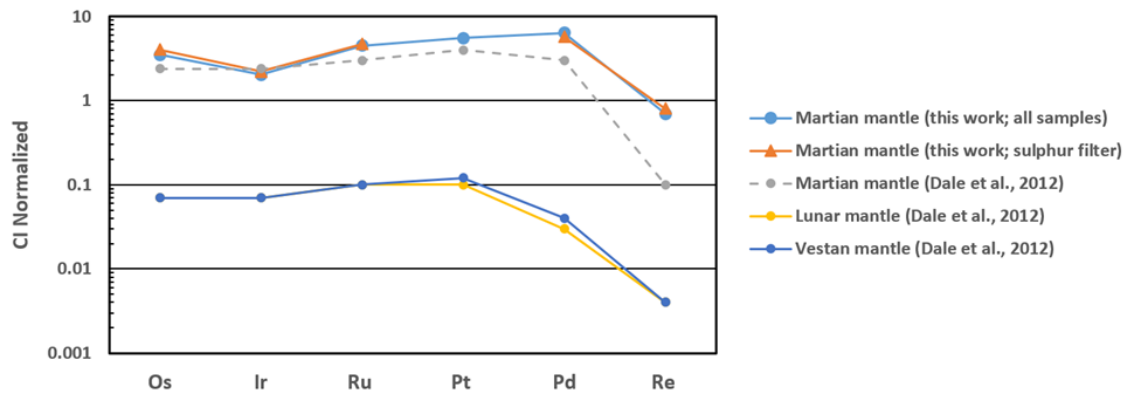


Fig. 6.2 - HSE abundances of the Martian mantle, compared with other planetary bodies. Three datasets are plotted: one plot using existing HSE abundances of four Martian meteorites (Treiman, 1986; Dale et al. 2012; Jones et al. 2003; Tait and Day, 2018), the high MgO shergottites from Brandon et al. (2012), and the new nakhlites analysed in this work; a second plot using the same data but applying the filter for sulphur (i.e., excluding samples with anomalous $\delta^{34}\text{S}$, likely affected by Martian regolith assimilation); the third dataset is from Dale et al. (2012). Data shows a slightly higher abundance of Os, Ir, Ru, and Re when the sulphur filter is applied. By adding the new data obtained in this work an increase in Os, Ru, Pt, Pd, and Re is noticeable in respect to Dale et al. (2012), while Ir is slightly in minor abundance.

There are minor but noteworthy differences between the two approaches. When only samples that were not affected also by regolith assimilation (based on non-magmatic $\delta^{34}\text{S}$) are considered the regression line gives higher values by a factor of ~ 0.25 ppb for Os, Ir, Ru, and Re than prior approaches. This may reflect the nature of HSE themselves since they behave as chalcophile elements when metals are absent, being partitioned into sulphides (Day et al., 2016); the Martian regolith is S-rich (Clark et al., 1976; Foley et al., 2003). By following this logic, it is clear that using existing approaches to estimate Mars' mantle HSE abundances may be flawed, and this new method based on excluding not only samples affected by impact contamination but also samples affected by assimilation of planetary surface material should be taken into account to constrain real HSE abundances of the Martian interior and other planetary bodies.

6.3 – Considerations on viscosity and energetics of the Martian mantle

The calculated mantle potential temperature (T_{mp}) of 1560°C for the Martian mantle in [Chapter 3](#) would imply the past presence of magmatic activity and related convection in the upper mantle of Mars at least until the late Amazonian ($\sim 574\text{ Ma}$). This may have implications on the viscosity and energetics of the Martian mantle, as is discussed below.

6.3.1 – Viscosity of the Martian mantle

The speed of convection in upper mantle environments can play a major role on the temperature of the whole mantle in terrestrial planets, and can be directly used to model viscosity (Breuher and Spohn, 2006). Convection speed is directly related to temperature. Estimations of viscosity for mantle temperatures within $\sim 1400\text{-}1700^{\circ}\text{C}$ for a wet ($< 36\text{ ppm H}_2\text{O}$) and for a dry ($> 36\text{ ppm H}_2\text{O}$) type of planetary mantle were previously calculated as 10^{20} and 10^{21} pascal second, respectively (Breuher and Spohn, 2006). Wet or dry conditions for the Martian mantle can be inferred by its water content. Estimates of water abundance in the Martian mantle vary widely: $\sim 100\text{ ppm H}_2\text{O}$ is inferred from apatite chemistry, equal to terrestrial MORBs (McCubbin et al., 2012; Gross et al., 2013), while other estimates from apatite in shergottites report a mantle source containing $36\text{-}73\text{ ppm H}_2\text{O}$ for the enriched shergottites and $14\text{-}23\text{ ppm}$ for the depleted shergottites (McCubbin et al., 2016). Both situations, however, reflect a wet condition for the Martian mantle. In both the wet and the dry conditions, the value of viscosity required for a mantle to develop continuous convective activity is achieved. The temperature for the upper mantle calculated here falls within the range of $1400\text{-}1700^{\circ}\text{C}$, permitting a high degree of convection, implying the presence of an active Martian mantle at the time of Tissint eruption - in agreement with inefficient cooling of the Martian interior.

6.3.2 – Energy of the Martian mantle

The T_{mp} derived from [Chapter 3](#) can be used to find the Martian mantle thermal energy (E_m) in order to better constrain the possibility of an active Martian mantle during the late Amazonian. In order to do this, the following equation from Zeng and Jacobsen (2017) can be used:

$$E_m = 2 \cdot M_p \cdot \frac{3R \cdot T_{mp}}{\mu} (1 - \sqrt{CMF})$$

(Equation 6.1)

where T_{mp} is the mantle potential temperature as calculated for Mars in this work (= 1833° K); M_p is the planet mass (= 6.36×10^{23} kg, for Mars); R is the gas constant (= $8.314 \text{ J K}^{-1} \text{ mol}^{-1}$); μ is the average atomic weight of the composition, that for Mg-silicate planets is = 0.02 kg mol^{-1} ; and CMF is the core mass fraction (= 0.217, for Mars).

The Martian mantle thermal energy calculated from [Equation 6.1](#) gives a value of 1.5×10^{30} J. The E_m value as calculated by Zeng and Jacobsen (2017) for the Earth is 0.1×10^{32} J - and we know that an active mantle is present. The evidence proposed about Martian mantle convection in [Chapter 3](#) implies that an active Martian mantle was still in place at ~574 Ma and, thus, that a mantle energy of 1.5×10^{30} J is still enough for a terrestrial planet with a stagnant-lid regime to retain internal activity.

In the future, by having the heat flux value for Mars, and assuming it has not changed over time, it would be possible to estimate the thermal energy of the present-day Martian mantle. The heat flux for Mars will likely be revealed by the ongoing NASA InSight (Interior Exploration using Seismic Investigations, Geodesy and Heat Transport) mission and that, compared with calculated T_{mp} and E_m , will be important in determining the present thermal energy and activity of the Martian mantle.

6.4 – Implications for thermal evolution of terrestrial planets

Evolution of planetary interiors, and their degassing to planetary atmospheres/cryospheres, is primarily dependent on the thermal state of their

mantles. In this work it has been shown that Mars could have retained heat in the long-term and this may have been critical to its different geodynamics regime with respect to the habitable Earth. The final paragraphs below summarize the evolution of the Martian mantle relative to the new data that were obtained in this work and to data that are available in the literature. In addition, a comparison is made between the interior evolution of Mars with other types of known terrestrial planets/exoplanets.

6.4.1 – Thermal evolution of terrestrial planets interior

The temperature of accretion and the thermal state of a planetary interior depend on its geodynamics mode, including the capacity of heat loss (Noack and Breuer, 2014). If plate tectonics are always or episodically present (as for Earth), this would transfer heat relatively efficiently from the planetary interior to the surface (Korenaga, 2010). On the other hand, the geodynamic type regime involving a stagnant lid (as for Mars) consist of only a single rigid and immobile plate: this regime occurs when the difference in viscosity between the surface and the planetary interior is of a magnitude of 4 (Reese et al., 1998). In this case, heat could be retained in a planetary interior for a longer time (Noack and Breuer, 2014). A plate tectonics regime can also be present only episodically, however this implies a progressive destruction of a rigid single-plate lid overlying the mantle that results in catastrophic global resurfacing events (Moresi and Solomatov, 1997). A global resurfacing event due to shifting in geodynamics mode may have happened on Venus (Strom et al., 1994).

With the new data acquired in this work, combined with the previous literature, we can better consider a model for planetary interior evolution for specific terrestrial planets that, as Mars, are characterized by a stagnant-lid regime (Fig. 6.3). Initially, accretionary material from a protoplanetary disk can build the proto-planet that, subsequently, can generate a magma ocean if there is enough accretionary heat and heat caused by radioactive elements. At this stage, buoyant crystalline phases would float on the upper part of the magma ocean (Elkins-Tanton, 2012), forming an early crust that is enriched in REE in respect to the magma ocean itself. The occasional occurrence of magma ocean overturn, due to differences and instabilities in density stratification between

the primitive crust and the magma, is able to induce crust material (magma ocean cumulates) to sink toward the interior of the magma ocean. Once the planetary differentiation is complete, a stagnant-lid crust is formed, capable of retaining heat efficiently and with the presence of local convective activity in the mantle that is unable to homogenize the whole mantle. At the same time and for this reason, the enriched magma ocean cumulates may still survive in the mantle and diverse mantle sources can be generated, including sources affected by assimilation of enriched magma ocean cumulates. These mantle sources can then be tapped by plumes that results in localized volcanism.

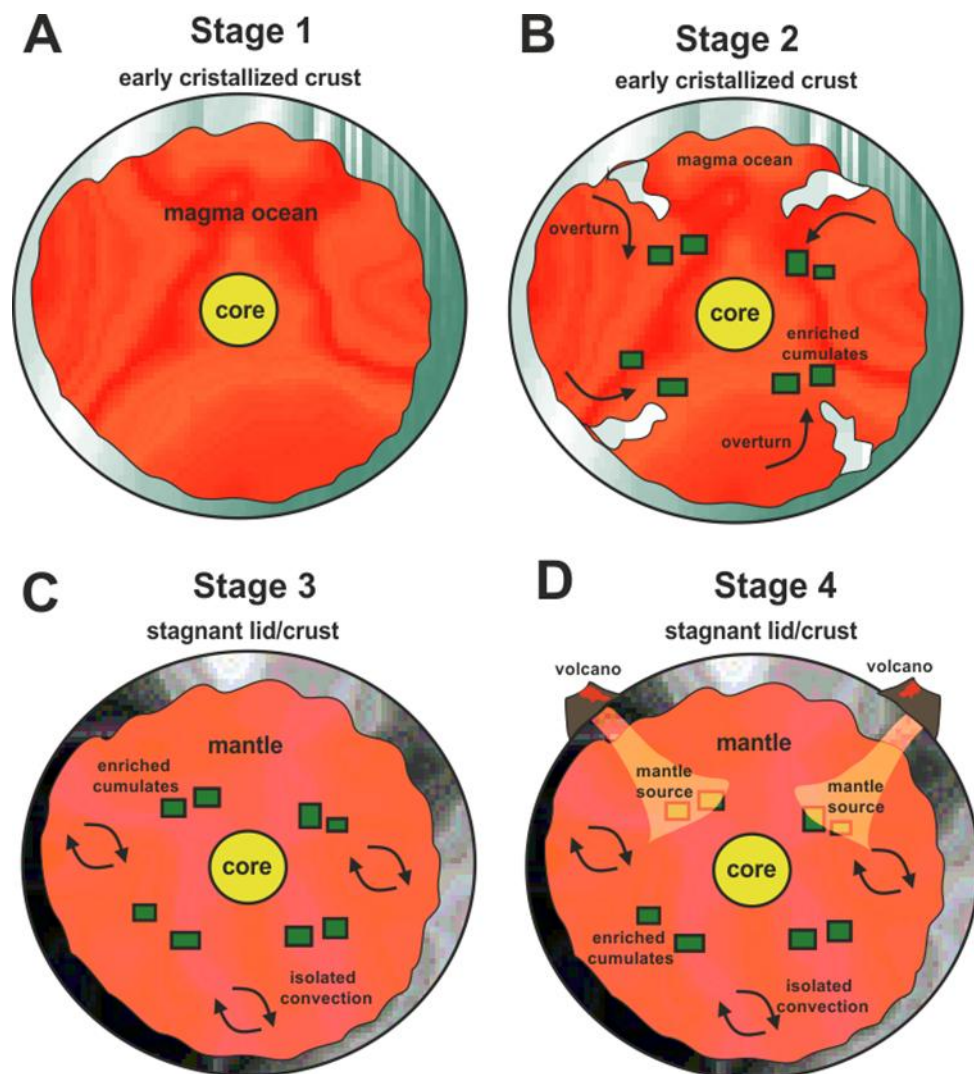


Fig. 6.3 - Interior evolution of a stagnant-lid terrestrial planet, based on the new data acquired in this work and on previous literature data. A) Stage 1: after accretion, if there is enough heat due to accretionary energy and radioactive elements a magma ocean is formed, with the upper part that initially crystallize to form an early crust; B) Stage 2: phenomena of magma ocean overturn, due to

differences in density between the primitive crust and the magma, move material from the early crystallized crust, enriched in REE, in the internal primitive mantle forming enriched magma ocean cumulates; C) Stage 3: several million years after magma ocean solidification and differentiation a stagnant-lid crust is formed if within the crust and the mantle there is a difference in viscosity of a magnitude of 4. Enriched magma ocean cumulates would still survive in the mantle and isolated convection cells are present; D) Stage 4: the limited convection activity would stabilize heterogeneity in the planetary interior, resulting in differing mantle sources. Plume volcanism can be fed by these different mantle sources, including sources that are affected by assimilation of enriched magma ocean cumulates, producing chemically diverse lavas.

6.4.2 – Comparison with terrestrial exoplanets

Going beyond the Solar System, the model presented in [Fig. 6.3](#) could be suitable for terrestrial exoplanets < 1 Earth mass (5.9×10^{24} kg; M_E) - where it is not physically possible to form very large convection cells, capable of destroying the planetary crust into plates. For comparison, Mars has a mass of $0.107 M_E$.

The likelihood for the occurrence of active geodynamics in a plate tectonics style on a terrestrial exoplanet is a function of planetary radius, temperature during planetary accretion, quantity of insolation, and water abundance on its surface (O'Neill and Lenardic, 2007; Valencia et al., 2007; Korenaga, 2010; Van Summeren et al., 2011). In addition, terrestrial planets can experience a shift in geodynamic mode during their geological histories (i.e., Venus; Strom et al., 1994). In particular, it has been shown how radiation from the planet's host star (insolation) is an important factor in determining the actual geodynamic regime of a planet - specifically, terrestrial exoplanets with a surface temperature (T_S) of 273° K can evolve from plate tectonics to episodic periods of stagnant lid regimes, when the available heat ends (Van Summeren et al., 2011). On the other hand, a hot exoplanet with a T_S of 759° K can evolve from an amorphous surface, exceeding the lithospheric yield stress, to a stagnant lid (Van Summeren et al., 2011). In addition, if exoplanets are tidally locked with their host star this

implies the presence of a colder nightside characterized by a plate tectonic regime, and a hot dayside with the presence of magma ocean(s), with a T_s difference between the two sides of $\sim 400^\circ \text{ K}$ (Leger et al., 2009; Van Summeren et al., 2011). In this case, the mobile lid of the dayside, characterized by vigorous volcanism, will likely be continuously subducted beneath the nightside.

The mantle energy calculated for Mars in this work ($1.5 \times 10^{30} \text{ J}$) can be compared to the thermal energy available for other terrestrial exoplanets, as calculated by Zeng and Jacobsen (2017). Gliese 1132b (39 light years from Earth) is a terrestrial exoplanet of $1.6 M_E$, tidally locked with its star, and characterized by a dayside and a nightside (Berta et al., 2015) - it has a calculated mantle energy of $2 \times 10^{31} \text{ J}$ that could be due to the high amount of insolation from the host star. Kepler-93b (313 light years from Earth) and Kepler-20b (929 light years from Earth) are super-Earths of $3.1 M_E$ and $9.7 M_E$, respectively (Ballard et al., 2014; Buchave et al., 2016), with the latest being an iron-rich super-Earth. - they have a calculated mantle energy of 5×10^{31} and $1.1 \times 10^{32} \text{ J}$, respectively. Given the current lack of more geological data about these exoplanets, and assuming a similar crustal thickness as for Mars or Earth, it is still possible to hypothesize from their mantle energy values and M_E that they should be characterized (or have been characterized for short periods) by a geodynamics style of plate tectonics.

6.5 – Conclusion

The main goal of this original research was to obtain new information on the formation and evolution of the Martian mantle by using Martian meteorites.

The two populations of olivine present in the Tissint depleted shergottite were investigated - olivine was present as large early-crystallising antecrysts/xenocrysts, and smaller later crystallising phenocrysts. Irregular oscillatory zoning of phosphorus has been studied within both antecrysts/xenocrysts and phenocrysts, with P-enriched bands containing up to 0.25 wt. % P_2O_5 . Mineral chemistry shows no evidence of melt mixing within the magma chamber, thus solute trapping caused by convective crystal movement from hotter to cooler regions of the magma chamber may explain oscillatory zone formation within Tissint olivine. Olivine equilibration temperatures for the

megacryst cores have been used to infer the potential temperature of the Tissint source region during the late Amazonian. These calculations suggested a temperature of 1655° C for the Tissint magma source, and a Martian mantle temperature of 1535° C - the latter being consistent with the ambient mantle temperature of Archean Earth. Ultimately, these calculations suggest the Martian mantle was still active during the late Amazonian, a conclusion that may be confirmed in the future via the ongoing NASA InSight mission, that will be capable of measuring the heat flow coming from the Martian interior.

Subsequently, sulphur isotopic compositions were determined for sulphides in five nakhlites (Nakhla, Lafayette, MIL 090032, Yamato 000749, and Yamato 000593) to ascertain the degree to which they have been affected by assimilation of the Martian regolith. Nakhla, Yamato 000749, and Yamato 000593 are the meteorites that have most faithfully retained a magmatic signature, and which is therefore the most reliable for using osmium isotopes and HSEs to reveal the nature of nakhlite petrogenesis. For the first time, Re-Os isotope systematics and HSE abundances have been investigated for two different nakhlites, to constrain the degree to which they have been affected by crustal assimilation and the ability of Martian meteorite HSE to testify to Mars' interior composition. The following results have been obtained: (1) The Lafayette and MIL 090032 lava flows acquired S-rich Martian regolith material that carry information about Martian atmospheric and hydrological processes. Results show that UV-photochemistry and hydrothermal processes are the main cause of $\Delta^{33}\text{S}$ and $\delta^{34}\text{S}$ fractionation. This result may have implications for the nature of the Martian atmosphere and hydrothermal activity prior to nakhlite eruption; (2) Nakhla, Yamato 000593, and Yamato 000749 retained a magmatic signature in their sulphides, and were unaffected by assimilation of Martian regolith. Using these meteorites the $\Delta^{33}\text{S}$ of the nakhlite source was estimated to be -0.11 ‰; (3) nakhlite HSE patterns are in agreement with the presence of a sulphide melt involved in nakhlite petrogenesis. Ruthenium-Os-Ir alloys likely formed in this sulphide-saturated melt and controlled the abundances of Ru, Os, Ir in the final lava products; (4) nakhlites formed from a primary magma that we consider to have been generated from a well-mixed Martian mantle that subsequently (at some point after the Nakhla emplacement) assimilated an enriched component during ascent toward the surface, and where this enriched mantle material was potentially represented by a late-stage crystallization cumulate from a Martian

magma ocean. The Re-Os isotope data for nakhlites collected in this work hint at perturbation and potential decoupling of nakhlite $^{187}\text{Os}/^{188}\text{Os}$ isotope systematics from other isotopic systems as a result of small degrees of assimilation of a S-rich regolith with low total HSE contents but highly radiogenic $^{187}\text{Os}/^{188}\text{Os}$.

Finally, amphibole and apatite phases have been investigated in the two shergottites Tissint and Zagami, in order to determine the abundance of Cl in the parental melts of these depleted and enriched shergottites. Scanning electron microscopy and transmission electron microscopy were used to identify these minerals and constrain their chemical structure. Cl-rich apatite grains are detected in Tissint. Both meteorites contain amphibole within pigeonite-hosted melt inclusions, with grains up to 10 μm diameter in Zagami and up to 4 μm in Tissint. Amphibole in both meteorites has low Cl abundances (< 2 wt.%), and calculations based on Tissint amphibole indicate a 0.8 wt.% Cl magma source for the depleted shergottites. These low Cl abundances are in contrast to the high amphibole Cl content of the nakhlite meteorites, reinforcing the conclusion that significant Cl assimilation occurred during crystallisation of the nakhlites.

In conclusion, by combining all this information, the formation and evolution of Mars has been better constrained and compared with previous data and, in addition, a model for the evolution of the terrestrial planets in a stagnant-lid regime has been considered. Future data from new meteorites and space missions are, however, needed to continue improving understanding of planetary evolution and the possibility of habitable worlds across the wider Universe.

Bibliography

- Abe Y. and Matsui T., 1985. The formation of an impact-generated H₂O atmosphere and its implications for the thermal history of the Earth. *J. Geophys. Res.*, vol. 90, pp. 545-59.
- Abe Y., 1997. Thermal and chemical evolution of the terrestrial magma ocean. *Phys. Earth Planet. Inter.*, vol. 100, pp. 27-39.
- Acuna M. H., Connerney J. E. P., Ness N. F., Lin R. P., Mitchell D., Carlson C. W., McFadden J., Anderson K. A., Rème H., Mazelle C., Vignes D., Wasilewski P., and Cloutier P., 1999. Global distribution of crustal magnetization discovered by the Mars Global Surveyor MAG/ER experiment. *Science*, vol. 284, pp. 790-793.
- Agee C. B., Muttik N., Ziegler K., McCubbin F. M., Herd C. D. K., Rochette P., and Gattacceca J., 2014. Discovery of a new martian meteorite type: Augite basalt—Northwest Africa 8159. *45th Lunar and Planetary Science Conference*, Abstract #2036.
- Agee C. B., Wilson N. V., McCubbin F. M., Ziegler K., Polyak V. J., Sharp Z. D., Asmerom Y., Nunn M. H., Shaheen R., Thiemens M. H., and others, 2013. Unique meteorite from early Amazonian Mars: Water-rich basaltic breccia Northwest Africa 7034. *Science*, vol. 339, pp. 780-785.
- Agerkvist D. P. and Vistisen L., 1993. Mössbauer spectroscopy of the SNC meteorite Zagami. *Lunar Planet. Sci. XXIV*, Abstract #1001.
- Amelin Y., Krot A. N., Hutcheon I. D. and Ulyanov A. A., 2002. Pb isotopic ages of chondrules and Ca-Al rich inclusions. *Science*, vol. 297, pp. 1678-1683.
- Amossé J., Allibert M., Fischer W., and Piboule M., 1990. Experimental study of the solubility of platinum and iridium in basic silicate melts – implications for the differentiation of platinum-group elements during magmatic processes. *Chem. Geol.*, vol. 81, pp. 45-53.
- Anderson R. C., Dohm J. M., Golombek M. P., Haldemann A. F. C., Franklin B., Tanaka K. L., Lias J., and Peer B., 2001. Primary centers and secondary concentrations of tectonic activity through time in the western hemisphere of Mars. *J. Geophys. Res.*, vol. 106, pp. 20,563-20,585.
- Andrews-Hanna J. C., Phillips R. J., and Zuber M. T., 2007. Meridiani Plains and the global hydrology of Mars. *Nature*, vol. 446, pp. 163-166.
- Armstrong J. T., 1988. Quantitative analysis of silicates and oxide minerals: Comparison of Monte-Carlo, ZAF and Phi-Rho-Z procedures. In: *Microbeam Analysis*, pp. 239-246.
- Arndt N. T., 1977. Thick, layered peridotite-gabbro lava flows in Munro township, Ontario. *Can. J. Earth Sci.*, vol. 14, pp. 2620-2637.
- Aziz M. J., 1982. Model for solute redistribution during rapid solidification. *Journal of Applied Physics*, vol. 53, issue 2, pp. 1158-1168.
- Ballard S., et al., 2014. Kepler-93b: A Terrestrial World Measured to within 120 km, and a Test Case for a New Spitzer Observing Mode. *The Astrophysical Journal*, vol. 790, issue 1.

- Balta J. B. and McSween H. Y., 2011. Are megacrysts in olivine-phyric shergottites xenocrysts, phenocrysts, or something else?. *42nd Lunar and Planetary Science Conference*, Abstract #1033.
- Balta J. B., Sanborn M. E., Udry A., Wadhwa M., and McSween H. Y., 2015. Petrology and trace element geochemistry of Tissint, the newest shergottite fall. *Meteoritics & Planetary Science*, vol. 50, issue 1, pp. 63-85.
- Balta J. B., Sanborn M., McSween H. Y. and Wadhwa M., 2013. Magmatic history and parental melt composition of olivine-phyric shergottite LAR 06319: Importance of magmatic degassing and olivine antecrysts in Martian magmatism. *Meteoritics & Planetary Science*, vol. 48, pp. 1359-1382.
- Bandfield J. L., Hamilton V. E., Christensen P. R., 2000. A global view of martian surface compositions from MGS-TES. *Science*, vol. 287, pp. 1626-1630.
- Baratoux D., Toplis M. J., Monnereau M., and Sautter V., 2013. The petrological expression of early Mars volcanism. *J. Geophys. Res. Planets*, vol. 118, pp. 59-64.
- Barnes S. J., Naldrett A. J., and Gorton M. P., 1985. The origin and fractionation of platinum group elements in terrestrial magmas. *Chem. Geol.*, vol. 53, pp. 303-323.
- Barrat J. A., Benoit M. and Cotton J., 2006. Bulk chemistry of the Nakhlite Miller Range 03346 (MIL 03346). *Lunar Planet. Sci. XXXVII*, Abstract #1569.
- Barton M., Varekamp J. C., and Van M. J., 1982. Complex zoning of clinopyroxenes in the lavas of vulsini, latium, Italy: Evidence for magma mixing. *Journal of Volcanology and Geothermal Research*, vol. 14, issue 3-4, pp. 361-388.
- Basilevsky A. T., Werner S. C., Neukum G., Head J. W., van Gasselt S., Gwinner K. and Ivanov B. A., 2006. Geologically recent tectonic, volcanic and fluvial activity on the eastern flank of the Olympus Mons volcano, Mars. *Geophysical Research Letters*, 33:13.
- Basu Sarbadhikari A. B., Babu E. V. S. S. K., Kumar T. V., and Chennaoui Aoudjehane H., 2016. Martian meteorite Tissint records unique petrogenesis among the depleted shergottites. *Meteoritics & Planetary Science*, vol. 51, issue 9, pp. 1588-1610.
- Basu Sarbadhikari A., Day J. M. D., Liu Y., Rumble D. III, and Taylor L. A., 2009. Petrogenesis of Olivine-Phyric Shergottite LAR 06319: Implications for Enriched Components in Martian Basalts. *Geochimica & Cosmochimica Acta*, vol. 73, issue 7, pp. 2190-2214.
- Basu Sarbadhikari A., Goodrich C. A., Liu Y., Day J. M. D., and Taylor L. A., 2011. Evidence for heterogeneous enriched shergottite mantle sources in Mars from olivine-hosted melt inclusions in Larkman Nunatak 06319. *Geochimica & Cosmochimica Acta*, vol. 75, pp. 6803-6820.
- Baziotis I. P., Liu Y., DeCarli P. S., Melosh H. J., McSween H. Y., Bodnar R. J., and Taylor L. A., 2013. The Tissint Martian meteorite as evidence for the largest impact excavation. *Nature Communications*, vol. 4, issue 1404.
- Beattie P., 1993. Olivine-melt and orthopyroxene-melt equilibria. *Contributions to Mineralogy and Petrology*, vol. 115, pp. 103-111.
- Beck P., Barrat J. A., Gillet P., Wadhwa M., Franchi I. A., Greenwood R. C., Bohn M., Cotten J., de Moortele B. V., and Reynard B., 2006. Petrography and geochemistry of

the chassignite Northwest Africa 2737 (NWA 2737). *Geochimica et Cosmochimica Acta*, vol. 70, pp. 2127-2139.

Becker R. H. and Pepin R. O., 1984. The case for a martian origin of the shergottites: nitrogen and noble gases in EETA 79001. *Earth and Planetary Science Letters*, vol. 69, pp. 225-242.

Berkley J. L., and Keil K., 1981. Olivine Orientation in the ALHA77005 Achondrite. *Am. Mineral.*, vol. 66, pp. 1233-1236.

Berkley J. L., Kiel K. and Prinz M., 1980. Comparative petrology and origin of Governador Valadares and other nakhlites. *Proc. Lunar Planet. Sci. Conf. 11th*, pp. 1089-1102.

Berman D. C. and Hartmann W. K., 2002. Recent fluvial, volcanic, and tectonic activity on the Cerberus Plains of Mars. *Icarus*, vol. 159, pp. 1-17.

Berta Z. K., Irwin J., Charbonneau D., Newton E. R., Dittmann J. A., Astudillo-Defru N., Bonfils X., Gillon M., and Jehin E., 2015. A rocky planet transiting a nearby low-mass star. *Nature*, vol. 527, issue 7577, pp. 204-207.

Bezmen N. I., Asif M., Brüggmann G. E., Romanenko I. M., and Naldrett A. J., 1994. Distribution of Pd, Rh, Ru, Ir and Au between sulfide and silicate metals. *Geochim. Cosmochim. Acta*, vol. 58, issue 4, pp. 1251-1260.

Bibring, J. P., Langevin Y., Mustard J. F., Poulet F., Arvidson R., Gendrin A., Gondet B., Mangold N., and the OMEGA Team, 2006. Global mineralogical and aqueous Mars history derived from OMEGA/Mars Express data. *Science*, vol. 312, pp. 400-404.

Birck J. L. and Allegre C. J., 1994. Contrasting Re/Os magmatic fractionation in planetary basalts. *Earth Planet. Sci. Lett.*, vol. 124, pp. 139-148.

Birck J. L., Roy-Barman M. and Capman F., 1997. Re-Os isotopic measurements at the femtomole level in natural samples. *Geostand. Newslett.*, vol. 20, pp. 19-27.

Bish D. L., Blake D. F., Vaniman D. T., Chipera S. J., Morris R. V., Ming D. W., Treiman A. H., Sarrazin P., Morrison S. M., Downs R. T., Achilles C. N., and others and the MSL Science Team, 2013. X-ray diffraction results from Mars Science Laboratory: Mineralogy of Rocknest at Gale crater. *Science*, vol. 341, issue 6153.

Blasius K. R., Cutts J. A., Guest J. E., and Masursky H., 1977. Geology of the Valles Marineris: first analysis of imaging from the Viking 1 orbiter primary mission. *J. Geophys. Res.*, vol. 82, pp. 4067-4091.

Blichert-Toft J., Gleason J. D., Telouk P., and Albarede F., 1999. The Lu-He isotope geochemistry of shergottites and the evolution of the Martian mantle-crust system. *Earth Planet. Sci. Lett.*, vol. 173, pp. 25-39.

Boctor N. Z., Meyer H. O. A. and Kullerud G., 1976. Lafayette meteorite: petrology and opaque mineralogy. *Earth and Planetary Science Letters*, vol. 32, pp. 69-76.

Bogard D. D. and Husain L., 1977. A new 1.3 aeon-young achondrite. *Geophys. Res. Lett.*, vol. 4, pp. 69-71.

Bohrson W. A. and Spera F. J., 2003. Energy-constrained open-system magmatic processes IV: geochemical, thermal and mass consequences of energy-constrained

recharge, assimilation and fractional crystallization (EC-RAFC). *Geochem. Geophys. Geosyst.*, vol.4(2), issue 8002.

Borg L. and Drake M. J., 2005. A review of meteorite evidence for the timing of magmatism and of surface or near-surface liquid water on Mars. *J. Geophys. Res.*, vol. 110, E12S03.

Borg L. E. and Draper D. S., 2003. A petrogenetic model for the origin and compositional variation of the Martian basaltic meteorites. *Meteoritics & Planetary Science*, vol. 38, pp. 1713-1731.

Borg L. E., Nyquist L. E., Taylor L. A., Wiesmann H., and Shih C. Y., 1997. Constraints on Martian differentiation processes from Rb-Sr and Sm-Nd isotopic analyses of the basaltic shergottite QUE94201. *Geochim. Cosmochim. Acta*, vol. 61, pp. 4915-4931.

Borg L. E., Nyquist L. E., Wiesmann H., Shih C. Y., and Reese Y., 2003. The age of Dar al Gani 476 and the differentiation history of the martian meteorites inferred from their radiogenic isotopic systematics. *Geochim. Cosmochim. Acta*, vol. 67, pp. 3519-3536.

Bottke W. F., Walker R. J., Day J. M. D., Nesvorny D. and Elkins-Tanton L., 2010. Stochastic late accretion to Earth, the Moon, and Mars. *Science*, vol. 330, issue 6010, pp. 1527-1530.

Bouvet de Maisonneuve C., Costa F., Huber C., Vonlanthen P., Bachmann O., and Dungan M. A., 2016. How do olivines record magmatic events? Insights from major and trace element zoning. *Contributions to Mineralogy and Petrology*, vol. 171, issue 56.

Bouvier A. and M. Wadhwa, 2010. The age of the Solar System redefined by the oldest Pb-Pb age of a meteoritic inclusion. *Nature Geoscience*, vol. 3, issue 9.

Bouvier A., Blichert-Toft J., Vervoort J., and Albarède F., 2005. The age of Zagami and other shergottites. 68th Annual Meteoritical Society Meeting, Abstract #5038.

Bouvier L. C., Costa M. M., Connelly J. N., Jensen N. K., Wielandt D., Storey M., Nemchin A. A., Whitehouse M. J., Snape J. F., Bellucci J. J., Moynier F., Agranier A., Gueguen B., Schönbächler M. and Bizzarro M., 2018. Evidence for extremely rapid magma ocean crystallization and crust formation on Mars. *Nature*, vol. 558, pp. 586-589.

Brandon A. D., Puchtel I. S., Walker R. J., Day J. M.D., Irving A. J., and Taylor L. A., 2012. Evolution of the martian mantle inferred from the 187Re-187Os isotope and highly siderophile element abundance systematics of shergottite meteorites. *Geochimica et Cosmochimica Acta*, vol. 76, pp. 206-235.

Brandon A. D., Walker R. J., Morgan J. W. and Goles G. G., 2000. Re-Os isotopic evidence for early differentiation of the Martian mantle. *Geochimica et Cosmochimica Acta*, vol. 64, issue 23, pp. 4083-4095.

Brenan J. M., 2008. Re-Os fractionation by sulfide melt silicate melt partitioning: a new spin. *Chem. Geol.*, vol. 248, pp. 140-165.

Brennecka G. A., Borg L. E., and Wadhwa M., 2014. Insights into the Martian mantle: The age and isotopics of the meteorite fall Tissint. *Meteoritics & Planetary Science*, vol. 49, pp. 412-418.

- Breton H., Lee M. R. and Mark D. F., 2015. Secondary minerals in the nakhlite meteorite Yamato 000593: distinguishing Martian from terrestrial alteration products. *46th Lunar and Planetary Science Conference*, Abstract #2010.
- Breuer D. and Spohn T., 2003. Early plate tectonics versus single-plate tectonics on Mars: Evidence from magnetic field history and crust evolution. *J. Geophys. Res.*, vol. 108, issue E7.
- Breuer D. and Spohn T., 2006. Viscosity of the Martian mantle and its initial temperature: Constraints from crust formation history and the evolution of the magnetic field. *Planetary and Space Science*, vol. 54, issue 2, pp. 153-169.
- Bridges J. C. and Grady M. M., 2000. Evaporite mineral assemblages in the nakhlite (martian) meteorites. *Earth and Planetary Science Letters*, vol. 176, pp. 267-279.
- Bridges J. C., Catling D. C., Saxton J. M., Swindle T. D., Lyon I. C., and Grady M. M., 2001. Alteration assemblages in Martian meteorites: implications for near-surface processes. In: Kallenbach, R., Geiss, J., Hartmann, W.K. (Eds.). *Chronology and Evolution of Mars*. Kluwer Academic Publishers, Dordrecht, pp. 365-392.
- Buchave L. A., Dressing C. D., Dumusque X., Rice K., Vanderburg A., Mortier A., Lopez-Morales M., Lopez E., Lundkvist M. S., and Kjeldsen H., 2016. A 1.9 Earth radius rocky planet and the discovery of a non-transiting planet in the Kepler-20 system. *The Astronomical Journal*, vol. 152, issue 6.
- Bunch T. E. and Reid A. M., 1975. The nakhlites, part 1: petrography and mineral chemistry. *Meteoritics*, vol. 10, pp. 303-315.
- Byerly B. L., Kareem K., Bao H., and Byerly G. R., 2017. Early Earth mantle heterogeneity revealed by light oxygen isotopes of Archaean komatiites. *Nature Geoscience*, vol. 10, pp. 871-875.
- Byrne S. and Murray B., 2002. North polar stratigraphy and the paleo-erg of Mars. *J. Geophys. Res.*, vol. 107, issue E6.
- Byrne S., 2009. The polar deposits of Mars. *Annu. Rev. Earth Planet. Sci.*, vol. 37, pp. 535-560.
- Canup R. M. and Salmon J., 2018. Origin of Phobos and Deimos by the impact of a Vesta-to-Ceres sized body with Mars. *Science Advances*, vol. 4, issue 4.
- Carey R. J., Manga M., Degruyter W., Gonnermann H., Swanson D., Houghton B., Orr T., and Patrick M., 2013. Convection in a volcanic conduit recorded by bubbles. *Geology*, vol. 41, issue 4, pp. 395-398.
- Carr M. H. and Head III J. W., 2010. Geologic history of Mars. *Earth and Planetary Science Letters*, vol. 294, pp. 185-203.
- Carr M. H., 2001. Mars Global Surveyor observations of martian fretted terrain. *J. Geophys. Res.*, vol. 106, pp. 23571-23594.
- Carr M. H., 2006. *The Surface of Mars*. Cambridge University Press. 307 p.
- Carroll M. R. and Webster J. D., 1994. Solubilities of sulfur, noble gases, nitrogen, chlorine, and fluorine in magmas. In: *Volatiles in Magmas*. Mineral. Soc. Amer., Washington, DC. pp. 231-280.

- Chambers J. E., 2004. Planetary accretion in the inner Solar System. *Earth Planet. Sci. Lett.*, vol. 223, pp. 241-252.
- Changela H. G. and Bridges J. C., 2011. Alteration assemblages in the nakhlites: Variation with depth on Mars. *Meteoritics & Planetary Science*, vol. 45, pp. 1847-1867.
- Chen C., Sedwick P. N. and Sharma M., 2009. Anthropogenic osmium in rain and snow reveals global-scale atmospheric contamination. *Proceedings of the National Academy of Sciences*, vol. 106, issue 19, pp. 7724-7728.
- Chen J., Inoue T., Weidner D. J., Wu Y., and Vaughan M. T., 1998. Strength and water weakening of mantle minerals, olivine, wadsleyite and ringwoodite. *Geophys. Res. Lett.*, vol. 25, pp. 575-578, correction in 25(7), pp. 1103-1104.
- Chennaoui Aoudjehane H., Avice G., Barrat J. A., Boudouma O., Chen G., Duke M. J. M., Franchi I. A., Gattacceca J., Grady M. M., Greenwood R. C., Herd C. D. K., Hewins R., Jambon A., Marty B., Rochette P., Smith C. L., Sautter V., Verchovsky A., Weber P., and Zanda B., 2012. Tissint Martian meteorite: A fresh look at the interior, surface, and atmosphere of Mars. *Science*, vol. 338, pp. 785-788.
- Chevrier V., Lorand J. P. and Sautter V., 2011. Sulfide petrology of four nakhlites: Northwest Africa 817, Northwest Africa 998, Nakhla, and Governador Valadares. *Meteoritics & Planetary Science*, vol. 46, issue 6, pp. 769-784.
- Chevrier V., Poulet F., and Bibring, J. P., 2007. Early geochemical environment of Mars as determined from thermodynamics of phyllosilicates. *Nature*, vol. 448, pp. 60-63.
- Chu Z. Y., Yan Y., Chen Z., Guo J. H., Yang Y. H., Li C. F. and Zhang Y. B., 2015. A Comprehensive Method for Precise Determination of Re, Os, Ir, Ru, Pt, Pd Concentrations and Os Isotopic Compositions in Geological Samples. *Geostandards and Geoanalytical Research*, vol. 39, pp. 151-169.
- Cioni R., Marianelli P., and Santacroce R., 1998. Thermal and compositional evolution of the shallow magma chambers of Vesuvius: Evidence from pyroxene phenocrysts and melt inclusions. *Journal of Geophysical Research-Solid Earth*, vol. 103, issue B8, pp. 18277-18294.
- Clark A. H., Pearce T. H., Roeder P. L., and Wolfson I., 1986. Oscillatory zoning and other microstructures in magmatic olivine and augite: Nomarski interference contrast observations on etched polished surfaces. *American Mineralogist*, vol. 71, pp. 734-741.
- Clark B. C., Baird A. K., Rose H. J., Toulmin P. III, Keil K., Castro A. J., Kelliher W. C., Rowe C. D., and Evans P. H., 1976. Inorganic analyses of Martian surface samples at the Viking landing sites. *Science*, vol. 194, pp. 1283-1288.
- Clayton R. N. and Mayeda T. K., 1996. Oxygen isotope studies of achondrites. *Geochim. Cosmochim. Acta*, vol. 60, pp. 1999-2017.
- Clifford S. M. and Parker T. J., 2001. The evolution of the martian hydrosphere: implications for the fate of a primordial ocean and the current state of the northern plains. *Icarus*, vol. 154, pp. 40-79.
- Cohen A. S. and Waters F. G., 1996. Separation of osmium from geological materials by solvent extraction for analysis by thermal ionisation mass spectrometry. *Anal. Chim. Acta*, vol. 332, pp. 269-275.

Cohen B. E., Mark D. F., Cassata W. S., Lee M. R., Tomkinson T., and Smith C. L., 2017. Taking the pulse of Mars via dating of a plume-fed volcano. *Nature Communications*, vol. 8, issue 640, pp. 1-9.

Connelly J., Bizzarro M., Alexander N. K., Nordlund A., Wielandt D. K. P., and Ivanova M. A., 2012. The Absolute Chronology and Thermal Processing of Solids in the Solar Protoplanetary Disk. *Science*, vol. 338, 651-655.

Connerney J. E. P., Acuna M. H., Wasilewski P. J., Ness N. F., Rème H., Mazelle C., Vignes D., Lin R. P., Mitchell D. L., Cloutier P. A., 1999. Magnetic lineations in the ancient crust of Mars. *Science*, vol. 284, pp. 794-800.

Corrigan C. M., Velbel M. A. and Vicenzi E. P., 2015. Modal abundances of pyroxene, olivine, and mesostasis in nakhlites: Heterogeneity, variation, and implications for nakhlite emplacement. *Meteoritics & Planetary Science*, vol. 50, issue 9, pp. 1497-1511.

Costard F., Séjourné A., Kelfoun K., Clifford S., Lavigne F., Di Pietro I., and Bouley S., 2017. Modeling tsunami propagation and the emplacement of thumbprint terrain in an early Mars ocean. *J. Geophys. Res. Planets*, vol. 122, pp. 633-649.

Craddock R. A. and Howard A. D., 2002. The case for rainfall on a warm, wet early Mars. *J. Geophys. Res.*, vol. 107, issue E11.

Creaser R. A., Papanastassiou D. A., and Wasserburg G. J., 1991. Negative thermal ion mass spectrometry of osmium, rhenium and iridium. *Geochimica et Cosmochimica Acta*, vol. 55, pp. 397-401.

Crozaz G., Floss C., and Wadhwa M., 2003. Chemical alteration and REE mobilization in meteorites from hot and cold deserts. *Geochim. Cosmochim. Acta*, vol. 67, pp. 4727-4741.

Dale C. W., Burton K. W., Greenwood R. C., Gannoun A., Wade J., Wood B. and Pearson D. G., 2012. Late accretion on the earliest planetesimals revealed by the highly siderophile elements. *Science*, vol. 336, pp. 72-75.

Dauphas N. and A. Pourmand, 2011. Hf-W-Th evidence for rapid growth of Mars and its status as a planetary embryo. *Nature*, vol. 473, pp. 489-491.

Davidson J. P., Morgan D. J., Charlier B. L. A., Harlou R., and Hora J. M., 2007. Microsampling and isotopic analysis of igneous rocks: Implications for the study of magmatic systems. *Annual Review of Earth and Planetary Sciences*, vol. 35, pp. 273-311.

Day J. M. D., Brandon A. D. and Walker R. J., 2016. Highly siderophile elements in Earth, Mars, the Moon, and Asteroids. *Reviews in Mineralogy & Geochemistry*, vol. 81, pp. 161-238.

Day J. M. D., Tait K. T., Udry A., Moynier F., Liu Y., and Neal C. R., 2018. Martian magmatism from plume metasomatized mantle. *Nature Communications*, vol. 9, issue 4799.

Day J. M. D., Taylor L. A., Floss C., and McSween H. Y., 2006. Petrology and chemistry of MIL 03346 and its significance in understanding the petrogenesis on nakhlites on Mars. *Meteoritics and Planetary Science*, vol. 41, issue 4, pp. 581-606.

- Debaille V., Brandon A. D., O'Neill C., Yin Q. Z. and Jacobsen B., 2009. Early martian mantle overturn inferred from isotopic composition of nakhlite meteorites. *Nature Geosciences*, vol. 2, pp. 548-552.
- Debaille V., Brandon A. D., Yin Q. Z., and Jacobsen B., 2007. Coupled ^{142}Nd - ^{143}Nd evidence for a protracted magma ocean in Mars. *Nature*, vol. 450, pp. 525-528.
- Debaille V., Yin Q. Z., Brandon A. D., and Jacobsen B., 2008. Martian mantle mineralogy investigated by the ^{176}Lu - ^{176}Hf and ^{147}Sm - ^{143}Nd systematics of shergottites. *Earth and Planetary Science Letters*, vol. 269, pp. 186-199.
- Delvigne J., 1998. Atlas of Micromorphology of Mineral Alteration and Weathering. *Canadian Mineralogist*, Special Publication #3, Mineralogical Association of Canada, Ottawa, 495 p.
- Domeneghetti M. C., Fioretti A. M., Camara F., McCammon C. and Alvaro M., 2013. Thermal history of nakhlites: A comparison between MIL 03346 and its terrestrial analogue Theo's flow. *Geochimica et Cosmochimica Acta*, vol. 121, pp. 571-581.
- Donovan J. J. and Tingle T. N., 1996. An Improved Mean Atomic Number Correction for Quantitative Microanalysis. *Journal of Microscopy*, vol. 2, issue 1, pp. 1-7.
- Donovan J. J., Singer J. W., and Armstrong J. T. 2016. A New EPMA Method for Fast Trace Element Analysis in Simple Matrices. *American Mineralogist*, vol. 101, pp. 1839-1853.
- Donovan J. J., Snyder D. A., and Rivers M. L., 1993. An Improved Interference Correction for Trace Element Analysis. *Microbeam Analysis*, vol. 2, pp. 23-28.
- Dottin III J. W., Labidi J., Farquhar J., Piccoli P., Liu M. C. and McKeegan K. D., 2018. Evidence for oxidation at the base of the nakhlite pile by reduction of sulfate salts at the time of lava emplacement. *Geochimica et Cosmochimica Acta*, vol. 239, pp. 186-197.
- Downes M. J., 1974. Sector and oscillatory zoning in calcic augites from M. Etna, Sicily. *Contributions to Mineralogy and Petrology*, vol. 47, issue 3, pp. 187-196.
- Dreibus G. and Wanke H., 1987. Volatiles on Earth and Mars: a comparison. *Icarus*, vol. 71, pp. 225-240.
- Dreibus G., Palme H., Rammensee W., Spettel B., Weckwerth G., and Wänke H., 1982. Composition of the Shergotty Parent Body: Further Evidence of a two Component Model for Planet Formation. *Proc. 13th Lunar Planet. Sci. Conf.*, pp. 186-187.
- Duncan A. M. and Preston R. M. F., 1980. Chemical variation of clinopyroxene phenocrysts from the trachybasaltic lavas of Mount Etna, Sicily. *Mineralogical Magazine*, vol. 43, pp. 765-770.
- Dyar M. D., Treiman A. H., Pieters C. M., Hiroi T., Lane M. D. and O'Connor V., 2005. MIL03346, the most oxidized Martian meteorite: A first look at spectroscopy, petrography, and mineral chemistry. *J. Geophys. Res.*, vol. 110, E09005.
- Ehlmann B. L., Mustard J. F., Murchie S. L., Bibring J. P., Meunier A., Fraeman A. A. and Langevin Y., 2011. Subsurface water and clay mineral formation during the early history of Mars. *Nature*, vol. 479, pp. 53-60.

- Eichelberger J. C., 1995. Silicic volcanism—Ascent of viscous magmas from crustal reservoirs. *Annual Review of Earth and Planetary Sciences*, vol. 23, pp. 41-63.
- Elardo S. M. and Shearer C. K., 2014. Magma chamber dynamics recorded by oscillatory zoning in pyroxene and olivine phenocrysts in basaltic lunar meteorite Northwest Africa 032. *American Mineralogist*, vol. 99, pp. 355-368.
- Elkins-Tanton L. T., 2008. Linked magma ocean solidification and atmospheric growth for Earth and Mars. *Earth Planet. Sci. Lett.*, vol. 271, pp. 181-191.
- Elkins-Tanton L. T., 2012. Magma Oceans in the Inner Solar System. *Annu. Rev. Earth Planet. Sci.*, vol. 40, pp. 113-39.
- Elkins-Tanton L. T., Parmentier E. M. and Hess P. C., 2003. Magma ocean fractional crystallization and cumulate overturn in terrestrial planets: Implications for Mars. *Meteoritics and Planetary Science*, vol. 38, issue 12, pp. 1753-1771.
- Ennis M. E. and McSween H. Y., 2014. Crystallization kinetics of olivine-phyric shergottites. *Meteoritics & Planetary Science*, vol. 49, issue 8, pp. 1440-1455.
- Eriksson S. C., 1985. Oscillatory zoning in clinopyroxenes from the Guide Copper Mine, Phalaborwa, South-Africa. *American Mineralogist*, vol. 70, pp. 74-79.
- Farquhar J., Kim S. T. and Masterson A., 2007. Implications from sulfur isotopes of the Nakhla meteorite for the origin of sulfate on Mars. *Earth Planet. Sci. Lett.*, vol. 264, pp. 1-8.
- Farquhar J., Savarino J., Jackson T. L. and Thiemens M. H., 2000. Evidence of atmospheric sulphur in the martian regolith from sulphur isotopes in meteorites. *Nature*, vol. 404, pp. 50-52.
- Farquhar J., Savarino J., Sabine A. and Thiemens M. H., 2001. Observation of wavelength-sensitive mass-independent sulfur isotope effects during SO₂ photolysis: Implications for the early atmosphere. *J. Geophys. Res.*, vol. 106, pp. 32829-32839.
- Fassett C. I. and Head J. W., 2008. The timing of Martian valley network activity: constraints from buffered crater counting. *Icarus*, vol. 195, pp. 61-89.
- Fassett C. I. and Head J. W., 2011. Sequence and timing of conditions on early Mars The timing of martian valley network activity: constraints from buffered crater counting. *Icarus*, vol. 211, pp. 1204-1214.
- Ferdous J., Brandon A. D., Peslier A. H. and Pirotte Z., 2017. Evaluating crustal contributions to enriched shergottites from the petrology, trace elements, and Rb-Sr and Sm-Nd isotope systematics of Northwest Africa 856. *Geochimica & Cosmochimica Acta*, vol. 211, pp. 280-306.
- Filiberto J. and Treiman A. H., 2009. Martian magmas contained abundant chlorine, but little water. *Geology*, vol. 37, pp. 1087-1090.
- Filiberto J., 2017. Geochemistry of Martian basalts with constraints on magma genesis. *Chemical Geology*, vol. 466, pp. 1-14.
- Filiberto J., Chin E., Day J. M. D., Franchi I. A., Gross J., Greenwood R. C., Penniston-Dorland S., Schwenzer S. and Treiman A., 2012. Geochemistry of intermediate olivine-phyric shergottite northwest Africa 6234, with similarities to basaltic shergottite

northwest Africa 480 and olivine-phyric shergottite northwest Africa 2990. *Meteor Planet Sci*, vol. 47, pp. 1256-1273.

Filiberto J., Gross J., and McCubbin F. M., 2016. Constraints on the water, chlorine, and fluorine content of the Martian mantle. *Meteoritics & Planetary Science*, vol. 51, issue 11, pp. 2023-2035.

Fischer-Gödde M., Becker H. and Wombacher F., 2011. Rhodium, gold and other highly siderophile elements in orogenic peridotites and peridotite xenoliths. *Chemical Geology*, vol. 280, pp. 365-383.

Fleet M. E., Crocket J. H., and Stone W. E., 1996. Partitioning of platinum-group elements (Os, Ir, Ru, Pt, Pd) and gold between sulfide liquid and basalt melt. *Geochim. Cosmochim. Acta*, vol. 60, issue 13, pp. 2397-2412.

Floran R. J., Prinz M., Hlava P. F., Keil K., Nehru C. E., and Hinthorne J. R., 1978. The Chassigny meteorite: A cumulate dunite with hydrous amphibole-bearing melt inclusions. *Geochimica et Cosmochimica Acta*, vol. 42, pp. 1213-1229.

Foley C. N., Economou T., and Clayton R. N., 2003. Final chemical results from the Mars Pathfinder Alpha Proton X ray Spectrometer. *Journal of Geophysical Research*, vol. 108, 8096.

Foley C. N., Wadhwa M., Borg L. E., Janney P. E., Hines R., Grove T. L., 2005. The early differentiation history of Mars from 182W-142Nd isotope systematics in the SNC meteorites. *Geochim. Cosmochim. Acta*, vol. 69, pp. 4557-4571.

Fonseca R. O. C., Laurenz V., Mallmann G., Luguet A., Hoehne N. and Jochum K. P., 2012. New constraints on the genesis and long-term stability of Os-rich alloys in the Earth's mantle. *Geochimica et Cosmochimica Acta*, vol. 87, pp. 227-242.

Fonseca R. O. C., Mallmann G., O'Neill H. S. C., Campbell I. H. and Laurenz V., 2011. Solubility of Os and Ir in sulphide melt: implications for Re/Os fractionation in the upper mantle. *Earth Planet. Sci. Lett.*, vol. 311, pp. 339-350.

Fonseca R. O. C., Mallmann G., O'Neill H. S. C. and Campbell I. H., 2007. How chalcophile is rhenium? An experimental study of the solubility of Re in sulfide mattes. *Earth Planet. Sci. Lett.*, vol. 260, pp. 537-548.

Fraeman A. A. and Korenaga J., 2010. The influence of mantle melting on the evolution of Mars. *Icarus*, vol. 210, pp. 43-57.

Franchi I. A., Wright I. P., Sexton A. S., and Pillinger C. T., 1999. The oxygen isotopic composition of Earth and Mars. *Meteorit. Planet. Sci.*, vol. 34, pp. 657-661.

Franz H. B., Danielache S. O., Farquhar J. and Wing B. A., 2013. Mass-independent fractionation of sulfur isotopes during broadband SO₂ photolysis: comparison between 16O- and 18O-rich SO₂. *Chem. Geol.*, vol. 362, pp. 56-65.

Franz H. B., McAdam A. C., Ming D. W., Freissinet C., Mahaffy P. R., Eldridge D. L., Fischer W. W., Grotzinger J. P., House C. H., Hurowitz J. A., McLennan S. M., Schwenzler S. P., Vaniman D. T., Archer P. D., Atreya S. K., Conrad P. G., Dottin J. W. III, Eigenbrode J. L., Farley K. A., Glavin D. P., Johnson S. S., Knudson C. A., Morris R. V., Navarro-González R., Pavlov A. A., Plummer R., Rampe E. B., Stern J. C., Steele A., Summons R. E. and Sutter B., 2017. Large sulfur isotope fractionations in Martian sediments at Gale crater. *Nature Geoscience*, vol. 10, pp. 658-662.

Franz H. B., Sang-Tae K., Farquhar J., Day J. M. D., Economos R. C., McKeegan K. D., Schmitt A. K., Irving A. J., Hoek J. and Dottin J., 2014. Isotopic links between atmospheric chemistry and the deep sulphur cycle on Mars. *Nature*, vol. 508, pp. 364-368.

Friedman-Lentz R. C., Taylor G. J., and Treiman A. H., 1999. Formation of a martian pyroxenite: a comparative study of the nakhlite meteorites and Theo's Flow. *Meteorit. Planet. Sci.*, vol. 34, pp. 919-932.

Gale N. H., Arden J. W. and Hutchison R., 1975. The chronology of the Nakhla achondritic meteorite. *Earth Planet. Sci. Lett.*, vol. 26, pp. 195-206.

Gattacceca J., Devouard B., Debaille V., Rochette P., Lorand J. P., Bonal L., Beck P., Sautter V., Meier M. M. M., Gounelle M., Marrocchi Y., Maden C. and Busemann H., 2018. Nakhlite Caleta el Cobre 022: Initial Description and Comparison with other Nakhrites. *81st Annual Meeting of The Meteoritical Society 2018*, Abstract #6227.

Gattacceca J., Hewins R. H., Lorand J. P., Rochette P., Lagroix F., Cournede C., Uehara M., Pont S., Sautter V., Scorzelli R. B., Hombourger C., Munayco P., Zanda B., Channaoui H. and Ferriere L., 2013. Opaque minerals, magnetic properties, and paleomagnetism of the Tissint Martian meteorite. *Meteoritics & Planetary Science*, vol. 48, pp. 1919-1936.

Gelman S., Elkins-Tanton L. T., and Seager S., 2011. Mantle evolution in tidally locked terrestrial planets: degree-1 convection and implications for habitability. *Astrophys. J.*, vol. 735, pp. 1-8.

Giesting P. A., Schwenzer S. P., Filiberto J., Starkey N. A., Franchi I. A., Treiman A. H., Tindle A. G., and Grady M. M., 2015. Igneous and shock processes affecting chassignite amphibole evaluated using chlorine/water partitioning and hydrogen isotopes. *Meteoritics & Planetary Science*, vol. 50, issue 3, pp. 433-460.

Gillis K. M., Coogan L. A., and Chaussidon M., 2003. Volatile element (B, Cl, F) behavior in the roof of an axial magma chamber from the East Pacific Rise. *Earth and Planetary Science Letters*, vol. 213, pp. 447-462.

Ginibre C., Kronz A., and Worner G., 2002. High-resolution quantitative imaging of plagioclase composition using accumulated backscattered electron images: new constraints on oscillatory zoning. *Contributions to Mineralogy and Petrology*, vol. 142, issue 4, pp. 436-448.

Golombek M. P., Grant J. A., Crumpler L., Greeley R., Arvidson R., Bell III J. F., Weitz C. M., Sullivan R., Christensen P. R., Soderblom L. A., and Squyres S. W., 2006. Erosion rates at the Mars Exploration Rover landing sites and long-term climate change on Mars. *J. Geophys. Res.*, vol. 111, issue E12.

Graham A. L., Bevan A. W. R., and Hutchison R., 1985. Catalogue of meteorites. 4th ed. Tucson: University of Arizona Press, 460 p.

Grant T. B. and Kohn S. C., 2013. Phosphorus partitioning between olivine and melt: An experimental study in the system Mg_2SiO_4 - $Ca_2Al_2Si_2O_9$ - $NaAlSi_3O_8$ - $Mg_3(PO_4)_2$. *American Mineralogist*, vol. 98, pp. 1860-1869.

Gray C. M. and Compston W., 1974. Excess ^{26}Mg in the Allende meteorite. *Nature*, vol. 251, pp. 495-97.

- Greeley R. and Guest J. E., 1987. Geologic map of the eastern equatorial region of Mars. *U.S. Geological Survey Misc. Inv.*, Map I-1802-B.
- Greeley R. and Schneid B. D., 1991. Magma generation on Mars: amounts, rates, and comparisons with Earth, Moon, and Venus. *Science*, vol. 254, pp. 996-998.
- Greeley R. and Spudis P., 1981. Volcanism on Mars. *Rev. Geophys. Space Phys.*, vol. 19, pp. 13-41.
- Green D. H., Falloon T. J., Eggins S. M., and Yaxley G. M., 2001. Primary magmas and mantle temperatures. *European Journal of Mineralogy*, vol. 13, pp. 437-451.
- Greenwood J. P. and Blake R. E., 2006. Evidence for an acidic ocean on Mars from phosphorus geochemistry of Martian soils and rocks. *Geology*, vol. 34, pp. 953-956.
- Greenwood J. P., Mojzsis S. J. and Coath C. D., 2000a. Sulfur isotopic compositions of individual sulfides in Martian meteorites ALH 84001 and Nakhla: implications for crust-regolith exchange on Mars. *Earth Planet. Sci. Lett.*, vol. 184, pp. 23-35.
- Greenwood J. P., Riciputi L. R., McSween H. Y. and Taylor L. A., 2000b. Modified sulfur isotopic compositions of sulfides in the nakhlites and Chassigny. *Geochimica et Cosmochimica Acta*, vol. 64, issue 6, pp. 1121-1131.
- Greshake A., Fritz J., and Stöffler D., 2004. Petrology and shock metamorphism of the olivine-phyric shergottite Yamato 980459: Evidence for a two-stage cooling and a single-stage ejection history. *Geochimica et Cosmochimica Acta*, vol. 68, pp. 3459-2377.
- Gross J., Filiberto J., and Bell A. S., 2013. Water in the Martian interior: evidence for terrestrial MORB mantle-like volatile contents from hydroxyl-rich apatite in olivine-phyric shergottite NWA 6234. *Earth and Planetary Science Letters*, vol. 369, pp. 120-128.
- Grott M. and Breuer D., 2010. On the spatial variability of the martian elastic lithosphere thickness: evidence for mantle plumes? *J. Geophys. Res.*, vol. 115, E03005.
- Grotzinger J. P., Sumner D. Y., Kah L. C., Stack S., Edgar L., Rubin D., Lewis K., Schieber J., Mangold N., Milliken R., Conrad P. G., and others and the MSL Science Team, 2014. A habitable fluvio-lacustrine environment at Yellowknife Bay, Gale crater, Mars. *Science*, vol. 343, issue 6169.
- Gunther D. and Hattendorf B., 2005. Solid sample analysis using laser ablation inductively coupled plasma mass spectrometry. *TrAC Trends in Analytical Chemistry*, vol. 24, issue 3, pp. 255-265.
- Halliday A. N., Wanke H., Birck J. L., Clayton R. N., 2001. The accretion, composition and early differentiation of Mars. *Space Sci. Rev.*, vol. 96, pp. 197-230.
- Hallis L. J. and Taylor G. J., 2011. Comparisons of the four Miller Range nakhlites, MIL 03346, 090030, 090032 and 090136: Textural and compositional observations of primary and secondary mineral assemblages. *Meteoritics & Planetary Science*, vol. 46, issue 12, pp. 1787-1803.
- Hallis L. J., 2013. Alteration assemblages in the Miller Range and Elephant Moraine regions of Antarctica: Comparisons between terrestrial igneous rocks and Martian meteorites. *Meteoritics & Planetary Science*, vol. 48, issue 2, pp. 165-179.

- Hallis L. J., Taylor G. J., Nagashima K. and Huss G. R., 2012. Magmatic water in the martian meteorite Nakhla. *Earth Planet. Sci. Lett.*, vol. 359-360, pp. 84-92.
- Hammer J. E. and Rutherford M. J., 2005. Experimental crystallization of Fe-rich basalt: Application to cooling rate and oxygen fugacity of nakhlite MIL 03346. *36th Lunar and Planetary Science Conference*, Abstract #1999.
- Hammer J. E., 2009. Application of a textural geospeedometer to the late-stage magmatic history of MIL 03346. *Meteorit. Planet. Sci.*, vol. 44, pp. 141-154.
- Harder H., 1976. Nontronite synthesis at low temperatures. *Chem. Geol.*, vol. 18, pp. 169-180.
- Harper C. L., Nyquist L. E., Bansal B., Wiesmann H., and Shih C. Y., 1995. Rapid accretion and early differentiation of Mars indicated by $^{142}\text{Nd}/^{144}\text{Nd}$ in SNC meteorites. *Science*, vol. 267, pp. 213-217.
- Hartmann W. K. and Berman D. C., 2000. Elysium Planitia lava flows: crater count chronology and geological implications. *J. Geophys. Res.*, vol. 105, issue E6, pp. 15011-15025.
- Hartmann W. K. and Neukum G., 2001. Cratering chronology and the evolution of Mars. *Space Sci. Rev.*, vol. 96, pp. 165-194.
- Harvey R. P. and McSween Jr. H. Y., 1992. The parent magma of the nakhlite meteorites: clues from melt inclusions. *Earth Planet. Sci. Lett.*, vol. 111, pp. 467-482.
- Harvey R. P., Wadhwa M., McSween H. Y. Jr., and Crozaz G., 1993. Petrography, Mineral Chemistry and Petrogenesis of Antarctic Shergottite LEW88516. *Geochim. Cosmochim. Acta*, vol. 57, pp. 4769-4783.
- Harvey J., Gannoun A., Burton K. W., Rogers N. W., Alard O. and Parkinson I. J., 2006. Ancient melt extraction from the oceanic upper mantle revealed by Re-Os isotopes in abyssal peridotites from the Mid-Atlantic ridge. *Earth and Planetary Science Letters*, vol. 244, issue 3-4, pp. 606-621.
- Hauck S.A. and Phillips R. J., 2002. Thermal and crustal evolution of Mars. *J. Geophys. Res.*, vol. 107, issue E7.
- Head J. W., Kreslavsky M. A., and Pratt S., 2002. Northern lowlands of Mars: evidence for widespread volcanic flooding and tectonic deformation in the Hesperian period. *J. Geophys. Res.*, vol. 107, issue E1.
- Head J. W., Wilson L., and Mitchell K. L., 2003. Generation of recent massive water floods at Cerberus Fossae, Mars by dike emplacement, cryospheric cracking, and confined aquifer groundwater release. *Geophys. Res. Lett.*, vol. 30, issue 11.
- Herd C. D. K., 2003. The oxygen fugacity of olivine-phyric Martian basalts and the components within the mantle and crust of Mars. *Meteoritics & Planetary Science*, vol. 38, pp. 1793-1805.
- Herd C. D. K., Borg L. E., Jones J. H., and Papike J. J., 2002. Oxygen fugacity and geochemical variations in the martian basalts: Implications for martian basalt petrogenesis and the oxidation state of the upper mantle of Mars. *Geochimica & Cosmochimica Acta*, vol. 66, pp. 2025-2036.

Herd C. D. K., Walton E. L., Agee C. B., Muttik N., Ziegler K., Shearer C. K., Bell A. S., Santos A. R., Burger P. V., Simon J. I., Tappa M. J., McCubbin F. M., Gattacceca J., Lagroix F., Sanborn M. E., Yin Q.-Z., Cassata W. S., Borg L. E., Lindvall R. E., Kruijjer T. S., Brennecke G. A., Kleine T., Nishiizumi K. and Caffee M. W., 2017. The Northwest Africa 8159 martian meteorite: Expanding the martian sample suite to the early Amazonian. *Geochimica et Cosmochimica Acta*, vol. 218, pp. 1-26.

Hidaka H., Yoneda S., and Nishiizumi K., 2009. Cosmic ray exposure histories of Martian meteorites studied from neutron capture of Sm and Gd isotopes. *Earth & Planetary Science Letters*, vol. 288, pp. 564-571.

Hirth G. and Kohlstedt D. L., 1996. Water in the oceanic mantle: Implications for rheology, melt extraction, and the evolution of the lithosphere. *Earth Planet. Sci. Lett.*, vol. 144, pp. 93-108.

Hollister L. S. and Hargraves R. B., 1970. Compositional zoning and its significance in pyroxenes from two coarse grained Apollo 11 samples. *Proceedings of the Apollo 11 Lunar Science Conference*, vol 1, pp. 541-550.

Howard A. D., Moore J. M., and Irwin III R. P., 2005. An intense terminal epoch of widespread fluvial activity on Mars: 1. valley network incision and associated deposits. *J. Geophys. Res.*, vol. 110, E12S14.

Howarth G., Pernet-Fisher J., Bodnar R., and Taylor L., 2015. Evidence for the exsolution of Cl-rich fluids in Martian magmas: apatite petrogenesis in the enriched lherzolitic shergottite Northwest Africa 7755. *Geochimica et Cosmochimica Acta*, vol. 166, pp. 234-248.

Hurowitz J. A., McLennan S. M., Tosca N. J., Arvidson R. E., Michalski J. R., Ming D. W., Schröder C., and Squyres S. W., 2006. In-situ and experimental evidence for acidic weathering on Mars. *Journal of Geophysical Research*, vol. 111, E02S19.

Hustoft J. W. and Kohlstedt D. L., 2006. Metal-silicate segregation in deforming dunitic rocks. *Geochem. Geophys. Geosyst.*, 7:Q02001.

Hynek B. M. and Phillips R. J., 2003. New data reveal mature, integrated drainage systems on Mars indicative of past precipitation. *Geology*, vol. 31, pp. 757-760.

Imae N., Ikeda Y. and Kojima H., 2005. Petrology of the Yamato nakhlites. *Meteoritics & Planetary Science*, vol. 40, n. 11, pp. 1581-1598.

Imae N., Ikeda Y., Shinoda K., Kojima H. and Iwata N., 2003. Yamato nakhlites: Petrography and mineralogy. *Antarct. Meteorite Res.*, vol. 16, pp. 13-33.

Imae N., Okazaki R., Kojima H. and Nagao K., 2002. The first nakhlite from Antarctica. *Lunar and Planetary Science XXXIII*, Abstract #1483.

Ioannis P. B., Liu Y., DeCarli P. S., Melosh H. J., McSween H. Y., Bodnar R. J. and Taylor L. A., 2013. The Tissint Martian meteorite as evidence for the largest impact excavation. *Nat. Commun.*, issue 4(1404).

Irving A. J., Kuehner S. M., Tanaka R., Herd C. D. K., Chen G. and Lapen T. J., 2012. The Tissint depleted permafic olivine-phyric shergottite: Petrologic, elemental, and isotopic characterization of a recent Martian fall in Morocco. *Meteoritics & Planetary Science* 47th, Abstract #2010.

Irwin III R. P. and Howard A. D., 2002. Drainage basin evolution in Noachian Terra Cimmeria, Mars. *J. Geophys. Res.*, vol. 107, issue E7.

Ishikawa A., Senda R., Suzuki K., Dale C. W. and Meisel T., 2014. Re-evaluating digestion methods for highly siderophile element and ^{187}Os isotope analysis: Evidence from geological reference materials. *Chemical Geology*, vol. 384, pp. 27-46.

Ito G., Shen Y., Hirth G., and Wolfe C. J., 1999. Mantle flow, melting and dehydration of the Iceland mantle plume. *Earth Planet. Sci. Lett.*, vol. 165, pp. 81-96.

Ivanov B. A., 2001. Mars/Moon cratering rate ratio estimates. *Space Sci. Rev.*, vol. 96, pp. 87-104.

Jakosky B. M. and Jones J. H., 1997. The history of martian volatiles. *Rev. Geophys.*, vol. 35, pp. 1-16.

Jean M. M., McCanta M., Howarth G. H., and Taylor L. A., 2017. The Martian olivine glossary: common textures and zoning patterns, and implications for ascent of Martian magmas and their plumbing systems. *Lunar and Planetary Science 48th*, Abstract #2067.

Jerram D. A. and Martin V. M., 2008. Understanding crystal populations and their significance through the magma plumbing system. *Geological Society of London Special Publication*, vol. 304, pp. 133-148.

Johnson M. C., Rutherford M. J., and Hess P. C., 1991. Chassigny petrogenesis: Melt compositions, intensive parameters, and water contents of Martian (?) magmas. *Geochimica et Cosmochimica Acta*, vol. 55, pp. 349-366.

Jones J. H., Neal C. R., and Ely J. C., 2003. Signatures of the highly siderophile elements in the SNC meteorites and Mars: a review and petrologic synthesis. *Chemical Geology*, vol. 196, pp. 21- 41.

Jull A. J. T., Beck J. W., and Burr G. S., 2000. Isotopic evidence for extraterrestrial organic matter in the Martian meteorite Nakhla. *Geochim. Cosmochim. Acta*, vol. 64, pp. 3763-3772.

Karato S. I., 2008. Deformation of Earth Materials. Cambridge University Press, 463 p.

Karato S., Paterson M. S., and Fitz Gerald J. D., 1986. Rheology of synthetic olivine aggregates: Influence of grain size and water. *J. Geophys. Res.*, vol. 91, pp. 8151-8176.

Kargel J. S. and Strom R. G., 1992. Ancient glaciation on Mars. *Geology*, vol. 20, pp. 3-7.

Kiefer W. S., 2003. Melting in the martian mantle: Shergottite formation and implications for present-day mantle convection on Mars. *Meteoritics & Planetary Science*, vol. 39, issue 12, pp. 1815-1832.

King P. L. and McLennan S. M., 2010. Sulfur on Mars. *Elements*, vol. 6, pp. 107-112.

Kinzler R. J. and Grove T. L., 1992. Primary magmas of mid-ocean ridge basalts 1. Experiments and methods. *Journal of Geophysical Research*, vol. 97, pp. 6885-6906.

Kleine T., Mezger K., Munker C., Palme H., Bischoff A., 2004. ^{182}Hf - ^{182}W isotope systematics of chondrites, eucrites, and martian meteorites: chronology of core formation and early mantle differentiation in Vesta and Mars. *Geochim. Cosmochim. Acta*, vol. 68, pp. 2935-46.

- Kleine T., Münker C., Mezger K., and Palme H., 2002. Rapid accretion and early core formation on asteroids and terrestrial planets from Hf-W chronometry. *Nature*, vol. 418, pp. 952-954.
- Korenaga J., 2010. On the likelihood of plate tectonics on superearths: does size matter? *The Astrophysical Journal Letters*, vol. 725, pp. 43-46.
- Korochantseva E. V., Schwenger S., Buikin A. I., Hopp J., Ott U. and Trieloff M., 2011. Cosmic ray exposure ages of nakhlites - Nakhla, Lafayette, Governador Valadares - and Chassigny: one ejection event? *42nd Lunar and Planetary Conference*, Abstract #1263.
- Kreslavsky M. A. and Head J. W., 2002. Fate of outflow channel effluents in the northern lowlands of Mars: the Vastitas Borealis Formation as a sublimation residue from frozen ponded bodies of water. *J. Geophys. Res.*, vol. 107, issue E12.
- Kubo T., Ohtani E., Kato T., Shinmei T., and Fujino K., 1998. Effects of water on the a-b transformation kinetics in San Carlos olivine. *Science*, vol. 281, pp. 85-87.
- La Tourrette T. and Wasserburg G. J., 1998. Mg diffusion in anorthite: implications for the formation of early solar system planetesimals. *Earth Planet. Sci. Lett.*, vol. 158, pp. 91-108.
- Labidi J., Cartigny P. and Jackson M. G., 2015. Multiple sulphur isotope composition of oxidized Samoan melts and the implications of a sulfur isotope “mantle array” in chemical geodynamics. *Earth Planet. Sci. Lett.*, vol. 417, pp. 28-39.
- Lang N. P., McSween H. Y., Tornabene L. L., Hardgrove C. J., and Christensen P. R., 2010. Re-examining the relationship between Apollinaris Patera and the basalts of the Gusev crater plains, Mars. *Journal of Geophysical Research*, vol. 115, E04006.
- Langenhorst F. and Poirier J-P., 2000. Anatomy of black veins in Zagami: Clues to the formation of high-pressure phase. *Earth Planet. Sci. Lett.*, vol. 184, pp. 37-55.
- Langevin Y., Poulet F., Bibring J. P., and Gondet B., 2005. Sulfates in the north polar region of Mars by OMEGA Mars Express. *Science*, vol. 307, pp. 1584-1585.
- Lapen T. J., Righter M., Andreasen R., Irving A. J., Satkoski A. M., Beard B. L., Nishiizumi K., Jull A. J. T. and Caffee M. W., 2017. Two billion years of magmatism recorded from a single Mars meteorite ejection site. *Science Advances*, vol. 3, issue 2:e1600922.
- Laskar J., Correia A. C. M., Gastineau M., Joutel F., Levrard B., and Robutel P., 2004. Long-term evolution and chaotic diffusion of the insolation quantities of Mars. *Icarus*, vol. 170, pp. 343-364.
- Lee D. C. and Halliday A. N., 1995. Hafnium-tungsten chronometry and the timing of terrestrial core formation. *Nature*, vol. 378, pp. 771-774.
- Lee D. C. and Halliday A. N., 1997. Core formation on Mars and differentiated asteroids. *Nature*, vol. 388, pp. 854-857.
- Lee M. R. and Chatzitheodoridis E., 2016. Replacement of glass in the Nakhla meteorite by berthierine: Implications for understanding the origins of aluminum-rich phyllosilicates on Mars. *Meteoritics & Planetary Science*, vol. 51, issue 9, pp. 1643-1653.

- Lee M. R., Bland P. A., and Graham G., 2003. Preparation of TEM samples by focused ion beam (FIB) techniques: Applications to the study of clays and phyllosilicates in meteorites. *Mineralogical Magazine*, vol. 67, pp. 581-592.
- Lee M. R., MacLaren I., Andersson S. M. L., Kovaks A., Tomkinson T., Mark D. F. and Smith C. L., 2015. Opal-A in the Nakhla meteorite: A tracer of ephemeral liquid water in the Amazonian crust of Mars. *Meteoritics & Planetary Science*, vol. 50, issue 8, pp. 1362-1377.
- Lee M. R., Tomkinson T., Mark D. F., Stuart F. M. and Smith C. L., 2013. Evidence for silicate dissolution on Mars from the Nakhla meteorite. *Meteoritics & Planetary Science*, vol. 48, issue 2, pp. 224-240.
- Lee T., Papanastassiou D. A., Wasserburg G. J., 1976. Demonstration of ^{26}Mg excess in Allende and evidence for ^{26}Al . *Geophys. Res Lett.*, vol. 3, pp. 109-112.
- Leger A. et al., 2009. Transiting exoplanets from the CoRoT space mission VIII. CoRoT-7b: the first super-Earth with measured radius. *Astronomy & Astrophysics*, vol. 506, pp. 287-302.
- Lentz R. C. F., McSween Jr. H. Y., Ryan J., and Riciputi L. R., 2001. Water in martian magmas: clues from light lithophile elements in shergottite and nakhlite pyroxenes. *Geochim. Cosmochim. Acta*, vol. 56, pp. 4551-5465.
- Li Q. and Kiefer W. S., 2007. Mantle convection and magma production on present-day Mars: Effects of temperature-dependent rheology. *Geophysical Research Letters*, 34:L16203.
- Liu J., Liu Q. Y., Guo B., Yuen D. A., and Song H. Z., 2007. Small-scale convection in the upper mantle beneath the Chinese Tian Shan Mountains. *Physics of the Earth and Planetary Interiors*, vol. 163, pp. 179-190.
- Liu Y., Baziotis I. P., Asimow P. D., Bodnar R. J., and Taylor L. A., 2016. Mineral chemistry of the Tissint meteorite: Indications of two-stage crystallization in a closed system. *Meteoritics & Planetary Science*, vol. 51, issue 12, pp. 2293-2315.
- Lodders K., 1998. A survey of Shergottite, Nakhlite and Chassigny meteorites whole-rock compositions. *Meteorit. & Planet. Sci.*, vol. 33, A183-190.
- Lofgren G. E., Huss G. R., and Wasserburg G. J., 2006. An experimental study of trace-element partitioning between Ti-Al-clinopyroxene and melt: Equilibrium and kinetic effects including sector zoning. *American Mineralogist*, vol. 91, issue 10, pp. 1596-1606.
- Lorand J. P., Luguet A., Alard O., Bezos A. and Meisel T., 2008. Abundance and distribution of platinum-group elements in orogenic lherzolites; a case study in a Fontete Rouge lherzolite (French Pyrénées). *Chemical Geology*, vol. 248, issue 3-4, pp.174-194.
- Lucchitta B. K., 1981. Mars and Earth: comparison of cold climate features. *Icarus*, vol. 45, pp. 264-303.
- Lunine L. I., Chambers J., Morbidelli A., and Leshin L. A., 2004. Origin of martian water. *Icarus*, vol. 165, pp. 1-8.
- Madden M. E., Bodnar R. J., and Rimstidt J. D., 2004. Jarosite as an indicator of water-limited chemical weathering on Mars. *Nature*, vol. 431, pp. 821-823.

- Mallmann G. and O'Neill H. S. C., 2007. The effect of oxygen fugacity on the partitioning of rhenium between crystals and silicate melt during mantle melting. *Geochim. Cosmochim. Acta*, vol. 71, issue 11, pp. 2837-2857.
- Mandeville C. W., Webster J. D., Tappen C., Taylor B. E., Timbal A., Sasaki A., Hauri E. and Bacon C. R., 2009. Stable isotope and petrologic evidence for open-system degassing during the climactic and pre-climactic eruptions of Mt. Mazama, Crater Lake, Oregon. *Geochim. Cosmochim. Acta*, vol. 73, pp. 2978-3012.
- Mangold N., Adeli S., Conway S., Ansan V., and Langlais B. A., 2012. Chronology of early Mars climatic evolution from impact crater degradation. *J. Geophys. Res.*, vol. 117, E04003.
- Marinova M. M., Aharonson O., Asphaug E., 2008. Mega-impact formation of the Mars hemispheric dichotomy. *Nature*, vol. 453, pp. 1216-1219.
- Marti K., Kim J. S., Thakur A. N., McCoy T. J. and Keil K., 1995. Signatures of the Martian Atmosphere in Glass of the Zagami Meteorite. *Science*, vol. 267, pp. 1981-1984.
- Martin D., Griffiths R. W., and Campbell I. H., 1987. Compositional and thermal convection in magma chambers. *Contributions to Mineralogy and Petrology*, vol. 96, pp. 465-475.
- Marty B. and Marti K., 2002. Signatures of early differentiation of Mars. *Earth Planet. Sci. Lett.*, vol. 196, pp. 251-263.
- Mather T. A., McCabe J. R., Rai V. K., Thiemens M. H., Pyle D. M., Heaton T. H. E., Sloane H. J. and Fern G. R., 2006. Oxygen and sulfur isotopic composition of volcanic sulfate aerosol at the point of emission. *J. Geophys. Res.*, 111:D18205.
- Matsui T. and Abe Y., 1987. Evolutionary tracks of the terrestrial planets. *Earth, Moon, Planets*, vol. 39, pp. 207-214.
- McBirney A. R. and Noyes R. M., 1979. Crystallization and Layering of the Skaergaard Intrusion. *Journal of Petrology*, vol. 20, issue 3, pp. 487-554.
- McCanta M. C., Beckett J. R., and Stolper E. M., 2016. Correlations and zoning patterns of phosphorus and chromium in olivine from H chondrites and the LL chondrite Semarkona. *Meteoritics & Planetary Science*, vol. 51, issue 3, pp. 520-546.
- McCoy T. J. and Lofgren G. E., 1999. Crystallization of the Zagami Shergottite: An experimental study. *Earth & Planetary Science Letters*, vol. 173, pp. 397-411.
- McCoy T. J., Taylor G. J. and Keil K., 1992. Zagami: Product of a two-stage magmatic history. *Geochimica & Cosmochimica Acta*, vol. 56, pp. 3571-3582.
- McCoy T. J., Wadhwa M., and Keil K., 1995. Zagami: another new lithology and a complex near-surface magmatic history. *26th Lunar & Planetary Science Conference*, Abstract #925-926.
- McCubbin F. M., Boyce J. W., Srinivasan P., Elardo S. M., Santos A. R., Filiberto J., and Shearer C. K. Jr. 2016. Heterogeneous distribution of H₂O in the Martian interior: Implications for the abundances of H₂O in depleted and enriched mantle sources. *Meteoritics and Planetary Science*, vol. 51, issue 11, pp. 2036-2060.
- McCubbin F. M., Elardo S. M., Shearer C. K., Smirnov A., Hauri E. H., and Draper D. S., 2013. A petrogenetic model for the comagmatic origin of chassignites and nakhlites:

Inferences from chlorine-rich minerals, petrology, and geochemistry. *Meteoritics & Planetary Science*, vol. 48, n. 5, pp. 819-853.

McCubbin F. M., Hauri E. H., Elardo S. M., Vander Kaaden K. E., Wang J., and Shearer C. K., 2012. Hydrous melting of the Martian mantle produced both depleted and enriched shergottites. *Geology*, vol. 40, pp. 683-686.

McCubbin F. M., Tosca N. J., Smirnov A., Nekvasil H., Steele A., Fries M., and Lindsley D. H., 2009. Hydrothermal jarosite and hematite in a pyroxene-hosted melt inclusion in martian meteorite Miller Range (ML) 03346: Implications for magmatic-hydrothermal fluids on Mars. *Geochimica et Cosmochimica Acta*, vol. 73, pp. 4907-4917.

McDonough W. F. and Sun S., 1995, The composition of the Earth. *Chem. Geol.*, vol. 120, pp. 223-254.

McKay C. P., Friedmann E. I., Frankel R. B., Bazylinski D. A., 2004. Magnetotactic bacteria on Earth and on Mars. *Astrobiology*, vol. 3, issue 2, pp. 263-270.

McKay D. S., Gibson E. K., Thomas-Keprta K. L., Vali H., Romanek C. S., Clemett S. J., Chillier X. D. F., Maechling C. R., and Zare R. N., 1996. Search for past life on Mars: Possible relic biogenic activity in martian meteorite ALH 84001. *Science*, vol. 273, pp. 924-930.

McKay G., Le L. and Wagstaff J., 1993. The Nakhla parent melt: REE partition coefficients and clues to major element composition. *24th Lunar and Planetary Science Conference*, pp. 965-966.

McSween H. Y. and Harvey R. P., 1993. Outgassed water on Mars: constraints from melt inclusions in SNC meteorites. *Science*, vol. 259, pp. 1890-1892.

McSween H. Y. and Huss G., 2010. *Cosmochemistry* (1st ed.). Cambridge University Press.

McSween H. Y. Jr., 2002. The rocks of Mars, from far and near. *Meteoritics & Planetary Science*, vol. 37, pp. 7-25.

McSween H. Y., 1984. SNC meteorites: are they Martian rocks? *Geology*, vol. 12, pp. 3-6.

McSween H. Y., 1994. What Have we Learned about Mars from SCN Meteorites. *Meteoritics*, vol. 29, pp. 757-779.

McSween H. Y., 2015. Petrology on Mars. *American Mineralogist*, vol. 100, pp. 2380-2395.

McSween H. Y., Grove T. L., Lentz R. C. F., Dann J. C., Holzheid A. H., Riciputi L. R., and Ryan J. G., 2001. Geochemical evidence for magmatic water within Mars from pyroxenes in the Shergotty meteorite. *Nature*, vol. 409, pp. 487-490.

McSween H. Y., Ruff S. W., Morris R. V., Bell J. F., Herkenhoff K., Gellert R., Schmidt M., 2006. Alkaline volcanic rocks from the Columbia Hills, Gusev crater, Mars. *Journal of Geophysical Research*, E: Planets, 111(9), E09S91.

McSween H. Y., Taylor G. J., and Wyatt M. B., 2009. Elemental composition of the martian crust. *Science*, vol. 324, pp. 736-739.

- Meado A. L., Schwenzer S. P., Hammond S. J., and Filiberto J., 2017. Crystallization history of gabbroic shergottite NWA 6963 as revealed by pyroxene zoning. *48th Lunar and Planetary Science Conference*, Abstract #1504.
- Médard E. and Grove T. L., 2006. Early hydrous melting and degassing of the Martian interior. *J. Geophys. Res.*, vol. 111, E11003.
- Meisel T. and Moser J., 2004. Reference materials for geochemical PGE analysis: new analytical data for Ru, Rh, Pd, Os, Ir, Pt and Re by isotope dilution ICP-MS in 11 geological reference materials. *Chemical Geology*, vol. 208, issue 1-4, pp. 319-338.
- Meisel T. and Moser J., 2004. Platinum-group element and rhenium concentrations in low abundance reference materials. *Geostandards and geoanalytical research*, vol. 28, issue 2, pp. 233-250.
- Melosh H. J. and Vickery A. M., 1989. Impact erosion of the primordial atmosphere of Mars. *Nature*, vol. 338, pp. 487-489.
- Mikouchi T. and Miyamoto M., 1997. Yamato-793605: A new Lherzolithic Shergottite from the Japanese Antarctic Meteorite Collection. *Antarct. Meteorite Res.*, vol. 10, pp. 41-60.
- Mikouchi T., Koizumi E., Monkawa A., Ueda Y., and Miyamoto M., 2003. Mineralogy and petrology of Yamato-000593: Comparison with other Martian nakhlite meteorites. *Antarctic Meteorite Research*, vol. 16, pp. 34-57.
- Mikouchi T., Miyamoto M., and McKay G. A., 1999. The role of undercooling in producing igneous zoning trends in pyroxenes and maskelynites among basaltic Martian meteorites. *Earth and Planetary Science Letters*, vol. 173, pp. 235-256.
- Mikouchi T., Monkawa A., Koizumi E., Chokai J., and Miyamoto M., 2005. MIL 03346 nakhlite and NWA 2737 ("Diderot") chassignite: Two new Martian cumulate rocks from hot and cold deserts. *36th Lunar and Planetary Science Conference*, Abstract #1994.
- Mikouchi T., Yamada I., and Miyamoto M., 2000. Symplectic exsolution in olivine from the Nakhla martian meteorite. *Meteorit. Planet. Sci.*, vol. 35, pp. 937-942.
- Milliken R. E., Edgett K. S., Swayze G. A., Clark R. N., Thomson B. J., Anderson R., and Bell III J. F., 2009. Clay and sulfate-bearing rocks in a stratigraphic sequence in Gale crater. *Lunar Planet. Sci.*, vol. 40, Abstract #1479.
- Milman-Barris M. S., Beckett J. R., Baker M. B., Hofmann A. E., Morgan Z., Crowley M. R., Vielzeuf D., and Stolper E., 2008. Zoning of phosphorus in igneous olivine. *Contributions to Mineralogy and Petrology*, vol. 155, pp. 739-765.
- Misawa K., Kojima H., Imae H. and Nakamura N., 2003a. The Yamato nakhlite consortium. *Antarct. Meteorite Res.*, vol. 16, pp. 1-12.
- Misawa K., Shih C. Y., Wiesmann H. and Nyquist L. E., 2003b. Crystallization and alteration ages of the Antarctic nakhlite Yamato 000593. *Lunar and Planetary Science XXXIV*, Abstract #1556.
- Misawa K., Shih C. Y., Wiesmann H., Garrison D. H., Nyquist L. E. and Bogard D. D., 2005. Rb-Sr, Sm-Nd and Ar-Ar isotopic systematics of Antarctic nakhlite Yamato 000593. *Antarctic Meteorite Research*, vol. 18, pp. 133-151.

- Mittlefehldt D. W., 1994. ALH84001, a cumulate orthopyroxenite member of the SNC meteorite group. *Meteoritics*, vol. 29, pp. 214-221.
- Miyamoto M., Duke M. B., and McKay D. S., 1985. Chemical Zoning and Homogenization of Pasamonte-type Pyroxene and Their Bearing on Thermal Metamorphism of a Howardite Parent Body. *Journal of Geophysical Research*, 90:C629-C635.
- Monkawa A., Mikouchi T., Koizumi E., Chokai J., and Miyamoto M., 2004. Fast cooling history of the Chassigny Martian meteorite. *35th Lunar and Planetary Science Conference*, Abstract #1535.
- Moore J. M. and Wilhelms D. E., 2001. Hellas as a possible site of ancient ice-covered lakes on Mars. *Icarus*, vol. 154, pp. 258-276.
- Morbidelli A., Lunine J. I., O'Brien D. P., Raymond S. N., and Walsh K. J., 2012. Building terrestrial planets. *Annual Review of Earth and Planetary Sciences*, vol. 40, pp. 251-275.
- Moresi L. and Solomatov V., 1997. Mantle convection with a brittle lithosphere: thoughts on the global tectonic styles of the Earth and Venus. *Geophysical Journal International*, vol. 133, pp. 669-682.
- Moussallam Y., Oppenheimer C., Scaillet B., Buisman I., Kimball C., Dunbar N., Burgisser A., Chipper C. I., Andujar J., and Kyle P., 2015. Megacrystals track magma convection between reservoir and surface. *Earth and Planetary Science Letters*, vol. 413, pp. 1-12.
- Mungall J. E. and Brenan J. M., 2014. Partitioning of platinum-group elements and Au between sulfide liquid and basalt and the origins of mantle-crust fractionation of the chalcophile elements. *Geochimica et Cosmochimica Acta*, vol. 125, pp. 265-289.
- Murchie S. L. and the CRISM Science and Engineering Teams, 2008. First results from the Compact Reconnaissance Imaging Spectrometer for Mars (CRISM). *Lunar Planet. Sci.*, vol. 39, Abstract #1472.
- Murchie S. L. et al., 2009. A synthesis of Martian aqueous mineralogy after 1 Mars year of observations from the Mars Reconnaissance Orbiter. *J. Geophys. Res.*, vol. 114, E00D06.
- Musselwhite D. S., Dalton H. A., Kiefer W. S., and Treiman A. H., 2006. Experimental petrology of the basaltic shergottite Yamato-980459: implications for the thermal structure of the Martian mantle. *Meteoritics & Planetary Science*, vol. 41, issue 9, pp. 1271-1290.
- Mustard J. F. et al., 2008. Hydrated silicate minerals on Mars observed by the Mars reconnaissance orbiter CRISM instrument. *Nature*, vol. 454, pp. 305-309.
- Mustard J. F., Cooper C. D., and Rifkin M. K., 2001. Evidence for recent climate change on Mars from the identification of youthful near-surface ground ice. *Nature*, vol. 412, pp. 411-414.
- Mustard J. F., Poulet F., Gendrin A., Bibring J. P., Langevin Y., Gondet B., Mangold N., Bellucci G., and Altieri F., 2005. Olivine and pyroxene diversity in the crust of Mars. *Science*, vol. 307, pp. 1594-1597.

- Nagao K., Park J., Okazaki R., Imae N. and Kojima H., 2009. Noble gas distributions in the Yamato 000593 nakhlite deciphered by laser ablation analysis and mineral separation. *Lunar Planet. Sci. XL*, Abstract #1682.
- Nakamura N., Unruh D. M., Tatsumoto M. and Hutchison R., 1982. Origin and evolution of the Nakhla meteorite inferred from the Sm-Nd and U-Pb systematics and REE, Ba, Sr, Rb and K abundances. *Geochimica & Cosmochimica Acta*, vol. 46, pp. 1555-1573.
- Neukum G., Basilevsky A. T., Chapman M. G., Werner S. C., van Gasselt S., Jaumann R., Hauber E., Hoffman H., Wolf U., Head J. W., Greeley R., McCord T. B., and the HRSC Co- Investigator Team, 2007. The geologic evolution of Mars: episodicity of resurfacing events and ages from cratering analysis of image data and correlation with radiometric ages of martian meteorites. *Seventh International Conference on Mars*, Abstract #3015.
- Niihara T., Misawa K., Nyquist L.E., Park J., Hirata D., Yamashita H. and Miya-moto H., 2015. Complicated magmatism of basaltic shergottites: implications from pyroxene zoning in Zagami. *46th Lunar and Planetary Science Conference*, Abstract #1721.
- Nimmo F. and Stevenson D. J., 2000. Influence of early plate tectonics on the thermal evolution and magnetic field of Mars. *J. Geophys. Res.*, vol. 105, pp. 11,969-11,979.
- Nimmo F. and Tanaka K., 2005. Early crustal evolution of Mars. *Ann. Rev. Earth Planet. Sci.*, vol. 33, pp. 133-161.
- Nininger H. H., 1935. The Lafayette meteorite. *Pop. Astron.*, vol. 1.
- Noack L. and Breuer D., 2014. Plate tectonics on rocky exoplanets: Influence of initial conditions and mantle rheology. *Planetary and Space Science*, vol. 98, pp. 41-49.
- Noguchi T., Nakamura T., Misawa K., Imae N., Aoki T. and Toh S., 2009. Laihunite and jarosite in the Yamato 00 nakhlites: Alteration products on Mars? *J. Geophys. Res.*, vol. 114, E10004.
- Norman M. D., 1999. The composition and thickness of the crust of Mars estimated from rare earth elements and neodymium-isotopic compositions of Martian meteorites. *Met. Planet. Sci.*, vol. 34, pp. 439-449.
- Nyquist L. E., 1995. "Martians" young and old: Zagami and ALH84001. *26th Lunar and Planetary Science Conference*, Abstract #1065-1066.
- Nyquist L. E., Bogard D. D., Shih C. Y., Greshake A., Stoffler D., and Eugster O., 2001. Ages and geologic histories of Martian meteorites. *Chronology and Evolution of Mars*, vol. 96, pp. 105-164.
- Nyquist L. E., Shih C. Y. and Reese Y. D., 2006. Initial isotopic heterogeneity in Zagami: Evidence of a complex magmatic history. *Meteorit. & Planet. Sci.* 41, Abstract #5143.
- Nyquist L. E., Shih C. Y., and Reese Y. D., 2010. Rb-Sr and Sm-Nd ages of Zagami DML and Sr isotopic heterogeneity in Zagami. *73th Meteoritics & Planetary Science Meeting*, Abstract #5243.
- O'Neill C. and Lenardic A., 2007. Geological consequences of super-sized Earths. *Geophysical Research Letters*, vol. 34, L19204.
- Ohmoto H. and Goldhaber M. B., 1997. Sulfur and carbon isotopes. In *Barnes, Geochemistry of Hydrothermal Ore Deposits* (3rd ed.). Wiley, pp. 517 - 611.

- Ojha L., Wilhelm M. B., Murchie S. L., McEwen A. S., Wray J. J., Hanley J., Massé M., and Chojnacki M., 2015. Spectral evidence for hydrated salts in recurring slope lineae on Mars. *Nature Geoscience*, vol. 8, pp. 829-832.
- Okazaki R., Nagao K., Imae N. and Kojima H., 2003. Noble gas signatures of Antarctic nakhlites, Yamato (Y) 000593, Y000749, and Y000802. *Antarct. Meteorite Res.*, vol. 16, pp. 58-79.
- Orosei R., Lauro S. E., Pettinelli E., Cicchetti A., Coradini M., Cosciotti B., Di Paolo F., Flamini E., Mattei E., Pajola M., Soldovieri F., Cartacci M., Cassenti F., Frigeri A., Giuppi S., Martufi R., Masdea A., Mitri G., Nenna C., Noschese R., Restano M. and Seu R., 2018. Radar evidence of subglacial liquid water on Mars. *Science*, vol. 361, issue 6401, pp. 490-493.
- Parker T. J., Gorsline D. S., Saunders R. S., Pieri D. C., and Schneeberger D. M., 1993. Coastal geomorphology of the Martian northern plains. *J. Geophys. Res.*, vol. 98, pp. 11,061-11,078.
- Parmentier E. M. and Hess P. C., 1992. Chemical differentiation of a convecting planetary interior: Consequences for a one plate planet such as Venus. *Geophys. Res. Lett.*, vol. 19, pp. 2015-2018.
- Parmentier E. M. and Zuber M. T., 2007. Early evolution of Mars with mantle compositional stratification or hydrothermal crustal cooling. *Journal of Geophysical Research*, 112:E02007.
- Parnell J., Boyce A., Thackrey S., Muirhead D., Lindgren P., Mason C., Taylor C., Still J., Bowden S., Osinski G. R. and Lee P., 2010. Sulfur isotope signatures for rapid colonization of an impact crater by thermophilic microbes. *Geology*, vol. 38, issue 3, pp. 271-274.
- Patino Douce A. E. and Roden M., 2006. Apatite as a probe of halogen and water fugacities in the terrestrial planets. *Geochimica & Cosmochimica Acta*, vol. 70, pp. 3173-3196.
- Pearce T. H. and Kolisnik A. M., 1990. Observations of plagioclase zoning using interference imaging. *Earth-Science Reviews*, vol. 29, pp. 9-26.
- Pearce T. H., 1994. Recent work on oscillatory zoning in plagioclase. *Feldspars and their reactions*, vol. 421, pp. 313-349.
- Pearson D. G. and Woodland S. J., 2000. Solvent extraction/anion exchange separation and determination of PGEs (Os, Ir, Pt, Pd, Ru) and Re-Os isotopes in geological samples by isotope dilution ICP-MS. *Chemical Geology*, vol. 165, issue 1-2, pp. 87-107.
- Pepin R. O., 1985. Evidence of Martian Origins. *Nature*, vol. 317, p. 473-475.
- Peslier A. H., Hnatyshin D., Herd C. D. K., Walton E. L., Brandon A. D., Lapen T. J., and Shafer J. T., 2010. Crystallization, melt inclusion, and redox history of a Martian meteorite: Olivine-phyric shergottite Larkman Nunatak 06319. *Geochimica et Cosmochimica Acta*, vol. 74, pp. 4543-4576.
- Peucker-Ehrenbrink B. and Jahn B. M., 2001. Rhenium-osmium isotope systematics and platinum group element concentrations: loess and the upper continental crust. *Geochem. Geophys. Geosys.*, 2: 2001GC000172.

- Pfalzner S., Davies M. B., Gounelle M., Johansen A., Munker C., Lacerda P., Zwart S. P., Testi L., Trielo M. and Veras D., 2015. The formation of the Solar System. *Physica Scripta*, vol. 90, n. 6, pp. 1-36.
- Phillips R. J. and Malin M. C., 1983. The interior of Venus and tectonic implications. In: Venus. *University of Arizona Press*, pp. 159-214.
- Phillips R. J., Zuber M. T., Solomon S. C., Golombek M. P., Jakosky B. M., Banerdt W. B., Smith D. E., Williams R. M., Hynes B. M., Aharonson O., and Hauck II S.A., 2001. Ancient geodynamics and global-scale hydrology on Mars. *Science*, vol. 291, pp. 2587-2591.
- Poldervaart A. and Hess H. H., 1951. Pyroxenes in the Crystallization of Basaltic Magma. *The Journal of Geology*, vol. 59, issue 5, pp. 472-489.
- Posodek F. A., 1973. Thermal history of the nakhlites by the ^{40}Ar - ^{39}Ar method. *Earth and Planetary Science Letters*, vol. 19, issue 2, pp. 135-144.
- Poulet F., Bibring J. P., Mustard J. F., Gendrin A., Mangold N., Langevin Y., Arvidson R., Gondet B., Gomez C., and the OMEGA Team, 2005. Phyllosilicates on Mars and implications for early martian climate. *Nature*, vol. 438, pp. 623-627.
- Puchtel I. S., Blichert-Toft J., Touboul Walker M., Byerly G. R., Nisbet E. G., and Anhaeusser C. R., 2013. Insights into early Earth from Barberton komatiites: evidence from lithophile isotope and trace element systematics. *Geochim. Cosmochim. Acta*, vol. 108, pp. 63-90.
- Puchtel I. S., Walker R. J., Brandon A. D. and Irving A. J., 2008. Highly Siderophile Element Abundances in SNC Meteorites: An Update. *Lunar Planet. Sci. XXXVIII*, Abstract #1650.
- Puchtel I. S., Walker R. J., Touboul M., Nisbet E. G., and Byerly G. R., 2014. Insights into early Earth from the Pt-Re-Os isotope and highly siderophile element abundance systematics of Barberton komatiites. *Geochim. Cosmochim. Acta*, vol. 125, pp. 394-413.
- Putirka K. D., Perfit M., Ryerson F. J., and Jackson M. G., 2007. Ambient and excess mantle temperatures, olivine thermometry, and active vs. passive upwelling. *Chemical Geology*, vol. 241, pp. 177-206.
- Putirka K., 2008. Thermometers and barometers for volcanic systems. In: Minerals, inclusions and volcanic processes. *Review in Mineralogy and Geochemistry*, vol. 69, edited by Putirka K. and Tepley F. pp. 61-120.
- Putirka K., 2016. Rates and style of planetary cooling on Earth, Moon, Mars and Vesta, using new models for oxygen fugacity, ferric-ferrous ratios, olivine-liquid Fe-Mg exchange, and mantle potential temperature. *American Mineralogist*, vol. 101, issue 4, pp. 819-840.
- Reese C. C., Solomatov V. S., Moresi L. N., 1998. Heat transport efficiency for stagnant lid convection with dislocation viscosity: Application to Mars and Venus. *Journal of Geophysical Research*, vol. 103(E6), pp. 13643-13657.
- Reid A. M. and Bunch T. E., 1975. The nakhlites—II: where, when, and how. *Meteoritics*, vol. 10, pp. 317-324.

- Reitano R., Smith P. M., and Aziz M. J., 1994. Solute trapping of Group-III, IV, and V elements in silicon by an aperiodic stepwise growth-mechanism. *Journal of Applied Physics*, vol. 76, issue 3, pp. 1518-1529.
- Reubi O., Nicholls I. A., and Kamenetsky V. S., 2003. Early mixing and mingling in the evolution of basaltic magmas: evidence from phenocryst assemblages, Slamet Volcano, Java, Indonesia. *Journal of Volcanology and Geothermal Research*, vol. 119, pp. 255-274.
- Rhodes J. M., Dungan M. A., Blanchard D. P., and Long P. E., 1979. Magma mixing at mid-ocean ridges: Evidence from basalts drilled near 22 degree on the Mid-Atlantic Ridge. *Tectonophysics*, vol. 55, issue 1-2, pp. 35-61.
- Riches A. J. V., Day J. M. D., Walker R. J., Simonetti A., Liu Y., Neal C. R. and Taylor L. A., 2012. Rhenium-osmium isotope and highly-siderophile-element abundance systematics of angrite meteorites. *Earth and Planetary Science Letters*, vol. 353-354, pp. 208-218.
- Riches A. J. V., Liu Y., Day J. M. D., Puchtel I. S., Rumble D., McSween H. Y., Walker R. J. and Taylor L. A., 2011. Petrology and geochemistry of Yamato 984028: A cumulate lherzolitic shergottite with affinities to Y 000027, Y 000047, and Y 000097. *Polar Science*, vol. 4, pp. 497-514.
- Righter K. and Chabot N. L., 2011. Moderately and slightly siderophile element constraints on the depth and extent of melting in early Mars. *Meteorit. Planet. Sci.*, vol. 46, pp. 157-176.
- Righter K., Hervig R. L., and Kring D. A., 1998. Accretion and core formation on Mars: molybdenum contents of melt inclusion glasses in three SNC meteorites. *Geochim. Cosmochim. Acta*, vol. 62, pp. 2167-2177.
- Roeder P. L. and Emslie R. F., 1970. Olivine-liquid equilibrium. *Contributions to Mineralogy and Petrology*, vol. 29, pp. 275-289.
- Rogers D. and Christensen P. R., 2007. Surface mineralogy of Martian low-albedo regions from MGS-TES data: implications for upper crustal evolution and surface alteration. *J. Geophys. Res.*, vol. 112, E01003.
- Rubie D. C., Frost D. J., Mann U., Asahara Y., Nimmo F., et al., 2011. Heterogeneous accretion, composition and core-mantle differentiation of the Earth. *Earth Planet. Sci. Lett.*, vol. 301, pp. 31-42.
- Ruedas T., 2006. Dynamics, crustal thicknesses, seismic anomalies, and electrical conductivities in dry and hydrous ridge-centered plumes. *Phys. Earth Planet. Inter.*, vol. 155, pp. 16-41.
- Ruedas T., Tackley P. J., and Solomon S. C., 2013. Thermal and compositional evolution of the martian mantle: Effects of water. *Physics of the Earth and Planetary Interiors*, vol. 220, pp. 50-72.
- Ruiz J., 2014. The early heat loss evolution of Mars and their implications for internal and environmental history. *Sci. Rep.*, vol. 4, issue 4338.
- Ruiz J., McGovern P. J., Jiménez-Díaz A., López V., Williams J. P., Hahn B. C., and Tejero R., 2011. The thermal evolution of Mars as constrained by paleo-heat flows. *Icarus*, vol. 215, pp. 508-517.

- Saal A. E., Hauri E. H., Langmuir C. H. and Perfit M. R., 2002. Vapour undersaturation in primitive mid-ocean-ridge basalt and the volatile content of Earth's upper mantle. *Nature*, vol. 419, pp. 451-455.
- Sakai H., Casadevall T. J. and Moore J. G., 1982. Chemistry and isotope ratios of sulfur in basalts and volcanic gases at Kilauea volcano, Hawaii. *Geochim. Cosmochim. Acta*, vol. 46, pp. 729-738.
- Santos A. R., Agee C. B., McCubbin F. M., Shearer C. K., and Burger P. V., 2013. Martian breccia NWA 7034: Basalt, mugearite, and trachyandesite clasts. *76th Meteoritical Society Meeting*, Abstract #5284.
- Sautter V., Fabre C., Forni O., Toplis M. J., Cousin A., Ollila A. M., Meslin P. Y., Maurice S., Wiens R. C., Baratoux D., and others, 2014. Igneous mineralogy at Bradbury Rise, The first ChemCam campaign at Gale crater. *Journal of Geophysical Research*, vol. 119, pp. 30-46.
- Savarino J., 2003. UV induced mass-independent sulfur isotope fractionation in stratospheric volcanic sulfate. *Geophys. Res. Lett.*, 30:2131.
- Schleicher J. M., Bergantz G. W., Breidenthal R. E., and Burgisser A., 2016. Time scales of crystal mixing in magma mushes. *Geophysical Research Letters*, vol. 43, issue 4, pp. 1543-1550.
- Schmidt M. E., Campbell J. L., Gellert R., Perrett G. M., Treiman A. H., Blaney D. L., Ollila A., Calef F. J., Edgar L., Elliott B. E., and others, 2014. Geochemical diversity in first rocks examined by the Curiosity rover in Gale crater: Evidence for and significance of an alkali and volatile-rich igneous source. *Journal of Geophysical Research*, vol. 119, pp. 64-81.
- Schmitt R. A. and Smith R. H., 1963. Implications of similarity in rare-earth fractionation of nakhlitic meteorites and terrestrial basalts. *Nature*, vol. 199, pp. 550-551.
- Scott D. H. and Carr M. H., 1978. Geologic map of Mars. *U.S. Geological Survey Misc. Inv.*, Map I-1083.
- Scott D. H. and Tanaka K. L., 1986. Geologic map of the western equatorial region of Mars. *U.S. Geological Survey Misc. Inv.*, Map I-1802-A.
- Scott D. H., Tanaka K., Greely R., and Guest J. E., 1986. Geologic maps of the western equatorial, eastern equatorial, and polar regions of Mars. *USGS, Maps I-1802A, B, C*.
- Scott P. W., 1980. Zoned pyroxenes and amphiboles from camptonites near Gran, Oslo region, Norway. *Mineralogical Magazine*, vol. 43, pp. 913-917.
- Segura N. H., Toon O. B., Colaprete A., and Zahnle K. J., 2002. Environmental effects of large impacts. *Science*, vol. 298, pp. 1977-1980.
- Sharp R. P., 1973. Mars: troughed terrain. *J. Geophys. Res.*, vol. 78, pp. 4063-4072.
- Shearer C. K., Aaron P. M., Burger P. V., Guan Y., Bell A. S., and Papike J. J., 2013. Petrogenetic linkages among fO₂, isotopic enrichments-depletions and crystallization history in Martian basalts: Evidence from the distribution of phosphorus in olivine megacrysts. *Geochimica et Cosmochimica Acta*, vol. 120, pp. 17-38.

- Shearer C. K., Burger P. V., Papike J. J., Borg L. E., Irving A. J. and Herd C. D. K., 2008. Petrogenetic linkages among Martian basalts: Implications based on trace element chemistry of olivine. *Meteorit. Planet. Sci.*, vol. 43, pp. 1241-1258.
- Sheehan F. and Barclay J., 2016. Staged storage and magma convection at Ambrym volcano, Vanuatu. *Journal of Volcanology and Geothermal Research*, vol. 322, pp. 144-157.
- Shih C. Y., Nyquist L. E., and Wiesmann H., 1999. Samarium-neodymium and rubidium-strontium systematics of nakhlite Governador Valadares. *Meteoritics*, vol. 34, pp. 647-655.
- Shih C. Y., Nyquist L. E., Bogard D. D., McKay G. A., Wooden J. L., Bansal B. M., and Wiesmann H., 1982. Chronology and petrogenesis of young achondrites, Shergotty, Zagami and ALHA 77005: Late magmatism on a geologically active planet. *Geochim. Cosmochim. Acta*, vol. 46, pp. 2323-2344.
- Shih C. Y., Nyquist L.E., Reese Y., Wiesmann H. and Lockheed M., 1998. The Chronology of the Nakhilite, Lafayette: Rb-Sr and Sm-Nd Isotopic Ages. 29th Lunar and Planetary Conference, Abstract #1145.
- Shore M. and Fowler A. D., 1996. Oscillatory zoning in minerals: a common phenomenon. *Canadian Mineralogist*, vol. 34, pp. 1111-1126.
- Siebach K. L., Grotzinger J. P., Kah L. C., Stack K. M., Malin M., Leveille R., and Sumner D. Y., 2014. Subaqueous shrinkage cracks in the Sheepbed mudstone: Implications for early fluid diagenesis, Gale crater, Mars. *Journal of Geophysical Research*, vol. 119, pp. 1597-1613.
- Simonetti A., Shore M., and Bell K., 1996. Diopside phenocrysts from nephelinite lavas, Napak volcano, eastern Uganda: Evidence for magma mixing. *Canadian Mineralogist*, vol. 34, pp. 411-421.
- Sleep N. H. and Zahnle K., 1998. Refugia from asteroid impacts on early Mars and the early Earth. *J. Geophys. Res.*, vol. 103, pp. 28529-28544.
- Smith K. L., Milnes A. R., and Eggleton R. A., 1979. Weathering of basalt: formation of iddingsite. *Clays and Clay Minerals*, vol. 35, pp. 418-428.
- Smoliar M. I., Walker R. J. and Morgan J. W., 1996. Re-Os ages of Group IIA, IIIA, IVA, and IVB Meteorites. *Science*, vol. 271, issue 5252, pp. 1099-1102.
- Solomon S. C., Aharonson O., Aurnou J. M., Banerdt W. B., Carr M. H., Dombard A. J., Frey H. V., Golombek M. P., Hauck II S.A., Head J. W., Jakosky B. M., Johnson C. L., McGovern P. J., Neumann G. A., Phillips R. J., Smith D. E., and Zuber M. T., 2005. New perspectives on ancient Mars. *Science*, vol. 307, pp. 1214-1220.
- Spear F. S. and Markussen J. C., 1997. Mineral Zoning, P-T-X-M Phase Relations, and Metamorphic Evolution of some Adirondack Granulites, New York. *Journal of Petrology*, vol. 38, issue 6, pp. 757-783.
- Spohn T., 1991. Mantle differentiation and thermal evolution of Mars, Mercury, and Venus. *Icarus*, vol. 90, pp. 222-236.
- Squyres S. W., Arvidson R. E., Blaney D. L., Clark B. C., Crumpler L., Farrand W. H., Gorevan S., Herkehoff K. E., Hurowitz J., Kusack A., and others, 2006. Rocks of the Columbia Hills. *Journal of Geophysical Research*, vol. 111, E02S11.

- Squyres S. W., et al., 2007. Pyroclastic activity at home plate in Gusev Crater, Mars. *Science*, vol. 316, pp. 738-742.
- Stepinski T. F. and O'Hara W.J., 2003. Vertical analysis of martian drainage basins. *Lunar Planet. Sci.*, vol. 35, Abstract #1659.
- Stevenson D. J., Spohn T., and Schubert G., 1983. Magnetism and thermal evolution of the terrestrial planets. *Icarus*, vol. 54, pp. 466-489.
- Stoffler D., 2000. Maskelynite confirmed as diaplectic glass: indication for peak shock pressures below 45 Gpa in all martian meteorites. *Lunar Planet. Sci. XXXI Lunar and Planetary Institute*, Abstract #1170.
- Stöffler D., Keil K., and Scott E. R. D., 1991. Shock metamorphism of ordinary chondrites. *Geochimica & Cosmochimica Acta*, vol. 55, pp. 3845-3867.
- Stolper E. M. and McSween H. Y., 1979. Petrology and origin of the Shergottite meteorites. *Geochimica & Cosmochimica Acta*, vol. 43, pp. 1475-1498.
- Stolper E. M., Baker M. B., Newcombe M. E., Schmidt M. E., Treiman A. H., Cousin A., Dyar M. D., Fisk M. R., Gellert R., King P. L., and others and the MSL Science Team, 2013. The petrochemistry of Jake_M: A martian mugearite. *Science*, vol. 341, issue 6153.
- Stopar J. D., Taylor G. J., Velbel M. A., Norman M. D., Vicenzi E. P. and Hallis L. J., 2013. Element abundances, patterns, and mobility in Nakhlite Miller Range 03346 and implications for aqueous alteration. *Geochimica et Cosmochimica Acta*, vol. 112, pp. 208-225.
- Strom R. G., Croft S. K., and Barlow N. G., 1992. In: Kieffer, H.H., Jakosky, B.M., Snyder, C.W., Matthews, M.S. (Eds.), *The Martian Impact Cratering Record*. The University of Arizona Press, pp. 383-423.
- Strom R. G., Schaber G. G., and Dawson D. D., 1994. The global resurfacing of Venus. *Journal of Geophysical Research - Planets*, vol. 99, issue E5, pp. 10899-10926.
- Sun W., Bennett V. C., Eggins S. M., Kamenetsky V. S. and Arculus R. J., 2003. Enhanced mantle-to-crust rhenium transfer in undegassed arc magmas. *Nature*, vol. 422, pp. 294-297.
- Symes S., Borg L., Shearer C. and Irving A., 2008. The age of the martian meteorite Northwest Africa 1195 and the differentiation history of the shergottites. *Geochim. Cosmochim. Acta*, vol. 72, pp. 1696-1710.
- Szymanski A., Brenker F. E., El Goresy A. and Palme H., 2003. Complex thermal history of Nakhla and Y000593. *Lunar and Planetary Science XXXIV*, Abstract #1922.
- Szymanski A., Brenker F. E., Palme H. and El Goresy A., 2010. High oxidation state during formation of Martian nakhlites. *Meteoritics & Planetary Science*, vol. 45, pp. 32-42.
- Tait K. T. and Day J. M. D., 2018. Chondritic late accretion to Mars and the nature of shergottite reservoirs. *Earth and Planetary Science Letters*, vol. 494, pp. 99-108.

- Tait K. T., Day J. M. D. and Liu Y., 2015. Update on highly-siderophile element abundances and Re-Os isotopic systematics of martian meteorites. *Lunar Planet. Sci. XXXVI*, Abstract #2138.
- Takeuchi H. and Sugi N., 1971. Polar wandering and mantle convection. *International Astronomical Union Symposium*, vol. 48, issue 212.
- Tanaka K. L., 1986. The stratigraphy of Mars. *J. Geophys. Res.*, vol. 91, E139-E158.
- Tanaka K. L., 1997. Sedimentary history and mass flow structures of Chryse and Acidalia Planitiae, Mars. *J. Geophys. Res.*, vol. 102, pp. 4131-4149.
- Tanaka K. L., Skinner J. A., and Hare T. M., 2005. Geologic map of the northern plains of Mars. U.S. *Geol. Surv., Sci. Inv.*, Map 2888.
- Taylor G. J. and Norman M. D., 1992. Evidence for magma oceans on asteroids, the Moon, and Earth. In: *Lunar and Planetary Institute Technical Report*, ed. CB Agee, J Longhi, pp. 58-65.
- Thompson R. N. and Gibson S. A., 2000. Transient high temperatures in mantle plume heads inferred from magnesian olivines in Phanerozoic picrites. *Nature*, vol. 407, pp. 502-506.
- Thompson R. N., 1972. Oscillatory and sector zoning in augite from a Vesuvian lava. *Carnegie Institution of Washington Yearbook*, vol. 71, pp. 463-470.
- Tomkinson T., Lee M. R., Mark D. F. and Smith C. L., 2013. Sequestration of Martian CO₂ by mineral carbonation. *Nature Communications*, vol. 4, issue 2662, pp. 1-6.
- Tomkinson T., Lee M. R., Mark D. F., Stuart F. M. and Smith C. L., 2012. Shock enhanced dissolution of olivine in the Martian crust - Evidence from the Nakhla meteorite. *75th Annual Meteoritical Society Meeting*, Abstract #5243.
- Tonks W. B., Melosh H. J., 1993. Magma ocean formation due to giant impacts. *J. Geophys. Res.*, vol. 98, pp. 5319-5333.
- Toplis M. J., Libourel G., and Carroll M. R., 1994. The role of phosphorus in crystallisation processes of basalt: an experimental study. *Geochimica & Cosmochimica Acta*, vol. 58, pp. 797-810.
- Tosca N. J. and McLennan S. M., 2006. Constraints on evaporation processes at Meridiani Planum: combining theoretical and experimental data. *Lunar Planet. Sci.*, vol. 37, Abstract #2278.
- Tosca N. J., McLennan S. M., Clark B. C., Grotzinger J. P., Hurowitz J. A., Knoll A. H., Schroder C., and Squyres S. W., 2005. Geochemical modeling of evaporation processes on Mars: insights from the sedimentary record at Meridiani Planum. *Earth Planet. Sci. Lett.*, vol. 240, pp. 122-148.
- Treguier E., d'Uston C., Pinet P. C., Berger G., Toplis M. J., McCoy T. J., Gellert R., and Brucker J. 2008. Overview of Mars surface geochemical diversity through Alpha Particle X-Ray Spectrometer data multidimensional analysis: First attempt at modeling rock alteration. *Journal of Geophysical Research-Planets*, 113:E12S34.
- Treiman A. H. and S. R. Sutton, 1992. Petrogenesis of the Zagami meteorite: inferences from synchrotron X-ray (SXRF) microprobe and electron microprobe analyses of pyroxene. *Geochim. Cosmochim. Acta*, vol. 56, pp. 4059-4074.

- Treiman A. H., 1985. Amphibole and Hercynite Spinel in Shergotty and Zagami: Magmatic Water, Depth of Crystallization, and Metasomatism. *Meteoritics*, vol. 20, pp. 229-243.
- Treiman A. H., 1986. The parental magma of the Nakhla achondrite: Ultrabasic volcanism on the shergottite parent body. *Geochimica et Cosmochimica Acta*, vol. 50, issue 6, pp. 1061-1070.
- Treiman A. H., 1990. Complex petrogenesis of the Nakhla (SNC) meteorite: evidence from petrography and mineral chemistry. *Proceedings of the 20th Lunar Planetary Science Conference*, pp. 273-280.
- Treiman A. H., 2003. Chemical compositions of martian basalts (shergottites): some inferences on basalt formation, mantle metasomatism, and differentiation in Mars. *Meteorit. Planet. Sci.*, vol. 38, pp. 1849-1864.
- Treiman A. H., 2005. The nakhlite meteorites: Augite-rich igneous rocks from Mars. *Chemie der Erde*, vol. 65, pp. 203-270.
- Treiman A. H., Dyar M. D., McCanta M., Noble S. K., and Pieters C. M., 2007. Martian dunite NWA 2737: Petrographic constraints on geological history, shock events, and olivine color. *Journal of Geophysical Research - Planets* 112:E04002.
- Udry A. and Day J. M. D., 2018. 1.34 billion-year-old magmatism on Mars evaluated from the co-genetic nakhlite and chassignite meteorites. *Geochimica et Cosmochimica Acta*, vol. 238, pp. 292-315.
- Udry A., McSween H. Y., Lecumberry-Sanchez P. and Bodnar R. J., 2012. Paired nakhlites MIL 090030, 090032, 090136, and 03346: Insights into the Miller Range parent meteorite. *Meteoritics & Planetary Science*, vol. 47, issue 10, pp. 1575-1589.
- Usui T., Alexander C. M. O. D., Wang J., Simon J. I. and Jones J. H., 2012. Origin of water and mantle-crust interactions on Mars inferred from hydrogen isotopes and volatile element abundances of olivine-hosted melt inclusions of primitive shergottites. *Earth Planet. Sci. Lett.*, vol. 357-358, pp. 119-129.
- Valencia D., O'Connell R. J. and Sasselov D., 2007. Inevitability of Plate Tectonics on SuperEarths. *The Astrophysical Journal*, vol. 670, pp. 45-48.
- Van Summeren J., Conrad C. P. and Gaidos E., 2011. Mantle convection, plate tectonics, and volcanism on hot exoearths. *The Astrophysical Journal Letters*, vol. 736, pp. 1-6.
- Velbel M. A., 2016. Aqueous corrosion of olivine in the Mars meteorite Miller Range (MIL) 03346 during Antarctic weathering: Implications for water on Mars. *Geochimica et Cosmochimica Acta*, vol. 180, pp. 126-145.
- Vicenzi E. P., Tobin K., Heaney P. J., Onstott T. C. and Chun J., 1997. Carbonate in Lafayette meteorite: a detailed microanalytical study. *60th Annual Meteoritical Society Meeting*, Abstract #5292.
- Volkening J., Walczyk T. and Heumann K. G., 1991. Osmium isotope ratio determinations by negative thermal ionization mass spectrometry. *Int. J. Mass Spectrom. Ion Proc.*, vol. 105, pp. 147-159.

- Wadhwa M. and Borg L. E., 2006. Trace element and ^{142}Nd systematics in the nakhlite MIL03346 and the orthopyroxenite ALH84001: Implications for the Martian mantle. *Lunar Planet. Sci. XXXVII*, Abstract #2045.
- Wadhwa M., 2001. Redox state of Mars' upper mantle and crust from Eu anomalies in shergottite pyroxene. *Science*, vol. 292, pp. 1527-1530.
- Wadhwa M., Crozaz G. and Barrat J. A., 2004. Trace element distributions in the Yamato 000593/000749, NWA 817 and NWA998 nakhlites: Implications for their petrogenesis and mantle source on Mars. *Antarctic Meteorite Research*, vol. 17, pp. 97-116.
- Wadhwa M., McCoy T. J., Keil K. and Crozaz G., 1993. The chemical and physical evolution of late stage melt in Zagami. *Meteoritics*, vol. 28, pp. 453-454.
- Wager L. R., Brown G. M. and Wadsworth W. J., 1960. Types of igneous cumulates. *J. Petrol.*, vol. 1, pp. 73-85.
- Walker R. J., Yin Q. Z. and Heck P. H., 2018. Rapid effects of terrestrial alteration on highly siderophile elements in the Sutter's Mill meteorite. *Meteoritics & Planetary Science*, vol. 53, issue 7, pp. 1500-1506.
- Walton E. L., Sharp T. G., Huc J. and Filiberto J., 2014. Heterogeneous mineral assemblages in martian meteorite Tissint as a result of a recent small impact event on Mars. *Geochimica et Cosmochimica Acta*, vol. 140, pp. 334-348.
- Wang Z. and Becker H., 2017. Chalcophile elements in the martian meteorites indicate a low sulfur content in the martian interior. *Earth Planet. Sci. Lett.*, vol. 463, pp. 56-68.
- Wanke H. and Dreibus G., 1994. Chemistry and accretion history of Mars. *Royal Society of London Philosophical Transactions*, ser. A, vol. 349, pp. 285-293.
- Warren P. H., 1985. The magma ocean concept and lunar evolution. *Annual Review of Earth and Planetary Sciences*, vol. 13, pp. 201-240.
- Warren P. H. and Kallemeyn G. W., 1996. Siderophile trace elements in ALHA84001, other SNC meteorites and eucrites: evidence of heterogeneity, possibly time-linked, in the mantle of Mars. *Meteor. Planet. Sci.*, vol. 31, pp. 97-105.
- Warren P. H., Kallemeyn G. W. and Kyte F. T., 1999. Origin of planetary cores: evidence from highly siderophile elements in martian meteorites. *Geochim. Cosmochim. Acta*, vol. 63, pp. 2105-2122.
- Watson E. B., Cherniak D. J., and Holycross M. E., 2015. Diffusion of phosphorus in olivine and molten basalt. *American Mineralogist*, vol. 100, pp. 2053-2065.
- Watters T. R. and Maxwell T. A., 1986. Orientation, relative age and extent of the Tharsis plateau ridge system. *J. Geophys. Res.*, vol. 91, pp. 8113-8125.
- Werner S. C., 2009. The global martian volcanic evolutionary history. *Icarus*, vol. 201, pp. 44-68.
- Wetherill G. W., 1980. Formation of the terrestrial planets. *Annu. Rev. Astron. Astrophys.*, vol. 18, pp. 77-113.

Wiens R. C., Becker R. H. and Pepin R. O., 1986. The case for a Martian origin of the shergottites, II. Trapped and indigenous gas components in EETA 79001 glass. *Earth and Planetary Science Letter*, vol. 77, pp. 149-158.

Williams K. B., Sonzogni Y., and Treiman A. H., 2014. Amphibole in the Tissint martian meteorite: composition and implication for volatile content of parental magma. *45th Lunar and Planetary Science Conference*, Abstract#1435.

Wilson J. H. and Mustard J. F., 2013. Exposures of olivine-rich rocks in the vicinity of Ares Vallis: implications for Noachian and Hesperian volcanism. *J. Geophys. Res.*, vol. 118, pp. 916-929.

Wilson L., Scott E. D., and Head J. W., 2001. Evidence for episodicity in the magma supply to the large Tharsis volcanoes. *J. Geophys. Res.*, vol. 106, pp. 1423-1433.

Winter J. D., 2010. Principles of igneous and metamorphic petrology, 2nd ed. Upper Saddle River, NJ: *Pearson Education Inc.*, pp. 222-243.

Wright I. P., Grady M. M., and Pillinger C. T., 1989. Organic material in a Martian meteorite. *Nature*, vol. 340, pp. 220-222.

Wright T. L. and Peck D. L., 1978. Crystallization and Differentiation of Alae Magma, Alae Lava Lake, Hawaii. *US Geological Survey Prof. Paper*, 935-C. US Government Printing Office, Washington 20pp.

Wyatt M. B., and McSween Jr. H.Y., 2002. Spectral evidence for weathered basalt as an alternative to andesite in the northern lowlands of Mars. *Nature*, vol. 417, pp. 263-266.

Yamashita K., Nakamura N., Imae N., Misawa K. and Kojima H., 2002. Pb isotopic signature of Martian meteorite Yamato 000593 (a preliminary report). *Antarct. Meteorites*, vol. 27, pp. 180-182.

Yoder C. F., Konopliv A. S., Yuan D. N., Standish E. M., and Folkner W. M., 2003. Fluid core size of Mars from detection of the solar core. *Science*, vol. 300, pp. 299-303.

Zahnle K. J., Kasting J. F., and Pollack J. B., 1988. Evolution of a steam atmosphere during Earth's accretion. *Icarus*, vol. 74, pp. 62-97.

Zeng L. and Jacobsen S. B., 2017. A Simple Analytical Model for Rocky Planet Interiors. *The Astrophysical Journal*, vol. 837, issue 2, pp. 164.

Zmolek P., Xu X. P., Jackson T., Thiemens M. H. and Trogler W. C., 1999. Large mass independent sulfur isotope fractionations during the photopolymerization of I₂CS₂ and I₃CS₂. *J. Phys. Chem. A*, vol. 103, pp. 2477-2480.

Zolotov M. Y. and Mironenko M. V., 2007. Formation and fate of phyllosilicates on the surface of Mars: geochemical modeling of aqueous weathering. *Int. Conf. Mars 7*, Abstract #3365.

Appendices

Appendix A - Experimental petrology data

A.1 - Attempts for studying Martian mantle oxidation state

An experimental petrology phase was in the PhD project plan as a complementary part of this PhD project. This part was meant to constrain the oxidation state of a parcel of the Martian mantle. Unfortunately, as described below, this idea was abandoned. However, here some work that has been done about this part is reported.

A.1.1 - Using oxygen fugacity to interpret the oxidation state of magmatic systems

In a geological material, iron can exist in three oxidation states depending on a variable: the oxygen fugacity (fO_2) (e.g., Frost, 1991). At very low oxygen fugacities (as those found in the Earth's core and in meteorites) iron is present as a metal (Fe^0). At higher oxygen fugacities and silica-bearing systems, iron is divalent and is incorporated into silicates. At higher oxygen fugacity iron has both the divalent (ferrous) and the trivalent (ferric) states and is mostly incorporated into magnetite. At very high oxygen fugacity iron is only in the trivalent (ferric) state, and is incorporated into hematite.

Oxygen fugacity is a variable that can inform whether iron can be found in its native state, or as a divalent ion in a silicate, or as a divalent or trivalent ion in an oxide (Frost, 1991). However, in natural systems an iron silicate can substitute its ferrous iron (Fe^{2+}) with magnesium resulting in a stabilization even in the presence of hematite (i.e., very high fO_2). Also, titanium and ferrous iron will substitute for ferric iron in magnetite and hematite, stabilizing these oxides at lower fO_2 conditions. As a result of all this: in each system containing silicates and oxides, the Fe/Mg ratio of the silicates, the titanium content and ferrous/ferric ratios of the oxides, and the fO_2 are all interrelated (Frost, 1991, and references therein). The fO_2 is thus very important in determining the occurrence of Fe-Ti oxides coexisting with silicates, and it can also be used to determine the composition of the fluid phases associated with the rock.

In igneous rocks, oxygen fugacity is the resultant of the composition of the primary magma and of mineral reactions that occurred during crystallization. The majority of igneous rocks have an fO_2 of a few log units above the Fayalite-Magnetite-Quartz (FMQ) buffer (Haggerty, 1976). Metamorphic rocks have a wider range of oxygen fugacities: from 5-6 log units above FMQ to 5-6 log units below FMQ (Frost, 1988).

In terrestrial magmas the ferric-ferrous equilibrium is a function of oxygen fugacity, temperature, and composition of the melt (Carmichael and Nicholls, 1967). Basalts often crystallize within a small range of fO_2 than felsic volcanic rocks, these last also crystallize at higher fO_2 . However, in all these cases the values of fO_2 fall between the Hematite-Magnetite (HM) buffer and FMQ buffer. Commonly, values of oxygen fugacity for basaltic magmas vary between -8 and -11 (from Nickel-Nickel-Oxide (NNO) to QFM -1 buffer) (Sato, 1978). When a basaltic magma is in its sub-liquidus conditions, the fO_2 value control its crystallization kinetics and the temperature at which the lava crystallize (Kolzenburg et al., 2018). Typically, the fO_2 analysed from erupted lava or emitted gas vary as one log unit in respect to that of the magma source (e.g., Gerlach, 1993).

Europium in igneous rocks can be used as an oxybarometer because it is the only REE that can exist not only in the trivalent state but also in a divalent state, and this is dependent on the fO_2 of the system (Wadhwa, 2001). In this sense, the partitioning of Eu in shergottite pyroxene was used to establish the redox state of the Martian upper mantle. The variation in fO_2 between mantle and crust on Mars is more than 3 log units, due to certain degrees of mantle-crust interaction (Wadhwa, 2001). The Mars' upper mantle has an fO_2 close to the Iron-Wustite (IW) buffer while the crust has an fO_2 higher than QFM buffer and is more oxidized because of aqueous alteration and the lack of crustal recycling (Wadhwa, 2001). A reducing mantle source for shergottites was also argued from Fe^{3+}/Fe^{2+} stoichiometric calculations in pyroxenes (Ghosal et al., 1998).

Electron microprobe and electron energy loss spectroscopy were used to calculate fO_2 of several Martian basalts by analysing Fe-Ti oxides (Herd et al., 2001). In Martian basalts oxygen fugacity varies between -3 and -1 relatively to the QFM buffer (Herd et al., 2002; Herd et al., 2001): QUE 94201 has an fO_2 of ~

-3 relatively to the QFM buffer; both lithologies of EETA 79001 and DaG 476 have an fO_2 of -1.8 and -1.5 below QFM, respectively; Shergotty, Zagami, and Los Angeles have fO_2 equal to QFM -1. Oxygen fugacity calculated on these shergottites is directly correlated to Sr and Nd isotope systematics and La/Yb ratios: this would imply a reduced mantle source for these basalts mixed with a crustal material (assimilation) that may be hydrothermally altered or amphibole-bearing basalts (Herd et al., 2002). QUE 94201 is the most reduced Martian basalt analysed for fO_2 and this may imply that the Martian mantle itself is reduced, basically close to the IW buffer (Herd et al., 2002): that would be also in accordance with proposed fO_2 during Martian core formation of -1.25 relatively to the IW buffer (Righter and Drake, 1996).

A.1.2 – Sample selected: NWA 8159

The Martian meteorite NWA 8159 was selected for this type of work. NWA 8159 is a new type of Martian meteorite, termed an augite basalt, because its pyroxene phases occur only as augite (Agee et al., 2014; Herd et al., 2017). It has a very old age compared with most other Martian meteorites, $\sim 2.37 \pm 0.25$ Ga based on Sm-Nd isochrons, making it early Amazonian (Herd et al., 2017; Simon et al., 2014). It is highly oxidized - unusual for a depleted Martian augite basalt (Herd et al., 2017; Agee et al., 2014): because generally all the depleted shergottites crystallized in reducing conditions, reversely to the enriched shergottites (Herd et al., 2002; Wadhwa, 2001).

NWA 8159 has an aphanitic texture consisting mostly of equigranular crystals of augite, plagioclase, olivine, and magnetite, with minor orthopyroxene and maghemite (Herd et al., 2017). It is the second most magnetic Martian meteorite. Minerals are affected by post-crystallization impact events as seen by plagioclase that sometime occur as maskelynite (Herd et al., 2017). The coexistence of crystalline plagioclase and maskelynite linked to the partial transformation of labradorite suggests a moderate shock pressure of 15 - 23 GPa (Herd et al., 2017; Sharp et al., 2015). Even secondary alteration is visible through the meteorite: this is represented by glassy shock veins and fractures filled by Ca-carbonate. Olivines in NWA 8159 appear to be oxidized preferentially in their P-rich cores (Hallis et al., 2016) and may reflect addition of Martian crustal material during its subsolidus crystallization (Charles et al., 2015). Also, olivine and magnetite are often replaced by Fe-oxides and

hydroxides likely due to terrestrial fluid alteration (Herd et al., 2017). This alteration likely occurred under low-T conditions in the terrestrial environment where the meteorite spent a long residence time (hot desert).

The interior is very fine-grained and gray-green in color, with some small melt veins (Agee et al., 2014). Its modal mineralogy consists of augite (~48%), plagioclase + maskelynite (~37%), olivine (~5%), magnetite (~5%), orthopyroxene (~1%), and maghemite (~0.5%), with minor phases of oxides (ilmenite), merrillite, apatite, spinel, and minor alteration minerals (Herd et al., 2017; Agee et al., 2014). The alteration could be Martian in origin (Vaci et al., 2016). Augite minerals in NWA 8159 are zoned with Fe and Ca that increase from core to rim, in a complete range of $\text{Fs}_{25}\text{En}_{37}\text{Wo}_{38}$ to $\text{Fs}_{66}\text{En}_7\text{Wo}_{27}$ (Herd et al., 2017; Agee et al., 2014).

The anhedral and normally zoned olivine range in composition from Fo_{41} to Fo_{20} (with an average of Fo_{33}), they are sometime mantled by slightly pigeonitic pyroxene and magnetite (Herd et al., 2017). The composition of plagioclase and maskelynite is the same and varies in a range of $\text{An}_{50-62}\text{Ab}_{38-49}\text{Or}_{0.1-0.5}$ (Herd et al., 2017). Magnetite ($\text{Mt}_{96-99.5}\text{Sp}_{0.1-0.6}\text{Usp}_{0.2-3.5}$) is present in three main locations: along with low-Ca pyroxene in olivine rims, in the groundmass (with a size $<20\ \mu\text{m}$), and as phenocrysts of $\sim 150\ \mu\text{m}$ (Herd et al., 2017). The augite rims composition in NWA 8159 have a metastable composition that would imply a rapid cooling rate on Mars (Herd et al., 2017). Stechiometrical calculations imply a low Fe^{3+} content that could refer to a QFM buffer from 0 to -2 (Herd et al., 2017). Ilmenite in NWA 8159 could be in equilibrium with titanomagnetite phases at around QFM +2. This titanomagnetite probably formed in the last stage of crystallization (Herd et al., 2017). The composition of olivine and augite cores is the same and this imply that they were in Fe-Mg equilibrium (Herd et al., 2017).

The most interesting textural characteristic of NWA 8159 is the presence of intergrowths of orthopyroxene and magnetite close to olivine crystals (Fig. A1) (Provencio et al., 2016). Magnetite is also extremely pure and this would imply the highest level of $f\text{O}_2$ yet observed in a Martian material (Agee et al., 2014; Herd et al., 2014). There are two possible ways in which the peculiar magnetite-orthopyroxene intergrowths in the olivine margins can form. The first possibility is a magmatic origin due to peritectic reactions of olivine with the melt at high $f\text{O}_2$ (Presnall, 1966). In a few words, the magmatic origin imply a

reaction of olivine + melt \rightarrow orthopyroxene + spinel (Kuno, 1960; Osborn, 1959), and a subsolidus origin imply a reaction of olivine + $O_2 \rightarrow$ orthopyroxene + spinel (Yoder and Tilley, 1962). The second possibility is due to variations in oxygen fugacity of the system (oxidation) that probably occurred at low temperature under subsolidus conditions (Yoder and Tilley, 1962; Morse, 1969). The second possibility seems to be the most likely for the formation of the olivine-orthopyroxene-magnetite assemblage in this meteorite. This is clearly evidenced by the quasi-euhedral olivine phenocrysts that in the case of peritectic reactions would be affected by large resorption rims; besides, orthopyroxene and magnetite crystals would be detected in the whole groundmass if a peritectic reaction occurred, instead they are present preferentially in the olivine margins (Herd et al., 2017). An analogue assemblage of olivine, low-Ca pyroxene, and magnetite likely due to subsolidus reaction with fO_2 above QFM characterize the NWA 998 nakhlite (Treiman and Irving, 2008), mostly in relation to the titanomagnetite phase rather than magnetite as in NWA 8159 (due to the lower Ti content of the magma).

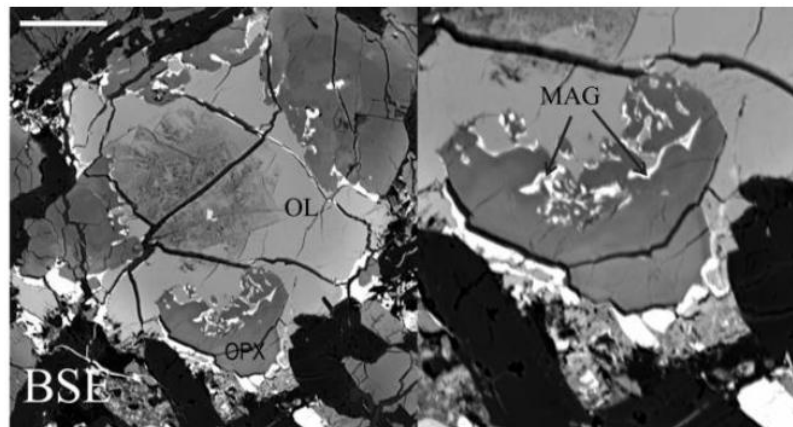


Fig. A1 - BSE images where it is possible to see the orthopyroxene and spinel intergrowths near the olivine rims in NWA 8159. The scale bar is ~50 micrometers (from Provencio et al., 2016). Opx, orthopyroxene; mt, magnetite; ol, olivine.

The crystallization of the NWA 8159 magma can be divided into three stages (Herd et al., 2017): (1) initially, the primary magma crystallized at fO_2 conditions $<$ QFM (even if not well constrained) with the olivine at higher content of Mg ($Fo = 41$) and augite of composition $Fs_{40}En_{30}Wo_{30}$ crystallizing as the first phases, followed by plagioclase formation as seen from mineral

textures; (2) successively, the melt increased its fO_2 to at least QFM +2, maybe due to introduction of an oxidizing fluid on Mars, destabilizing the olivine phenocrysts and replacing their rims with the orthopyroxene-magnetite assemblage. During this stage, the subsolidus reaction that formed orthopyroxene from olivine occurred, also phenocrysts of magnetite likely formed maybe followed by other phases that were then destabilized by the increase in fO_2 ; (3) finally, the groundmass of augite, plagioclase, magnetite crystallized at $fO_2 > \text{QFM} +2$, with crystallization of ilmenite as the very last phase. An increase in fO_2 of ~ 2 log units is detected in the olivine-phyric shergottites (Herd, 2006; Peslier et al., 2010), even if the fO_2 of the liquidus is lower (around QFM -3 to QFM -2) than NWA 8159. The fO_2 of NWA 8159 is, however, poorly constrained due to the disequilibrium of some of the mineralogical phases and to the incompleteness of the subsolidus reaction of oxidation.

A comparison of the abundance of incompatible/compatible elements to the oxygen fugacity for all shergottites results in two different redox states of the shergottite mantle source: the source depleted in incompatible elements is less oxidized, while the source enriched in incompatible elements is more oxidized (Herd, 2003; Wadhwa, 2001). The NWA 8159 is instead LREE depleted but at the same time has a high fO_2 , implying generation from a magma of a different mantle source (Kayzar et al., 2015; Agee et al., 2014; Herd et al., 2017; Simon et al., 2014; Charles et al., 2015). Further evidence for the derivation of NWA 8159 from a different Martian mantle reservoir is represented by its Cr isotopic composition, that differs from all the other Martian meteorites, also suggesting a Cr isotopic heterogeneity in the Martian mantle (Herd et al., 2017). In addition, the $\epsilon^{182}\text{W}$ and the $\epsilon^{142}\text{Nd}$ are different from all the other shergottites, but are similar only to NWA 7635 (Herd et al., 2017; Lapen et al., 2017) - this could in some way suggest that the two meteorites were launched in pair from Mars even if they are not from the same mantle source.

A.1.3 - Description of the experimental work planned and preliminary SEM-EDS data

Experimental petrology can help in modelling the oxygen fugacity of a magmatic system (e.g., Hammer, 2006; Hammer, 2009). During high-T and high-P crystallization experiments of Fe-rich basalts, the composition and modal

mineralogy of olivine, pyroxene, and titanomagnetite is dependent on fO_2 and their textures are modeled by the cooling rate (Hammer, 2006). The magnesium content in augite and titanomagnetite is directly correlated to fO_2 . In addition, the Ti/Al ratio and partitioning of magnesium between crystals and melt is inversely correlated with fO_2 (Hammer, 2006). In reducing condition a basalt would result higher in crystallinity but its matrix glasses would be not much evolved (tholeiitic) as much as in oxidized conditions (calc-alkaline) (Hammer, 2006).

Petrological experiments could, at the same time, be used to infer the cooling rates of a lava and its emplacement on the surface of a planetary body (e.g., First & Hammer, 2016; Hammer, 2009). For example, it is directly possible to see how phenocrystic texture with very fine groundmass occur at constant cooling rates, while a population of both phenocrysts and microphenocrysts occur only if conditions of cooling rates are $< 70^\circ\text{C/h}$ (Hammer, 2006; Hammer, 2009). In a case study, from textural analysis it was possible to see how the MIL 03346 nakhlite have two different Ca-pyroxene populations: one it is phenocrystic and the other is microphenocrystic. Comparing this texture with experimental analog it is possible to infer a cooling rate of around 20°C/h using information from the 3D aspect ratios of both crystal populations of pyroxene (Hammer, 2009). This cooling rates are in agreement with lava that solidified at ~ 0.4 m beneath the Martian surface with a minimum thickness of > 0.8 m, consistent with MIL 03346 being generated from a sub-surface reservoir and successively emplaced as a pahoehoe lava flow (Hammer, 2009).

In order to acquire information about the oxidation state of the Martian mantle it has been planned to use an experimental petrology methodology at the Experimental Petrology Facility of the University of Hawai'i (USA). In particular, the focus of the problem was related on how the orthopyroxene/magnetite overgrowth textures on the outside of the NWA 8159 Martian meteorite were formed. These textures formed around olivine grains. Current arguments are either for a very high oxygen fugacity during crystallisation (Presnall, 1966), or for some kind of sub-solidus reaction (Morse, 1969).

The presence of intergrowths of orthopyroxene and magnetite close to olivine crystals is the most interesting textural characteristic of NWA 8159 (Fig. A.1) (Provencio et al., 2016). Magnetite is also extremely pure and this would imply

the highest level of fO_2 yet observed in a Martian material (Agee et al., 2014). There are two possible ways in which the peculiar magnetite-orthopyroxene intergrowths in the olivine margins can form: 1) magmatic origin due to peritectic reactions of olivine with the melt at high fO_2 (Presnall, 1966); 2) variations in oxygen fugacity of the system (oxidation) that probably occurred at low temperature under subsolidus conditions (Morse, 1969).

Olivine grains of similar composition to NWA 8159 phenocrysts were planned to be used to recreate the sub-solidus reaction environment at low oxygen fugacity (without re-melting the olivine), and to see whether similar textures to that present around olivine grains in NWA 8159 would have been able to form. Subsequently, the analysis of the textures and chemistry of the experimental products was planned using the SEM at the University of Glasgow, and then comparing these textures and chemical data to those in NWA 8159. From the textural/chemical results it was planned to have some constraints on magmatic conditions during emplacement, especially fO_2 since that NWA 8159 is peculiar for this - and seems to derive from a completely different mantle reservoir on Mars (Herd et al., 2017).

Before the experimental phase, two thin sections of NWA 8159 were checked and analysed via SEM-EDS in order to find areas containing ilmenite-magnetite co-growth areas and acquire chemical data of these peculiar mineral textures (Fig. A2; Table A1). These textures were meant to be used to compare with similar textures in the experimentally produced sample in order to infer new constraints on fO_2 .

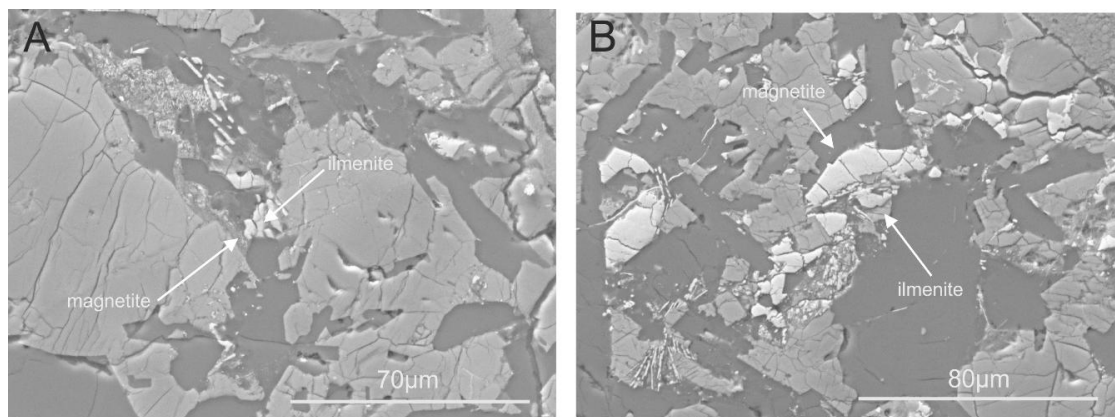


Fig. A2 - Backscattered electron images of two magnetite-ilmenite co-growth areas (A and B) in NWA 8159.

Table A1 - SEM-EDS analysis of three magnetite-ilmenite co-growth areas in NWA 8159.

Wt. %	magnetite 1	ilmenite 1	magnetite 2	ilmenite 2	magnetite 3	ilmenite 3
SiO ₂	4.67	14.75	0.26	30.16	0.23	8.03
S ₂	1.36	1.98	0.02	0.38	0.07	7.18
CaO	0.69	4.14	0.26	2.00	0.22	0.90
TiO ₂	1.31	24.19	0.52	29.65	0.52	1.53
MnO	0.15	0.57	0.12	0.93	0.11	0.19
FeO	84.2	46.2	92.1	37.4	91.8	80.0
CoO	1.23	0.59	1.31	0.48	1.35	0.92
NiO	0.19	0.11	0.16	0.02	0.20	0.14
CuO	0.06	0.09	0.00	0.17	0.05	0.09
Total	93.88	92.59	94.73	101.23	94.57	99.01

A.1.4 - Acquisition of the experimental material

In order to setup this experimental phase two main geological materials were needed: olivine of the same composition as in NWA 8159, that are high-Fe olivines (hortonolite/ferrohortonolite); a basaltic glass, like tachylite, hyaloclastite, or Pele's hairs. Both are uncommon geological materials.

High-Fe olivine was tried to be recreated at the University of Edinburg. The goal was to reproduce a type of olivine with a Mg# = 0.30-0.60 similar to orthopyroxene/olivine in NWA 8159 (Agee et al., 2014; Shearer et al., 2015), with a Fo = 17-41 (Herd et al., 2017; Agee et al., 2014; Provencio et al., 2016; Hallis et al., 2016), and with an high phosphorus content of 1.4-2 wt% (Shearer et al., 2015; Hallis et al., 2016).

In order to set up the experiment to recreate these peculiar high-Fe olivine, initially the correct formula for that type of olivine was calculated, with the correct percentages of Fe, Mg, Si, and O. The formula was equivalent to an hortonolite = $(\text{Fe}_{1.5}\text{Mg}_{0.5})_2 \text{SiO}_4$. A mixture was made based on the correct percentage of elements, based on 1 gr of olivine: %Mg = 0.0856; %Fe = 0.5901; %Si = 0.0989; %O = 0.225411. The mixture was then grounded under acetone using pestle and mortar. Successively, the mixture was put in the furnace at 1350°C and dwelled for 1 hour. Then, it was ramped down to 750°C over 18 hours and then it was left at 750°C for > 72 hours.

This methodology was, however, unsuccessful. The main cause was the absence of any available literature about how to create synthetic olivine of this

composition. High-Fe olivine are in fact extremely hard to recreate synthetically. At the first attempt, the temperature difference between pure Fo and the Mg-Fe mix was underestimated, and this resulted in the chemical powder that did not initially melted. This powder was then reutilized with an increase in the starting temperature. This was tried again for three times but it was not possible to get olivine to grow out of a Fe-Mg mix. This is actually an open problem in olivine petrogenesis.

Luckily, a natural substitute for olivine of similar composition to the NWA 8159 olivine phenocrysts was found in a dunite from Onverwacht (South Africa) (Table A2) (Rudashevsky et al., 1992). A sample of hortonolite dunite from Onverwacht (Transvaal, South Africa), collected in the Onverwacht Pipe of the Bushveld Igneous Complex, was given by the Hunterian Museum in the University of Glasgow: this dunite (code GLAHM 111722) was crushed using an automatic machine until the final size of the olivine reached the same size of NWA 8159 olivine (~200 μm).

The basaltic glass of the right composition to NWA 8159 whole rock (that is a normal basaltic composition) was found and collected in São Miguel Island (Azores): part of the basaltic glasses were collected in the Lagoa do Carvão area and some sample was collected from the wall/ceiling of lava tubes. Part of this material was also crushed with pestle and mortar until a relatively fine grain size was reached.

Table A2 - Comparison between the chemical composition of major elements of NWA 8159 (data taken from Herd et al., 2017) and the Onverwacht dunite (data taken from Rudashevsky et al., 1992).

wt.%	NWA8159	Onverwacht dunite
SiO ₂	32.4	33.6
TiO ₂	b.d.	b.d.
Al ₂ O ₃	b.d.	b.d.
FeO	49.38	44.3
Cr ₂ O	0.12	0.2
MnO	1.04	0.6
MgO	15.72	21.2
CaO	0.6	b.d.
Na ₂ O	b.d.	b.d.
K ₂ O	b.d.	b.d.
Fo%	0.36	0.32
Total	99.26	99.9

A.1.5 - Withdrawal of the experimental phase

This experimental petrology phase was in the plan as a complementary part of the main work. This part was thought to constrain the oxidation state of the parcel of Martian mantle that generated NWA 8159. Unfortunately, due to a combination of both scientific and logistic problems this idea was subsequently abandoned.

The main reason for withdrawal of this experimental phase was due to the difficulty of reproducing the type of ilmenite-magnetite-orthopyroxene textures surrounding the olivine grains as seen in NWA 8159 (Hammer, personal communication). This because both the NWA 8159 and the Onverwacht olivines are too ferroan to be in equilibrium with the whole rock, and this would likely have resulted in a lot of overgrowth, depending on temperature.

Another reason for disposal was the timing available for reaching the planned goal. The Experimental Petrology Facility at the University of Hawai'i is always very busy and finding the time for these experiments would have been a real problem. Also, this experimental phase was intended to be done in a short visit period, as a supplementary part of the main work, but finding the time for making all these experiments would have been extremely long and not flexible for a short visit.

The experimental material (high-Fe olivine grains and basaltic glass) was however kept in case it needs for future works, as for example, finding a new

way to reproduce experimentally the peculiar ilmenite-magnetite-orthopyroxene overgrowth as seen in NWA 8159.

Appendix B - Supplementary information of chapters

B.1 - Supplementary information on Chapter 3

In the following paragraph supplementary information about the chemistry of the Tissint phases of the samples used in [Chapter 3 \(Table A3\)](#) are shown.

All the specific mineral chemistry for Tissint, calculated via SEM-EDS, is displayed in [Table A4-A11](#); while the chemistry for all the EMPA transects is displayed in [Table A12-A15](#), and the olivine crystals were the EMPA transects were made (that were not present in the main text) are shown in [Fig. A3](#). Correlation of elements due to solute trapping during each point of the EMPA transects are shown in [Fig. A4](#).

In addition, Rhodes diagrams for both Mg-pyroxene and Ca-pyroxene of the same samples ([Fig. A5, A6](#)) are shown. The displacement of the pyroxenes from the equilibration curve is pretty similar both when using the black glass and the groundmass composition of Tissint obtained by Chennaoui Aoudjehane et al. (2012).

In addition, Rare Earth Elements (REE; including La, Ce, Sm, Gd, Dy, Yb, Lu) were also collected for Tissint by using an iCAP-RQ inductively coupled plasma-mass spectrometer (ICP-MS), equipped with a RESOLUTION 193 nm Excimer laser ablation (LA), at the University of Glasgow. However, results were not used in the main discussion because of unknown errors during data acquisition.

Data were collected in two olivine megacrysts (to explore the possible occurrence of xenocrysts) and several olivine (divided into Mg rich, Fe-rich, and intermediate), pyroxene (divided into Ca-rich and Mg-rich), low-Ti chromite, and fusion crust (for an indicative bulk composition of the sample). A NIST 612 glass standard was used at the start and at the end of each analytical session. The gas carrier of the laser was Ar. The dwell time for the laser analysis was 0.11 s. A different spot size of the laser for different minerals analysed was used: 100µm for all REEs, but with 80µm for pyroxene and chromite, in order to avoid low signal. Elemental abundances were acquired with the GeoStar software, while data processing was made with the Lolite Data reduction analytical software, by quantifying the trace element abundances in the flat regions of the time-lapse plots. The detection limits for each element of the LA-ICP-MS analyses are shown in [Table A16](#).

Ca-rich pyroxenes have already been investigated by Balta et al. (2015) and Liu et al. (2016). Here additional REE data from Ca-poor Mg-rich pyroxenes are provided (Table A16): REE are slightly more abundant in Ca-rich pyroxene. Yb and Lu more abundant in Mg-rich pyroxenes. However, REE abundances normalized to CI chondrite (Anders and Grevesse, 1988) for the two populations of pyroxenes is similar to the bulk Tissint REE composition of the bulk of this Tissint sample (Fig. A7). These values are similar to bulk REE abundances measured by Liu et al. (2016) and Chennaoui Aoudjehane et al. (2012).

Trace elements were collected in both the populations of olivines. Here it was possible to measure more REEs data that complement previous LA-ICP-MS REEs analysis in Tissint olivines (Balta et al., 2015; Liu et al., 2016), both on Mg-rich and Fe-rich olivine phenocrysts: La, Sm, Gd, and Dy show an increase in abundances with decreasing Mg#, while Er, Yb, and Lu are more abundant in Fe-poor olivines (Table A16; Fig. A7). In addition, two olivine megacrysts were analysed with LA-ICP-MS in this work, both in the cores and in the rims. REE that we analysed in these olivine megacrysts show some differences: La is on average 0.19 ppm in the cores but below detection limits in the rims, while Gd, Dy, Yb, and Lu contents are slightly more abundant in the cores than in the rims (Table A16). However, due to an unknown issue, an higher abundance of REE normalized to CI chondrite (Anders and Grevesse, 1988) was obtained here for olivine in respect to Balta et al. (2015).

The olivine antecryst hypothesis is also in accordance with the calculated similar REE abundances among mega- and pheno-crysts. The measured REE distributions for olivine megacrysts and olivine phenocrysts in Tissint show a correlation with Fe-olivine phenocrysts, less depleted in REE than the Mg-olivine phenocrysts (Fig. A8a). The REE abundances for the two pyroxene populations is pretty similar both between them and the Tissint bulk composition (Fig. A8b).

Table A3 - Averages major elements of phases in Tissint.

Wollastonite, Wo = $100 \times \text{Ca}/(\text{Ca}+\text{Mg}+\text{Fe}_{2+})$; Enstatite, En = $100 \times \text{Mg}/(\text{Ca}+\text{Mg}+\text{Fe}_{2+})$, Ferrosilite, Fs = $100 \times \text{Fe}_{2+}/(\text{Ca}+\text{Mg}+\text{Fe}_{2+})$

wt. %	Olivine avg (n = 26)		Pyroxene avg (n = 20)			Maskelynite avg (n = 6)	Chromite avg (n = 5)	Merrillite avg (n = 4)
	core	rim	core	mantle	rim			
SiO ₂	38	35,9	53,7	52,1	52,6	52,5	0,27	0,23
TiO ₂	0,02	0,02	0,13	0,25	0,28	0,11	0,82	0,1
Al ₂ O ₃	0,23	0,26	0,87	1,18	1,06	28,7	7,3	0,13
Cr ₂ O ₃	0,21	0,23	0,51	0,58	0,55	0,02	57,3	–
MgO	37,2	29	22,5	19,3	19,6	0,17	5,26	2,29
CaO	0,24	0,27	4,68	6,95	7,03	12,2	0,08	46,6
MnO	0,47	0,62	0,58	0,57	0,58	0,09	0,69	–
FeO	23,6	33,2	16,5	17,4	17,3	0,64	27,2	3,33
NiO	–	–	0,11	–	0,19	0,07	–	–
Na ₂ O	0,14	0,15	0,14	0,15	0,15	3,87	0,15	0,76
K ₂ O	–	0,01	–	–	0,06	0,14	–	–
P ₂ O ₅	0,13	0,13	0,07	0,01	0,03	0,24	0,05	0,22
S ₂	0,14	0,18	0,16	0,21	0,16	0,11	0,14	43,6
Total	100,38	99,97	99,95	98,7	99,59	98,86	99,26	97,26
Mg#	61	46	57	52	53	–	–	–
En	–	–	51	44	44	–	–	–
Wo	–	–	10	15	16	–	–	–

Table A4 - SEM-EDS chemistry of olivine in Tissint - Part 1.

wt. %	Olivine										
Na ₂ O	0.12	Na ₂ O	0.13	Na ₂ O	0.14	Na ₂ O	0.16	Na ₂ O	0.14	Na ₂ O	0.09
MgO	28	MgO	27.5	MgO	29.9	MgO	27.6	MgO	29.1	MgO	20.2
Al ₂ O ₃	0.20	Al ₂ O ₃	0.25	Al ₂ O ₃	0.22	Al ₂ O ₃	0.23	Al ₂ O ₃	0.25	Al ₂ O ₃	1.2
SiO ₂	34.6	SiO ₂	34.9	SiO ₂	35.6	SiO ₂	34.8	SiO ₂	35	SiO ₂	32.6
P ₂ O ₅	0.3	P ₂ O ₅	0.08	P ₂ O ₅	n. d.	P ₂ O ₅	0.15	P ₂ O ₅	n. d.	P ₂ O ₅	0.14
S ₂	n. d.	S ₂	0.06	S ₂	n. d.	S ₂	n. d.	S ₂	0.14	S ₂	0.18
K ₂ O	n. d.										
CaO	0.27	CaO	0.31	CaO	0.25	CaO	0.28	CaO	0.30	CaO	0.31
TiO ₂	n. d.	TiO ₂	0.02	TiO ₂	n. d.						
Cr ₂ O ₃	0.12	Cr ₂ O ₃	n. d.	Cr ₂ O ₃	0.1	Cr ₂ O ₃	0.13	Cr ₂ O ₃	n. d.	Cr ₂ O ₃	n. d.
MnO	0.62	MnO	0.67	MnO	0.58	MnO	0.64	MnO	0.62	MnO	0.73
FeO	33.5	FeO	34.9	FeO	32.5	FeO	34.8	FeO	32.4	FeO	39.2
wt. %	Olivine										
Na ₂ O	0.1	Na ₂ O	0.14	Na ₂ O	0.12	Na ₂ O	0.13	Na ₂ O	n. d.	Na ₂ O	0.11
MgO	29.8	MgO	28.6	MgO	33.3	MgO	29.9	MgO	27.8	MgO	40.3
Al ₂ O ₃	0.2	Al ₂ O ₃	0.22	Al ₂ O ₃	0.2	Al ₂ O ₃	0.22	Al ₂ O ₃	0.19	Al ₂ O ₃	0.22
SiO ₂	35.5	SiO ₂	35.2	SiO ₂	36.6	SiO ₂	35.4	SiO ₂	35.1	SiO ₂	38.7
P ₂ O ₅	n. d.	P ₂ O ₅	0.08	P ₂ O ₅	n. d.	P ₂ O ₅	0.09	P ₂ O ₅	n. d.	P ₂ O ₅	n. d.
S ₂	0.09	S ₂	0.03	S ₂	0.11	S ₂	0.06	S ₂	n. d.	S ₂	n. d.
K ₂ O	n. d.										
CaO	0.27	CaO	0.28	CaO	0.24	CaO	0.28	CaO	0.28	CaO	0.22
TiO ₂	n. d.										
Cr ₂ O ₃	n. d.	Cr ₂ O ₃	n. d.	Cr ₂ O ₃	0.1	Cr ₂ O ₃	n. d.	Cr ₂ O ₃	n. d.	Cr ₂ O ₃	0.32
MnO	0.57	MnO	0.65	MnO	0.52	MnO	0.62	MnO	0.63	MnO	0.39
FeO	32.1	FeO	33.8	FeO	28.4	FeO	31.6	FeO	34.7	FeO	20.2

Table A5 - SEM-EDS chemistry of olivine in Tissint - Part 2.

wt.% Olivine	wt.% Olivine	wt.% Olivine	wt.% Olivine	wt.% Olivine	wt.% Olivine	wt.% Olivine	wt.% Olivine	wt.% Olivine	wt.% Olivine
Na ₂ O 0.11	Na ₂ O 0.13	Na ₂ O n. d.	Na ₂ O 0.11	Na ₂ O n. d.	Na ₂ O n. d.	Na ₂ O n. d.	Na ₂ O n. d.	Na ₂ O n. d.	Na ₂ O 0.17
MgO 35.5	MgO 35.9	MgO 36.1	MgO 31.4	MgO 30.7	MgO 31.7	MgO 30.7	MgO 31.7	MgO 31.7	MgO 37.1
Al ₂ O ₃ 0.15	Al ₂ O ₃ 0.18	Al ₂ O ₃ 0.21	Al ₂ O ₃ 0.17	Al ₂ O ₃ 0.16	Al ₂ O ₃ 0.19	Al ₂ O ₃ 0.16	Al ₂ O ₃ 0.19	Al ₂ O ₃ 0.19	Al ₂ O ₃ 0.14
SiO ₂ 37.9	SiO ₂ 37.8	SiO ₂ 37.8	SiO ₂ 36.6	SiO ₂ 36.7	SiO ₂ 36.9	SiO ₂ 36.7	SiO ₂ 36.9	SiO ₂ 36.9	SiO ₂ 39
P ₂ O ₅ n. d.	P ₂ O ₅ 0.08	P ₂ O ₅ n. d.	P ₂ O ₅ n. d.	P ₂ O ₅ n. d.	P ₂ O ₅ 0.04	P ₂ O ₅ n. d.	P ₂ O ₅ 0.04	P ₂ O ₅ 0.04	P ₂ O ₅ 0.14
S ₂ n. d.	S ₂ 0.19	S ₂ n. d.	S ₂ n. d.	S ₂ n. d.	S ₂ n. d.	S ₂ n. d.	S ₂ n. d.	S ₂ 0.2	K ₂ O n. d.
K ₂ O n. d.	K ₂ O n. d.	K ₂ O n. d.	K ₂ O n. d.	K ₂ O n. d.	K ₂ O n. d.	K ₂ O n. d.	K ₂ O n. d.	K ₂ O n. d.	CaO 0.23
CaO 0.26	CaO 0.24	CaO 0.31	CaO 0.26	CaO 0.25	CaO 0.37	CaO 0.25	CaO 0.37	CaO 0.37	MnO 0.48
TiO ₂ n. d.	TiO ₂ n. d.	TiO ₂ n. d.	TiO ₂ n. d.	TiO ₂ n. d.	TiO ₂ n. d.	TiO ₂ n. d.	TiO ₂ n. d.	TiO ₂ n. d.	FeO 23.7
Cr ₂ O ₃ n. d.	Cr ₂ O ₃ 0.15	Cr ₂ O ₃ 0.63	Cr ₂ O ₃ n. d.	Cr ₂ O ₃ n. d.	Cr ₂ O ₃ 0.27	Cr ₂ O ₃ n. d.	Cr ₂ O ₃ 0.27	Cr ₂ O ₃ 0.27	
MnO 0.52	MnO 0.52	MnO 0.50	MnO 0.62	MnO 0.6	MnO 0.58	MnO 0.6	MnO 0.58	MnO 0.58	
FeO 27.1	FeO 26.1	FeO 24.9	FeO 31.6	FeO 32.6	FeO 30.8	FeO 32.6	FeO 30.8	FeO 30.8	
wt.% Olivine	wt.% Olivine	wt.% Olivine	wt.% Olivine	wt.% Olivine	wt.% Olivine	wt.% Olivine	wt.% Olivine	wt.% Olivine	wt.% Olivine
Na ₂ O 0.17	Na ₂ O 0.18	Na ₂ O 0.17	Na ₂ O 0.17	Na ₂ O 0.16	Na ₂ O 0.17	Na ₂ O 0.16	Na ₂ O 0.17	Na ₂ O 0.17	Na ₂ O 0.15
MgO 37.2	MgO 33.2	MgO 35.6	MgO 28.8	MgO 27.2	MgO 38.6	MgO 27.2	MgO 38.6	MgO 38.6	MgO 31.1
Al ₂ O ₃ 0.31	Al ₂ O ₃ 0.3	Al ₂ O ₃ 0.25	Al ₂ O ₃ 0.23	Al ₂ O ₃ 0.23	Al ₂ O ₃ 0.26	Al ₂ O ₃ 0.23	Al ₂ O ₃ 0.26	Al ₂ O ₃ 0.26	Al ₂ O ₃ 0.2
SiO ₂ 39.3	SiO ₂ 38.5	SiO ₂ 39.2	SiO ₂ 37.1	SiO ₂ 37.1	SiO ₂ 38.8	SiO ₂ 37.1	SiO ₂ 38.8	SiO ₂ 38.8	SiO ₂ 37.4
P ₂ O ₅ n. d.	P ₂ O ₅ n. d.	P ₂ O ₅ n. d.	P ₂ O ₅ n. d.	P ₂ O ₅ 0.14	P ₂ O ₅ 0.07	P ₂ O ₅ 0.14	P ₂ O ₅ 0.07	P ₂ O ₅ 0.07	P ₂ O ₅ n. d.
K ₂ O n. d.	K ₂ O n. d.	K ₂ O n. d.	K ₂ O n. d.	K ₂ O n. d.	K ₂ O n. d.	K ₂ O n. d.	K ₂ O n. d.	K ₂ O n. d.	K ₂ O n. d.
CaO 0.23	CaO 0.23	CaO 0.22	CaO 0.24	CaO 0.28	CaO 0.21	CaO 0.28	CaO 0.21	CaO 0.21	CaO 0.22
MnO 0.51	MnO 0.59	MnO 0.55	MnO 0.63	MnO 0.68	MnO 0.41	MnO 0.68	MnO 0.41	MnO 0.41	MnO 0.57
FeO 23.3	FeO 29.2	FeO 26.6	FeO 33.7	FeO 36.6	FeO 20.6	FeO 36.6	FeO 20.6	FeO 20.6	FeO 30.4

Table A6 - SEM-EDS chemistry of pyroxene in Tissint - Part 1.

wt.% Pyroxene									
Na ₂ O 0.14	Na ₂ O 0.15	Na ₂ O 0.14	Na ₂ O 0.14	Na ₂ O n. d.	Na ₂ O 0.13				
MgO 17.9	MgO 16.9	MgO 20.5	MgO 21.8	MgO 21.8	MgO 18.6	MgO 21.8	MgO 18.6	MgO 18.6	MgO 18.9
Al ₂ O ₃ 0.86	Al ₂ O ₃ 1.23	Al ₂ O ₃ 1.13	Al ₂ O ₃ 0.86	Al ₂ O ₃ 0.86	Al ₂ O ₃ 1.16	Al ₂ O ₃ 0.86	Al ₂ O ₃ 1.16	Al ₂ O ₃ 1.16	Al ₂ O ₃ 1.21
SiO ₂ 50.8	SiO ₂ 50.6	SiO ₂ 51.8	SiO ₂ 52.2	SiO ₂ 52.2	SiO ₂ 51.3	SiO ₂ 52.2	SiO ₂ 51.3	SiO ₂ 51.3	SiO ₂ 52.6
P ₂ O ₅ n. d.	P ₂ O ₅ n. d.	P ₂ O ₅ 0.02	P ₂ O ₅ n. d.	P ₂ O ₅ 0.01					
S ₂ 0.01	S ₂ n. d.	S ₂ 0.05	S ₂ n. d.	S ₂ 0.05	S ₂ 0.05	S ₂ n. d.			
K ₂ O n. d.									
CaO 4.9	CaO 7.89	CaO 7.29	CaO 4.8	CaO 4.8	CaO 8.16	CaO 4.8	CaO 8.16	CaO 8.16	CaO 8.94
TiO ₂ 0.29	TiO ₂ 0.3	TiO ₂ 0.17	TiO ₂ 0.15	TiO ₂ 0.15	TiO ₂ 0.29	TiO ₂ 0.15	TiO ₂ 0.29	TiO ₂ 0.29	TiO ₂ 0.31
Cr ₂ O ₃ 0.35	Cr ₂ O ₃ 0.5	Cr ₂ O ₃ 0.65	Cr ₂ O ₃ 0.5	Cr ₂ O ₃ 0.5	Cr ₂ O ₃ 0.57	Cr ₂ O ₃ 0.5	Cr ₂ O ₃ 0.57	Cr ₂ O ₃ 0.57	Cr ₂ O ₃ 0.61
MnO 0.67	MnO 0.6	MnO 0.53	MnO 0.6	MnO 0.6	MnO 0.59	MnO 0.6	MnO 0.59	MnO 0.59	MnO 0.56
FeO 22.3	FeO 19.8	FeO 15.8	FeO 17.2	FeO 17.2	FeO 17.7	FeO 17.2	FeO 17.7	FeO 17.7	FeO 17.3
wt.% Pyroxene									
Na ₂ O n. d.	Na ₂ O 0.13	Na ₂ O n. d.	Na ₂ O 0.12	Na ₂ O 0.12	Na ₂ O 0.11	Na ₂ O n. d.	Na ₂ O 0.11	Na ₂ O 0.11	Na ₂ O 0.11
MgO 22.2	MgO 22	MgO 21.1	MgO 20.3	MgO 20.3	MgO 20.2	MgO 20.3	MgO 20.2	MgO 20.2	MgO 21.5
Al ₂ O ₃ 0.9	Al ₂ O ₃ 0.83	Al ₂ O ₃ 0.94	Al ₂ O ₃ 1.34	Al ₂ O ₃ 1.34	Al ₂ O ₃ 1.09	Al ₂ O ₃ 1.34	Al ₂ O ₃ 1.09	Al ₂ O ₃ 1.09	Al ₂ O ₃ 0.85
SiO ₂ 53.7	SiO ₂ 53.5	SiO ₂ 52.6	SiO ₂ 52.6	SiO ₂ 52.6	SiO ₂ 52.1	SiO ₂ 52.6	SiO ₂ 52.1	SiO ₂ 52.1	SiO ₂ 52.4
P ₂ O ₅ n. d.									
S ₂ 0.08	S ₂ n. d.								
K ₂ O n. d.									
CaO 5.38	CaO 5.22	CaO 5.77	CaO 6.14	CaO 6.14	CaO 6.7	CaO 6.14	CaO 6.7	CaO 6.7	CaO 4.72
TiO ₂ 0.13	TiO ₂ 0.16	TiO ₂ 0.1	TiO ₂ 0.23	TiO ₂ 0.23	TiO ₂ n. d.	TiO ₂ 0.23	TiO ₂ n. d.	TiO ₂ n. d.	TiO ₂ 0.15
Cr ₂ O ₃ 0.57	Cr ₂ O ₃ 0.48	Cr ₂ O ₃ 0.55	Cr ₂ O ₃ 0.53	Cr ₂ O ₃ 0.53	Cr ₂ O ₃ 0.55	Cr ₂ O ₃ 0.53	Cr ₂ O ₃ 0.55	Cr ₂ O ₃ 0.55	Cr ₂ O ₃ 0.51
MnO 0.59	MnO 0.58	MnO 0.52	MnO 0.51	MnO 0.51	MnO 0.53	MnO 0.51	MnO 0.53	MnO 0.53	MnO 0.57
FeO 17.1	FeO 17.5	FeO 15.7	FeO 16.5	FeO 16.5	FeO 15.8	FeO 16.5	FeO 15.8	FeO 15.8	FeO 16.4

Table A7 - SEM-EDS chemistry of olivine in Tissint - Part 2.

wt.%	Pyroxene										
Na ₂ O	0.16	Na ₂ O	0.16	Na ₂ O	0.23	Na ₂ O	0.16	Na ₂ O	0.16	Na ₂ O	0.14
MgO	20.5	MgO	24.4	MgO	17.5	MgO	21.1	MgO	23.6	MgO	21.5
Al ₂ O ₃	1.14	Al ₂ O ₃	0.71	Al ₂ O ₃	1.59	Al ₂ O ₃	1.13	Al ₂ O ₃	0.7	Al ₂ O ₃	1.05
SiO ₂	55	SiO ₂	56.4	SiO ₂	53.9	SiO ₂	55.1	SiO ₂	55.9	SiO ₂	55.3
P ₂ O ₅	n. d.	P ₂ O ₅	0.02	P ₂ O ₅	n. d.						
K ₂ O	n. d.										
CaO	6.44	CaO	3.21	CaO	12	CaO	6.79	CaO	3.48	CaO	4.99
MnO	0.65	MnO	0.6	MnO	0.54	MnO	0.62	MnO	0.59	MnO	0.64
FeO	17.5	FeO	16.4	FeO	14.2	FeO	16.3	FeO	16.9	FeO	17.7

Table A8 - SEM-EDS chemistry of maskelynite in Tissint.

wt.%	Maskelynite	wt.%	Maskelynite	wt.%	Maskelynite
Na ₂ O	3.94	Na ₂ O	3.84	Na ₂ O	3.71
MgO	0.16	MgO	0.14	MgO	0.19
Al ₂ O ₃	28.7	Al ₂ O ₃	28.4	Al ₂ O ₃	29.1
SiO ₂	52.7	SiO ₂	52.7	SiO ₂	52
CaO	12.2	CaO	12	CaO	12.5
TiO ₂	n. d.	TiO ₂	0.08	TiO ₂	n. d.
Cr ₂ O ₃	n. d.	Cr ₂ O ₃	n. d.	Cr ₂ O ₃	n. d.
MnO	n. d.	MnO	n. d.	MnO	n. d.
FeO	0.60	FeO	0.59	FeO	0.67

wt.%	Maskelynite	wt.%	Maskelynite
Na ₂ O	4.03	Na ₂ O	3.85
MgO	0.18	MgO	0.1
Al ₂ O ₃	28.4	Al ₂ O ₃	28.8
SiO ₂	52.8	SiO ₂	52.4
CaO	11.85	CaO	12.3
TiO ₂	0.05	TiO ₂	n. d.
Cr ₂ O ₃	0.00	Cr ₂ O ₃	n. d.
MnO	0.07	MnO	n. d.
FeO	0.7	FeO	0.65

Table A9 - SEM-EDS chemistry of chromite in Tissint.

wt.%	Chromite	wt.%	Chromite	wt.%	Chromite
Na ₂ O	0.13	Na ₂ O	0.18	Na ₂ O	0.12
MgO	5.67	MgO	4.91	MgO	3.49
Al ₂ O ₃	7.05	Al ₂ O ₃	5.44	Al ₂ O ₃	6.26
SiO ₂	0.31	SiO ₂	0.23	SiO ₂	0.15
P ₂ O ₅	0.05	P ₂ O ₅	n. d.	P ₂ O ₅	0.01
S ₂	0.10	S ₂	n. d.	S ₂	n. d.
CaO	n. d.	CaO	n. d.	CaO	0.07
TiO ₂	0.78	TiO ₂	8.96	TiO ₂	6.82
Cr ₂ O ₃	57.9	Cr ₂ O ₃	42.9	Cr ₂ O ₃	45.7
MnO	0.66	MnO	0.68	MnO	0.64
FeO	26.4	FeO	34.9	FeO	34.8

wt.%	Chromite	wt.%	Chromite
Na ₂ O	n. d.	Na ₂ O	0.11
MgO	5.56	MgO	3.6
Al ₂ O ₃	7.47	Al ₂ O ₃	6.6
SiO ₂	0.32	SiO ₂	0.23
P ₂ O ₅	n. d.	P ₂ O ₅	n. d.
S ₂	n. d.	S ₂	n. d.
CaO	n. d.	CaO	0.1
TiO ₂	0.69	TiO ₂	6.54
Cr ₂ O ₃	57.5	Cr ₂ O ₃	45.7
MnO	0.7	MnO	0.67
FeO	27.1	FeO	34.8

Table A10 - SEM-EDS chemistry of merrillite in Tissint.

wt.%	Merrillite	wt.%	Merrillite	wt.%	Merrillite	wt.%	Merrillite
Na ₂ O	0.46	Na ₂ O	0.53	Na ₂ O	0.79	Na ₂ O	0.62
MgO	5.46	MgO	5.4	MgO	1.91	MgO	6.12
Al ₂ O ₃	0.56	Al ₂ O ₃	0.39	Al ₂ O ₃	0.14	Al ₂ O ₃	n. d.
SiO ₂	23.9	SiO ₂	16.1	SiO ₂	0.3	SiO ₂	19.1
P ₂ O ₅	43.4	P ₂ O ₅	43.3	P ₂ O ₅	43.8	P ₂ O ₅	44.1
S ₂	0.03	S ₂	0.14	S ₂	0.07	S ₂	0.14
CaO	27.7	CaO	33.5	CaO	46.7	CaO	31
TiO ₂	0.36	TiO ₂	n. d.	TiO ₂	n. d.	TiO ₂	0.3
MnO	0.44	MnO	n. d.	MnO	n. d.	MnO	n. d.
FeO	16.9	FeO	11.7	FeO	3.98	FeO	11.5

Table A11 - SEM-EDS chemistry of ilmenite in Tissint.

wt.%	Ilmenite	wt.%	Ilmenite	wt.%	Ilmenite
Na ₂ O	n. d.	Na ₂ O	0.11	Na ₂ O	n. d.
MgO	0.93	MgO	1.28	MgO	2.4
Al ₂ O ₃	0.31	Al ₂ O ₃	0.22	Al ₂ O ₃	0.28
SiO ₂	0.12	SiO ₂	0.09	SiO ₂	0.15
TiO ₂	49.7	TiO ₂	49.7	TiO ₂	50.4
Cr ₂ O ₃	0.24	Cr ₂ O ₃	0.33	Cr ₂ O ₃	0.55
MnO	0.6	MnO	0.6	MnO	0.63
FeO	43.5	FeO	43.5	FeO	41.5

wt.%	Ilmenite	wt.%	Ilmenite
Na ₂ O	0.13	Na ₂ O	n. d.
MgO	1.79	MgO	1.82
Al ₂ O ₃	0.28	Al ₂ O ₃	0.34
SiO ₂	n. d.	SiO ₂	n. d.
TiO ₂	49.8	TiO ₂	49.9
Cr ₂ O ₃	0.38	Cr ₂ O ₃	0.27
MnO	0.61	MnO	0.66
FeO	42.2	FeO	42.8

Table A12 - EMPA chemistry of olivine megacryst 1 in Tissint.

	Distance (µm)	Location	Si WT%	±2σ	Ti WT%	±2σ	Al WT%	±2σ	Cr WT%	±2σ	Mg WT%	±2σ	Ca WT%	±2σ	Mn WT%	±2σ
Ol megacryst 1	0	Core	18,55	0,03	0,00	0,00	0,02	0,00	0,13	0,02	25,56	0,04	0,15	0,01	0,27	0,01
Ol megacryst 1	100	Core	18,11	0,03	0,00	0,00	0,02	0,00	0,16	0,02	25,62	0,04	0,15	0,01	0,26	0,01
Ol megacryst 1	150	Core	17,17	0,03	0,00	0,00	0,02	0,00	0,16	0,02	24,71	0,04	0,14	0,01	0,26	0,01
Ol megacryst 1	200	Core	18,04	0,03	0,00	0,00	0,01	0,00	0,12	0,02	25,81	0,04	0,15	0,01	0,27	0,01
Ol megacryst 1	250	Core	17,85	0,03	0,01	0,02	0,01	0,00	0,19	0,02	25,80	0,04	0,15	0,01	0,28	0,01
Ol megacryst 1	300	Core	17,81	0,03	0,00	0,00	0,01	0,00	0,16	0,02	25,16	0,04	0,16	0,01	0,30	0,01
Ol megacryst 1	350	Core	17,63	0,03	0,00	0,00	0,02	0,00	0,16	0,02	25,07	0,04	0,16	0,01	0,29	0,01
Ol megacryst 1	400	Rim	17,60	0,03	0,01	0,02	0,01	0,00	0,10	0,02	25,70	0,04	0,14	0,01	0,29	0,01
Ol megacryst 1	450	Rim	17,71	0,03	0,00	0,00	0,03	0,00	0,16	0,02	25,24	0,04	0,15	0,01	0,26	0,01
Ol megacryst 1	500	Rim	17,53	0,03	0,00	0,02	0,01	0,00	0,13	0,02	25,25	0,04	0,15	0,01	0,27	0,01
Ol megacryst 1	550	Rim	17,71	0,03	0,03	0,02	0,01	0,00	0,09	0,02	25,70	0,04	0,14	0,01	0,26	0,01
Ol megacryst 1	600	Rim	17,13	0,03	0,00	0,02	0,02	0,00	0,16	0,02	24,53	0,04	0,15	0,01	0,29	0,01
Ol megacryst 1	650	Rim	16,83	0,03	0,00	0,02	0,01	0,00	0,13	0,02	23,93	0,04	0,13	0,01	0,26	0,01
Ol megacryst 1	700	Rim	17,70	0,03	0,00	0,00	0,02	0,00	0,13	0,02	25,59	0,04	0,16	0,01	0,33	0,01
Ol megacryst 1	750	Rim	17,61	0,03	0,01	0,02	0,01	0,00	0,19	0,02	25,08	0,04	0,14	0,01	0,32	0,01
Ol megacryst 1	800	Rim	17,46	0,03	0,03	0,02	0,01	0,00	0,20	0,02	24,82	0,04	0,15	0,01	0,31	0,01
Ol megacryst 1	850	Rim	17,31	0,03	0,02	0,02	0,03	0,00	0,13	0,02	23,62	0,04	0,19	0,01	0,35	0,01
Ol megacryst 1	900	Rim	17,38	0,03	0,01	0,02	0,02	0,00	0,05	0,01	22,51	0,04	0,14	0,01	0,35	0,01
Ol megacryst 1	950	Rim	17,06	0,03	0,32	0,03	0,19	0,00	0,09	0,02	17,07	0,04	0,68	0,01	0,50	0,01

(...continued...)

	Fe WT%	±2σ	Na WT%	±2σ	K WT%	±2σ	P WT%	±2σ	O WT%	Ni WT%	±2σ	TOTAL	Mg#
Ol megacryst 1	13,05	0,04	0,00	0,00	0,00	0,00	0,02	0,01	41,95	0,07	0,01	99,8	66,2
Ol megacryst 1	13,03	0,04	0,00	0,01	0,00	0,00	0,01	0,01	41,48	0,08	0,01	98,9	66,3
Ol megacryst 1	13,10	0,04	0,02	0,01	0,01	0,00	0,02	0,01	39,86	0,07	0,01	95,5	65,3
Ol megacryst 1	13,15	0,04	0,02	0,01	0,00	0,00	0,01	0,01	41,56	0,08	0,01	99,2	66,3
Ol megacryst 1	13,28	0,04	0,00	0,00	0,00	0,00	0,02	0,01	41,42	0,08	0,01	99,1	66,0
Ol megacryst 1	13,27	0,04	0,00	0,00	0,00	0,00	0,01	0,01	40,92	0,07	0,01	97,9	65,5
Ol megacryst 1	13,06	0,04	0,01	0,01	0,00	0,00	0,00	0,01	40,59	0,08	0,01	97,1	65,7
Ol megacryst 1	13,22	0,04	0,00	0,00	0,00	0,00	0,01	0,01	41,00	0,09	0,01	98,2	66,0
Ol megacryst 1	13,31	0,04	0,00	0,01	0,00	0,00	0,01	0,01	40,87	0,08	0,01	97,8	65,5
Ol megacryst 1	13,52	0,04	0,01	0,01	0,00	0,00	0,02	0,01	40,72	0,08	0,01	97,7	65,1
Ol megacryst 1	13,39	0,04	0,02	0,01	0,00	0,00	0,02	0,01	41,19	0,07	0,01	98,6	65,7
Ol megacryst 1	13,58	0,04	0,00	0,00	0,00	0,00	0,01	0,01	39,82	0,07	0,01	95,8	64,4
Ol megacryst 1	13,42	0,04	0,00	0,00	0,00	0,00	0,01	0,01	39,01	0,07	0,01	93,8	64,1
Ol megacryst 1	14,03	0,04	0,00	0,01	0,00	0,00	0,02	0,01	41,31	0,08	0,01	99,4	64,6
Ol megacryst 1	14,43	0,04	0,00	0,00	0,00	0,00	0,01	0,01	40,99	0,08	0,01	98,9	63,5
Ol megacryst 1	14,74	0,04	0,01	0,01	0,00	0,00	0,01	0,01	40,76	0,07	0,01	98,6	62,7
Ol megacryst 1	15,78	0,05	0,02	0,01	0,00	0,00	0,01	0,01	40,10	0,07	0,01	97,6	60,0
Ol megacryst 1	17,79	0,05	0,00	0,01	0,00	0,00	0,01	0,01	39,95	0,07	0,01	98,3	55,9
Ol megacryst 1	25,52	0,06	0,07	0,01	0,00	0,00	0,25	0,01	39,19	0,03	0,01	101,0	40,1

Table A13 - EMPA chemistry of olivine megacryst 2 in Tissint.

	Distance (µm)	Location	Si WT%	±2σ	Ti WT%	±2σ	Al WT%	±2σ	Cr WT%	±2σ	Mg WT%	±2σ	Ca WT%	±2σ	Mn WT%	±2σ
Ol megacryst 2	0	Core	18,65	0,03	0,02	0,03	24,80	4,86	0,14	0,02	0,32	0,00	14,49	0,56	0,01	0,00
Ol megacryst 2	50	Core	16,06	0,03	0,03	0,00	21,19	2,24	0,11	0,02	0,24	0,00	12,61	0,54	0,00	0,00
Ol megacryst 2	100	Core	19,34	0,03	0,04	0,00	24,72	2,34	0,12	0,02	0,30	0,00	14,13	0,56	0,00	0,00
Ol megacryst 2	200	Core	18,88	0,03	0,02	0,34	25,11	4,24	0,17	0,02	0,28	0,00	13,91	0,53	0,00	0,00
Ol megacryst 2	250	Core	19,01	0,03	0,02	0,03	25,28	3,97	0,13	0,02	0,28	0,00	14,10	0,53	0,00	0,00
Ol megacryst 2	300	Core	19,18	0,03	0,02	0,13	25,21	4,27	0,15	0,02	0,29	0,00	14,11	0,55	0,01	0,00
Ol megacryst 2	350	Core	19,09	0,03	0,02	0,00	25,09	4,40	0,13	0,02	0,31	0,00	13,94	0,53	0,00	0,00
Ol megacryst 2	400	Core	19,13	0,03	0,02	0,03	25,36	4,57	0,09	0,02	0,27	0,00	13,90	0,57	0,00	0,00
Ol megacryst 2	450	Rim	19,43	0,03	0,02	0,02	25,36	4,22	0,14	0,02	0,31	0,00	14,25	0,57	0,00	0,00
Ol megacryst 2	500	Rim	14,46	0,03	0,13	0,13	18,87	0,64	0,12	0,02	0,21	0,00	12,99	0,59	0,00	0,00
Ol megacryst 2	550	Rim	19,17	0,03	0,02	0,00	24,72	4,49	0,13	0,02	0,29	0,00	14,41	0,56	0,00	0,00
Ol megacryst 2	600	Rim	19,32	0,03	0,02	0,00	24,31	3,50	0,13	0,02	0,32	0,00	14,91	0,53	0,00	0,00
Ol megacryst 2	650	Rim	19,45	0,03	1,38	0,91	21,33	0,15	0,16	0,02	0,29	0,00	15,24	0,65	0,00	0,00
Ol megacryst 2	700	Rim	19,24	0,03	0,02	0,00	22,62	3,51	0,15	0,02	0,37	0,00	18,19	0,77	0,00	0,00
Ol megacryst 2	750	Rim	19,66	0,03	0,11	0,00	23,41	0,89	0,08	0,02	0,34	0,00	17,18	0,67	0,01	0,00
Ol megacryst 2	800	Rim	19,24	0,03	0,03	0,10	22,76	2,65	0,13	0,02	0,34	0,00	17,21	0,65	0,01	0,00
Ol megacryst 2	850	Rim	18,19	0,03	0,03	0,38	21,70	2,42	0,10	0,02	0,33	0,00	17,04	0,64	0,00	0,00
Ol megacryst 2	900	Rim	19,18	0,03	0,01	0,00	22,92	5,62	0,11	0,02	0,35	0,00	17,14	0,68	0,00	0,00
Ol megacryst 2	950	Rim	19,05	0,03	0,01	0,00	22,15	6,89	0,10	0,02	0,34	0,00	18,21	0,70	0,00	0,00

(...continued...)

	Fe WT%	±2σ	Na WT%	±2σ	K WT%	±2σ	P WT%	±2σ	O WT%	Ni WT%	±2σ	TOTAL	Mg#
Ol megacryst 2	0,14	0,00	0,01	0,01	0,06	0,03	0,02	0,01	42,01	0,00	0,00	100,7	68,8
Ol megacryst 2	0,12	0,00	0,00	0,00	0,05	0,00	0,01	0,01	36,07	0,00	0,00	86,5	65,4
Ol megacryst 2	0,14	0,00	0,00	0,00	0,10	0,00	0,02	0,01	42,63	0,00	0,00	101,5	68,3
Ol megacryst 2	0,15	0,00	0,00	0,00	0,07	0,13	0,02	0,01	42,31	0,00	0,00	100,9	65,9
Ol megacryst 2	0,15	0,00	0,02	0,00	0,07	0,00	0,02	0,01	42,63	0,00	0,00	101,7	65,3
Ol megacryst 2	0,14	0,00	0,00	0,00	0,07	0,03	0,02	0,01	42,77	0,00	0,00	102,0	67,5
Ol megacryst 2	0,15	0,00	0,00	0,00	0,08	0,00	0,01	0,01	42,52	0,00	0,00	101,3	67,8
Ol megacryst 2	0,13	0,00	0,01	0,00	0,07	3,20	0,03	0,01	42,73	0,00	0,00	101,7	67,1
Ol megacryst 2	0,14	0,00	0,02	0,01	0,07	0,00	0,03	0,01	43,21	0,00	0,00	103,0	69,1
Ol megacryst 2	0,12	0,00	0,02	0,00	0,05	0,00	0,01	0,01	32,94	0,00	0,00	79,9	64,8
Ol megacryst 2	0,14	0,00	0,00	0,00	0,07	0,00	0,00	0,01	42,47	0,00	0,00	101,4	67,1
Ol megacryst 2	0,16	0,00	0,00	0,00	0,08	0,09	0,01	0,01	42,56	0,00	0,00	101,8	66,4
Ol megacryst 2	0,13	0,00	0,03	0,02	0,09	0,14	0,01	0,01	42,07	0,00	0,00	100,2	69,6
Ol megacryst 2	0,13	0,00	0,00	0,00	0,06	0,00	0,02	0,01	42,31	0,00	0,00	103,1	74,2
Ol megacryst 2	0,14	0,00	0,00	0,00	0,07	0,06	0,00	0,01	43,05	0,00	0,00	104,1	70,1
Ol megacryst 2	0,15	0,00	0,01	0,00	0,07	0,04	0,02	0,01	42,13	0,00	0,00	102,1	69,7
Ol megacryst 2	0,15	0,00	0,00	0,00	0,07	0,36	0,01	0,01	40,16	0,00	0,00	97,8	68,9
Ol megacryst 2	0,14	0,00	0,00	0,00	0,07	0,00	0,03	0,01	42,14	0,00	0,00	102,1	71,9
Ol megacryst 2	0,15	0,00	0,00	0,00	0,06	0,00	0,01	0,01	41,75	0,00	0,00	101,8	70,0

Table A14 - EMPA chemistry of olivine phenocryst 1 in Tissint.

	Distance (µm)	Location	Si WT%	±2σ	Ti WT%	±2σ	Al WT%	±2σ	Cr WT%	±2σ	Mg WT%	±2σ	Ca WT%	±2σ	Mn WT%	±2σ
Ol phenocryst 1	10	Rim	15,66	0,03	0,01	0,02	0,00	0,00	0,04	0,01	13,26	0,03	0,22	0,01	0,62	0,01
Ol phenocryst 1	20	Rim	15,65	0,03	0,00	0,00	0,02	0,00	0,08	0,01	13,99	0,03	0,21	0,01	0,55	0,01
Ol phenocryst 1	30	Rim	16,16	0,03	0,02	0,02	0,01	0,00	0,05	0,01	15,03	0,03	0,20	0,01	0,54	0,01
Ol phenocryst 1	40	Rim	9,86	0,02	0,01	0,02	1,81	0,01	0,06	0,01	6,70	0,02	0,16	0,01	0,39	0,01
Ol phenocryst 1	50	Rim	16,50	0,03	0,00	0,02	0,01	0,00	0,08	0,01	16,79	0,04	0,18	0,01	0,48	0,01
Ol phenocryst 1	60	Rim	16,59	0,03	0,02	0,02	0,01	0,00	0,08	0,02	17,16	0,04	0,17	0,01	0,47	0,01
Ol phenocryst 1	70	Rim	16,48	0,03	0,01	0,02	0,01	0,00	0,05	0,01	17,68	0,04	0,17	0,01	0,48	0,01
Ol phenocryst 1	80	Rim	16,73	0,03	0,00	0,00	0,01	0,00	0,03	0,01	18,34	0,04	0,16	0,01	0,45	0,01
Ol phenocryst 1	90	Core	16,75	0,03	0,00	0,00	0,03	0,00	0,10	0,02	18,51	0,04	0,16	0,01	0,48	0,01
Ol phenocryst 1	100	Core	16,80	0,03	0,00	0,00	0,01	0,00	0,07	0,01	18,79	0,04	0,18	0,01	0,44	0,01
Ol phenocryst 1	110	Core	16,79	0,03	0,02	0,02	0,01	0,00	0,08	0,01	18,79	0,04	0,16	0,01	0,45	0,01
Ol phenocryst 1	120	Core	16,92	0,03	0,01	0,02	0,01	0,00	0,12	0,02	19,26	0,04	0,17	0,01	0,45	0,01
Ol phenocryst 1	130	Core	16,47	0,03	0,00	0,00	0,01	0,00	0,08	0,02	18,83	0,04	0,17	0,01	0,44	0,01
Ol phenocryst 1	140	Core	16,63	0,03	0,00	0,00	0,01	0,00	0,09	0,02	19,37	0,04	0,17	0,01	0,44	0,01
Ol phenocryst 1	150	Core	16,88	0,03	0,00	0,02	0,01	0,00	0,11	0,02	19,47	0,04	0,16	0,01	0,40	0,01
Ol phenocryst 1	160	Core	16,89	0,03	0,00	0,02	0,02	0,00	0,12	0,02	19,54	0,04	0,16	0,01	0,44	0,01
Ol phenocryst 1	170	Core	16,69	0,03	0,01	0,02	0,01	0,00	0,13	0,02	19,37	0,04	0,17	0,01	0,43	0,01
Ol phenocryst 1	180	Rim	16,63	0,03	0,02	0,02	0,01	0,00	0,14	0,02	19,18	0,04	0,16	0,01	0,44	0,01
Ol phenocryst 1	190	Rim	16,64	0,03	0,03	0,02	0,01	0,00	0,16	0,02	18,76	0,04	0,17	0,01	0,41	0,01
Ol phenocryst 1	200	Rim	16,25	0,03	0,00	0,00	0,06	0,00	0,12	0,02	18,51	0,04	0,16	0,01	0,43	0,01
Ol phenocryst 1	210	Rim	15,86	0,03	0,02	0,02	0,06	0,00	0,13	0,02	15,95	0,03	0,17	0,01	0,47	0,01
Ol phenocryst 1	220	Rim	15,95	0,03	0,03	0,02	0,00	0,00	0,12	0,02	15,05	0,03	0,16	0,01	0,54	0,01
Ol phenocryst 1	230	Rim	15,11	0,03	0,05	0,02	0,01	0,00	0,10	0,02	12,67	0,03	0,20	0,01	0,58	0,01
Ol phenocryst 1	240	Rim	14,86	0,03	0,07	0,02	0,07	0,00	0,13	0,02	10,93	0,03	0,20	0,01	0,63	0,01

(...continued...)

	Fe WT%	±2σ	Na WT%	±2σ	K WT%	±2σ	P WT%	±2σ	O WT%	Ni WT%	±2σ	TOTAL	Mg#
Ol phenocryst 1	31,61	0,06	0,01	0,01	0,00	0,00	0,02	0,01	35,96	0,01	0,01	97,4	29,6
Ol phenocryst 1	30,63	0,06	0,00	0,00	0,00	0,00	0,07	0,01	36,20	0,01	0,01	97,4	31,3
Ol phenocryst 1	29,91	0,06	0,01	0,01	0,00	0,00	0,08	0,01	37,27	0,02	0,01	99,3	33,4
Ol phenocryst 1	25,29	0,06	0,00	0,00	0,00	0,00	0,00	0,01	24,71	0,00	0,00	69,0	21,0
Ol phenocryst 1	27,19	0,06	0,01	0,01	0,00	0,00	0,04	0,01	37,96	0,01	0,01	99,3	38,2
Ol phenocryst 1	26,15	0,06	0,01	0,01	0,00	0,00	0,05	0,01	38,02	0,02	0,01	98,7	39,6
Ol phenocryst 1	24,99	0,06	0,00	0,00	0,00	0,00	0,06	0,01	37,91	0,02	0,01	97,9	41,4
Ol phenocryst 1	25,02	0,06	0,00	0,01	0,01	0,00	0,04	0,01	38,58	0,03	0,01	99,4	42,3
Ol phenocryst 1	24,55	0,06	0,00	0,00	0,00	0,00	0,04	0,01	38,63	0,03	0,01	99,3	43,0
Ol phenocryst 1	23,79	0,06	0,01	0,01	0,00	0,00	0,05	0,01	38,65	0,03	0,01	98,8	44,1
Ol phenocryst 1	23,71	0,06	0,02	0,01	0,00	0,00	0,07	0,01	38,65	0,04	0,01	98,8	44,2
Ol phenocryst 1	23,03	0,06	0,01	0,01	0,00	0,00	0,05	0,01	38,90	0,05	0,01	99,0	45,5
Ol phenocryst 1	23,04	0,06	0,01	0,01	0,00	0,00	0,05	0,01	38,07	0,04	0,01	97,2	45,0
Ol phenocryst 1	22,59	0,05	0,00	0,00	0,01	0,00	0,10	0,01	38,56	0,04	0,01	98,0	46,2
Ol phenocryst 1	22,48	0,05	0,00	0,00	0,00	0,00	0,05	0,01	38,81	0,05	0,01	98,4	46,4
Ol phenocryst 1	22,47	0,05	0,01	0,01	0,00	0,00	0,05	0,01	38,89	0,04	0,01	98,6	46,5
Ol phenocryst 1	22,66	0,05	0,01	0,01	0,00	0,00	0,07	0,01	38,63	0,05	0,01	98,2	46,1
Ol phenocryst 1	23,11	0,06	0,00	0,01	0,00	0,00	0,08	0,01	38,59	0,04	0,01	98,4	45,4
Ol phenocryst 1	23,51	0,06	0,00	0,01	0,01	0,00	0,08	0,01	38,46	0,05	0,01	98,3	44,4
Ol phenocryst 1	24,65	0,06	0,01	0,01	0,00	0,00	0,07	0,01	38,16	0,03	0,01	98,4	42,9
Ol phenocryst 1	26,15	0,06	0,00	0,00	0,00	0,00	0,05	0,01	36,46	0,02	0,01	95,3	37,9
Ol phenocryst 1	29,66	0,06	0,00	0,01	0,01	0,00	0,01	0,01	36,90	0,03	0,01	98,5	33,7
Ol phenocryst 1	32,82	0,06	0,00	0,01	0,00	0,00	0,05	0,01	35,38	0,02	0,01	97,0	27,9
Ol phenocryst 1	34,99	0,07	0,00	0,00	0,02	0,00	0,14	0,01	34,77	0,00	0,01	96,8	23,8

Table A15 - EMPA chemistry of olivine phenocryst 2 in Tissint.

	Distance (µm)	Location	Si WT%	±2σ	Ti WT%	±2σ	Al WT%	±2σ	Cr WT%	±2σ	Mg WT%	±2σ	Ca WT%	±2σ	Mn WT%	±2σ
Ol phenocryst 2	10	Rim	15,41	0,03	0,01	0,00	11,84	7,97	0,05	0,01	0,62	0,00	34,11	0,92	0,00	0,00
Ol phenocryst 2	20	Rim	14,75	0,03	0,05	0,05	11,47	0,92	0,04	0,01	0,60	0,00	33,49	0,93	0,01	0,00
Ol phenocryst 2	30	Rim	15,80	0,03	0,01	0,01	13,20	6,66	0,04	0,01	0,58	0,00	32,56	0,92	0,01	0,00
Ol phenocryst 2	40	Rim	15,86	0,03	0,00	0,00	14,07	10,21	0,08	0,01	0,51	0,00	30,97	0,85	0,00	0,00
Ol phenocryst 2	50	Rim	15,45	0,03	0,04	0,00	14,32	1,46	0,06	0,01	0,49	0,00	29,45	0,92	0,00	0,00
Ol phenocryst 2	60	Rim	16,13	0,03	0,06	0,05	15,34	0,94	0,09	0,02	0,46	0,00	29,07	0,92	0,00	0,00
Ol phenocryst 2	70	Rim	16,36	0,03	0,01	0,01	16,07	8,30	0,07	0,01	0,50	0,00	28,19	0,92	0,01	0,00
Ol phenocryst 2	80	Rim	16,50	0,03	0,01	0,01	16,61	10,69	0,08	0,01	0,51	0,00	27,15	0,88	0,00	0,00
Ol phenocryst 2	90	Rim	16,57	0,03	0,01	0,01	17,10	6,10	0,07	0,01	0,47	0,00	25,93	0,85	0,00	0,00
Ol phenocryst 2	100	Rim	16,70	0,03	0,01	0,00	17,63	6,62	0,09	0,02	0,45	0,00	25,35	0,85	0,00	0,00
Ol phenocryst 2	110	Rim	16,77	0,03	0,01	0,07	18,09	8,06	0,09	0,02	0,43	0,00	24,65	0,81	0,00	0,00
Ol phenocryst 2	120	Core	16,97	0,03	0,01	0,00	18,44	7,90	0,09	0,02	0,48	0,00	24,40	0,81	0,01	0,00
Ol phenocryst 2	130	Core	16,88	0,03	0,04	0,10	18,38	1,73	0,07	0,01	0,43	0,00	24,01	0,78	0,01	0,00
Ol phenocryst 2	140	Core	17,09	0,03	0,00	0,00	18,88	19,11	0,06	0,01	0,43	0,00	23,53	0,81	0,00	0,00
Ol phenocryst 2	150	Core	17,13	0,03	0,01	0,00	19,21	7,27	0,06	0,01	0,42	0,00	23,51	0,80	0,00	0,00
Ol phenocryst 2	160	Core	17,20	0,03	0,01	0,02	19,36	9,24	0,10	0,02	0,42	0,00	23,23	0,74	0,00	0,00
Ol phenocryst 2	170	Core	17,24	0,03	0,01	0,03	19,44	6,73	0,21	0,02	0,45	0,00	22,81	0,76	0,00	0,00
Ol phenocryst 2	180	Core	17,36	0,03	0,01	0,01	19,48	11,72	0,15	0,02	0,44	0,00	22,66	0,75	0,00	0,00
Ol phenocryst 2	190	Core	17,44	0,03	0,01	0,81	19,48	6,47	0,12	0,02	0,42	0,00	22,83	0,76	0,01	0,00
Ol phenocryst 2	200	Core	17,37	0,03	0,01	0,02	19,53	7,39	0,07	0,01	0,41	0,00	22,86	0,71	0,00	0,00
Ol phenocryst 2	210	Core	17,49	0,03	0,05	0,11	19,43	1,46	0,15	0,02	0,44	0,00	22,77	0,68	0,00	0,00
Ol phenocryst 2	220	Core	17,63	0,04	0,00	0,00	19,51	0,19	0,11	0,05	0,46	0,00	22,75	1,17	0,01	0,00
Ol phenocryst 2	240	Core	17,55	0,03	0,00	0,05	19,33	12,99	0,09	0,02	0,44	0,00	22,67	0,71	0,00	0,00
Ol phenocryst 2	250	Core	17,34	0,03	0,01	0,01	19,00	5,99	0,08	0,01	0,42	0,00	22,55	0,71	0,00	0,00
Ol phenocryst 2	260	Core	17,20	0,03	0,00	0,00	18,80	0,00	0,07	0,01	0,41	0,00	22,95	0,74	0,00	0,00
Ol phenocryst 2	270	Rim	17,81	0,03	0,01	0,02	19,31	9,64	0,05	0,01	0,43	0,00	22,99	0,73	0,00	0,00
Ol phenocryst 2	280	Rim	17,89	0,03	0,00	0,01	19,15	13,70	0,11	0,02	0,45	0,00	23,48	0,76	0,00	0,00
Ol phenocryst 2	290	Rim	17,89	0,03	0,00	0,00	18,86	16,48	0,12	0,02	0,49	0,00	23,59	0,74	0,00	0,00
Ol phenocryst 2	300	Rim	17,87	0,03	0,00	0,01	18,72	14,91	0,13	0,02	0,48	0,00	23,64	0,77	0,00	0,00
Ol phenocryst 2	310	Rim	18,09	0,03	0,04	0,24	18,74	1,86	0,13	0,02	0,46	0,00	24,04	0,73	0,00	0,00
Ol phenocryst 2	320	Rim	17,72	0,03	0,01	0,02	18,55	6,87	0,09	0,02	0,46	0,00	24,27	0,78	0,00	0,00
Ol phenocryst 2	330	Rim	17,56	0,03	0,02	0,00	17,74	3,88	0,10	0,02	0,47	0,00	24,47	0,75	0,00	0,00
Ol phenocryst 2	340	Rim	17,61	0,03	0,02	0,00	17,79	3,44	0,13	0,02	0,47	0,00	24,71	0,78	0,00	0,00
Ol phenocryst 2	350	Rim	17,23	0,03	0,07	0,00	17,01	0,95	0,09	0,02	0,48	0,00	25,47	0,77	0,01	0,00
Ol phenocryst 2	360	Rim	17,64	0,03	0,00	0,01	17,21	13,42	0,08	0,01	0,50	0,00	26,00	0,81	0,00	0,00
Ol phenocryst 2	370	Rim	17,54	0,03	0,01	0,02	17,01	11,49	0,07	0,01	0,50	0,00	26,73	0,84	0,00	0,00
Ol phenocryst 2	380	Rim	17,35	0,03	0,03	0,08	16,05	2,24	0,07	0,01	0,51	0,00	27,45	0,84	0,00	0,00
Ol phenocryst 2	390	Rim	17,18	0,03	0,01	0,00	15,58	8,78	0,07	0,01	0,51	0,00	28,75	0,85	0,00	0,00
Ol phenocryst 2	400	Rim	17,30	0,03	0,00	0,00	15,04	0,00	0,08	0,01	0,55	0,00	29,40	0,85	0,00	0,00

(...continued...)

	Fe WT%	±2σ	Na WT%	±2σ	K WT%	±2σ	P WT%	±2σ	O WT%	Ni WT%	±2σ	TOTAL	Mg#
Ol phenocryst 2	0,24	0,00	0,00	0,00	0,00	0,00	0,03	0,01	35,47	0,00	0,00	97,8	71,9
Ol phenocryst 2	0,23	0,00	0,02	0,08	0,01	0,00	0,04	0,01	34,34	0,00	0,00	95,0	72,5
Ol phenocryst 2	0,22	0,00	0,01	0,01	0,01	0,01	0,03	0,01	36,36	0,00	0,00	98,8	71,9
Ol phenocryst 2	0,23	0,00	0,00	0,00	0,02	0,05	0,08	0,01	36,60	0,00	0,00	98,4	68,9
Ol phenocryst 2	0,19	0,00	0,00	0,00	0,02	0,00	0,10	0,01	35,88	0,00	0,00	96,0	72,0
Ol phenocryst 2	0,19	0,00	0,03	0,00	0,03	0,08	0,10	0,01	37,27	0,00	0,00	98,8	70,8
Ol phenocryst 2	0,18	0,00	0,02	0,00	0,03	0,02	0,09	0,01	37,69	0,00	0,00	99,2	73,3
Ol phenocryst 2	0,18	0,00	0,01	0,01	0,02	0,00	0,09	0,01	37,89	0,00	0,00	99,0	73,5
Ol phenocryst 2	0,18	0,00	0,02	0,00	0,02	0,02	0,10	0,01	37,96	0,00	0,00	98,4	72,5
Ol phenocryst 2	0,18	0,00	0,00	0,00	0,03	0,04	0,12	0,01	38,31	0,00	0,00	98,9	71,7
Ol phenocryst 2	0,18	0,00	0,00	0,00	0,02	0,00	0,12	0,01	38,49	0,00	0,00	98,9	70,7
Ol phenocryst 2	0,18	0,00	0,00	0,00	0,04	0,01	0,07	0,01	38,83	0,00	0,00	99,5	72,8
Ol phenocryst 2	0,18	0,00	0,01	0,01	0,03	0,02	0,03	0,01	38,53	0,00	0,00	98,6	70,5
Ol phenocryst 2	0,17	0,00	0,00	0,00	0,05	0,00	0,05	0,01	38,94	0,00	0,00	99,2	71,7
Ol phenocryst 2	0,17	0,00	0,00	0,00	0,04	0,00	0,03	0,01	39,17	0,00	0,00	99,7	71,1
Ol phenocryst 2	0,19	0,00	0,01	0,01	0,04	0,24	0,03	0,01	39,30	0,00	0,00	99,9	69,4
Ol phenocryst 2	0,18	0,00	0,01	0,00	0,04	0,00	0,03	0,01	39,34	0,00	0,00	99,7	71,7
Ol phenocryst 2	0,18	0,00	0,02	0,02	0,03	0,00	0,01	0,01	39,41	0,00	0,00	99,8	71,3
Ol phenocryst 2	0,18	0,00	0,00	0,00	0,04	0,03	0,00	0,01	39,52	0,00	0,00	100,1	70,3
Ol phenocryst 2	0,19	0,00	0,01	0,01	0,05	0,00	0,01	0,01	39,48	0,00	0,00	100,0	67,9
Ol phenocryst 2	0,21	0,00	0,01	0,00	0,03	0,09	0,03	0,01	39,62	0,00	0,00	100,2	68,1
Ol phenocryst 2	0,18	0,00	0,02	0,00	0,04	0,00	0,01	0,01	39,75	0,00	0,00	100,5	72,2
Ol phenocryst 2	0,19	0,00	0,00	0,00	0,04	0,04	0,05	0,01	39,55	0,00	0,00	99,9	69,3
Ol phenocryst 2	0,19	0,00	0,02	0,02	0,03	0,00	0,05	0,01	39,05	0,00	0,00	98,7	68,4
Ol phenocryst 2	0,19	0,00	0,02	0,00	0,04	0,00	0,01	0,01	38,82	0,00	0,00	98,5	68,9
Ol phenocryst 2	0,19	0,00	0,01	0,00	0,05	0,00	0,03	0,01	39,87	0,00	0,00	100,7	69,4
Ol phenocryst 2	0,18	0,00	0,01	0,00	0,04	0,00	0,03	0,01	40,05	0,00	0,00	101,4	71,2
Ol phenocryst 2	0,19	0,00	0,00	0,00	0,04	0,00	0,04	0,01	39,89	0,00	0,00	101,1	71,7
Ol phenocryst 2	0,18	0,00	0,01	0,01	0,02	0,00	0,06	0,01	39,83	0,00	0,00	101,0	72,4
Ol phenocryst 2	0,20	0,00	0,00	0,00	0,04	0,31	0,08	0,01	40,25	0,00	0,00	102,1	69,5
Ol phenocryst 2	0,19	0,00	0,01	0,00	0,03	0,00	0,06	0,01	39,71	0,00	0,00	101,1	71,3
Ol phenocryst 2	0,20	0,00	0,00	0,00	0,04	0,04	0,05	0,01	39,05	0,00	0,00	99,7	70,4
Ol phenocryst 2	0,19	0,00	0,00	0,00	0,02	0,00	0,03	0,01	39,19	0,00	0,00	100,2	71,0
Ol phenocryst 2	0,20	0,00	0,02	0,00	0,03	0,01	0,02	0,01	38,50	0,00	0,00	99,1	69,9
Ol phenocryst 2	0,19	0,00	0,01	0,00	0,03	0,00	0,03	0,01	39,19	0,00	0,00	100,9	72,2
Ol phenocryst 2	0,19	0,00	0,01	0,09	0,02	0,00	0,05	0,01	39,17	0,00	0,00	101,3	72,3
Ol phenocryst 2	0,20	0,00	0,01	0,00	0,02	0,00	0,01	0,01	38,50	0,00	0,00	100,2	71,9
Ol phenocryst 2	0,21	0,00	0,00	0,00	0,02	0,00	0,01	0,01	38,37	0,00	0,00	100,7	70,8
Ol phenocryst 2	0,22	0,00	0,02	0,00	0,02	0,00	0,04	0,01	38,39	0,00	0,00	101,0	71,6

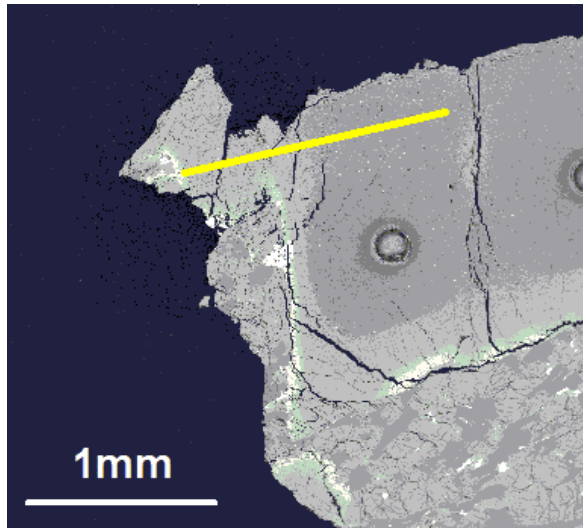


Fig. A3 - Olivine megacryst 1 and location of the EMPA transect (yellow line).

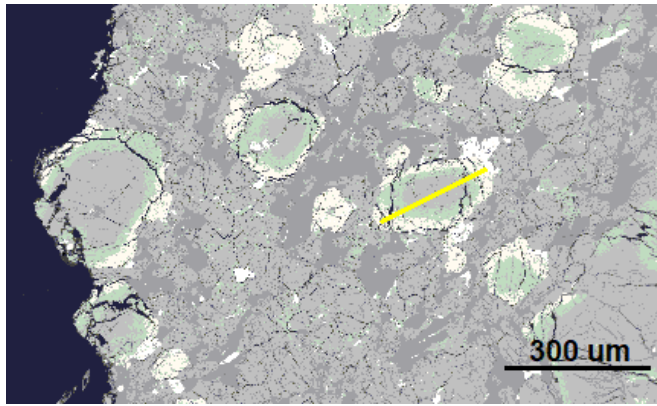


Fig. A4 - Olivine phenocryst 2 and location of the EMPA transect (yellow line).

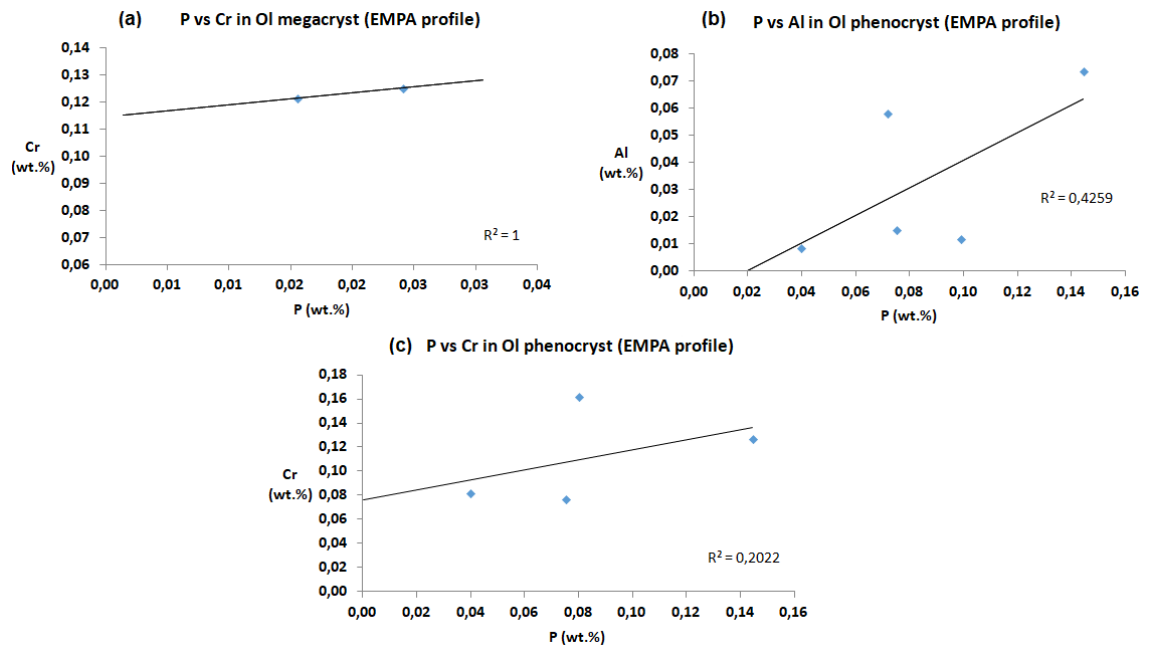


Fig. A5 - Cross plots (a, b, c) indicating the degree of correlation (linked to co-variation) of the points in the EMPA transect argued to be influenced by the solute trapping (for P, Al, and Cr; where the orange arrows are shown in Fig. 3.4). A trendline has been calculated to show this correlation.

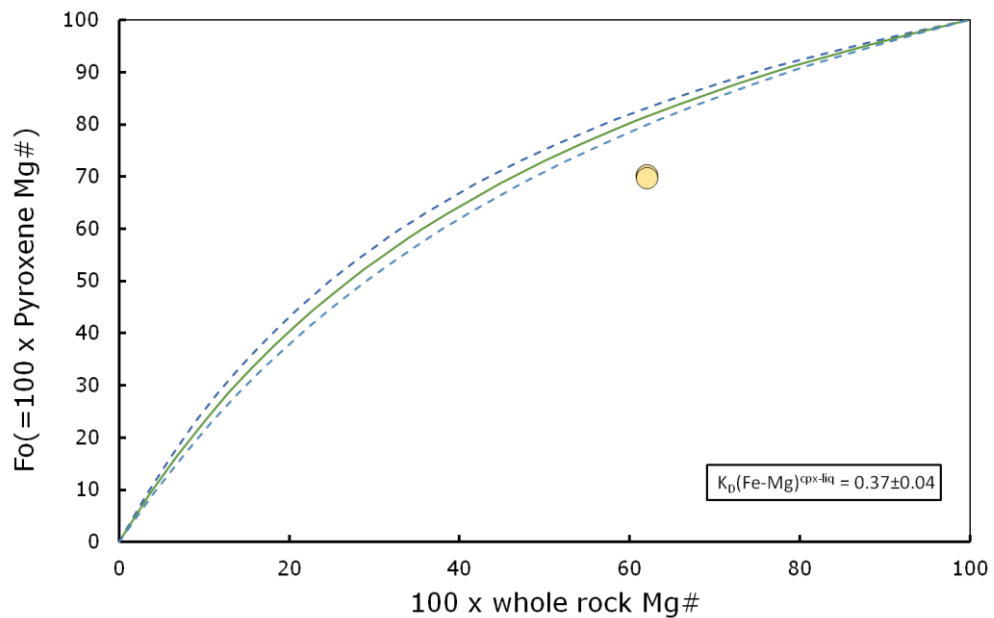


Fig. A6 - Rhodes diagram for Mg-pyroxene in Tissint using the black glass composition from (Chennaoui Aoudjehane et al., 2012).

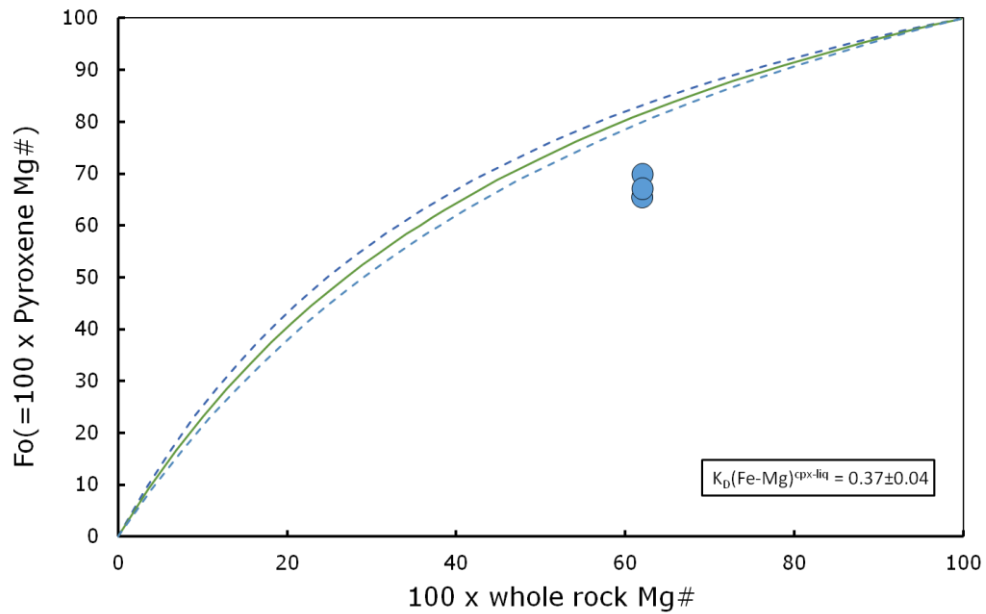


Fig. A7 - Rhodes diagram for Ca-pyroxene in Tissint using the black glass composition from (Chennaoui Aoudjehane et al., 2012).

Table A16 - LA-ICP-MS trace elements composition of typical Tissint minerals; n. m. = not measured.

ppm	Olivine megacryst avg (n = 2)				Olivine phenocryst avg (n = 9)				Fe-rich	$\pm 2\sigma$
	core	$\pm 2\sigma$	rim	$\pm 2\sigma$	Mg-rich	$\pm 2\sigma$	Intermediate	$\pm 2\sigma$		
La	0.8	2	0	0	0.8	1.5	0.8	1.2	1.5	0.6
Ce	n.m.	n.m.	n.m.	n.m.	n.m.	n.m.	n.m.	n.m.	n.m.	n.m.
Sm	4.1	17.7	3.4	9.9	2.5	10.6	3.4	7.6	8.5	3.4
Gd	6.2	8.6	5	7.3	7.7	7.4	5.8	5.5	13.7	3.2
Dy	21.1	6.8	19.1	7.8	18.4	5.3	19	4.6	22.8	3.1
Er	36	11.5	37.1	11.9	36.5	9	35	8.2	32.7	5.1
Yb	68.7	19.7	74	19.1	62.2	17.6	60.3	12	46.8	6.6
Lu	82.7	23	56.8	25.9	75.4	20	80.7	22.2	54.5	10.3

ppm	Pyroxene avg (n = 4)				Chromite avg (n = 2)		Fusion crust avg (n = 2)	
	Ca-rich	$\pm 2\sigma$	Mg-rich	$\pm 2\sigma$	$\pm 2\sigma$	$\pm 2\sigma$	$\pm 2\sigma$	
La	1.9	0.3	1.6	0.6	1.3	2.6	4.2	0.9
Ce	2.8	0.6	2.3	0.9	2.9	3.7	5.2	0.7
Sm	13.9	2.1	12	3.2	15.6	13.6	19.4	2
Gd	22.1	1.9	19.2	3	20.1	17.8	26.1	2.1
Dy	28.6	1.8	27.3	2.7	28.8	10.1	29	1.5
Er	28.4	2	28.8	2.8	39.5	19.1	27.3	1.5
Yb	27.1	2.3	29.8	3.3	37.6	18.2	23.8	2.5
Lu	26.7	2.5	29.8	4.2	30.7	23	22.8	2.3

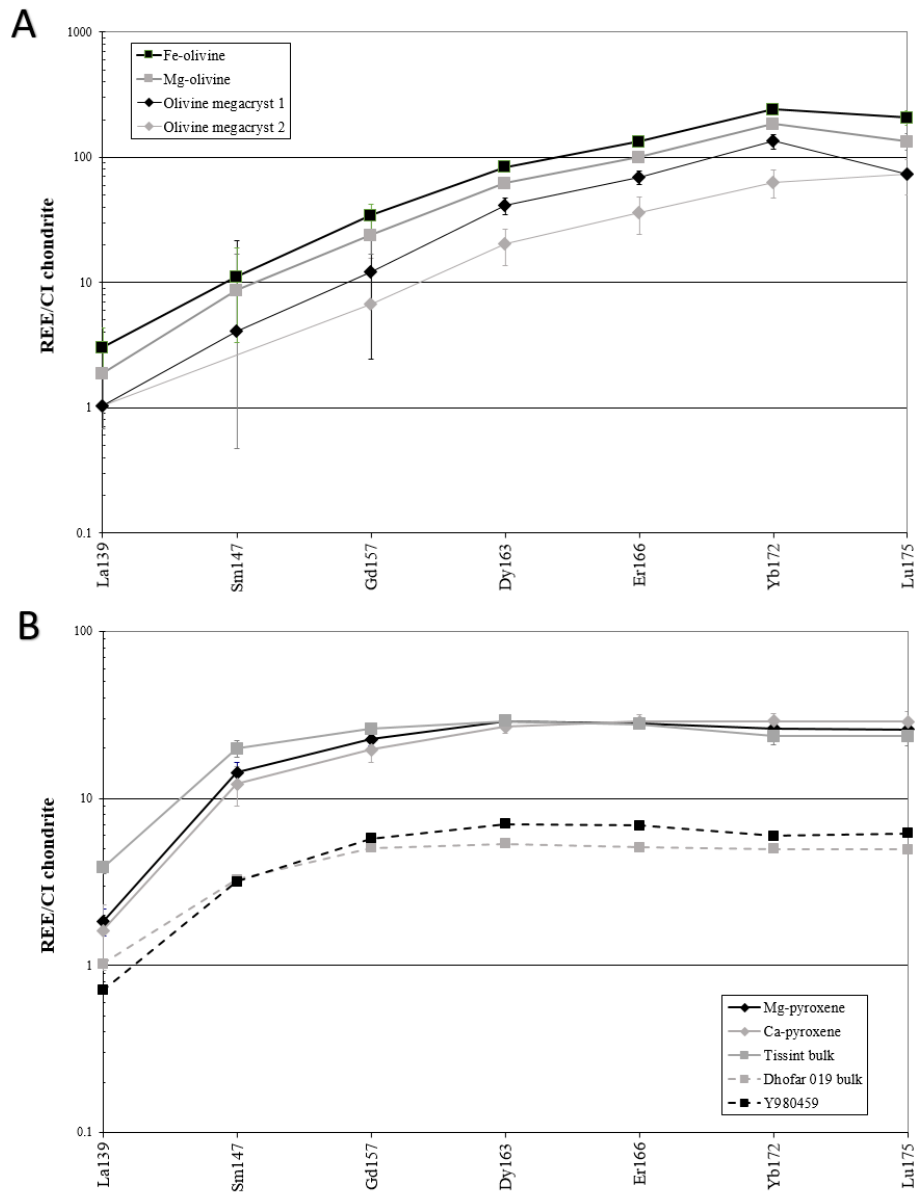


Fig. A8 - REE abundance normalized to CI chondrite in Tissint; (A) for the olivine megacrysts and olivine phenocrysts; (B) for the pyroxenes, the bulk composition of Tissint (data acquired from the fusion crust), the bulk composition of Dhofar 019 (data from Taylor et al., 2002) and Y-980459 (data from Shirai and Ebihara, 2004) for comparison. Error bars are shown to represent the standard error of LA-ICP-MS analysis for each REE.

B.2 – Supplementary information on Chapter 4

Textural characteristics and location of all sulphides subject to sulphur-isotope analyses by ion microprobe in the samples of Nakhla, Lafayette, MIL 090032, Yamato 000749, and Yamato 000593 are represented in Fig. A9-A12. Most of the sulphides can be found near the mesostasis and in contact with pyroxene phases. Sulphide chemistry can be seen in Table A17. Plots on sulphide chemistry can be seen in Fig. A13.

The comparison between the nakhlite stratigraphy that was proposed by Cohen et al. (2017) from argon isotope geochronology with the sulphur isotope systematics is shown in Fig. A14. Preliminary magma/crustal mixing hypothesis is shown in Fig. A15. The $^{187}\text{Os}/^{188}\text{Os}$ versus $1/\text{Os}$ graph suggest that Lafayette and Nakhla were affected by some sort of mixing within two different isotopical end-members, that could be the crust or a magma/mantle component.

Other processes as sulphide-sulphide partitioning, sulphide melt-silicate melt partitioning, and metal-silicate partitioning can affect the sulphur isotope systematics of nakhlites. However, although investigating these processes are not within the scope of this work, here these processes are considered to have potential for only negligible and non-MIF fractionations, as can be inferred from previous studies (e.g., Thode, 1970). Sulphate-reducing bacteria could be another mechanism of the large sulphur isotopic fractionation as seen in the samples (e.g., Parnell et al., 2010) and compared with the recent Curiosity rover analysis of $\delta^{34}\text{S}$ on Gale Crater on Mars (Franz et al., 2017). However, at this stage and with the data presently available it is not possible to discern this process versus the abiogenic pathways facilitating $\delta^{34}\text{S}$ fractionation.

In addition, the Re-Os isotope systematics and HSE abundances were also analysed in four different fragments (~10 to 40 mg) of the Tissint olivine-phyric shergottite - but this was not included in the main discussion of this work because then this part of the project was focused solely on nakhlites. Four Tissint fragments (Tissint-A, Tissint-B, Tissint-C, and Tissint-D; 0.04 g, 0.05 g, 0.04 g, and 0.01 g, respectively) that had a flat surface and did not require polishing were used (Fig. A16). These fragments were cut from Tissint sample 2-3-3/1 from the University of Alberta Museum. The Re-Os and HSE chemical separation for the four Tissint fragments (Tissint-A, Tissint-B, Tissint-C, and Tissint-D) was conducted in the ultra-clean laboratory at the Durham

Geochemistry Centre of Durham University. Within 0.1-0.4 g of powder for chosen fragments of Tissint were obtained. The method used is the same as described in [Chapter 4](#), but a picrite spike was used for the Tissint fragments. Results from the Re-Os isotope analysis and HSE abundances of the four Tissint fragments can be found in [Fig. A17](#), [Fig. A18](#), and [Table A18](#). Tissint likely assimilated crustal sulphur due to shock events on the Martian surface (Gattacceca et al., 2013). Thus, the higher HSE abundances of our fragments in respect to previous Tissint HSE analysis (Tait and Day, 2018) may be interpreted as heterogeneous assimilation of Martian crustal material during the impact ejection event of Tissint.

The procedure for the estimates of the HSE of the Martian mantle as was reported in [Chapter 6](#) is displayed in [Fig. A19](#).

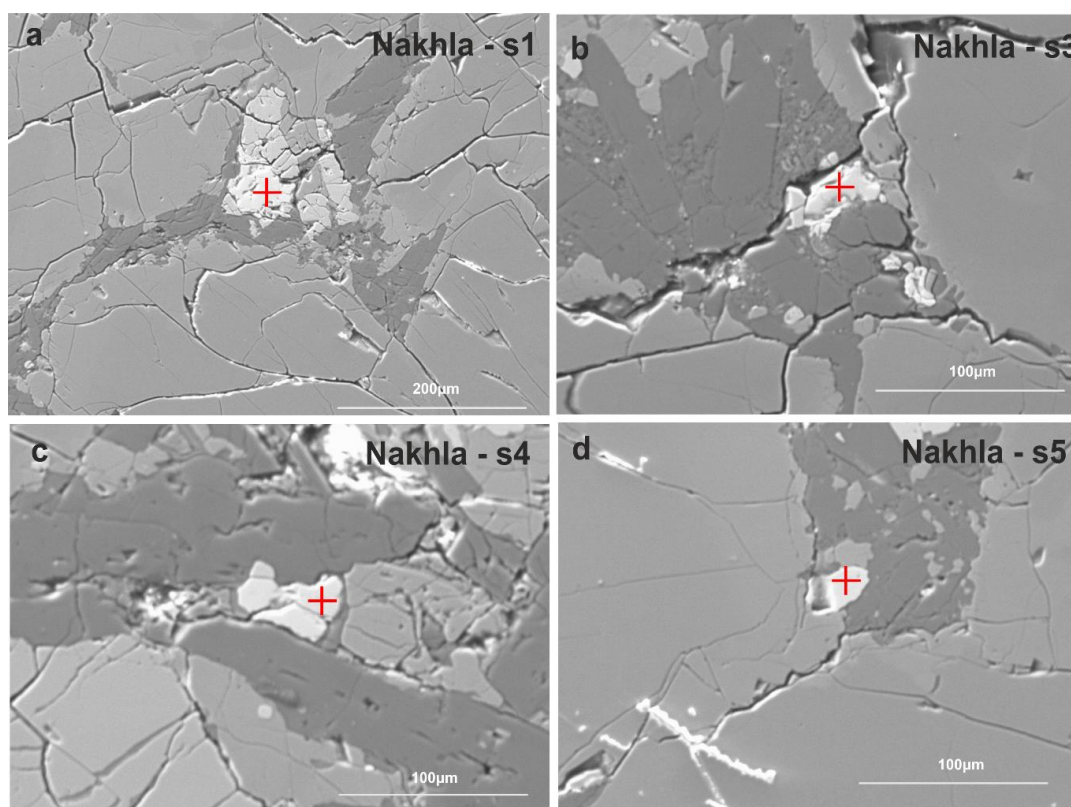


Fig. A9 - Sulphide locations in Nakhla (a, b, c, d).

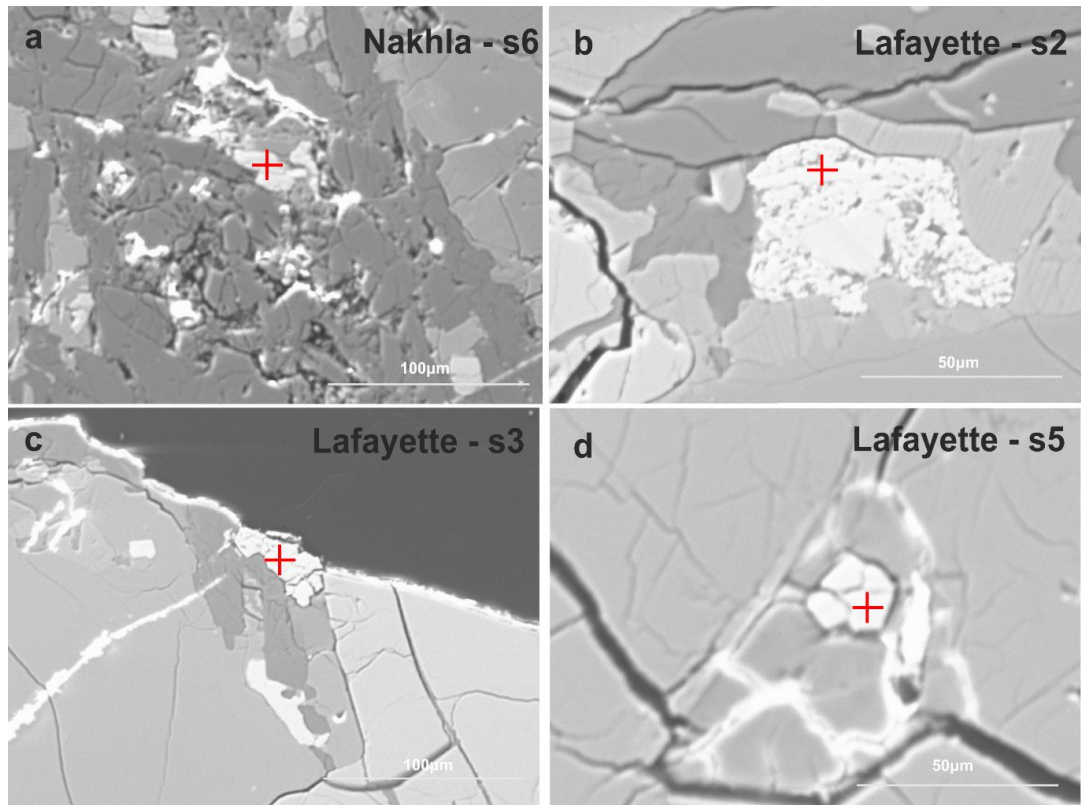


Fig. A10 - Sulphide locations in Nakhla (a) and in Lafayette (b, c, d).

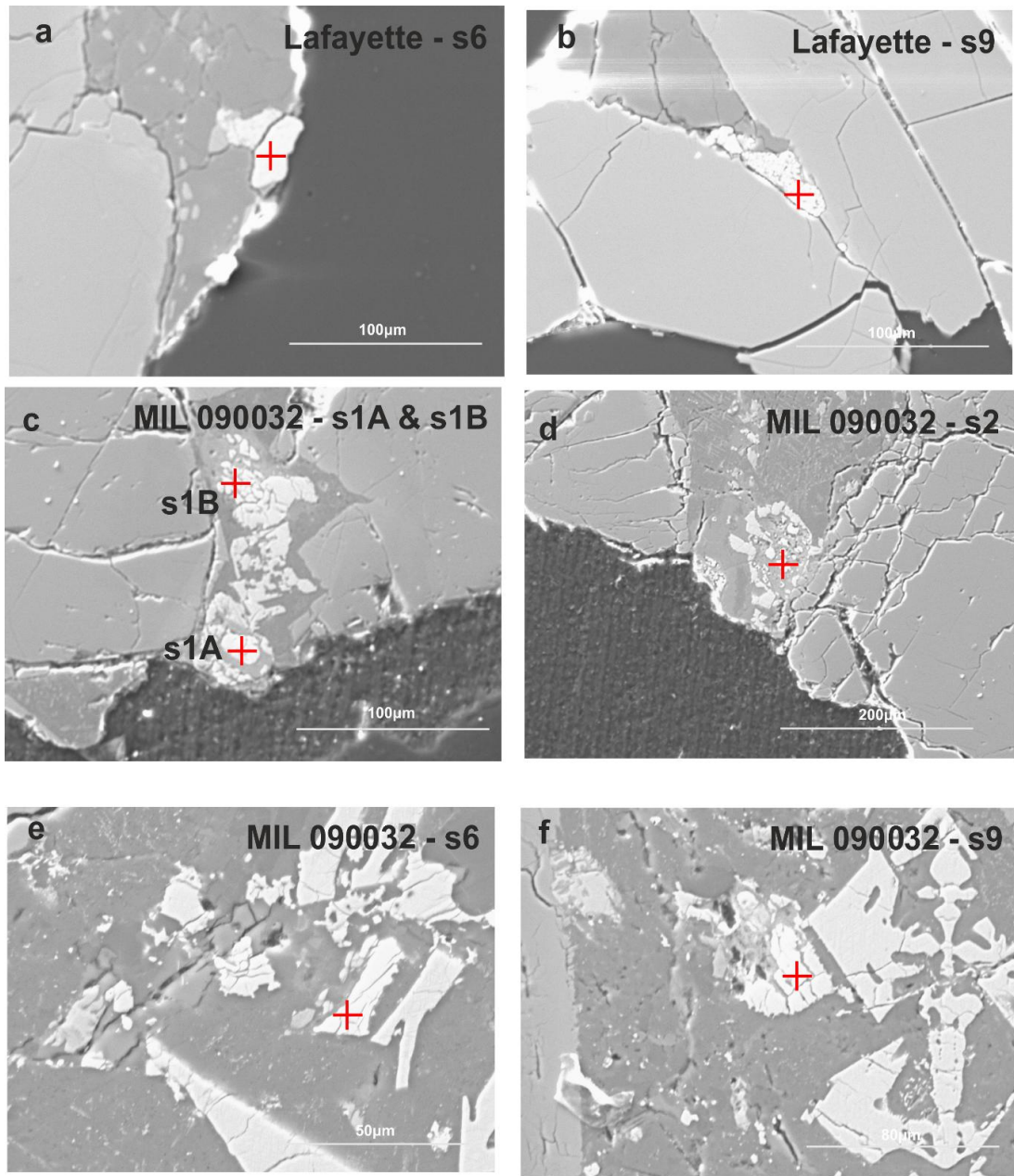


Fig. A11 - Sulphide locations in Lafayette (a, b) and MIL 090032 (c, d, e, f).

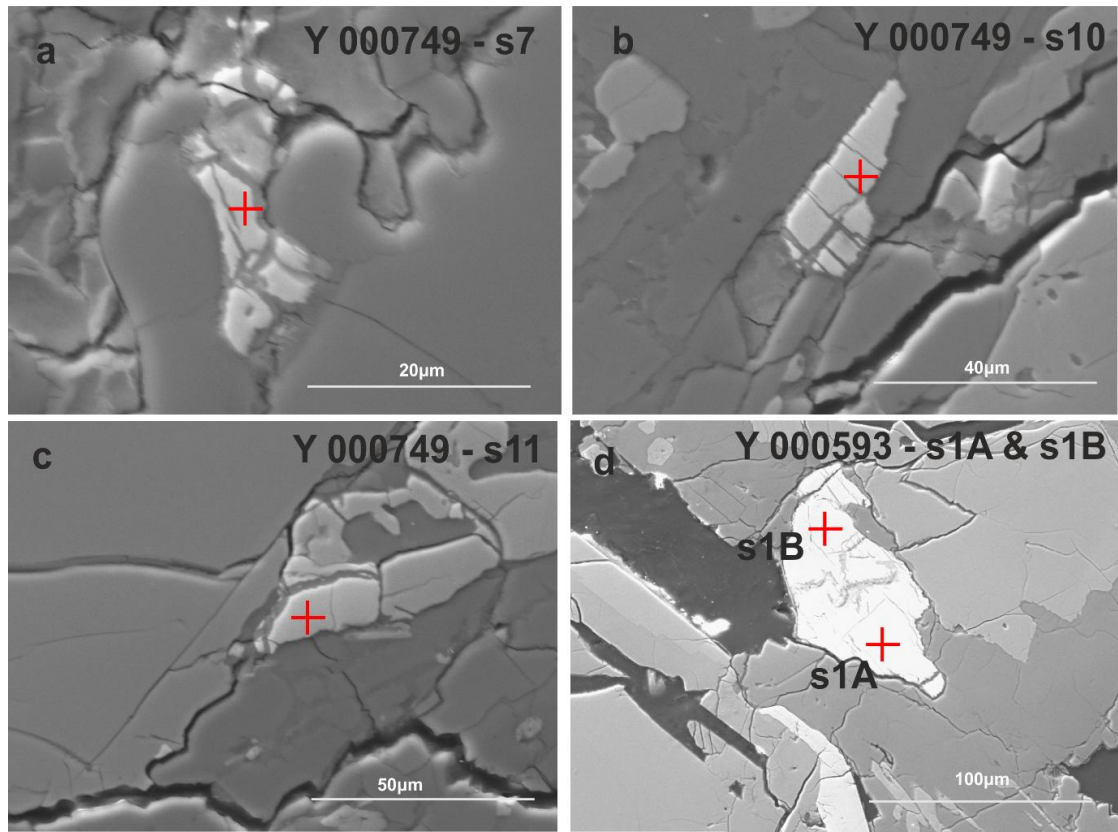


Fig. A12 - Sulphide locations in Yamato 000749 (a, b, c) and Yamato 000593 (d).

Table A17 - SEM-EDS sulphide chemistry.

Nakhla sulphides

Element wt.%	sulphide 1	sulphide 3	sulphide 4	sulphide 5	sulphide 6
SiO2	0.05	0.05	0.08	0.08	0.11
S2	38.63	40.06	39.37	39.92	39.67
CaO	0.08	0.06	0.11	0.09	0.08
TiO2	0.45	0.16	0.11	0.16	0.09
MnO	0.01	-0.01	0.00	0.05	0.02
FeO	59.36	60.01	59.84	60.16	59.54
Co	0.46	0.43	0.39	0.44	0.40
NiO	0.47	0.27	0.66	0.30	0.34
Cu	-0.09	-0.06	-0.13	-0.14	-0.08
Total	99.42	100.96	100.44	101.02	100.17

Lafayette sulphides

Element wt.%	sulphide 2	sulphide 3	sulphide 5	sulphide 6	sulphide 9
SiO2	0.07	0.04	0.05	0.17	0.05
S2	54.04	53.89	53.13	48.91	51.93
CaO	0.08	0.06	0.11	0.09	0.22
TiO2	0.24	0.27	0.28	0.17	0.23
MnO	0.03	0.03	0.02	-0.01	0.01
FeO	45.66	46.52	46.09	47.40	44.38
Co	0.60	0.28	0.25	0.48	0.47
NiO	0.57	0.26	0.04	0.54	1.71
Cu	-0.05	-0.08	-0.05	-0.07	-0.10
Total	101.25	101.26	99.91	97.68	98.91

MIL 090032

Element wt.%	sulphide 1A	sulphide 1B	sulphide 2	sulphide 6	sulphide 9
SiO2	0.08	0.05	0.09	0.56	0.08
S2	40.45	40.96	39.10	38.71	39.56
CaO	0.13	0.06	0.06	0.34	0.06
TiO2	0.09	0.13	0.08	0.37	0.23
MnO	-0.01	-	-0.02	0.02	-0.04
FeO	60.58	61.29	60.92	59.56	59.73
Co	0.39	0.33	0.37	0.32	0.32
NiO	0.04	0.13	0.04	0.05	0.05
Cu	-0.05	-	-0.07	-0.04	-0.11
Total	101.70	102.85	100.57	99.90	99.87

Yamato 000749

Element wt.%	sulphide 6	sulphide 7	sulphide 8	sulphide 10	sulphide 11
SiO2	0.07	0.31	0.16	0.14	0.09
S2	39.38	41.34	40.30	41.53	39.50
CaO	0.08	0.13	0.14	0.19	0.18
TiO2	0.19	0.08	0.06	0.12	0.08
MnO	-0.01	-0.01	0.03	0.02	0.01
FeO	59.24	57.16	59.24	57.67	59.01
Co	0.32	0.28	0.44	0.33	0.42
NiO	0.06	0.09	0.10	0.17	0.11
Cu	-0.03	-0.07	-0.07	-0.03	-0.06
Total	99.30	99.31	100.39	100.13	99.33

Yamato 000593

Element wt.%	sulphide 1	sulphide 2	sulphide 3	sulphide 4	sulphide 6
SiO2	0.03	0.11	0.06	0.08	0.10
S2	40.71	39.94	40.19	40.03	40.75
CaO	0.00	0.21	0.13	0.34	0.08
TiO2	0.08	0.07	0.09	0.10	0.07
MnO	-0.01	-0.01	0.02	-0.02	0.01
FeO	59.88	59.16	59.54	59.14	60.27
Co	0.42	0.28	0.45	0.50	0.44
NiO	0.56	0.58	0.52	0.44	0.33
Cu	-0.08	-0.09	-0.19	-0.04	-0.06
Total	101.60	100.25	100.81	100.56	101.98

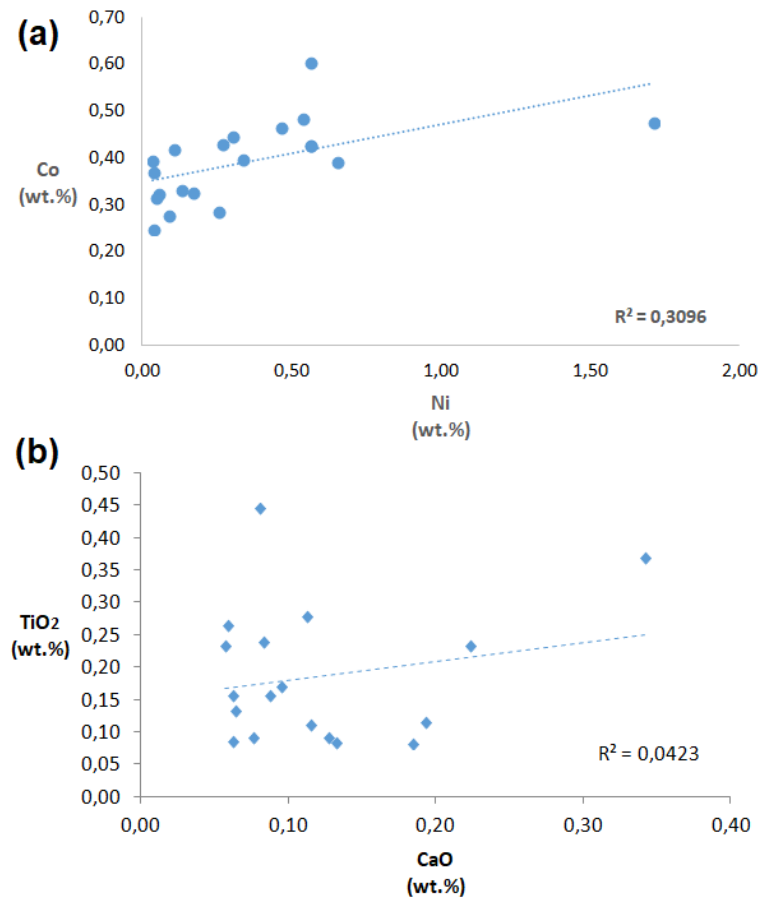


Fig. A13 - Sulphide chemistry in nakhlites. (a) Ni vs. Co content; (b) CaO vs. TiO₂ content.

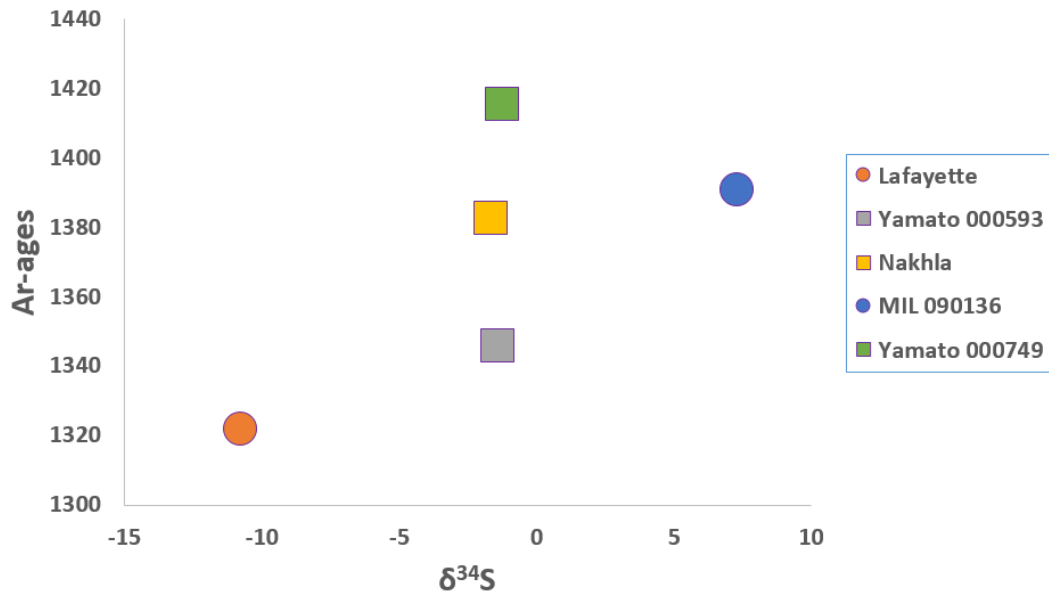


Fig. A14 - Comparison between $\delta^{34}\text{S}$ versus nakhlite age of crystallisation from Cohen et al. (2017). This stratigraphic model placed Nakhla and MIL 03346 (paired with MIL 090032) at an intermediate depth in the stack of lava flows, with MIL 03346 older in age (1390.9 Ma) than Nakhla (1382.5 Ma). This is followed by the emplacement of the NWA 5790 unit (1350.1 Ma). Error bars for 2σ uncertainties are less than symbol size.

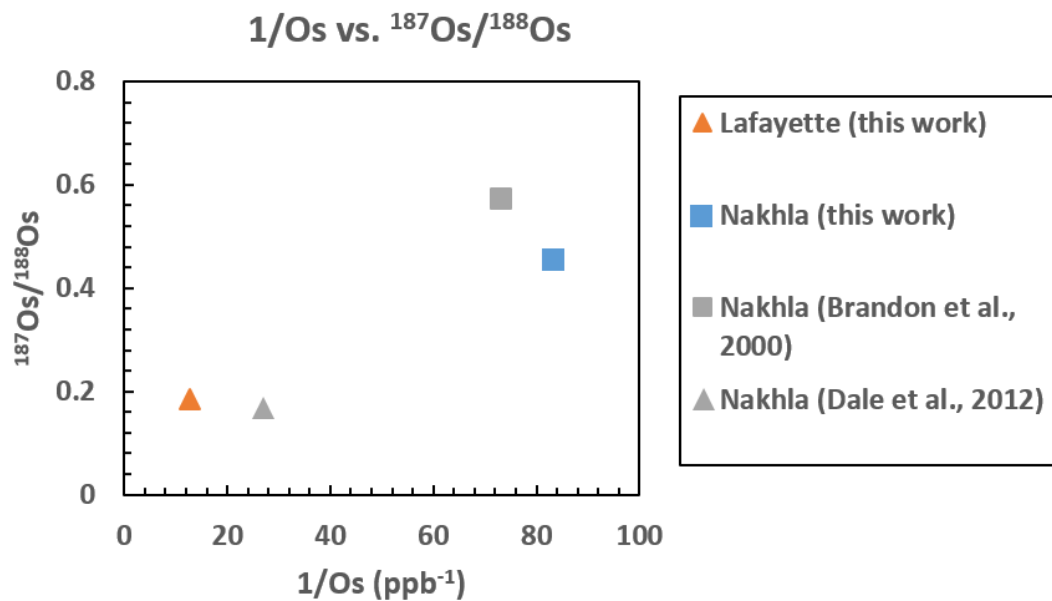


Fig. A15 - $^{187}\text{Os}/^{188}\text{Os}$ vs. $1/\text{Os}$ used to preliminarily assess a magma/crustal mixing hypothesis.

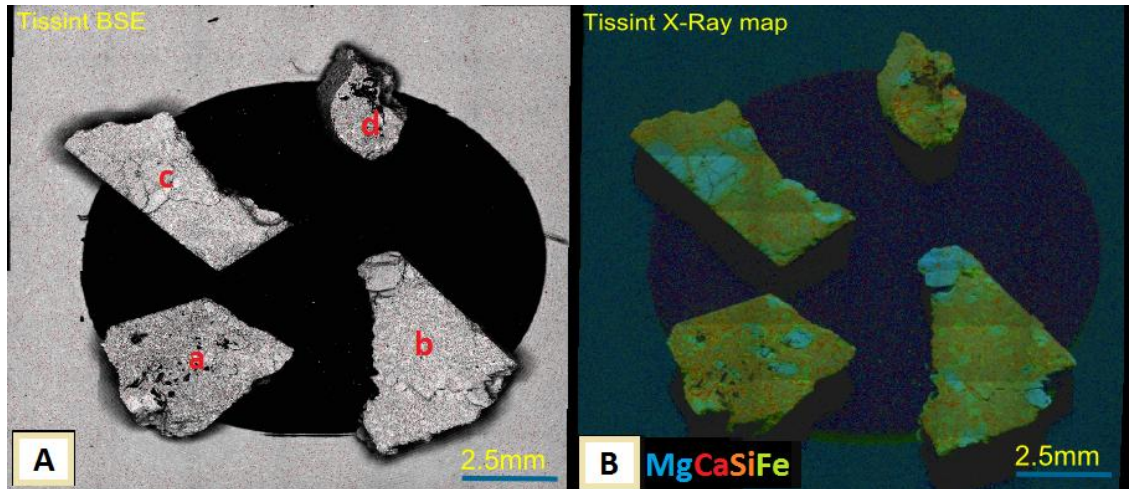


Fig. A16 - Characterization of the four Tissint fragments (labelled a, b, c, and d) used in this work. (A) Backscattered electron images (BSE); and (B) Mg, Ca, Si, Fe X-ray elemental maps used to retain information on textural characterization of our samples prior to destructive isotopic analyses.

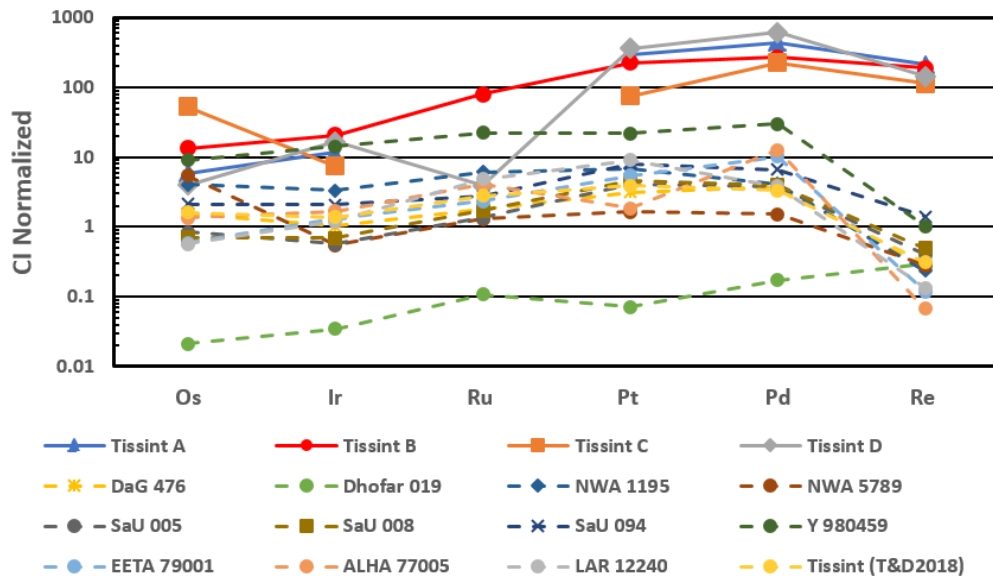


Fig. A17 - Highly siderophile elements abundances in the four Tissint fragments. Previous literature data on depleted shergottites (high MgO wt.%) are shown for comparison (from Jones et al., 2003; Brandon et al., 2012; Tait and Day, 2018).

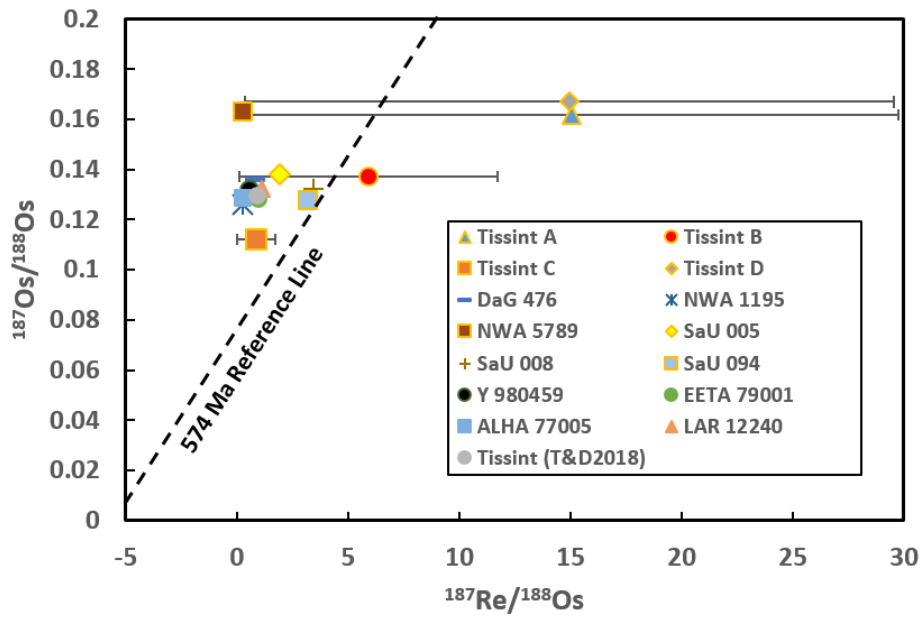


Fig. A18 - Re-Os isotope systematics in the Tissint fragments. The $^{187}\text{Re}/^{188}\text{Os}$ vs. $^{187}\text{Os}/^{188}\text{Os}$ data for Tissint are shown, along with previous literature data (from Brandon et al., 2012; Tait and Day, 2018). The 574 Ma reference line is shown for comparison and represents single-stage Re-Os isotope evolution from a chondritic $^{187}\text{Os}/^{188}\text{Os}$ reservoir, assuming a Solar System initial $^{187}\text{Os}/^{188}\text{Os} = 0.9524$ (Smoliar et al., 1996). Uncertainty for the Tissint fragments are 2σ , vertical error bars are less than symbol size.

Table A18 - Re-Os isotope systematics and HSE abundances (in ppb) for all Tissint fragments. The Os-isotope composition of the sample at the time of crystallization is represented by $^{187}\text{Os}/^{188}\text{Os}_i$. The YO_s notation is defined by $\text{YO}_s = 100 \times [(^{187}\text{Os}/^{188}\text{Os}_{\text{sample}(t)}) / (^{187}\text{Os}/^{188}\text{Os}_{\text{chondrite}(t)}) - 1]$. HSE ratios normalized to Orgueil chondrite are denoted by (N). Initial ^{143}Nd are from Nakamura et al. (1982) and Shih et al. (1998).

Sample	Type	Mass (g)	Os	blk (%)	Ir	blk (%)	Ru	blk (%)	Pt	blk (%)	Pd	blk (%)	Re	blk (%)
Tissint-A	shergottite	0.03630	0.271	2.10	0.520	0.05	-	-	25.6	0.18	24.8	0.88	0.843	0.65
Tissint-B	shergottite	0.04689	0.612	0.73	0.913	0.02	5.17	0.72	19.6	0.18	15.2	1.10	0.753	0.56
Tissint-C	shergottite	0.03873	2.420	0.20	0.329	0.07	-	-	6.52	0.66	12.8	1.59	0.446	1.14
Tissint-D	shergottite	0.01224	0.182	8.70	0.738	0.10	0.25	36.21	31.0	0.44	34.52	1.85	0.563	2.82

Sample	$^{187}\text{Re}/^{188}\text{Os}$	$\pm 2\sigma$	$^{187}\text{Os}/^{188}\text{Os}$	$\pm 2\sigma$	$^{187}\text{Os}/^{188}\text{Os}_i$	$\pm 2\sigma$	YO_s	$\pm 2\sigma$	Re/Os	Pt/Os	Os/Ir	(Pt/Pd) _N	(Pd/Os) _N
Tissint-A	15.047	14.70	0.1619	0.0007	0.0173	0.14	-86	119	3.10	94.4	0.52	0.67	73.8
Tissint-B	5.9325	5.81	0.1370	0.0004	0.0800	0.14	-36	270	1.23	32	0.67	0.84	19.9
Tissint-C	0.8857	0.87	0.1122	0.0001	0.1037	0.14	-17	1068	0.18	2.69	0.35	0.33	4.25
Tissint-D	14.974	14.68	0.1669	0.0009	0.0230	0.14	-82	80	3.09	170.3	0.24	0.58	153

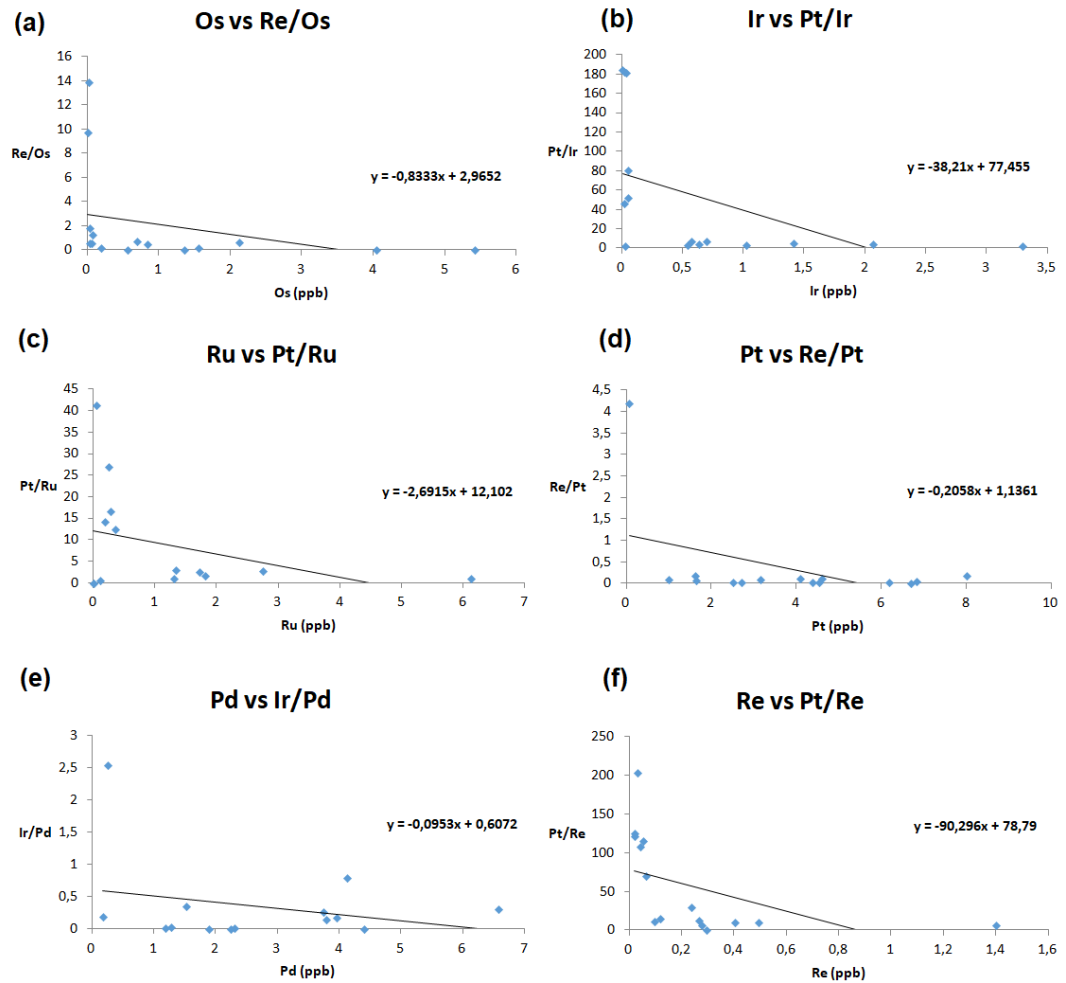


Fig. A19 - Procedure for the estimates of the HSE of the Martian mantle using the new data obtained in this work with previous data from Jones et al. (2003), Dale et al. (2012), Brandon et al. (2012), and Tait and Day (2018). Regression lines and their equations are shown, in order to obtain mantle abundance for Os (a), Ir (b), Ru (c), Pt (d), Pd (e), and Re (f).

B.3 - Supplementary information on Chapter 5

Complete FIB-section images of amphiboles and apatites in the Tissint and Zagami shergottites can be seen in [Fig. A20](#), [A21](#), [A22](#), and [A23](#). The location of the two FIB-sections used in [Chapter 5](#) is displayed in [Fig. A24](#). Labels are used to display the locations where TEM-EDS analyses reported in [Table A19](#) have been conducted in each FIB-section.

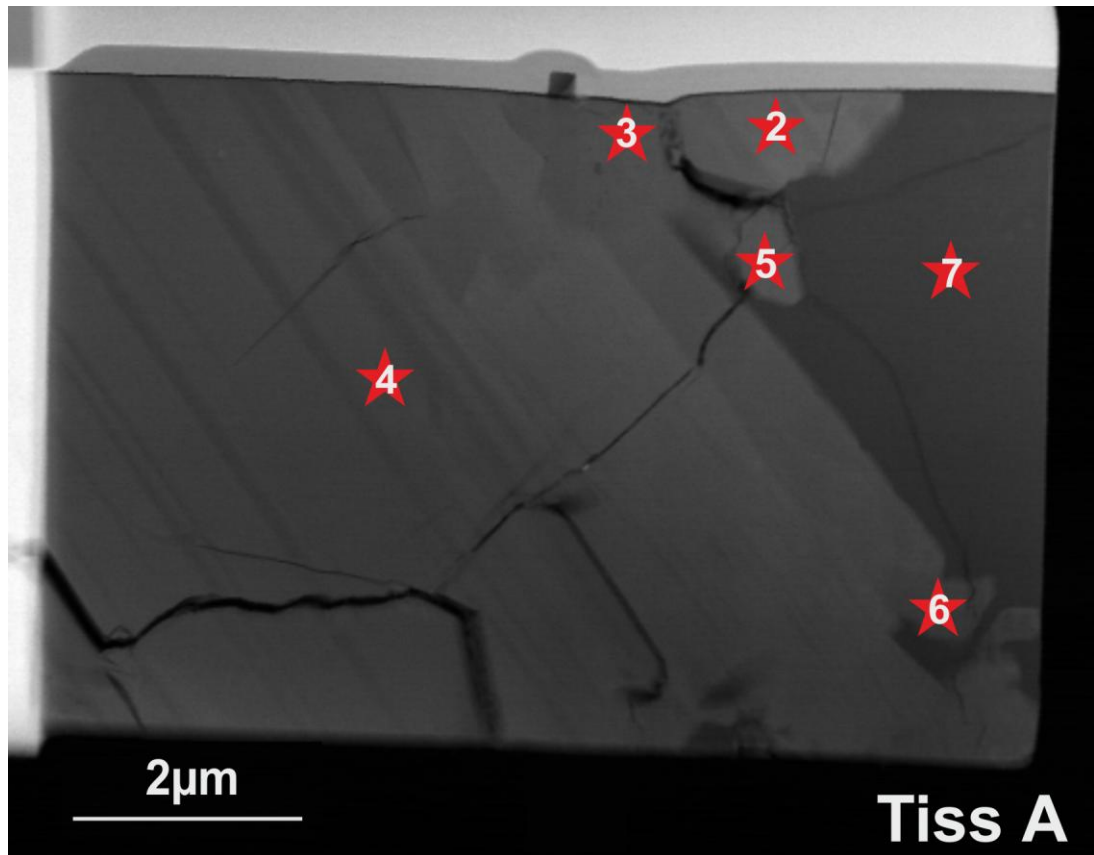


Fig. A20 - FIB-section of the amphibole area Tiss A. Symbol and labels are used to identify the location of the TEM-EDS analysis as reported in [Table 5.2](#) and in [Table A19](#).

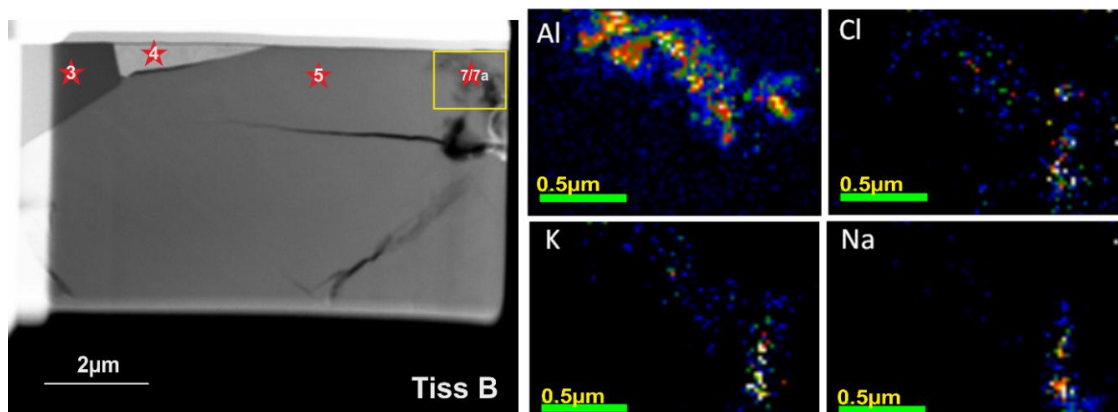


Fig. A21 - FIB-section of the amphibole area Tiss B (left) with Al, Cl, K, and Na elemental maps (right) taken on the yellow-marked area of the FIB-section. Symbol and labels are used to identify the location of the TEM-EDS analysis as reported in [Table 5.2](#) and in [Table A19](#).

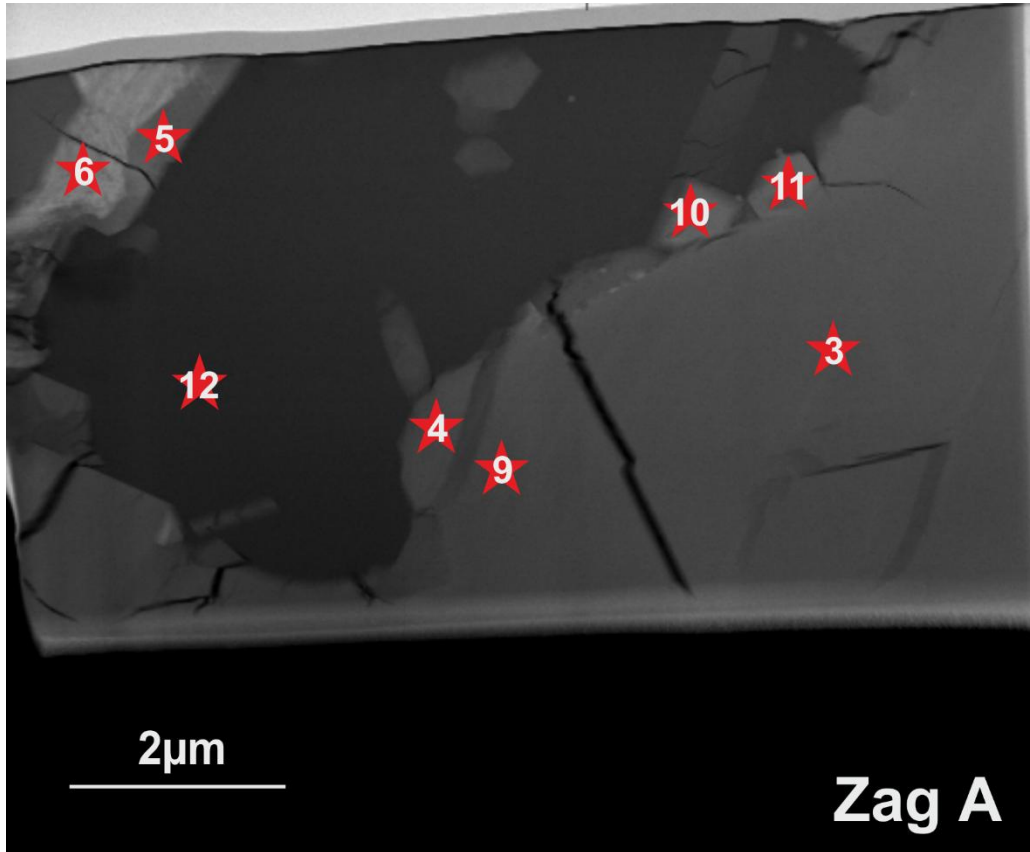


Fig. A22 - FIB-section of the amphibole area Zag A. Symbol and labels are used to identify the location of the TEM-EDS analysis as reported in [Table 5.2](#) and in [Table A19](#).

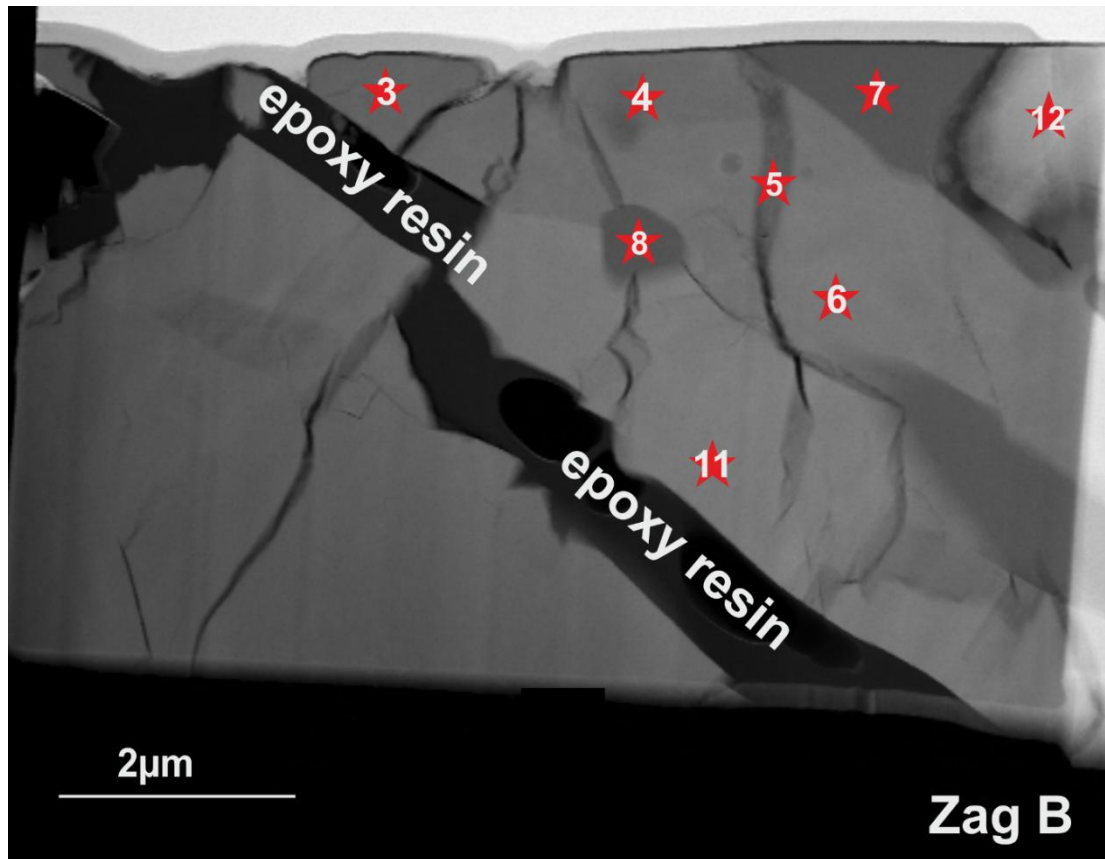


Fig. A23 - FIB-section of the amphibole area Zag B. Symbol and labels are used to identify the location of the TEM-EDS analysis as reported in [Table 5.2](#) and in [Table A19](#).

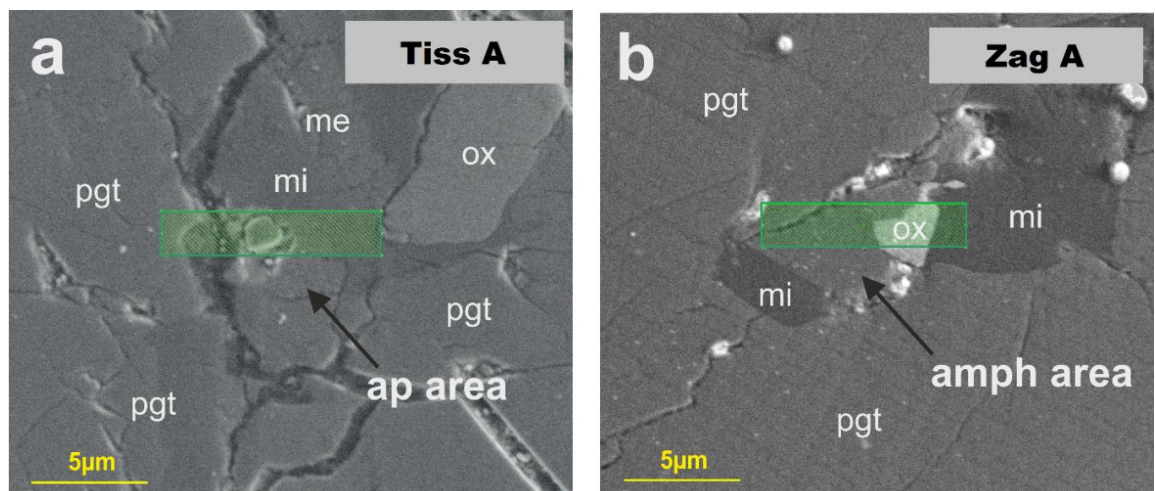


Fig. A24 - FIB-section location (green area) of the amphibole area Tiss A and Zag A used in [Chapter 5](#).

Appendix C – Sample information and logistics

Information on codes, characteristics, measurements, and loan agreement about each sample used in this work can be found in [Table A20](#).

All the raw data acquired in this work are stored and can be accessed at the URL address https://gla-my.sharepoint.com/personal/n_mari_1_research_gla_ac_uk/_layouts/15/onedrive.aspx.

Table A20 - Sample information.

Meteorite Name	Code	Morphology	SEM-EDS	X-ray elemental maps	LA-ICP-MS	Re-O isotopes and HfE	Schotoppe	FB-TEM	Loan
Tissint (thin section)	P28897	Square	Yes (cl, px, msk, ilm, med, cr, pyr, mel)	Yes	Yes	No	No	Yes	NHM
Tissint (thin section)	P28895	Triangular	Yes (cl, px, msk, ilm, med, cr, pyr, mel)	Yes	Yes	No	No	No	NHM
Tissint (thin section)	P28894	Square	Yes (cl, px, msk, ilm, med, cr, pyr, mel)	Yes	Yes	No	No	Yes	NHM
Tissint (thin section)	P28892	Triangular	Yes (cl, px, msk, ilm, med, cr, pyr, mel)	Yes	Yes	No	No	No	NHM
Tissint (4 fragments)	2-3-3-91	Variable	No	Yes	No	Yes	No	Yes	Cris Herd
Zagami (polished fragment)	BM1993M10	Triangle	Yes (px, msk, mel)	Yes	No	No	No	No	SIERC
Nakhla (chip)	BM1913,35	Circle	No	Yes	No	No	No	No	NHM
Nakhla (thin section)	BM1913,26 #2	Square	Yes (scapolite)	Yes	No	No	Yes	No	NHM
Lafayette (chip)	BM1559,755	Circle	No	Yes	No	No	No	No	NHM
Lafayette (thin section)	BM1559,755	Variable	Yes (scapolite)	Yes	No	No	Yes	No	NHM
Mill 0900321 (chip)	100	Irregular	No	Yes	No	Yes, HfE only	No	No	NASA
Mill 0900321 (thin section)	MIL 090032,28	Irregular	Yes (scapolite)	Yes	No	No	Yes	No	NASA
Yamato 000593 (thin section)	37	Circle	No	Yes	No	No	No	No	JAXA
Yamato 000593 (thin section)	37	Many circles	No	Yes	No	No	No	No	JAXA
Yamato 000749 (thin section)	59	Many irregular	No	Yes	No	No	Yes	No	JAXA
Yamato 000749 (thin section)	59	Circle	No	Yes	No	No	No	No	JAXA
Yamato 000749 (thin section)	59	Many irregular	No	Yes	No	No	No	No	JAXA
MWA 8159 (thin section)	Home (purchased)	Square	No	Yes	No	No	No	No	SIERC

Appendix D – Supplementary references

- Anders E. and Grevesse N., 1988. Abundances of the elements: meteoritic and solar. *Geochimica & Cosmochimica Acta*, vol. 53, pp. 197-214.
- Carmichael I. S. E. and Nicholls J., 1967. Iron-titanium oxides and oxygen fugacities in volcanic rocks. *Journal of Geophysical Research*, vol. 72, issue 18, pp. 4665-4687.
- Charles K., Shearer C. K., Bell A. S., Burger P. V., McCubbin F. M., Agee C., Simon J. and Papike J. J., 2015. The mineralogical record of fO₂ variation and alteration in Northwest Africa 8159 (NWA 8159). Evidence for the interaction between a mantle derived martian basalt and a crustal component(s). *46th Lunar and Planetary Science Conference*, Abstract #2010.
- First E. and Hammer J. E., 2016. Igneous cooling history of olivine-phyric shergottite Yamato 980459 constrained by dynamic crystallization experiments. *Meteoritics & Planetary Science*, vol. 51, issue 7, pp. 1233-1255.
- Frost B. R., 1988. A review of graphite-sulphide-oxide-silicate equilibria in metamorphic rocks. *Rendiconti Societa' Italiana Mineral. Petro.*, vol. 43, pp. 25-40.
- Frost B. R., 1991. Introduction to oxygen fugacity and its petrologic importance. *Reviews in Mineralogy and Geochemistry*, vol. 25, issue 1, pp. 1-9.
- Gerlach T. M., 1993. Oxygen buffering of Kilauea volcanic gases and the oxygen fugacity of Kilauea basalt. *Geochim. Cosmochim. Acta*, vol. 57, pp. 795-814.
- Ghosal S., Sack R. O., Ghiorso M. S., and Lipschutz M. E., 1998. Evidence for a reduced, Fe-depleted Martian mantle source region of Shergottites. *Contrib. Mineral. Petrology*, vol. 130, pp. 346-357.
- Haggerty S. E., 1976. Opaque mineral oxides in terrestrial igneous rocks. *Rev. Mineral.*, vol. 3, Hg101-Hg300.
- Hallis L. J., Simpson S., Mark D. and Lee M. R., 2016. Martian alteration in unique meteorite NWA 8159? *79th Annual Meeting of the Meteoritical Society*, Abstract #6442.

Hammer J. E., 2006. Influence of fO_2 and cooling rate on the kinetics and energetics of Fe-rich basalt crystallization. *Earth and Planetary Science Letters*, vol. 248, pp. 618-637.

Herd C. D. K., 2006. Insights into the redox history of the NWA 1068/1110 martian basalt from mineral equilibria and vanadium oxybarometry. *Am. Miner.*, vol. 91, pp. 1616-1627.

Herd C. D. K., Agee C. B., Muttik N. and Walton E. L., 2014. The NWA 8159 Martian augite basalt: Possible eruptive from the nakhlite suite. *45th Lunar and Planetary Science Conference*, Abstract #2423.

Herd C. D. K., Papike J. J., and Brearley A. J., 2001. Oxygen fugacity of martian basalts from electron microprobe oxygen and TEM-EELS analyses of Fe-Ti oxides. *Am. Mineral.*, vol. 86, pp. 1015-1024.

Kayzar T. M., Borg L., Kruijer T. S., Kleine T., Brennecka G. and Agee C., 2015. Neodymium and tungsten isotope systematics of Mars inferred from the augite basaltic meteorite NWA 8159. *46th Lunar and Planetary Science Conference*, Abstract #2357.

Kolzenburg S., Di Genova D., Giordano D., Hess K. U., and Dingwell D. B., 2018. The effect of oxygen fugacity on the rheological evolution of crystallizing basaltic melts. *Earth and Planetary Science Letters*, vol. 487, pp. 21-32.

Kuno H., 1960. High-alumina basalt. *J. Petrol.*, vol. 1, pp. 121-145.

Morse S. A., 1969. The Kiglapait layered intrusion, Labrador. *Geol. Soc. Am. Mem.*, vol. 112, pp. 1-198.

Osborn E. F., 1959. Role of oxygen pressure in the crystallization and differentiation of basaltic magma. *American Journal of Science*, vol. 257, issue 9, pp. 609-647.

Presnall D. C., 1966. The join forsterite-diopside-iron oxide and its bearing on the crystallization of basaltic and ultramafic magmas. *Am. J. Sci.*, vol. 264, pp. 753-809.

Provencio P., Shearer C. K., Bell A. S. and Burger P. V., 2016. Nano-scale investigation of spinel-orthopyroxene intergrowths in Northwest Africa 8159. A record of fO_2 but at what temperature? *47th Lunar and Planetary Science Conference*, Abstract #2411.

Richter K. and Drake M. J., 1996. Core Formation in Earth's Moon, Mars and Vesta. *Icarus*, vol. 124, pp. 513-529.

Rudashevsky N. S., Avdontsev S. N., and Dneprovskaya M. B., 1992. Evolution of PGE mineralization in hortonolitic dunites of the Mooihoek and Onverwacht pipes, Bushveld Complex. *Mineralogy and Petrology*, vol. 47, issue 1, pp. 37-54.

Sato M., 1978. Oxygen fugacity of basaltic magmas and the role of gas-forming elements. *Geophys. Res. Lett.*, vol. 5, pp. 447-449.

Sharp T. G., Walton E. L. and Hu J., 2015. Shock effect in NWA 8159: evidence for a modest shock pressure and a large impacting body. *46th Lunar and Planetary Science Conference*, Abstract #1939.

Shearer C. K., Bell A. S., Burger P. V., McCubbin F. M., Agee C., Simon J., and Papike J. J., 2015. The Mineralogical Record of fO₂ Variation and Alteration in Northwest Africa 8159 (NWA 8159). Evidence for the Interaction Between a Mantle Derived Martian Basalt and a Crustal Component(s). *46th Lunar and Planetary Science Conference*, Abstract #1483.

Shirai N. and Ebihara M., 2004. Chemical characteristics of a Martian meteorite, Yamato 980459. *Antarctic Meteorite Research*, vol. 17, pp. 55-67.

Simon J. I., Peters T. J., Tappa M. J. and Agee C. B., 2014. Northwest Africa 8159: An approximately 2.3 Billion-Year Old Martian Olivine-Bearing Augite Basalt. *77th Annual Meeting of the Meteoritical Society*, Abstract #5363.

Taylor L. A., Nazarov M. A., Shearer C. K., McSween H. Y., Cahill J., Neal C. R., Ivanova M. A., Barsukova L. D., Lentz R. C., Clayton R. N., and Mayeda T. K., 2002. Martian meteorite Dhofar 019: A new shergottite. *Meteorit. Planet. Sci.*, vol. 37, issue 8, pp. 1107-1128.

Thode H. G., 1970. Sulphur isotope geochemistry and fractionation between coexisting sulphide minerals. *Mineral. Soc. Amer.*, vol. 3, pp. 133-144.

Treiman A. H. and Irving A. J., 2008. Petrology of Martian meteorite Northwest Africa 998. *Meteorit. Planet. Sci.*, vol. 43, pp. 829- 854.

Vaci Z., Newsom H. E., Agee C. B., Brearley A. J., Tschauner O. and Herd C. D. K., 2016. Electron Probe Microanalysis, Micro X-Ray Diffraction, and Deuterium-Hydrogen Analysis of Hydrous Alteration in Martian Meteorites Northwest Africa 10416 and 8159. *47th Lunar and Planetary Science Conference*, Abstract #2538.

Yoder H. S. and Tilley C. E., 1962. Origin of basalt magmas: an experimental study of natural and synthetic rock systems. *J. Petrol*, vol. 3, pp. 342-532.